Pharmacological and nanotherapeutic modulators of glioblastoma and its microenvironment

by

Issan Zhang

Department of Pharmacology and Therapeutics

McGill University, Montreal

August 2020

A thesis submitted to McGill University in partial fulfillment of the requirements of the degree of Doctor of Philosophy

Dédiée à Georgette Sinclair,

professeure hors pair

& AW

Abstract

Glioblastoma multiforme is a devastating disease for which available treatments consistently fail. The current clinical standard, temozolomide, is ineffective in most patients due to resistance mechanisms such as the upregulation of DNA repair enzymes. The main objective of this thesis is to report on pharmacological and nanotherapeutic modulators of glioblastoma, focusing on 1) the mechanism of action of a novel histone deacetylase inhibitor (sahaquine), 2) combination treatments targeting tumor defenses and 3) effects on microglia and astrocytes in the tumor microenvironment.

Histone deacetylase 6 inhibitors are promising therapeutic agents for glioblastoma due to their effect on cytoplasmic targets (cytoskeleton, kinase signalling) important for cancer invasiveness and growth. We explored the mechanisms of sahaquine, a novel hybrid molecule combining two FDA-approved drugs: primaquine and vorinostat. We showed sahaquine to be a selective histone deacetylase 6 inhibitor effective against glioblastoma as well as different cell types in the tumor microenvironment, from simple monolayer cultures to three-dimensional brain tumor stem cell neurospheres, tumoroids and cerebral organoids. Given the heterogeneous nature of glioblastoma, we also tested synergistic combination treatments tackling key aspects of tumor survival such as antioxidative defenses and lipid droplets. We focused on the role of lipid droplets in trapping hydrophobic molecules such as curcumin, a promising natural compound with anti-cancer properties. One of the main challenges of emerging therapeutic agents for the brain is their limited permeability at the blood brain barrier, which is why nanostructures can be attractive as both drug carriers and molecules with inherent pharmacological effects. In this context, we explored the use of dendritic polyglycerol sulfate

as anti-inflammatory agents to modulate activated microglia and astrocytes, which infiltrate and contribute to the maintenance of the tumor microenvironment.

Taken together, the results from this work support the use of rational combination treatments that take into account mechanisms of adaptation in glioblastoma and the contribution of neural cells surrounding the tumor.

Résumé

Le glioblastome multiforme est une maladie terrible pour laquelle les traitements existants échouent. La référence clinique actuelle, témozolomide, est inefficace pour la plupart des patients dû à des mécanismes de résistance telle la surrégulation des enzymes de réparation d'ADN. L'objectif principal de cette thèse est de faire rapport sur les modulateurs pharmaceutiques et nanothérapeutiques pour le glioblastome, focalisant sur 1) le mécanisme d'action d'un nouvel inhibiteur d'histone désacétylase 6 (sahaquine), 2) les traitements combinés visant les défenses tumorales et 3) les effets sur la microglie et les astrocytes dans le microenvironnement tumoral.

Les inhibiteurs d'histone désacétylase 6 sont des agents thérapeutiques prometteurs pour le glioblastome car leurs cibles cytoplasmiques (cytosquelette, signalisation de kinases) sont importantes pour l'envahissement et la croissance des tumeurs. Nous avons exploré les mécanismes de sahaquine, une nouvelle molécule hybride combinant deux médicaments approuvés par la FDA : primaquine et vorinostat. Nous avons démontré que sahaquine est un inhibiteur d'histone désacétylase 6 sélectif efficace envers le glioblastome et plusieurs types de cellules faisant partie du microenvironnement tumoral, non seulement en cultures monocouches, mais aussi en cultures tridimensionnelles de cellules souches de tumeurs cérébrales (neurosphères), tumoroïdes et organoïdes cérébraux. À cause de l'hétérogénéité du glioblastome, nous avons aussi testé des traitements combinés synergiques visant des défenses tumorales essentielles, tels les défenses antioxydantes et les gouttelettes lipidiques. Nous avons focalisé sur le rôle des gouttelettes lipidiques dans le piégeage de molécules hydrophobes, telle la curcumine, un composé anticancer naturel prometteur. L'un des principaux défis des agents thérapeutiques pour le cerveau est leur perméabilité limitée à la barrière hématoencéphalique.

C’est pourquoi certaines nanostructures sont attrayantes à la fois comme vecteurs de médicament et en tant que molécules pharmaceutiques. Dans ce contexte, nous avons exploré l’utilisation de sulfonates de polyglycérol dendritiques comme agents anti-inflammatoires pour moduler l’activation de microglie et d’astrocytes qui infiltrent le microenvironnement tumoral et contribuent à son maintien.

En somme, les résultats de cette thèse appuient l’utilisation de traitements combinés rationnels qui tiennent compte des mécanismes d’adaptation du glioblastome et la contribution des cellules neurales autour de la tumeur.

Table of Contents

List of Figures and Tables

FIGURES

TABLES

List of Abbreviations

Akt ……. Protein kinase B

ABCB1 ..…… ATP Binding Cassette Subfamily B Member 1

ABCG2 …….. ATP Binding Cassette Subfamily G Member 2

ANOVA ……. Analysis of variance

ATP …… Adenosine Triphosphate

BBB …… Blood brain barrier

bFGF ……... Basic fibroblast growth factor

BSO ……. Buthionine sulfoximine

BTSC ……... Brain tumor stem cells

CAC ……. Critical aggregation concentration

CI ……. Combination index

CO2 ……. Carbon dioxide

CNS ……. Central nervous system

cPLA2 ……. Cytosolic Phospholipase A2

CTIP2 …….. COUP-TF-interacting protein 2

Cur ……... Curcumin

Cy5 …….. Cyanine5

DAPI …… 4’,6-diamidino-2-phenylindole

DHA ……. Docosahexaenoic acid

DIEA …… *N,N*-diisopropylethylamine

DMEM ……. Dulbecco's Modified Eagle Medium

DMSO …….. Dimethyl sulfoxide

DNA ……. Deoxyribonucleic acid

DOPC …… 1,2-dioleoyl-sn-glycero-3-phosphocholine

dPG ……... Dendritic polyglycerol

dPGS ……. Dendritic polyglycerol sulfates

EBs …… Embryoid bodies

ECG …….. Electrocardiogram

EDTA …… Ethylenediaminetetraacetic acid

EGFR ……. Epidermal growth factor receptor

EGF …… Epidermal growth factor

EPR …… Enhanced permeability and retention effect

ER …….. Endoplasmic reticulum

ERK1/2 …….. Extracellular signal-regulated kinases 1 and 2

FBS ……..... Fetal bovine serum

FDA ……... Food and Drug Administration (U.S.)

FGF-b …… Fibroblast Growth Factor-basic

GA ……. Green fluorescent protein subunit

GABA …… Gamma-Aminobutyric acid

GBM …….. Glioblastoma multiforme

GFP …… Green fluorescent protein

GSH …… Glutathione

G2/M …….. Growth 2 and mitotic phases

GM-CSF ……. Granulocyte-macrophage colony-stimulating factor

HATU ……. 1-[*bis*(dimethylamino)methylene]-1*H*-1,2,3-triazolo[4,5-86 *b*]pyridinium 3-oxid hexafluorophosphate

HDAC ……. Histone deacetylase

HDACi …… Histone deacetylases inhibitor

hESC ……... Human embryonic stem cells

HIF …….. Hypoxia-inducible factor

HMGB1 …….. High mobility group box 1

HRP ……. Horseradish peroxidase

HSP90 ……. Heat shock protein 90

IC50 …… Half maximal inhibitory concentration

IF ……. Immunofluorescence

IL-6 ……. Interleukin-6

IL-10 ……... Interleukin-10

iPSCs …….. Induced pluripotent stem cells

IR …… Infrared

JAK1/2 …… Janus kinases 1 and 2

LCN2 ……... Lipocalin-2

LD …… Lipid droplet

LPS …….. Lipopolysaccharide

MAP-2 ……. Microtubule-associated protein 2

MEM-NEAA ….. MEM non-essential amino acids solution

MGMT ……. O^6-methylguanine-DNA methyltransferase

MMPs …….. Matrix metalloproteinases

MS ……... Mass spectrometry

MTT ……. 3-(4,5-Dimethylthiazol-2-yl)-2,5-diphenyltetrazolium bromide

NES …….. Nuclear export signal

NFκB …… Nuclear factor kappa-light-chain-enhancer of activated B cells

NLS …….. Nuclear localization signal

NMR ……. Nuclear magnetic resonance

NIM …….. Neuronal induction media

OCT …….. Optimum cutting temperature

PBS ……... Phosphate buffered saline

PD-L1 ……... Programmed death-ligand 1

PI …….. Propidium iodide

PVDF ……... Polyvinylidene difluoride

Pyr-2 …… Pyrrolidine-2

RA ……..... Red fluorescent protein subunit

RFP …….. Red fluorescent protein

RIPA ……. Radioimmunoprecipitation assay

ROCK ……... Rho kinase

ROS ……... Reactive oxygen species

RT …….. Room temperature

SAHA …… Suberanilohydroxamic acid

SD ……. Standard deviation

SDS-PAGE ……... Sodium dodecyl sulfate–polyacrylamide gel electrophoresis

SEM …….. Standard error of the mean

siRNA ……... Small interfering ribonucleic acid

SOX-2 ……... Sex determining region Y-box 2

SREBP …….. Sterol regulatory element-binding protein

SRSF3 ……... Serine/arginine-rich splicing factor 3

STAT3 …….. Signal transducer and activator of transcription 3

STS ……... Staurosporine

TAMs ……... Tumor-associated macrophages

TGF-β ……... Transforming growth factor beta

TMZ ……. Temozolomide

TNF-α ……... Tumor necrosis factor alpha

TOF-SIMS …… Time-of-flight secondary ion mass spectrometry

VEGF ……... Vascular endothelial growth factor

2D ……. Two-dimension

3D ……. Three-dimension

Contribution to Original Knowledge

1. Inhibition of glioblastoma cell proliferation, invasion, and mechanism of action of a novel hydroxamic acid hybrid molecule. Zhang, I.*, Beus, M.*, Stochaj, U., Le, P. U., Zorc, B., Rajic, Z., Petrecca, K., & Maysinger, D. (2018). Cell Death Discovery, 4, 41.

This study was first to report on the mechanisms of action of the novel HDAC6 inhibitor sahaquine in glioblastoma multiforme, showing effects on pathways directly (e.g. α-tubulin), and indirectly (e.g. EGFR, ERK1/2) regulated by HDAC6. The study addressed several challenging variables in the disease, namely tumor heterogeneity (killing of patient-derived brain tumor stem cells), multidrug resistance (P-glycoprotein inhibition and combination treatments) and invasiveness (3D invasion assay). Taken together, these results showed the potential of sahaquine as an anti-cancer agent and the importance of testing different aspects of glioblastoma aggressiveness prior to *in vivo* studies.

2. Pharmacological inhibition of lipid droplet formation enhances the effectiveness of curcumin in glioblastoma. Zhang, I.*, Cui, Y.*, Amiri, A., Ding, Y., Campbell, R. E., & Maysinger, D. (2016). European Journal of Pharmaceutics and Biopharmaceutics: Official Journal of Arbeitsgemeinschaft Fur Pharmazeutische Verfahrenstechnik e.V, 100, 66–76.

This work investigated an emerging mechanism of resistance in glioblastoma associated with lipid droplets. The implications of modulating these organelles on the effectiveness of lipophilic agents (e.g. curcumin) go beyond pharmacological applications in cancer, particularly given the diverse and dynamic functions of lipid droplets in neural cells and inflammatory processes. Moreover, this study employed a new dimerization-dependent biosensor in tumoroids, making use of 3D models

to investigate cellular pathways at the single-cell level. Altogether, these results underlined the relevance of lipid droplets as pharmacological targets in cancer cells and the importance of combination treatments for glioblastoma.

3. Nanotherapeutic Modulation of Human Neural Cells and Glioblastoma in Organoids and Monocultures. Zhang, I., Lépine, P., Han C., Lacalle-Aurioles M., Chen C. X.-Q., Haag R., Durcan T. M. & Maysinger D. (2020). Cells, 9, 2434.

In Chapter 4, I show the new use of cerebral organoids to investigate nanostructure-glia interactions. I also established co-cultures of human neural cells with glioblastoma as an *in vitro* 3D system to study crosstalk between the glioblastoma and normal neural cells, which is a key component of the tumor microenvironment. The results provide a basis for future studies of human 3D co-cultures (organoids, embedded tumoroids) for answering some questions typically investigated in animal models, and for testing nanostructures as modulators of human glial cells.

*Shared first authorship

Contribution of Authors

This thesis is in a manuscript-based format in accordance to the Guidelines for Thesis Preparation from the Graduate and Postdoctoral Studies Office of McGill University. It comprises three manuscripts, of which the contribution of each author is described:

Chapter 2: Inhibition of glioblastoma cell proliferation, invasion, and mechanism of action of a novel hydroxamic acid hybrid molecule**. Issan Zhang***, Maja Beus*, Ursula Stochaj, Phuong Uyen Le, Branka Zorc, Zrinka Rajić, Kevin Petrecca, Dusica Maysinger. Cell Death Discovery. 2018; 4:41.

Immunocytochemistry and migration assays were performed by Issan Zhang. Human brain tumor stem cells and human brain sections were provided by Dr. Kevin Petrecca and assays using these (viability, immunohistochemistry, invasion assay) were performed by Issan Zhang with the help of Dr. Phuong Uyen Le. Issan Zhang and Maja Beus performed viability assays (cell counting, MTT). Dr. Ursula Stochaj performed Western blots. Biological experiments were conducted under the guidance of Dr. Dusica Maysinger. Maja Beus synthesized sahaquine under the guidance of Drs. Branka Zorc and Zrinka Rajić. The manuscript was drafted by Issan Zhang and Maja Beus and reviewed by Dr. Dusica Maysinger. The text was further edited by Drs. Ursula Stochaj, Phuong Uyen Le, Branka Zorc, Zrinka Rajić and Kevin Petrecca.

Chapter 3: Pharmacological inhibition of lipid droplet formation enhances the effectiveness of curcumin in glioblastoma. **Issan Zhang***, Yiming Cui*, Abdolali Amiri, Yidan Ding, Robert E. Campbell, Dusica Maysinger. Eur J Pharm Biopharm. 2016; 100:66-76.

Issan Zhang performed all biological experiments (transfections, imaging) using the caspase-3 biosensor and contributed to cell viability data. Yiming Cui performed viability measurements with the help of Abdolali Amiri, as well as lipid droplet labelling and imaging. Biological experiments were conducted under the guidance of Dr. Dusica Maysinger. The caspase biosensor was developed and provided by Drs. Yidan Ding and Robert E. Campbell. The manuscript was written by Issan Zhang and Dr. Dusica Maysinger, with editing from Yiming Cui, Abdolali Amiri, Dr. Yidan Ding and Dr. Robert E. Campbell.

Chapter 4: Nanotherapeutic modulation of human neural cells and glioblastoma in organoids and monocultures. **Issan Zhang**, Paula Lépine, Chanshuai Han, Maria Lacalle-Aurioles, Carol X.-C. Chen, Rainer Haag, Thomas M. Durcan, and Dusica Maysinger. Cells. 2020; 9:2434.

Experiments with dendrimeric polyglycerol sulfates were performed by Issan Zhang under the guidance of Dr. Dusica Maysinger, including immunocytochemistry, immunohistochemistry, fluorescence imaging, viability assays and Western blotting of treated cerebral organoids, human astrocytes and microglia. Issan Zhang prepared the tumoroids and developed the invasion assay in co-culture. Cerebral organoids were prepared and characterized by Paula Lépine and Dr. Chanshuai Han, with the assistance of Drs. Maria Lacalle-Aurioles and Xiuqing-C. Chen, and under the supervision of Dr. Thomas M. Durcan. Dr. Rainer Haag provided the dendrimeric polyglycerol sulfates. The manuscript was written by Issan Zhang with editing from Dr. Dusica Maysinger, Paula Lépine, Dr. Chanshuai Han and Dr. Thomas M. Durcan.

*Shared first authorship

List of Publications

Ratiometric biosensors based on dimerization-dependent fluorescent protein exchange.

Ding Y, Li J, Enterina JR, Shen Y, **Zhang I**, Tewson PH, Mo GCH, Zhang J, Quinn AM, Hughes TE, Maysinger D, Alford SC, Zhang Y, Campbell RE. 2015.

Nature Methods, 12:195-8.

A fast track strategy toward highly functionalized dendrimers with different structural layers: "Onion peel approach".

Sharma,R, **Zhang I**, Abbassi L, Rej R, Maysinger D, Roy R. 2015.

Polymer Chemistry, 6:1436-1444.

Low generation Polyamine Dendrimers Bearing Flexible Tetraethylene Glycol as nanocarriers for plasmids and siRNA.

Sharma R, **Zhang I,** Shiao TC, Pavan GM, Maysinger D, Roy R. 2016.

Nanoscale, 8:5106-19.

Boron nitride nanotubes as vehicles for intracellular delivery of fluorescent drugs and probes.

Niskanen J, **Zhang I**, Xue Y, Golberg D, Maysinger D, Winnik FM. 2016.

Nanomedicine (Lond), 11:447-63.

Pharmacological inhibition of lipid droplet formation enhances the effectiveness of curcumin in glioblastoma.

Zhang I*, Cui Y*, Amiri A, Ding Y, Campbell RE and Maysinger D. 2016.

European Journal of Pharmaceutics and Biopharmaceutics, 100:66-76.

Remodeling of lipid bodies by docosahexaenoic acid in activated microglial cells.

Tremblay ME, **Zhang I**, Bisht K, Savage JC, Lecours C, Parent M, Titorenko V, Maysinger D. 2016.

Journal of Neuroinflammation, 13:116.

Nutritional and Nanotechnological Modulators of Microglia.

Maysinger D, **I Zhang**. 2016.

Frontiers in Immunology, 7:270.

Dendritic Polyglycerol Sulfates in the Prevention of Synaptic Loss and Mechanism of Action on Glia.

Maysinger D, Ji J, Moquin A, Hossain S, Hancock MA, **Zhang I**, Chang PKY, Rigby M, Anthonisen M, Grütter P, Breitner J, McKinney RA, Reimann S, Haag R, Multhaup G. 2017.

ACS Chemical Neuroscience, 9:260-271.

Inhibition of glioblastoma cell proliferation, invasion, and mechanism of action of a novel hydroxamic acid hybrid molecule.

Zhang I*, Beus M*, Stochaj U, Le PU, Zorc B, Rajić Z, Petrecca K, Maysinger D. 2018.

Cell Death Discovery, 4:41.

Unraveling Aqueous Self-Assembly of Telodendrimers to Shed Light on Their Efficacy in Drug Encapsulation.

Moquin A, Sturn J, **Zhang I**, Ji J, Celsing R, Vali H, Maysinger M, Kakkar A. 2019.

ACS Applied Bio Materials, 10:4515-4526.

Ratiometric pH Sensing in Living Cells Using Carbon Dots.

Macairan JR*, **Zhang I***, Clermont-Paquette A, Naccache R, Maysinger D. 2019.

Particle and Particle Systems Characterization, 37:1900430.

Dually-functionalized boron nitride nanotubes to target glioblastoma multiforme.

Niskanen J, **Zhang I**, Xue Y, Golberg D, Maysinger D, Winnik FM. 2020.

Materials Today Chemistry, 16:100270.

Nanotherapeutic Modulation of Human Neural Cells and Glioblastoma in Organoids and Monocultures.

Zhang I, Lépine, P, Han C, Lacalle-Aurioles M, Chen CXC, Haag R, Durcan TM, Maysinger D. 2020.

Cells, 9:2434.

*Shared first authorship

Acknowledgements

First and foremost, I would like to thank **Dr. Dusica Maysinger** for her unwavering support, humour and enthusiasm for science. The lab has been a second home for me, and much of my personal growth and confidence as a young woman was spurred by Dr. Maysinger's encouragements. I learned as much from our scientific discussions as from daily chats about life, music and more. I am very grateful for this opportunity received as an undergraduate and very happy to cherish our enduring friendship.

I would like to thank my committee members **Dr. John W. Gillard** and **Dr. Bastien Castagner** for their continued guidance and sensible advices through the many iterations of my thesis. Special thanks are due to my advisor **Dr. Lisa M. Münter** for her kindness and generosity.

Many thanks to past and present collaborators for their assistance and professionalism: **Dr. Kevin Petrecca**, **Dr. Phuong U. Le**, **Dr. Jukka Niskanen, Dr. Thomas M. Durcan, Dr. Chanshuai Han**, **Paula Lépine, Dr. Rafik Naccache** and **Jun-Ray Macairan**, among many others.

I would like to thank all my friends and colleagues for making the lab such a happy place. From **Angela Choi**, who patiently guided by first steps in the lab along with **Sebastien Boridy**, **Kevin Neibert** and **Diana Mejia**, to **Alexandre Moquin** and **Eliza Hutter**, who were always helpful and supportive throughout so many projects. To the lab guys, **David Cui**, **Jason Choi** and **Jeff Ji**, thank you for the teamwork and *camaraderie*. To the students, **Shiraj Dawadi, Lucas Ciancimino**, **Radu Grovu, Linda Liu, Otilia Popa, Winston Kwok, Samer Jaber**, **Rashad Yusifov, Haisam Shah,** thank you for your trust and hard work while (mostly) listening and (sometimes) taking notes. To my favorite gals, **Evan Rizzel Gran**, **Emma Meng**,

Jussânia Gnoatto, **Maja Beus**, **Hanna Koeppe**, **Esha Kaul**, **Qiaochu Zhang, Katerina Jabbour, Andrea Mebert, Melanie Chan, Morgan Foret** and **Aileen Yan,** thank you for the daily support and laughter through success and disaster. Many came and went through the years, but few have lost touch, which is what makes our ***Nanofamily*** so special.

Great appreciation goes to members of the Department of Pharmacology and Therapeutics, **Nadee Buddhiwickrama**, **Anna Cuccovia**, **Bobbi Bidochka**, **Dr. Nicolas Audet**, **Dr. Dominic Devost, Dr. Wolfgang Reintsch, Hélène Duplessis** and **Dr. David Kalant**, without whom little would have been possible. I would like to particularly thank **Tina Tremblay** and **Chantal Grignon**, whose contagious smiles and comforting words graced floor 13th every day.

Many thanks to the J.P. Collip Fellowship as well as funding agencies (CIHR and NSERC) for their financial support.

My personal, deepest gratitude goes to my family and close ones. To my parents **Ze Zhang** and **Jin Yang** for their unconditional love and dedication across time and continents, and to my brother **Roger Zhang**, whose support I can always count on (except for appreciating my jokes). To my most definitely human friends, **Emilie Bernatchez**, **Tianyu Zhang** and **Jérôme Boisvert-Chouinard**, with whom I continue to share so much through thick and thin, time and (social)distancing. To my teachers who had me love knowledge and learning. To **Marie-Christine Savard**, **Liliane Thériault**, **Nicolas Piètte-Lauzière, Philippe Bélanger** and **Olivier Boily,** whose precious friendship span more than a decade or two.

Lastly, to **John Mark Jose Alfonso and Petit Pot**, whose hearts are brighter than the sun.

Chapter 1. General Introduction

1.1. Overview of glioblastoma multiforme

Glioblastoma multiforme (GBM) is a devastating disease for which current therapeutic options are largely ineffective (Mary Elizabeth Davis, 2016; Shergalis et al., 2018). GBM is defined as grade IV glioma and is the most common and aggressive of brain tumors. The incidence is estimated at 4 per 100,000 people per year in Canada, and accounts for 50-60% of astrocytic tumors. The disease burden of GBM is significantly high due to the difficult tumor location and high mortality rate (Shergalis et al., 2018).

Traditionally, anti-cancer drugs used against GBM aimed at damaging the DNA of fast-proliferating cells. Carmustine and lomustine, are two nitrosureas first approved for GBM (Weller et al., 2013). Despite their severe side effects and poor outcomes, they are still given to resistant tumors as last recourse drugs (Rahman et al., 2014; Weller et al., 2013). The current clinical gold standard for GBM is temozolomide (TMZ)(Stupp et al., 2005, 2017). Although better tolerated than the nitrosureas, TMZ prevents disease progression in only 20-30% of patients. Since its FDA approval in 2005, little progress was achieved in terms of treatment effectiveness; median survival remains at 15-16 months and 5-year survival rates are dismal due to the prevalence of tumor resistance and recurrence (Mary Elizabeth Davis, 2016; S. Y. Lee, 2016a).

1.2. Limitations of current clinical standards

The propensity of GBM for recurrence is partly due to the infiltrative nature of the tumor. Single cells and cell clusters invade the surrounding normal tissue in a diffuse pattern, making complete surgical resection often impossible (Claes et al., 2007; C. Li et al., 2019). To preserve neurological functions and patient quality of life, subtotal resection is sometimes required, despite the risk of

residual tumor tissue. Following maximal resection, radiotherapy with concomitant chemotherapy is administered once the wound is healed. Treatment is aimed at killing residual tumor cells left in the lesion but is often ineffective due to the upregulation of DNA repair mechanisms in GBM and the presence of radiotherapy, chemotherapy-resistant brain tumor stem cells. It was reported that 90% of patients show recurrence at 2-3 cm of the original tumor site (S. W. Lee et al., 1999; Narayana et al., 2006).

The DNA repair enzyme most relevant in clinical settings is O6-methylguanine-DNA-methyltransferase (MGMT), which removes the methyl group added to guanine by TMZ, thus preventing DNA damage and cancer cell death (Hegi et al., 2005a). The methylation of MGMT promoter is predictive of TMZ treatment outcome; patients with methylated (silenced) promoters respond significantly better to TMZ compared to those with unmethylated promoters (Donson et al., 2007). Other DNA-repair mechanisms include base excision repair, single-strand break repair and mismatch repair machinery; all these can limit the effectiveness of genotoxic treatments (Erasimus et al., 2016a).

To avoid the burden of drug resistance, we proposed to investigate therapeutic agents with mechanisms of action distinct form that of "classical" anti-cancer drugs such as TMZ. In Chapter 2, we investigated the potential of a novel compound, sahaquine, acting as a selective inhibitor of HDAC6, and showed superior effectiveness compared to TMZ alone and even greater effectiveness as a component of combination therapy (*in vitro*). In Chapter 3, we demonstrated the effectiveness of combining the mechanisms of action of two agents, curcumin and pyrrolidine-2, to achieve synergistic cell killing in GBM. Finally, we used a dendrimeric nanostructure to modulate the GBM microenvironment and inhibit tumor growth (Chapter 4).

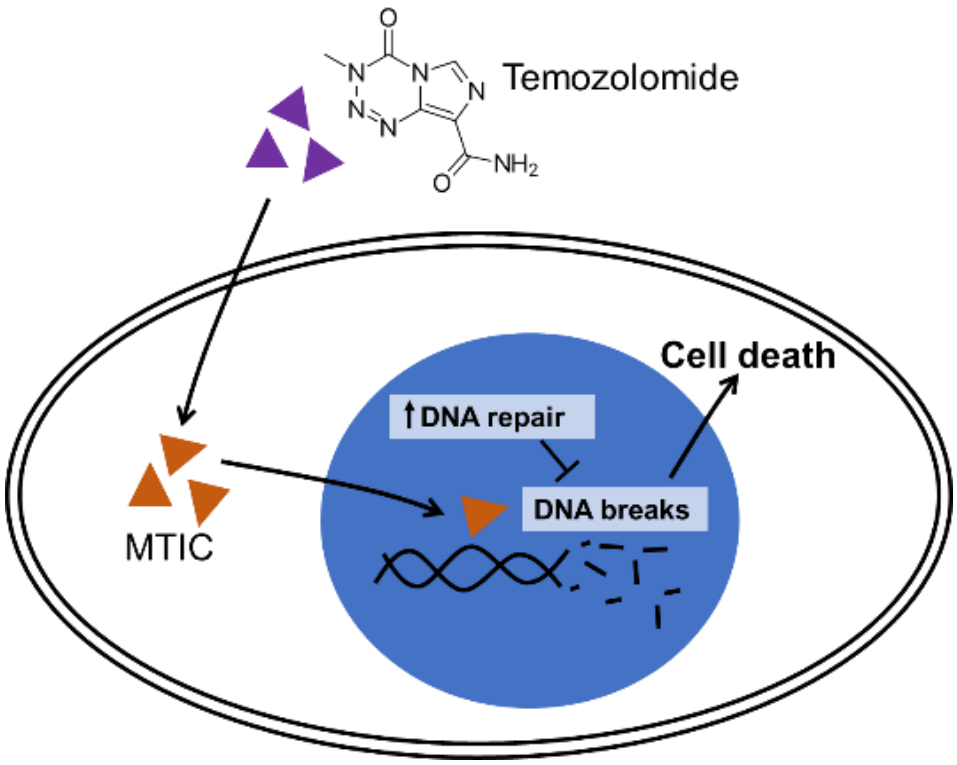

Figure 1.1. Mechanism of action of temozolomide and mechanisms of resistance in GBM to TMZ

1.3. Histone deacetylase inhibitors for GBM

Recently, histone deacetylase inhibitors (HDACi) have received increased attention as therapeutic agents in cancer research (Y. Li & Seto, 2016; Suraweera et al., 2018). HDACi have a long history as medications acting on the central nervous system, particularly in psychiatry and neurology, serving to stabilize mood and improve symptoms of neurodegenerative diseases, respectively (Shukla & Tekwani, 2020). Valproate, for instance, has been used since the 1960s for epilepsy thanks to its effects on voltage-gated sodium channels and GABA signalling. It was also shown to mediate epigenetic changes by selectively inhibiting Class I histone deacetylases and to inhibit growth of glioma cells *in vitro* (Driever et al., 1999). Vorinostat, a non-selective inhibitor acting on both Class I, Class IIa and Class IIb HDACs, was FDA-approved in 2006 for cutaneous T-cell lymphoma. It has since reached clinical trials for GBM in monotherapy and in combination with other drugs (e.g. TMZ)(Galanis et al., 2018; Hummel et al., 2013a).

However, several serious side effects are associated with inhibitors of Class I HDACs (HDAC1, 2, 3 and 8). Aside from primary toxicities such as nausea, diarrhea, fatigue and decreased blood cell counts (e.g. platelets, white blood cells), they also caused adverse cardiac events (ECG changes)(Subramanian et al., 2010).

1.3.1. Selective HDAC6 inhibitors for cancer research

To prevent the serious adverse effects associated with pan-HDACi, efforts were made to develop more selective HDAC inhibitors, particularly toward HDAC6. HDAC6 was distinguished from other HDACs as the first HDAC shown to be actively maintained in the cytoplasm, giving it a unique set of substrates. Furthermore, HDAC6 is often upregulated in cancer. In breast cancer,

HDAC6 contributes to invasiveness and metastasis; in melanoma, HDAC6 inhibition promotes cancer cell death; in ovarian cancer, HDAC6 inhibition synergized with anti-PD-L1 immune-checkpoint blockade to suppress tumor growth (Fukumoto et al., 2019).

Despite the interest in HDAC6, few HDAC6-selective inhibitors have been extensively studied for GBM. Ricolinostat (ACY-1215), the first orally available HDAC6-selective inhibitor to reach clinical trials, was well tolerated up to 160 mg daily, with less severe toxicities compared to that of non-selective HDAC inhibitors (e.g. vorinostat, panobinostat). However, the access of ricolinostat to the brain is limited, and recent studies showed potential resistance mechanisms in cancer cells due to the upregulation of multidrug resistance transporters (Wu et al., 2018).

1.3.2. Sahaquine, a hybrid molecule

To show if some limitations of ricolinostat could be overcome, we investigated a novel HDAC6-selective inhibitor named sahaquine. Sahaquine is a hybrid molecule comprising of two FDA-approved drugs, primaquine and vorinostat as active moieties. The hydroxamate moiety from vorinostat confers HDAC inhibitory effects to sahaquine, whereas the primaquine moiety was hypothesized to serve two main purposes: 1. give the molecule bulkiness, limiting its accessibility to the active site of Class I/Class IIa HDACs, thereby conferring selectivity to HDAC6; 2. give the molecule P-glycoprotein inhibitory properties (A.-R. Choi et al., 2016).

The higher level of HDAC6 in GBM compared for normal astrocytes and brain tissues helps GBM invade the surrounding normal tissues and is correlated with worse prognosis in patients. We hypothesized that sahaquine would be effective in killing and limiting invasiveness in GBM. We also hypothesized that sahaquine would inhibit P-glycoprotein, thus being

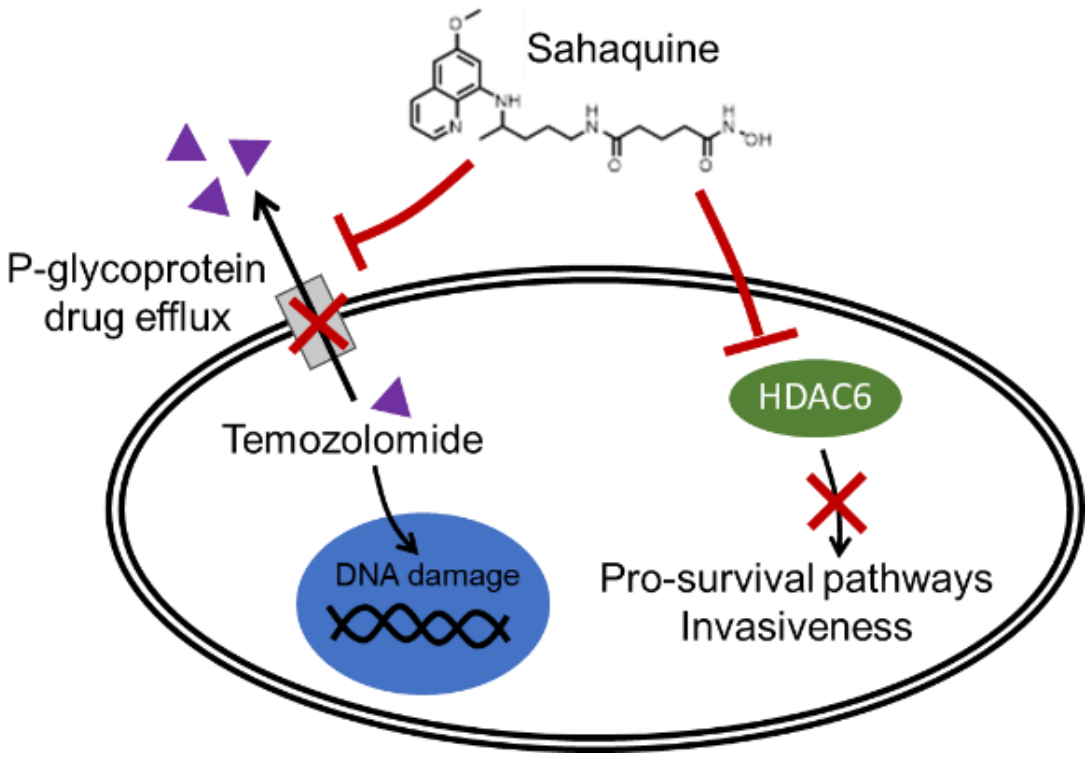

Figure 1.2. Structure of sahaquine and intracellular targets downstream of HDAC6 inhibition

advantageous in combination with drugs susceptible to multidrug resistance transporters. Our studies on sahaquine were published in Cell Death and Discovery and are the subject of Chapter 2.

Complementary supplemental studies in Chapter 4 further examined the effect of modulating cells of the tumor microenvironment, namely normal astrocytes and microglia, which can contribute importantly to disease progression. These studies explored the activation of several key transcription factors implicated in GBM (e.g. STAT3), as well as the use of advanced 3D *in vitro* brain models, cerebral organoids, to investigate tumor growth. 3D tumoroids were also useful glioblastoma models to test other compounds aside from sahaquine (e.g. curcumin, a natural compound).

1.4. Curcumin, a natural compound with multiple mechanisms of action

Due to the limitations of TMZ as monotherapy for GBM (standard clinical regimen 6-12 cycles of 28 days), we explored combination therapy with TMZ, curcumin and other compounds (J. Choi et al., 2017; I. Zhang et al., 2016). The rationale for combination therapy is that GBM is a heterogeneous disease (Dirkse et al., 2019; C. Li et al., 2019) with genetic and epigenetic differences not only between single cancer cells, but also between different niches of the tumor tissue (e.g. hypoxic, necrotic, semi-vascularized)(Z. Chen & Hambardzumyan, 2018; Hambardzumyan & Bergers, 2015). Thus, drug combinations and drugs with multiple mechanisms of action were proposed to have lower risks of encountering significant drug resistance in GBM compared to drugs with a single mode of action (e.g. TMZ).

Several natural compounds have multiple anti-cancer mechanisms of action. Phenolic compounds isolated from natural sources, such as curcumin and quercetin, are particularly interesting due to their tumor-killing properties and low toxicity to normal cells. Curcumin is the main curcuminoid in turmeric, the powdered form of *Curcuma longa*. Turmeric is a spice consumed by millions of people around the world everyday and has long being used in traditional Asian medicine for different disorders. Curcumin has an excellent safety record and has been marked as "Generally Recognized As Safe" by the FDA. Dose escalation studies showed minimal toxicity, even at 8,000 mg per day for 3 months (Cheng et al., 2001).

1.4.1. Combination treatment to enhance the effect of curcumin

Despite its promising properties, curcumin is limited by its low bioavailability *in vivo*. It is a lipophilic molecule (logP ~3.0) that can be retained in hydrophobic cell areas, such as membrane bilayers and lipid droplets (Barry et al., 2009). Lipid droplets are cellular organelle serving as storage sites for neutral lipids (Olzmann & Carvalho, 2019). They are particularly numerous in GBM cells, while normal astrocytes have fewer and smaller lipid droplets. As such, they not only serve as energy storage for the cancer cells, but can also entrap lipophilic agents such as curcumin, preventing it from reaching its intracellular targets.

Thus, we hypothesized that combining curcumin with pyrrolidine-2, which decreases lipid droplet formation acting through the inhibition of cytoplasmic phospholipase A2, will significantly increase the effectiveness of curcumin in killing GBM cells *in vitro.* The results of these studies were published in the European Journal of Pharmaceutics and Biopharmaceutics, and are presented in Chapter 3.

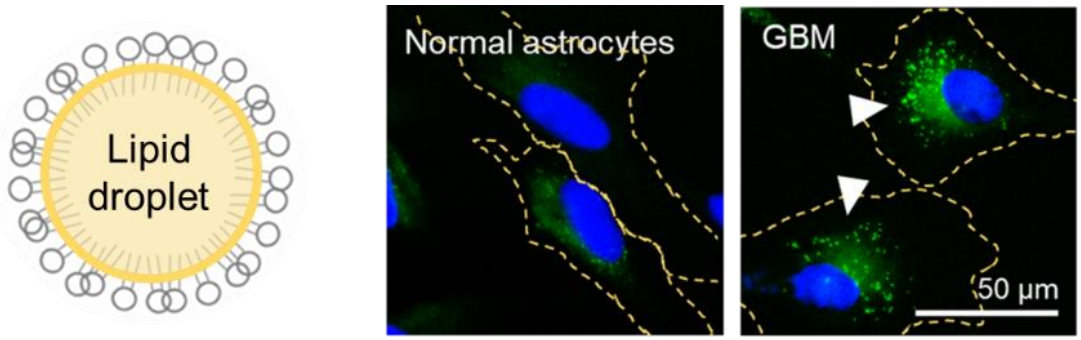

Figure 1.3. Structure and characteristics of lipid droplets in GBM and normal astrocytes

Lipid droplets are commonly found in almost all cell types, and their number and size can significantly change under adaptive and pathological conditions. Lipids are essential components of the brain, making up an estimated 50% of its dry weight. They are key to neuronal and glial function, although neurons themselves have no significant lipid droplets in storage. Instead, it's the astrocytes that primarily utilize fatty acid oxidation to produce metabolites subsequently taken up by neurons. Astrocytes were also shown to uptake peroxidized lipid released from neurons under stressful conditions, storing them into their own lipid droplets, thereby protecting neurons from lipotoxicity (Ioannou et al., 2019).

Astrocytes themselves release lipids (e.g. palmitic acid, stearic acid, oleic acid). The nature and quantity of these lipids is changed in response to stressful stimuli, such as the bacterial pro-inflammogen lipopolysaccharide (LPS)(Aizawa et al., 2016). These lipids can modulate other neural cells; the increased release of docosahexaenoic acid (DHA), for example, could downregulate several markers of microglial activation (Tremblay et al., 2016). Microglia and astrocytes surrounding GBM were investigated in our studies as key cell types in the GBM microenvironment. The interactions of GBM with normal astrocytes and microglia are shown in Chapter 4, along with studies on pharmacological and nanotherapeutic modulators of these interactions.

1.5. The GBM microenvironment

Treatment paradigms for GBM have shifted from focusing solely on cancer cells to consider the role of the tumor microenvironment. The development of bevacizumab (Avastin), currently in fast-track approval for GBM, showed that inhibiting vascular endothelial growth factor (VEGF)-

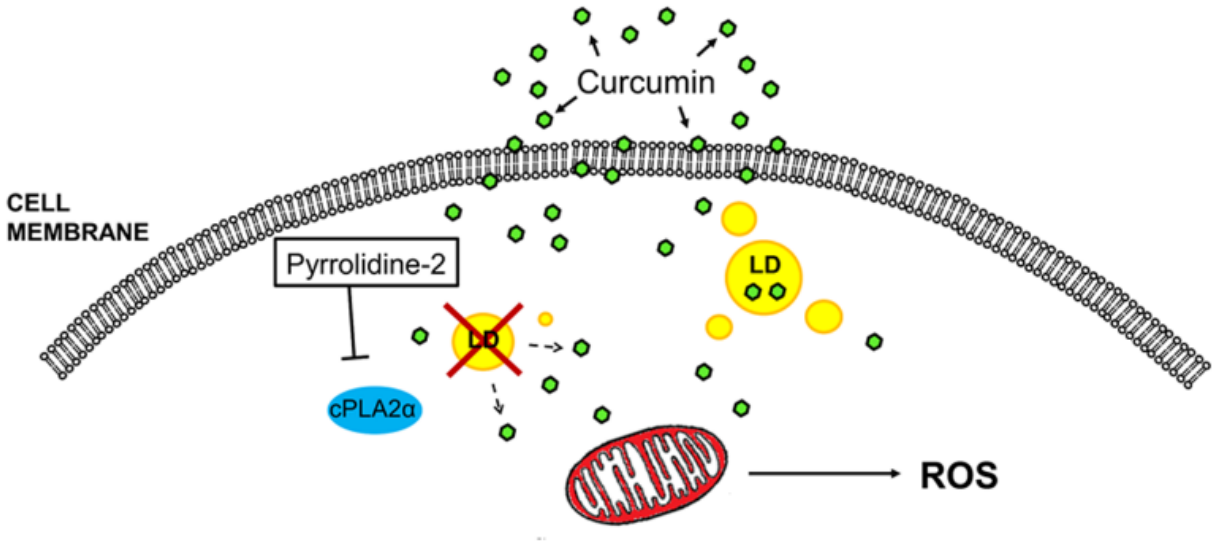

Figure 1.4. Proposed mechanisms of action of curcumin and pyrrolidine-2 in GBM

stimulated angiogenesis using humanized monoclonal antibodies has significant potential for GBM treatment. Tumor cells secrete factors such as VEGF and nitric oxide to stimulate the formation of blood vessels that irrigate the tumor, supplying cancer cells with nutrients and growth factors. These vessels are often leaky and serve as channels for local and peripheral immune cells to reach the tumor. These microglia and macrophages form a population of cells termed "tumor-associated macrophages" or TAMs. These cells can make up to 30-50% of the tumor mass and are major contributors to disease progression (Hambardzumyan et al., 2016). GBM-secreted factors (e.g. interleukin-10, interleukin-6, TGF-β, GM-CSF) act as chemokines that recruit TAMs to the tumor site. In turn, these normal cells, along with normal astrocytes and neurons, participate in the maintenance of the tumor microenvironment by secreting tumor-supportive cytokines and growth factors (Z. Chen & Hambardzumyan, 2018; Gieryng et al., 2017).

1.5.1. Modulating the GBM microenvironment

The importance of modulating the tumor microenvironment was recently highlighted by the 2018 Nobel Prize in Physiology or Medicine, awarded Dr. James P. Allison and Dr. Tasuku Honjo for their joint research on immunotherapy (Chamoto et al., 2020; Sharma et al., 2011). Because of their tumor-supportive role, efforts are aimed at either targeting the cells that make up the tumor microenvironment, or the factors communicated between these cells. However, not all types of immunomodulation are adequate. Global immunosuppression – as a side effect of radiotherapy, chemotherapy and steroids – was shown as detrimental to overall survival, as patients with low lymphocytic count had a median survival of only 3.5 months.

GBM can benefit from several aspects of immunosuppression and is still labeled as an immunosuppressive tumor. However, evidence showed that TAMs adopt an activation mode alternative to classical M1 and M2 polarizations. Therefore, immunomodulation – i.e. normalization – of TAMs functions would be preferable to global immunosuppression or excessive inflammation. Several immunotherapeutic options are presently explored in clinical trials for cancer, but none have explored the use of nanostructures for modulating the tumor microenvironment in GBM. We opted to investigate biocompatible dendritic polyglycerols as modulators of microglia and astrocytes. The rationale, properties and key experiments are presented in section 3.5.

1.6. Dendritic polyglycerol sulfates as nanotherapeutic agents

Nanostructures have been introduced in oncology mainly as drug nanocarriers (Senapati et al., 2018). Hundreds of candidate nanostructures have been in clinical trials at different stages (Anselmo & Mitragotri, 2016). In some tumors where the enhanced permeability and retention (EPR) effect is present, nanostructures can preferentially accumulate at the tumor site. An attractive feature of nanostructures is that they can be easily tailored to the task at hand by modifying their size, shape or functional groups. Lastly, many nanostructures can not only serve as drug carriers, but can also exert therapeutic effect themselves (Mark E. Davis et al., 2008; Parveen et al., 2012). Dendritic polyglycerol sulfates (dPGS) is particularly interesting due to its excellent safety profile *in vivo* and its inherent anti-inflammatory effects (Maysinger et al., 2015; Maysinger, Ji, et al., 2018; Maysinger, Lalancette-Hébert, et al., 2019). dPGS is a dendrimeric nanostructures with sulfated terminal groups; its structures mimics that of heparan sulfate, which is a linear polysaccharide found throughout our body.

Our previous studies showed that dPGS had protective effects against inflammatory cytokines upregulated in response to pathogen-derived and amyloid-β insults (Maysinger et al., 2015). Modelling *in silico* showed putative binding of dPGS to interleukin-6 (Maysinger, Lalancette-Hébert, et al., 2019; Rades et al., 2018). Our studies have extended these *in silico* investigations on other cytokines with less investigated roles in the brain, such as lipocalin-2 (LCN2) and a transcription factor, high mobility group box 1 (HMGB1). We investigated dPGS in 1) normal human neural cells subjected to the pro-inflammogen LPS, and examined the anti-inflammatory effect of dPGS in relation to microglial activation; 2) the context of the GBM microenvironment, where LCN2 and HMGB1 levels are greatly upregulated, and hypothesized that dPGS can downregulate tumor-supportive cytokines in GBM and its microenvironment, thereby decreasing tumor growth.

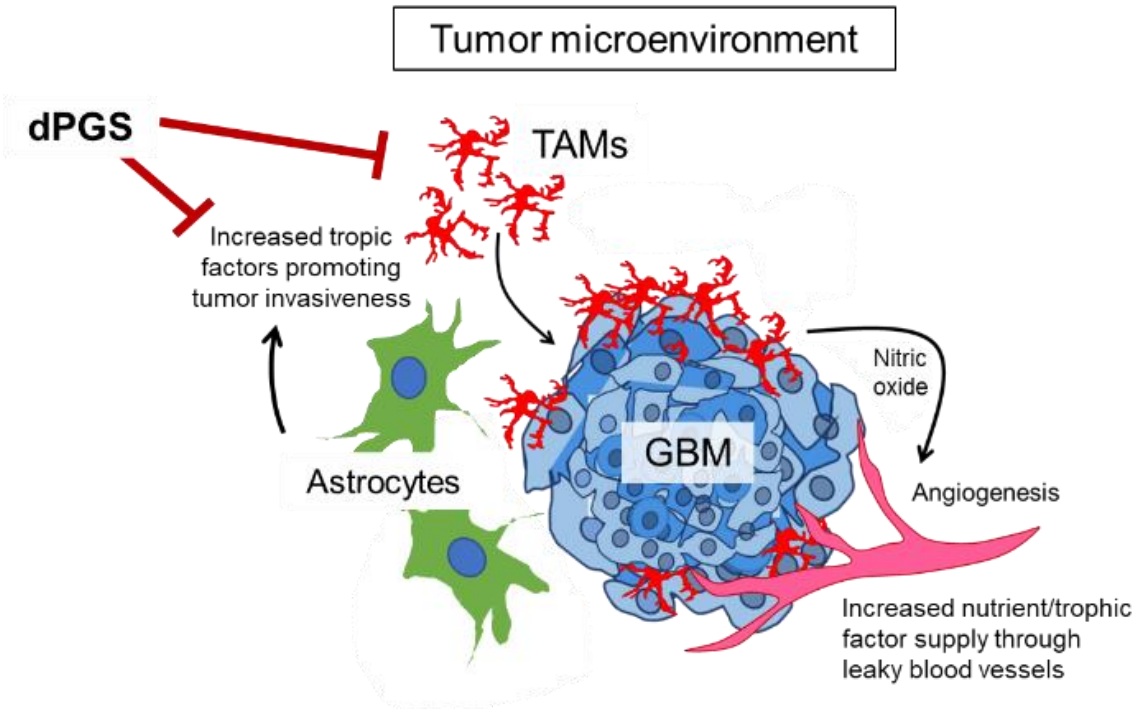

Figure 1.5. Proposed mechanisms of action of dPGS on the GBM microenvironment

Connecting Text

New therapeutic options are urgently needed for glioblastoma multiforme as the current clinical standard (i.e. temozolomide) is widely ineffective. Pan-histone deacetylase inhibitors have reached clinical trials for different cancers, but their use was limited by toxicities attributed to the inhibition of Class I HDACs, which deacetylate nuclear targets (histones).

In Chapter 2, we elected to investigate sahaquine, a novel hybrid molecule combining pan-histone deacetylase inhibitor vorinostat with primaquine, a P-glycoprotein inhibitor. Sahaquine is selective for HDAC6, which deacetylates cytoplasmic targets important for cancer invasiveness and survival. We report the concentration- and time-dependent effects of sahaquine compared to temozolomide in glioblastoma cells as well as brain tumor stem cells and three-dimensional tumor models (tumoroids). Several therapeutic effects were explored based on the role of HDAC6 in cytoskeletal rearrangement and kinase signalling, and the role of P-glycoprotein in multidrug resistance. We demonstrated that sahaquine inhibits key pro-survival pathways upregulated in glioblastoma and explored synergistic combination treatments.

This Chapter reveals the advantages of HDAC6 inhibition in glioblastoma using sahaquine, particularly in combination with selected therapeutic agents to address the different mechanisms of resistance in this disease.

Chapter 2. Inhibition of glioblastoma cell proliferation, invasion, and mechanism of action of a novel hydroxamic acid hybrid molecule

Zhang I, Beus M, Stochaj U, Le PU, Zorc B, Rajić Z, Petrecca K, Maysinger D. Cell Death Discovery. 2018; 4:41.

Abstract

Glioblastoma multiforme is one of the most aggressive brain tumors and current therapies with temozolomide or suberoylanilide hydroxamic acid (SAHA, vorinostat) show considerable limitations. SAHA is a histone deacetylase (HDAC) inhibitor that can cause undesirable side effects due to the lack of selectivity. We show here properties of a novel hybrid molecule, sahaquine, which selectively inhibits cytoplasmic HDAC6 at nanomolar concentrations without markedly suppressing class I HDACs. Inhibition of HDAC6 leads to significant α-tubulin acetylation, thereby impairing cytoskeletal organization in glioblastoma cells. The primaquine moiety of sahaquine reduced the activity of P-glycoprotein, which contributes to glioblastoma multiforme drug resistance. We propose the mechanism of action of sahaquine to implicate HDAC6 inhibition together with suppression of epidermal growth factor receptor and downstream kinase activity, which are prominent therapeutic targets in glioblastoma multiforme. Sahaquine significantly reduces the viability and invasiveness of glioblastoma tumoroids, as well as brain tumor stem cells, which are key to tumor survival and recurrence. These effects are augmented with the combination of sahaquine with temozolomide, the natural compound quercetin or buthionine sulfoximine, an inhibitor of glutathione biosynthesis. Thus, a combination of agents disrupting glioblastoma and brain tumor stem cell homeostasis provides an effective anti–cancer intervention.

Introduction

Glioblastoma multiforme (GBM) is the most common and aggressive form of brain cancer, with limited treatment options and dismal survival rates. Current treatment involves surgical resection followed by radiotherapy and chemotherapy with temozolomide (TMZ)(Weller et al., 2017). However, more than half of GBM patients do not respond to TMZ due to the overexpression of DNA repair enzymes, notably O^6-methylguanine transferase (Erasimus et al., 2016b; Hegi et al., 2005b; Weller et al., 2010).

Histone deacetylase (HDAC) inhibitors exert anticancer effects by inducing cell differentiation, cell cycle arrest, and apoptotic cell death through the upregulation of tumor suppressor and cell cycle-regulatory genes (Johnstone, 2002). Suberoylanilide hydroxamic acid (SAHA, vorinostat) is a Food and Drug Administration-approved drug for the treatment of cutaneous T cell lymphoma. It is currently in clinical trials for GBM as monotherapy and combined with radiotherapy (Galanis et al., 2009; Hummel et al., 2013b; E. Q. Lee et al., 2012; *Vorinostat and Radiation Therapy Followed by Maintenance Therapy With Vorinostat in Treating Younger Patients With Newly Diagnosed Diffuse Intrinsic Pontine Glioma - Full Text View - ClinicalTrials.Gov*, n.d.). Despite advancements in treatments, the median survival rate for GBM remains low (14-16 months) and new therapeutic options are urgently needed (Hegi et al., 2005c; Weathers & Gilbert, 2014).

In this study, we combined hydroxamic acid – the active moiety of SAHA exerting biological effects in cancer cells – with primaquine to generate a new class of hybrid anticancer agents: sahaquines. Hydroxamic acid inhibits HDACs; these enzymes are overexpressed in many cancers, including GBM (Glozak & Seto, 2007; D. H. Lee et al., 2017). The hydroxamic acid pharmacophore of SAHA chelates metal ions, thereby inhibiting metalloenzymes such as HDACs

and matrix metalloproteinases (MMPs), which promote cancer growth and invasiveness (Bertrand et al., 2013; Gialeli et al., 2011; Grant et al., 2007). Hydroxamic acid is a weak acid, which is favorable in the acidic tumor microenvironment as weak bases become protonated, resulting in ion trapping, lysosomal accumulation, elimination by lysosomal exocytosis, and overall decreased biological activity (Corbet & Feron, 2017; Mahoney et al., 2003; Zhitomirsky & Assaraf, 2017). Primaquine can directly interfere with endosomal trafficking to the plasma membrane (van Weert et al., 2000), inhibit the multidrug resistance transporter P-glycoprotein, and autophagy, thereby sensitizing cancer cells to anti-mitotic drugs (Kim et al., 2013; Z. J. Yang et al., 2011). Considering that monotherapies have limited effectiveness in GBM, we tested sahaquine in combination with TMZ, the standard of care for GBM, quercetin, and buthionine sulfoximine. Quercetin is an abundant flavonoid found in fruits and vegetables, such as apples and onions. Its estimated daily intake ranges from 3-40 mg, but supplements up to 1000 mg per day are considered safe (Andres et al., 2018). Although it shows no toxicity in normal cells, several studies have shown that quercetin has anti-cancer effects. Its mechanism of action involves the upregulation of pro-apoptotic and downregulation of anti-apoptotic factors, cell cycle arrest, and DNA intercalation, resulting in DNA damage, activation of apoptosis, and cell death (Srivastava et al., 2016). In animal studies, quercetin inhibited tumor growth and improved the lifespan of tumor-bearing mice (Calgarotto et al., 2018; Srivastava et al., 2016). Furthermore, the anti-cancer effects of quercetin are enhanced in combination with chemotherapeutic agents or other drugs (S. Sun et al., 2018; Zanini et al., 2007; Xian Zhang et al., 2015).

We investigated the loss of cell viability and invasiveness in GBM as functional read-outs of the effects of sahaquine alone or in combination with TMZ and quercetin. Sahaquine was tested in both differentiated GBM cells and brain tumor stem cells (BTSCs), which are key to tumor

survival and recurrence (Bao et al., 2006; J. Chen et al., 2012; Dagogo-Jack & Shaw, 2018; B. E. Johnson et al., 2014). Our study supports the model that sahaquine-induced cell death of GBM is mediated through multiple pathways, including inhibition of HDAC6, reduction of epidermal growth factor receptor (EGFR) protein abundance, and decreased activation of downstream kinases AKT and ERK1/2. The primaquine moiety of sahaquine contributes to the inhibition of P-glycoprotein. Considering that sahaquine significantly reduced BTSC viability and markedly inhibited GBM invasion by disruption of GBM homeostasis, further systematic studies are warranted in patient-derived organoids.

Materials and methods

Synthesis of sahaquine

Sahaquine **5** was synthesized in four reaction steps (Fig. 1) adapted from the synthetic approach of Zhang *et al.* (Xuan Zhang et al., 2013). Details of these steps are provided in the Supplementary Information. The first step included amide bond formation between mono-methyl glutarate (**1**, Sigma-Aldrich, St. Louis, MO, USA) and primaquine (Sigma-Aldrich, St. Louis, MO, USA), with 1-[*bis*(dimethylamino)methylene]-1*H*-1,2,3-triazolo[4,5-*b*]pyridinium 3-oxid hexafluorophosphate (HATU, Alfa Aesar, Thermo Fisher, Kandel, Germany) as a coupling agent and *N,N*-diisopropylethylamine (DIEA, Alfa Aesar, Thermo Fisher, Kandel, Germany) as a base. The prepared product **2** was further hydrolyzed with lithium hydroxide (Sigma-Aldrich, St. Louis, MO, USA) and gave carboxylic acid **3**. In the next step, **3** was coupled with *O*-benzylhydroxylamine (Sigma-Aldrich, St. Louis, MO, USA) in the presence of HATU/DIEA and yielded *O*-benzylhydroxamic acid **4**, which was deprotected by catalytic hydrogenation and gave the target compound **5** (sahaquine). All reactions proceeded at room temperature.

Cell culture and tissue samples

U251N human glioblastoma cells were originally obtained from the American Type Culture Collection. Cells were cultured in Dulbecco's modified Eagle's Media (DMEM, Gibco, Thermo Fischer Scientific, Grand Island, NY, USA) supplemented with 5% (v/v) fetal bovine serum (Wisent, St. Bruno, Canada) and 1% (v/v) penicillin-streptomycin (Pen-Strep; Thermo Fisher Scientific, Eugene, OR, USA) at 37 °C with 5% CO_2 and 95% relative humidity, unless otherwise indicated. Glioblastoma samples were harvested under a protocol approved by the Montreal

Neurological Hospital's research ethics board (NEU-10-066). Consent was given by all patients. At least 116 brain sections from GBM patients aged 55-76 and controls were used. Tissues were from the frontal, temporal, or parietal lobes of the cerebral cortex. Human BTSCs were expanded as neurospheres in complete NeuroCult^{TM} proliferation media (Stemcell Technologies, Vancouver, BC, Canada). NeuroCult^{TM} basal medium contained: NeuroCult^{TM} NS-A proliferation supplement (1/10), recombinant human epidermal growth factor EGF (20 ng/ml), recombinant human basic fibroblast growth factor (20 ng/ml), and heparin (2 μg/ml).

Cell counting assay

U251N cells were seeded in 96-well black plates (Costar, Corning, NY, USA) at 5,000 cells per well in 0.1 ml media and cultured for 24 h. Cells were treated with sahaquine (0.001, 1, 5, 10, 20, 25, 30, 40, and 50 μM), TMZ (0.001, 1, 10, 50, 100, 200, 300, 400, and 500 μM, Sigma-Aldrich, St. Louis, MO, USA), quercetin (0.001, 1, 10, 25, 50, 75, 100, 200, and 300 μM, Sigma-Aldrich, St. Louis, MO, USA) or SAHA (0.001, 0.1, 1, 2, 5, 8, 10, 25, and 50 μM, Cayman Chemical, Ann Arbor, MI, USA) for 24 h or 72 h. Combination treatments included increasing concentrations of sahaquine (0.001, 1, 3, 5, 7, 10, 20, and 50 μM) with quercetin (100 μM), increasing concentrations of quercetin (0.001, 1, 10, 25, 50, 100, and 200 μM) with sahaquine (10 μM), TMZ (30 μM) with sahaquine (10 μM), quercetin (140 μM) or SAHA (1 μM), and buthionine sulfoximine (100 μM, Sigma-Aldrich, St. Louis, MO, USA) with sahaquine (10 μM) for 24 h or 72 h. Following treatment, cells were fixed with 4% paraformaldehyde (w/v, 10 min, BDH, Toronto, ON, Canada). Nuclei were labeled with Hoechst 33342 (10 μM, 10 min, Thermo Fisher Scientific, Eugene, OR, USA). Cells were washed with phosphate-buffered saline and imaged using a fluorescence microscope (Leica DMI4000B, Toronto, ON, Canada).

BTSC viability

48EF human brain tumor cells were seeded at 5,000 cells per well in 96-well plates (Sarstedt, Nümbrecht, Germany) and treated for 7 days. Cells were then imaged using light microscopy (Leica DMI4000B) and the surface areas of the neurospheres were measured in ImageJ (version 1.51s).

Scratch assay

U251N cells were seeded in 6-well plates (Sarstedt, Nümbrecht, Germany) at 1,500,000 cells per well in 1 ml media and cultured for 24 h. The scratch was performed by gently dragging a 200 µl pipette tip across the cell monolayer, after which cells were washed with phosphate-buffered saline and incubated in DMEM with or without treatment. Cytochalasin D (40 nM, Sigma-Aldrich, St. Louis, MO, USA) served as positive control. Predetermined areas of the wells were imaged using light microscopy immediately after the scratch (time = 0 h) and after 24 h. The cell-free area of the scratch was measured in ImageJ.

Cell invasion assay

U251N tumoroids were prepared using the hanging drop method78. Drops of 30,000 cells in 20 µl medium were pipetted onto the inner side of a 10 cm Petri dish (Thermo Fisher Scientific, Eugene, OR, USA) lid. The lid was quickly flipped to cover the Petri dish filled with 20 ml phosphate-buffered saline. Hanging drops were cultured at 37 °C for 48 h to allow tumoroids to form. Tumoroids were then gently scooped into a medium-filled Petri dish coated with 2% agarose and

cultured for 48 h. Tumoroids were implanted in collagen gel (Advanced BioMatrix, San Diego, CA, USA) mixed with DMEM (1×) and sodium hydroxide (10 mM, Sigma-Aldrich, St. Louis, MO, USA). Gels were covered with 500 µl DMEM with or without treatment. Tumoroids were imaged using light microscopy immediately after implantation (time = 0 day) and after 4 days. The area of cell invasion was measured in ImageJ.

Immunocytochemistry

Following treatment, U251N human glioblastoma cells were fixed with 4% paraformaldehyde (10 min), and then permeabilized using 0.1% Triton X-100 (v/v, 10 min, Sigma-Aldrich, St. Louis, MO, USA). Blocking was performed with 10% goat serum (v/v, 1 h, Thermo Fisher Scientific, Eugene, OR, USA) in phosphate-buffered saline, and then samples were incubated with primary antibodies (acetyl-histone H3 K9/K14, 1/500, Cell Signalling, #9677; acetyl-α-tubulin K40, 1/500, Santa Cruz, sc-23950; α-tubulin, 1/1000, Abcam, ab7291) overnight at 4 °C in a humidified chamber. Samples were washed three times with phosphate-buffered saline with 5 min incubation between washes. Secondary antibodies (anti-rabbit Alexa Fluor 488, 1/500, Thermo Fisher Scientific, A11008; anti-mouse Alexa Fluor 647, 1/500, Thermo Fisher Scientific, A28181) were incubated with samples for 1 h in the dark, and then washed off three times with phosphate-buffered saline with 5 min incubation in between washes. Nuclei were labeled with Hoechst 33342 (10 µM, 10 min). Samples were mounted on microscope slides using Aqua-Poly/Mount (Polysciences, Warrington, PA, USA) and dried overnight before imaging with a fluorescence microscope (Leica DMI4000B).

Immunohistochemistry

Human brain sections were dewaxed in xylene, and then rehydrated in ethanol. Antigen retrieval was performed in citrate buffer using a decloaking chamber for 3 h. Samples were washed twice with double-distilled water, three times with phosphate-buffered saline, and then blocked with Protein Block (10 min, Spring Biosciences, Pleasanton, CA, USA). Samples were incubated with primary antibodies (HDAC6, 1/100, Santa Cruz, sc-11420; EGFR, 1/100, Oncogene Science Ab-1; phospho-AKT Ser473, Cell Signalling, #9271; phospho-p44/42 Erk1/2 Thr202/Tyr204, 1/100, Cell Signalling, #9101) overnight at 4 °C in a humidified chamber. Samples were washed twice with IF buffer (0.05% (v/v) Tween 20, 0.2% (v/v) Triton X-100 in phosphate-buffered saline). Secondary antibodies (anti-rabbit Alexa Fluor 647, 1/500, Thermo Fisher Scientific, A21245; anti-rabbit Alexa Fluor 488, 1/1000, Thermo Fisher Scientific, A27034; anti-mouse Alexa Fluor 647, 1/1000, Thermo Fisher Scientific, A-21235) diluted in 2% (w/v) bovine serum albumin (Sigma-Aldrich, St. Louis, MO, USA) in phosphate-buffered saline were incubated with samples for 1 h in the dark at room temperature. Samples were washed three times with IF buffer, and then nuclei were labeled with DAPI (4′,6-diamidino-2-phenylindole; 1 μg/ml, 5 min, Molecular Probes, Eugene, OR, USA). Samples were washed three times with phosphate-buffered saline, then mounted on microscope slides using mounting media (Dako, Mississauga, ON, Canada), and air-dried for at least 30 min. Samples were imaged using a fluorescence microscope (Leica DMI4000B).

Western blotting

Western blot analysis followed published procedures (Maysinger, Moquin, et al., 2018). In brief, crude extracts were separated by sodium dodecyl sulfate–polyacrylamide gel electrophoresis (SDS-PAGE) and blotted onto nitrocellulose membranes. Blocked filters were probed with antibodies against acetyl-α-tubulin K40 (1/10,000, Sigma-Aldrich, St. Louis, MO, USA, #T7451), α-tubulin (1/1000, Santa Cruz, sc-5286), phospho-AKT Ser473 (1/2000, Santa Cruz, sc-7985), pan-AKT (1/1500, Cell Signaling, #9272), HDAC6 (1/1000, Santa Cruz, sc-11420), EGFR (1/1000, Santa Cruz, sc-03), phospho-ERK1/2 Thr202/Tyr204 (1/2000, Cell Signaling, #9106), pan-ERK1/2 (1/2000, Cell Signaling, #4695), and actin (1/100,000, Chemicon, MAB1501). Signals for enhanced chemiluminescence were acquired with a Bio-Rad ChemiDoc™ MP imaging system and quantified.

MTT assay

U251N cells were seeded in 24-well plates (Sarstedt, Nümbrecht, Germany) at 50,000 cells per well in 300 µl media and cultured for 24 h. Cells were treated with sahaquine (0.001, 1, 5, 10, 25, and 50 µM), TMZ (50, 100, 200, 300, 400, and 500 µM), quercetin (10, 50, 100, and 200 µM), or SAHA (0.1, 1, 2, 5, 8, 10, and 50 µM) for 72 h. Combination treatments included increasing concentrations of sahaquine (1, 10, and 50 µM) with a fixed concentration of quercetin (100 µM), or increasing concentrations of quercetin (10, 100, and 200 µM) with a fixed concentration of sahaquine (10 µM) for 72 h. Following treatment, MTT (Sigma-Aldrich, St. Louis, MO, USA) dissolved in phosphate-buffered saline was added to cells (0.5 mg/ml) for 1 h at 37 °C. After MTT-containing media were removed, dimethyl sulfoxide (0.5 ml) was added to each well to lyse cells

and dissolve formazan. Wells were sampled in triplicate and the optical density was measured at 595 nm using a microplate reader (Asys UVM 340, Biochrom, Holliston, MA, USA).

Gelatin zymography

U251N cells were seeded in 60-mm tissue culture dishes (Thermo Fisher Scientific, Rochester, NY, USA) at 1,500,000 cells per dish in 3 ml media and cultured for 24 h. Cells were treated in serum-deprived DMEM for 24 h. Following treatment, culture media were collected and concentrated 15-fold using 30 kDa centrifugal filters (Millipore, Cork, Ireland) following the manufacturer's recommendations. Concentrated media were separated by SDS-PAGE using gelatin (0.1%, w/v) and acrylamide (7.5%, w/v) gels under non-reducing conditions. Gels were washed for 30 min in renaturing solution (2.5% (v/v) Triton X-100 in double-distilled water) and 30 min in developing buffer (50 mM Tris, pH 7.8; 1% (v/v) Triton X-100; 1 μM ZnCl2, 5 mM CaCl2, adjusted to pH 7.45). Gels were then incubated in fresh developing buffer at 37 °C overnight. Gels were stained with 0.5% (w/v) Coomassie Blue G250 (Bio-Rad, Richmond, CA, USA) dissolved in 40% (v/v) ethanol and 10% (v/v) acetic acid for 1 h, and then destained in 40% ethanol and 10% acetic acid diluted in double-distilled water, until clear bands appeared. Quantification of MMP-9 and MMP-2 abundance (as band area) was done in ImageJ.

Tumoroid viability

U251N tumoroids were prepared using the liquid overlay system (Dhanikula et al., 2008). The 96-well cell culture plates were coated with 75 μl of 2% (w/v) agarose (Life Technologies, Gaithersburg, MD, USA) dissolved in serum-deprived DMEM. The agarose was cooled for 30 min,

then cells were seeded at 5,000 cells per well in 200 µl media, and cultured for 4 days before treatment. Cells were treated for 7 days, and then imaged using a microscope (Leica DMI4000B). The surface area of tumoroids was analyzed in ImageJ.

Calcein-AM uptake

U251N cells were seeded in 96-well black plates at 5,000 cells per well in 0.1 ml media and cultured for 24 h before treatment. Cyclosporine A (Calbiochem, Toronto, Canada) served as a positive control for the inhibition of P-glycoprotein. Following treatment, cells were incubated in phenol-free Hanks' balanced Salt solution containing calcein-AM (0.5 µM, Thermo Fisher Scientific, Eugene, OR, USA) and propidium iodide (3 µM, Sigma-Aldrich, St. Louis, MO, USA) for 30 min at 37 °C. The media were replaced with fresh Hanks' balanced salt solution and cells were imaged using a fluorescence microscope (Leica DMI4000B). Cells positively labeled with propidium iodide were excluded from the analysis.

Statistics

Experiments were performed independently at least three times. Unless otherwise indicated, data are shown as mean (SD). Normality of data distribution was assessed by the Shapiro–Wilk test. For sample sizes larger than 30, the Central Limit Theorem allows the assumption of normal distribution. Equality of variances was assessed by Levene's test. If the assumptions of normality and homogeneity of variance were met, two-tailed one-way analysis of variance (ANOVA) with Tukey–Kramer's post hoc test were performed. If homogeneity of variance was not observed,

Welch's ANOVA with the Games–Howell post hoc test were used. A p value smaller than 0.05 was considered statistically significant: *$p < 0.05$, **$p < 0.01$, and ***$p < 0.001$.

Results

Sahaquine synthesis and physicochemical properties of the selected anticancer agents

Sahaquine is a primaquine and hydroxamic acid derivative linked with glutaric acid. It is synthesized in four steps (Fig. 1). The pharmacophore, hydroxamic acid, was introduced in the last step. Yields were good to excellent (50-88%). Sahaquine was fully characterized by conventional spectroscopic and analytical methods (melting point, IR, MS, ^{1}H-NMR, ^{13}C-NMR), and the data were consistent with the proposed structure (Supplementary Fig. S1). The quinoline ring of sahaquine acts as the capping group and the hydroxamic acid binds zinc. Calculations of physicochemical properties showed that TMZ is a hydrophilic compound (log P = –0.28), whereas sahaquine and particularly quercetin are more lipophilic (log P = 0.92 and 2.16, respectively) (Table 1). The isoelectric point (pI) values of these compounds vary from 2.9 (quercetin) to 9.2 (SAHA)(*Chemicalize - Instant Cheminformatics Solutions*, n.d.).

Sahaquine is more potent than TMZ for killing human glioblastoma and BTSCs

The half maximal inhibitory concentration (IC_{50}) value of sahaquine (10 μM) was about three-fold lower than that of TMZ (31 μM), whereas it was less potent than its parent compound SAHA after 72 h incubation (Fig. 2). Sahaquine precursors were also tested, but because of the relatively high IC_{50} values (>50 μM), further experiments were not pursued (Supplementary Table S1). Enhanced cell killing was achieved by combining quercetin with sahaquine in a dose-dependent manner, although quercetin alone showed limited cytotoxicity (IC_{50} = 140 μM after 72 h) (Fig. 2e-f). Combination of TMZ with sahaquine, quercetin, or SAHA at IC_{50} concentrations was more effective than any of the compounds alone (Supplementary Fig. S2). Similar results were obtained by measurements of mitochondrial metabolic activity using the MTT (3-[4,5-dimethylthiazol-2-yl]-2,5-diphenyl tetrazolium bromide) assay (Supplementary Fig. S3).

We further tested the selected compounds on GBM tumoroids, which are more drug-resistant and representative models of brain tumors *in vivo*. Sahaquine and TMZ reduced tumoroid sizes by 37% and 40%, respectively, while quercetin did not have a significant effect after 7 days (Supplementary Fig. S4).

Based on the results shown in Fig. 2, we investigated the cytotoxic effects of the selected compounds on BTSCs. BTSCs are a key subpopulation of GBM tumors implicated in tumor initiation, propagation and recurrence (Bao et al., 2006; Dagogo-Jack & Shaw, 2018). *In vitro* BTSC cultures spontaneously formed neurospheres of approximately 100 μm in diameter within 7 days. Sahaquine and quercetin were most effective at reducing the size of BTSC aggregates and abolishing the formation of neurospheres (Fig. 3).

Sahaquine inhibits GBM invasion and P-glycoprotein activity

GBM is characterized by a diffuse brain tissue distribution (Holland, 2000). Tumors commonly reoccur within a few centimeters of the original lesion, making surgical resection difficult (Holland, 2000). We tested the effect of sahaquine and quercetin on GBM migration using a scratch assay, and invasion using a three-dimensional (3D) collagen matrix. Sahaquine did not significantly inhibit cell migration over 24 h, while quercetin reduced cell migration by 20% (Fig. 4a). The combination of sahaquine with quercetin was most effective, reducing migration by 42%. This effect was not observed when combining sahaquine with TMZ. In contrast, sahaquine significantly inhibited GBM invasiveness, whereas quercetin and TMZ reduced cell invasion by 35% and 45% after 4 days, respectively (Fig. 4c). Interestingly, the combination of sahaquine with quercetin was less effective than sahaquine alone, suggesting interference between these two compounds. GBM invasiveness is enabled by MMP degradation of the extracellular matrix and basement membranes (Alaseem et al., 2017; Nakada et al., 2003). We investigated the effect of the selected compounds on the abundance of secreted MMPs using gelatin zymography, and showed that quercetin decreases MMP abundance in a dose-dependent manner (Supplementary Fig. S5). Neither sahaquine nor TMZ reduced MMP concentrations, although the hydroxamic acid moiety in sahaquine can bind zinc within

the MMP structure (Jacobsen et al., 2010). The primaquine moiety of sahaquine contributed to the inhibition of P-glycoprotein, as assessed by intracellular retention of calcein-AM (Supplementary Fig. S6). The primaquine concentration within sahaquine (10 μM) effectively inhibited P-glycoprotein activity, whereas 60 μM of unincorporated primaquine was required to achieve a comparable effect. A smaller extent of P-glycoprotein inhibition by SAHA was obtained with equimolar sahaquine concentrations (10 μM)(Supplementary Fig. S6).

Sahaquine selectively inhibits HDAC6

We further examined the HDAC inhibitory activity of sahaquine compared to its parent compound SAHA. SAHA is a pan-HDAC inhibitor that caused an increase in both acetylated α-tubulin (K40) and acetylated histone H3 (K9/K14) (Fig. 5). We hypothesized sahaquine to be selective toward HDAC6, because its bulky capping group would fit better into the wide binding site of the enzyme (Bieliauskas & Pflum, 2008; Schäfer et al., 2008). Nanomolar concentrations (100 nM) of sahaquine resulted in a 1.5-fold increase in acetylated α-tubulin compared to the untreated control, but did not affect histone acetylation (Fig. 5a-b). Similar results were obtained with the HDAC6-selective inhibitor ACY-1215 (Supplementary Fig. S7). TMZ and quercetin did not inhibit HDAC6. These results were supported by Western blot analyses (Fig. 5c). HDAC6 abundance was comparable following all treatments, suggesting that sahaquine inhibited the enzyme activity without affecting its protein levels (Fig. 5d).

Sahaquine reduces EGFR abundance, ERK1/2, and AKT phosphorylation

EGFR overexpression and downstream hyperactivity of ERK1/2 and AKT are associated with worse prognosis in GBM (Sanchez-Vega et al., 2018; Shinojima et al., 2003). We assessed the abundance of these markers and HDAC6 in GBM by immunohistochemistry, and showed an increase in EGFR, dually phosphorylated (active) ERK1/2, and phosphorylated (active) AKT, and HDAC6 compared to control brains (Fig. 6a). To test whether sahaquine impinges on EGFR and the activation of downstream kinases, we measured EGFR abundance, dual ERK1/2 phosphorylation (Thr202/Tyr204), and AKT phosphorylation (Ser473) by Western blotting (Fig. 6b-d). Sahaquine reduced EGFR concentrations in GBM. Interestingly, combining sahaquine and TMZ abrogated this inhibitory effect. Sahaquine also reduced levels of phosphorylated ERK1/2 and phosphorylated AKT, alone and in combination with quercetin or TMZ. Total ERK1/2 and AKT protein levels remained unchanged (Supplementary Fig. S8).

Discussion

Results from this study show that sahaquine is more effective than TMZ in killing glioblastoma and BTSCs, as well as inhibiting glioblastoma invasiveness. The mode of action of sahaquine implicates in part excessive acetylated α-tubulin acetylation due to the selective inhibition of HDAC6, resulting in cytoskeletal reorganization (Supplementary Fig. S9) and reduced invasiveness. Additional modes of action involve decreased EGFR abundance and downstream activity of AKT and ERK1/2. These results are particularly striking in combination with TMZ or quercetin.

TMZ is one of few clinically approved drugs for the treatment of GBM, but a substantial portion of newly diagnosed tumors and recurrent tumors are resistant to this drug (Hegi et al., 2005b; S. Y. Lee, 2016b). HDAC inhibitors are of particular interest for GBM treatment, as their effectiveness is unaltered by mechanisms of resistance upregulated in GBM, such as mismatch-repair, O^6-methylguanine methyltransferase and base-excision repair (Caporali et al., 2004; Erasimus et al., 2016b; Hegi et al., 2005b). The pan-HDAC inhibitor SAHA is currently in clinical trials for GBM, but results so far showed marginal improvement in overall survival (5.7 months compared to 4.4 months) and several serious side effects (Galanis et al., 2009; Hummel et al., 2013b; E. Q. Lee et al., 2012; Peters et al., 2018; *Vorinostat and Radiation Therapy Followed by Maintenance Therapy With Vorinostat in Treating Younger Patients With Newly Diagnosed Diffuse Intrinsic Pontine Glioma - Full Text View - ClinicalTrials.Gov*, n.d.; Yin et al., 2007a). This and other current therapeutic interventions for GBM are ineffective (Bao et al., 2006; J. Chen et al., 2012; B. E. Johnson et al., 2014).

Thus, our goal was to test a new hybrid compound. The development of hybrid molecules is one of the most active areas in therapeutics. Hybrid compounds can have multiple targets, reducing the risk of resistance, lowering effective doses, and decreasing side effects (Meunier, 2008; Xuan Zhang et al., 2013). Sahaquine is a hybrid molecule consisting of hydroxamic acid and primaquine linked by a dicarboxylic acid. Primaquine is a strong base (pI = 13.7), but addition of the hydroxamic acid group lowers its pI to 6.48, making sahaquine a weak acid. Weak acids are more advantageous than weak bases as anticancer therapeutics, because they will not be protonated in the acidic tumor environment or trigger lysosomal exocytosis (Corbet & Feron, 2017; Mahoney et al., 2003; Zhitomirsky & Assaraf, 2017). Similarly to primaquine, sahaquine can also inhibit P-glycoprotein activity (Supplementary Fig. S6), thereby preventing multidrug resistance.

One of the great challenges in GBM treatment is heterogeneity, both within and between tumors (Cavalli et al., 2017; Hunter et al., 2018; C.-C. J. Lin et al., 2017; Meacham & Morrison, 2013). Interpatient heterogeneity has been shown through genomic and transcriptomic analyses by the Cancer Genome Atlas research network (Cancer Genome Atlas Research Network, 2008; Verhaak et al., 2010). Intratumoral heterogeneity can be attributed to the different cellular lineages and subtypes present in different parts of the same tumor (Morrissy et al., 2017; Sottoriva et al., 2013), or even in individual cells within a tumor (Patel et al., 2014; Verhaak et al., 2010). Another cause of GBM heterogeneity is the presence of BTSCs, a subset of glioma cells with the abilities of self-renewal, differentiation, and recapitulation of the original tumor upon xenotransplantation (Galli et al., 2004; J. Lee et al., 2006; Singh et al., 2004). They are resistant to radiation (Bao et al., 2006) and chemotherapy (Bleau et al., 2009; S.-F. Chen et al., 2012; G. Liu et al., 2006), and are thought to promote tumor recurrence (Dagogo-Jack & Shaw, 2018; B. E. Johnson et al., 2014). Therefore, effective GBM treatment demands a better understanding of tumor origin and

heterogeneity to identify new therapeutic targets (Fouse et al., 2014; Hegi et al., 2005b). Sahaquine (10 μM) abolished the formation of BTSC neurospheres and significantly reduced the size of BTSC aggregates. TMZ was less effective, even at a ten-fold higher concentration (100 μM). Quercetin was as effective as sahaquine in killing BTSCs, but showed limited cytotoxicity toward differentiated GBM cells. Sahaquine eliminated both BTSCs and differentiated cancer cells.

Another factor contributing considerably to GBM recurrence is tumor invasiveness. While sahaquine abolished invasiveness and contributed to the loss of tumoroid viability, it did not markedly affect the abundance of secreted MMPs. In contrast, quercetin had limited effects on tumoroid viability, but decreased GBM invasion by inhibiting MMP secretion. Quercetin inhibits nuclear factor-κB (NFκB) nuclear translocation, which could alter MMP expression (Bond et al., 2001; Soubannier & Stifani, 2017) and enhance cell death through NFκB-dependent regulation of apoptosis.

In an effort to reduce undesirable side effects in normal cells, selective HDAC inhibitors have been developed (J.-H. Lee et al., 2013; Santo et al., 2012). Ricolinostat (ACY-1215) is a selective HDAC6 inhibitor currently in clinical trials (phase I and II) in combination with pomalidomide for multiple myeloma (*ACY-1215 (Ricolinostat) in Combination With Pomalidomide and Low-Dose Dex in Relapsed-and-Refractory Multiple Myeloma - Full Text View - ClinicalTrials.Gov*, n.d., p. 1215). Ricolinostat inhibits heat shock protein 90 deacetylation, resulting in an accumulation of unfolded proteins, disruption of protein homeostasis and cell death (Kekatpure et al., 2009). We show that sahaquine selectively inhibits HDAC6 at nanomolar concentrations, which distinguishes it from SAHA, which is non-selective at equimolar concentrations. Interestingly, sahaquine significantly reduced the abundance of heat shock protein 70s in GBM (Supplementary Fig. S10) and altered α-tubulin organization. We have previously

shown that celastrol disrupts protein homeostasis (Boridy et al., 2014) and the organization of the F-actin cytoskeleton in GBM (Maysinger, Moquin, et al., 2018). Future studies will have to evaluate how sahaquine affects proteostasis in relation to cytoskeletal dynamics.

Many drugs currently in clinical trials aim at inhibiting proteins and proliferation pathways deregulated in GBM, notably HDAC6, EGFR, AKT, and ERK1/2 (Combs et al., 2006; Emrich et al., 2002; *ONC201 in Adults With Recurrent H3 K27M-Mutant Glioma - Full Text View - ClinicalTrials.Gov*, n.d.; Quang & Brady, 2004). Our *in vitro* studies showing enhanced ERK1/2 and AKT phosphorylation are corroborated by immunohistochemical data in tumor sections from GBM patients (Fig. 6a), also showing markedly stronger signals for HDAC6, EGFR, phosphorylated ERK1/2, and phosphorylated AKT compared to normal brain tissue (Fig. 6a). Sahaquine can decrease the abundance of EGFR, phosphorylated AKT, and phosphorylated ERK1/2 in GBM (Fig. 6b-d), thereby suggesting that similar hybrid molecules are viable candidates for GBM combination therapy. Interestingly, AKT deacetylation by HDAC6 promotes cancer growth and proliferation (Iaconelli et al., 2017), indicating that sahaquine could reduce AKT activation through HDAC6 inhibition.

Drug resistance is a major problem in glioblastoma therapy (Hegi et al., 2005c; S. Y. Lee, 2016b). A recent study of HDAC inhibitors in drug-resistant melanoma implicated increased levels of reactive oxygen species (L. Wang et al., 2018). Combination of sahaquine with buthionine sulfoximine, which depletes endogenous glutathione levels (Du et al., 2016), sensitized GBM cells to reactive oxygen species and enhanced cell death (Supplementary Fig. S11), although buthionine sulfoximine alone in the tested concentration had no effect on GBM viability. Further analysis of the effect of sahaquine on reactive oxygen species production in GBM is warranted.

Taken together, our study reveals sahaquine as a therapeutic agent affecting multiple cellular factors and processes that are critical for GBM treatment (Fig. 7). Sahaquine is superior to the clinical standard TMZ in reducing GBM and BTSC viability, invasiveness, and markers of key survival pathways. These effects are even more profound when sahaquine is combined with TMZ, buthionine sulfoximine, or quercetin. In conclusion, sahaquine is an effective cell death inducer which eliminates not only GBM cells but also BTSCs, thus suggesting that evaluation of sahaquine in combination with other drugs merit further investigations in patient-derived organoids, and eventually in humans.

Acknowledgements

We wish to thank J. Choi and E. Gran for their contribution to initial experiments related to this study. D.M. thanks the Canadian Institute for Health Research (MOP-119425) and the Natural Sciences and Engineering Council of Canada (RGPIN 04994-15). K.P. is grateful to the Brilliant Night Foundation, and B.Z. thanks the Croatian Science Foundation (IP-2014-09-1501) for financial support.

Figure 2.1. Synthesis of sahaquine and its precursors

Reagents and conditions: (i) HATU, DIEA, dichloromethane, 1 h, (ii) LiOH, methanol, H2O, 1 h, (iii) O-benzylhydroxylamine, HATU, DIEA, dichloromethane, 2 h, (iv) H2, 10% Pd/C, methanol, 4 h. All reactions were performed at room temperature. Yields are shown in brackets. HATU 1-[bis(dimethylamino)methylene]-1H-1,2,3-triazolo[4,5-b]pyridinium 3-oxid hexafluorophosphate, DIEA N,N-diisopropylethylamine, LiOH lithium hydroxide).

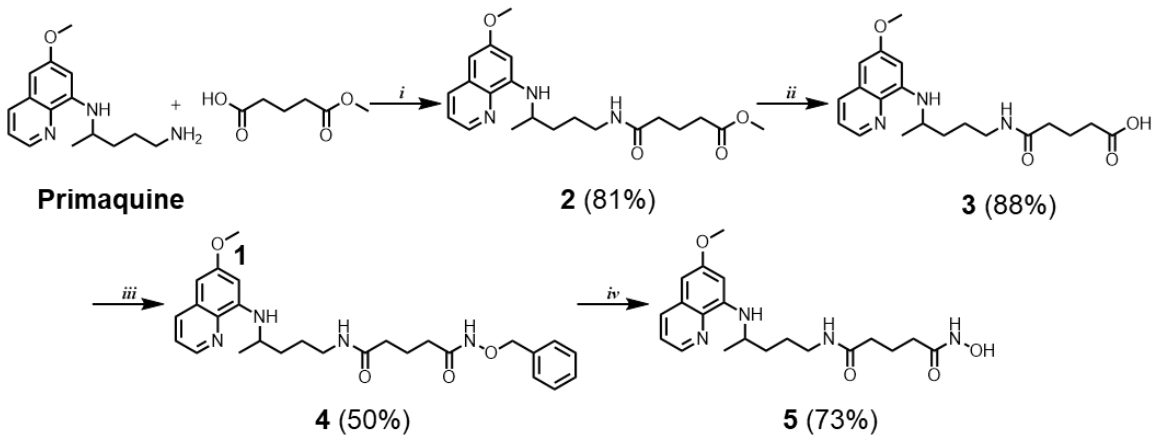

Figure 2.1.

Table 2.1. Structures of sahaquine, temozolomide, quercetin, and SAHA with basic physicochemical properties

The physicochemical properties are calculated with the Chemicalize.org program (Instant Cheminformatics Solutions. Available online at http://www.chemicalize.org/ (accessed on 10 October 2017)).

Structure	IUPAC name	Molecular mass	log*P*	pI
Sahaquine 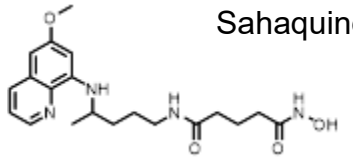	*N*-hydroxy-*N*'-{4-[(6-methoxyquinolin-8-yl)amino]pentyl}pentanediamide	388.47	0.92	6.48
Temozolomide 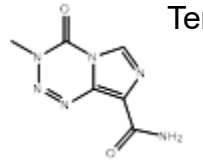	3-methyl-4-oxo-3*H*,4*H*-imidazo[4,3-*d*][1,2,3,5]tetrazine-8-carboxamide	194.15	-0.28	7.1
Quercetin 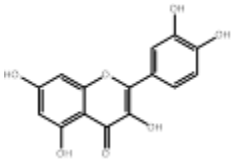	2-(3,4-dihydroxyphenyl)-3,5,7-trihydroxy-4*H*-chromen-4-one	302.24	2.16	2.9
SAHA 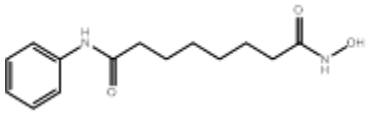	*N*'-hydroxy-*N*-phenyloctanediamide	264.33	1.0	9.2

Table 2.1.

Figure 2.2. Sahaquine kills human glioblastoma cells in a dose-dependent and time-dependent manner

GBM cell viability (n = 9) following treatment with (a) sahaquine (Sq, 0.001–50 μM), (b) temozolomide (TMZ, 0.001–500 μM), c) quercetin (Q, 0.001–300 μM), and d) SAHA (0.001–50 μM) for 24 or 72 h. Shown is the mean (SEM) percentage cell viability compared to untreated controls from three independent experiments.(e, f) Dose-dependent decrease in cell viability (72 h) with the combination of either a fixed concentration of quercetin (100 μM, n = 41) and increasing concentrations of sahaquine (Sq 1 μM, n = 21, Sq 10 μM, n = 30, Sq 20 μM, n = 21, Sq 1 μM + Q, n = 25, Sq 10 μM + Q, n = 29, Sq 20 μM + Q, n = 27), or a fixed concentration of sahaquine (10 μM n = 30) and increasing concentrations of quercetin (Q 10 μM, n = 37, Q 100 μM, n = 41, Q 200 μM, n = 28, Q 10 μM + Sq, n = 34, Q 100 μM + Sq, n = 35, Q 200 μM + Sq, n = 21). Each point represents a percentage value normalized to the untreated control (e n = 47, f n = 125). Horizontal bars represent the mean (SD) from at least three independent experiments (***$p < 0.001$ compared to the untreated control; ###$p < 0.001$ compared to e Q 100 μM alone or f Sq 10 μM alone; Welch's ANOVA with Games–Howell post hoc test). Cell viability was measured by counting Hoechst 33342-labeled nuclei imaged using a fluorescence microscope.

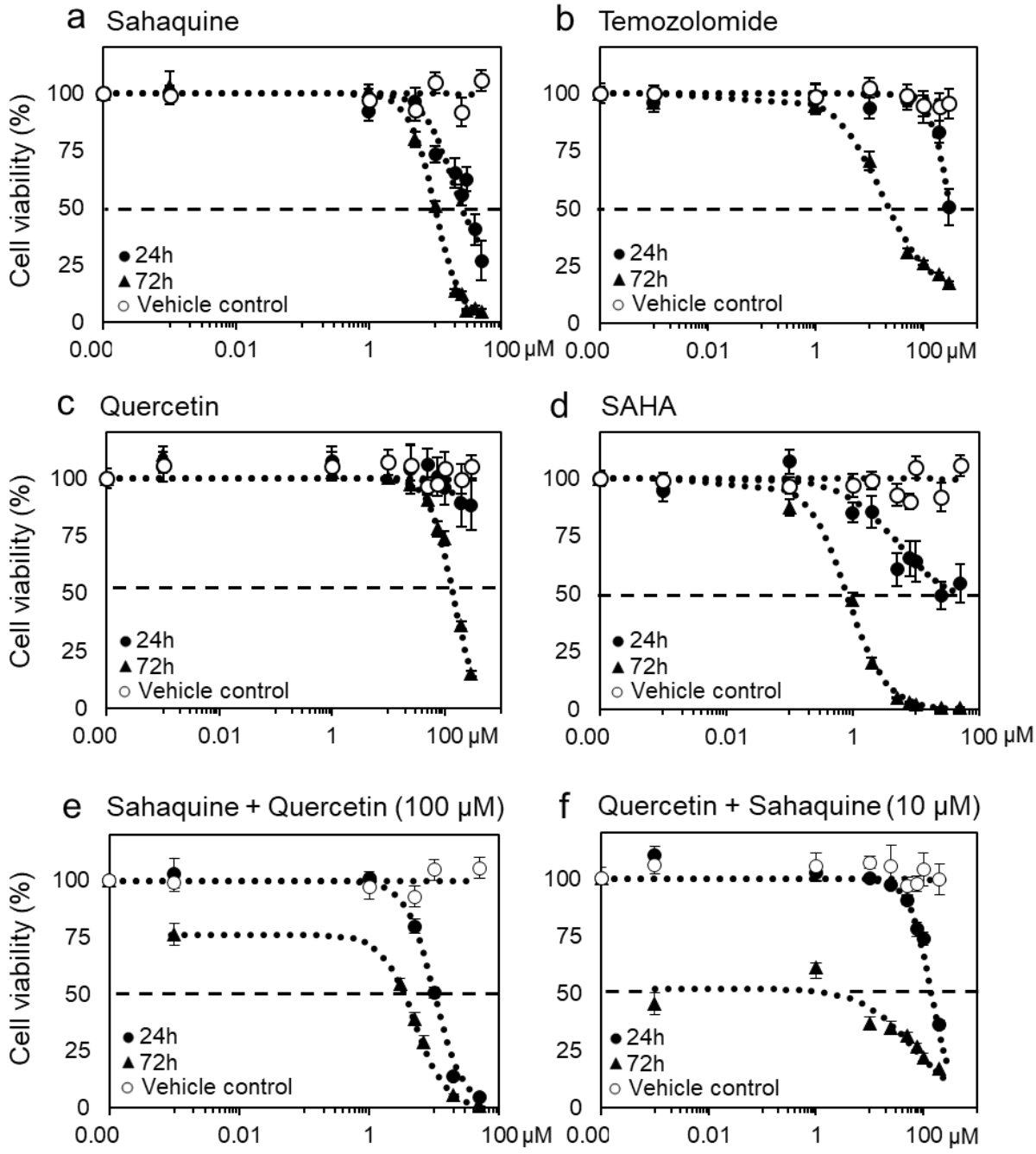
a Sahaquine
b Temozolomide
c Quercetin
d SAHA
e Sahaquine + Quercetin (100 μM)
f Quercetin + Sahaquine (10 μM)
Cell viability (%)
100
75
50
25
0
0.00
0.01
1
100 μM
24h
72h
Vehicle control

Figure 2.2.

Figure 2.3. Sahaquine and quercetin are most effective in killing human brain cancer stem cells

(a) Representative micrographs of BTSCs treated with temozolomide (100 μM, n = 99), sahaquine (10 μM, n = 183) or quercetin (100 μM, n = 264) for 7 days. (b) The surface area of neurospheres was measured based on 2D micrographs from three independent experiments. Shown are average values (SD) normalized to the untreated controls (set to 1, n = 334) (***$p < 0.001$, Welch's ANOVA with Games–Howell post hoc test).

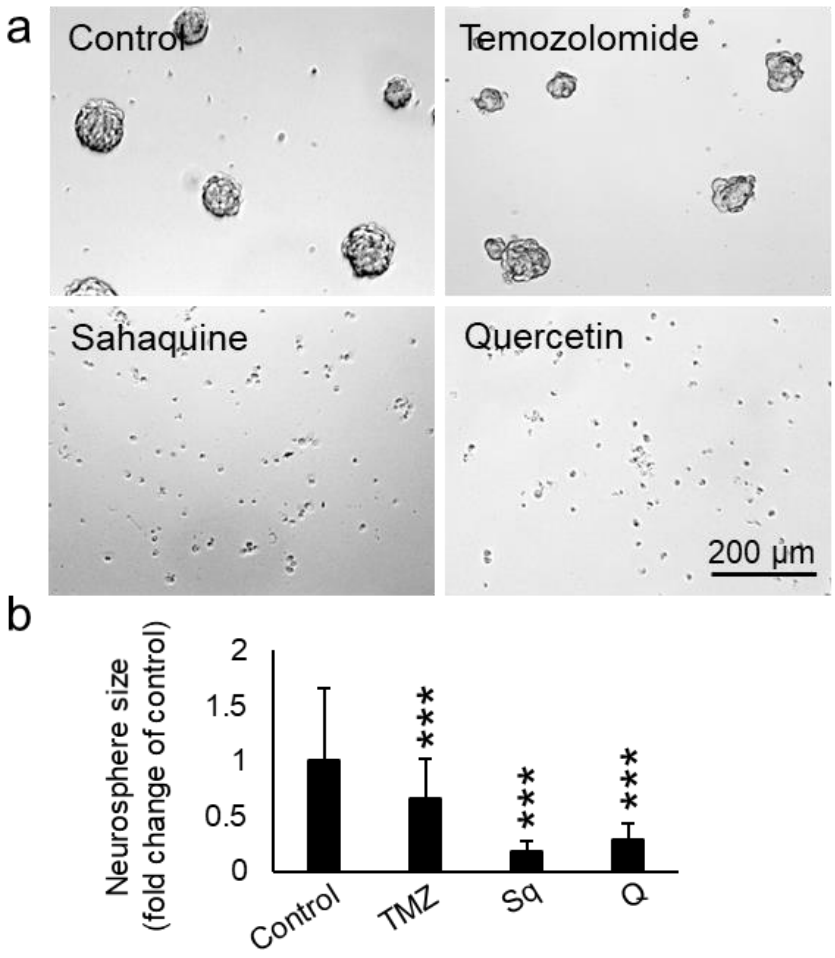
a
Control
Temozolomide
Sahaquine
Quercetin
200 μm
b
Neurosphere size
(fold change of control)
2
1.5
1
0.5
0
***
***
***
Control
TMZ
Sq
Q

Figure 2.3.

Figure 2.4. Sahaquine inhibits human glioblastoma cell migration and invasion

Cell migration was measured using the scratch assay, as schematically represented in (a). Representative micrographs show migration of cells into the scratch (delineated by vertical black bars) after treatment with temozolomide (100 μM, n = 12), sahaquine (Sq, 10 μM, n = 10), quercetin (Q, 100 μM, n = 12) or SAHA (10 μM, n = 10), alone or in combination (Sq + TMZ, n = 12; Sq + Q, n = 12) for 24 h. Cytochalasin D (40 nM, n = 13) served as a positive control. (b) Cell migration was quantified as the area covered by migrating cells. Each point represents a value normalized to the untreated control (set to 1, n = 35). Horizontal bars represent the mean (SD) from at least three independent experiments (*$p < 0.05$, **$p < 0.01$, ***$p < 0.001$, Welch's ANOVA with Games–Howell post hoc test). (c) Cell invasion was measured from the radial movement of cells from 3D tumoroids embedded in a collagen matrix, as schematically represented in the first panel. Representative micrographs show cell movement from 3D tumoroids treated with temozolomide (100 μM, n = 7), sahaquine (Sq, 10 μM, n = 7), quercetin (Q, 100 μM, n = 10), or SAHA (10 μM, n = 5), alone or in combination (Sq + TMZ, n = 5; Sq + Q, n = 8) after 4 days. (d) Cell invasion was quantified from the area covered by invading cells. Each point represents a value normalized to the untreated control (set to 1, n = 11). Horizontal bars represent the mean from at least three independent experiments (***$p < 0.001$, two-tailed one-way ANOVA with Tukey–Kramer's post hoc test).

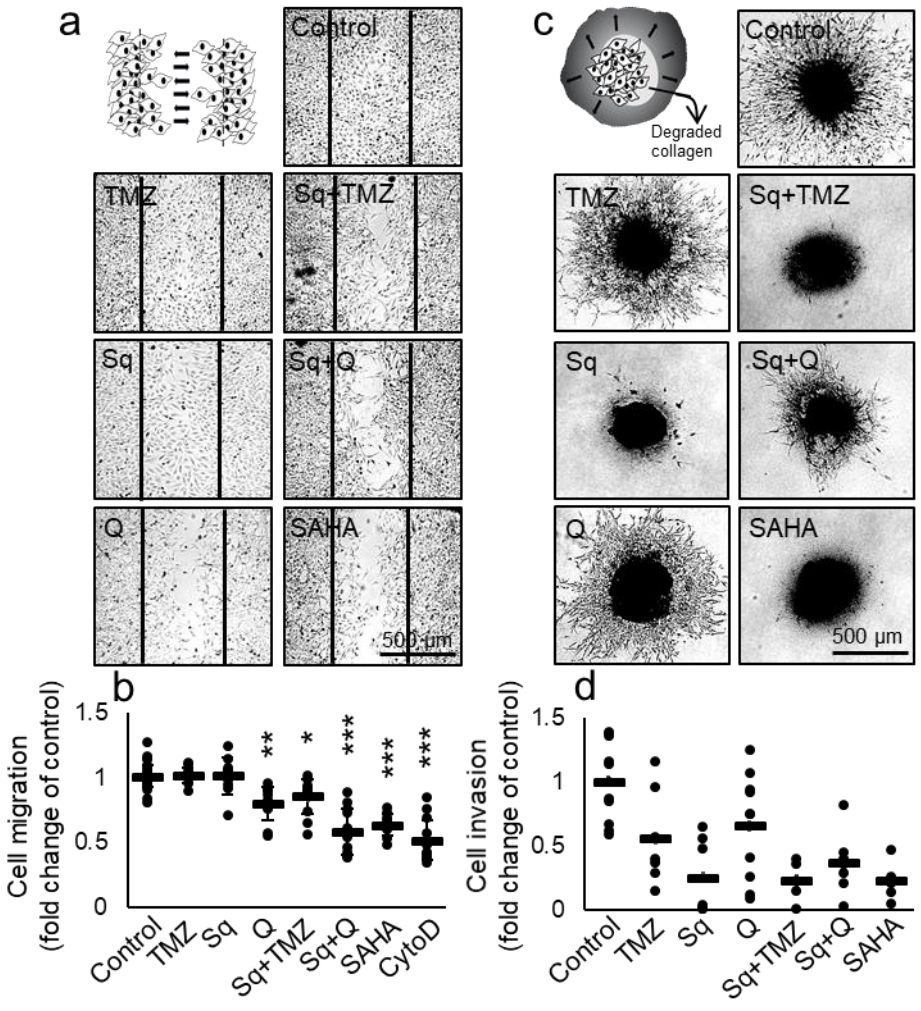
a
Control
TMZ
Sq+TMZ
Sq
Sq+Q
Q
SAHA
500 μm
c
Degraded collagen
Control
TMZ
Sq+TMZ
Sq
Sq+Q
Q
SAHA
500 μm
b
Cell migration (fold change of control)
1.5
1
0.5
0
**
*
***
***
***
Control
TMZ
Sq
Q
Sq+TMZ
Sq+Q
SAHA
CytoD
d
Cell invasion (fold change of control)
1.5
1
0.5
0
Control
TMZ
Sq
Q
Sq+TMZ
Sq+Q
SAHA

Figure 2.4.

Figure 2.5. Sahaquine-mediated HDAC6 inhibition results in selective α-tubulin hyperacetylation at nanomolar concentrations

(a) Representative fluorescence micrographs of GBM α-tubulin acetylation (green) at lysine 40 in response to sahaquine (Sq, 100 nM, n = 121 cells), SAHA (100 nM, n = 54 cells) or primaquine (PQ, 10 μM, n = 30 cells) treatment for 24 h. (b) Representative fluorescence micrographs of GBM histone H3 acetylation (red) at lysine 9/lysine 14 in response to sahaquine (Sq, 100 nM, n = 120 cells), SAHA (100 nM, n = 90 cells) or primaquine (PQ, 10 μM, n = 83 cells) for 24 h. Nuclei (blue) were labeled with Hoechst 33342. Cells were imaged using a fluorescence microscope and fluorescence was analyzed in ImageJ. Shown are averages of fluorescence per cell (SD) normalized to the untreated controls (set to 1) from at least three independent experiments (***$p < 0.001$, Welch's ANOVA with Games–Howell post hoc test). (c) Acetylated α-tubulin (n = 3) and (d) HDAC6 protein abundance (n = 4) in GBM cells treated with temozolomide (TMZ, 100 μM), sahaquine (Sq, 10 μM) or quercetin (Q, 100 μM) alone or in combination for 24 h, measured by Western blotting. Acetylated α-tubulin and HDAC6 were normalized to total α-tubulin and actin, respectively. Each point represents a value normalized to the untreated control (set to 1). Horizontal bars represent the mean from at least three independent experiments. (e) Representative fluorescence micrographs of GBM α-tubulin acetylation (green) at lysine 40 in response to temozolomide (TMZ, 100 μM, n = 76 cells), sahaquine (Sq, 10 μM, n = 56 cells), quercetin (Q, 100 μM, n = 32 cells) or SAHA (10 μM, n = 36 cells) alone or in combination for 24 h. Nuclei (blue) were labeled with Hoechst 33342. (f) Shown are averages (SD) of fluorescence per cell normalized to the untreated control (set to 1, n = 197 cells) from at least three independent experiments (***$p < 0.001$, Welch's ANOVA with Games–Howell post hoc test).

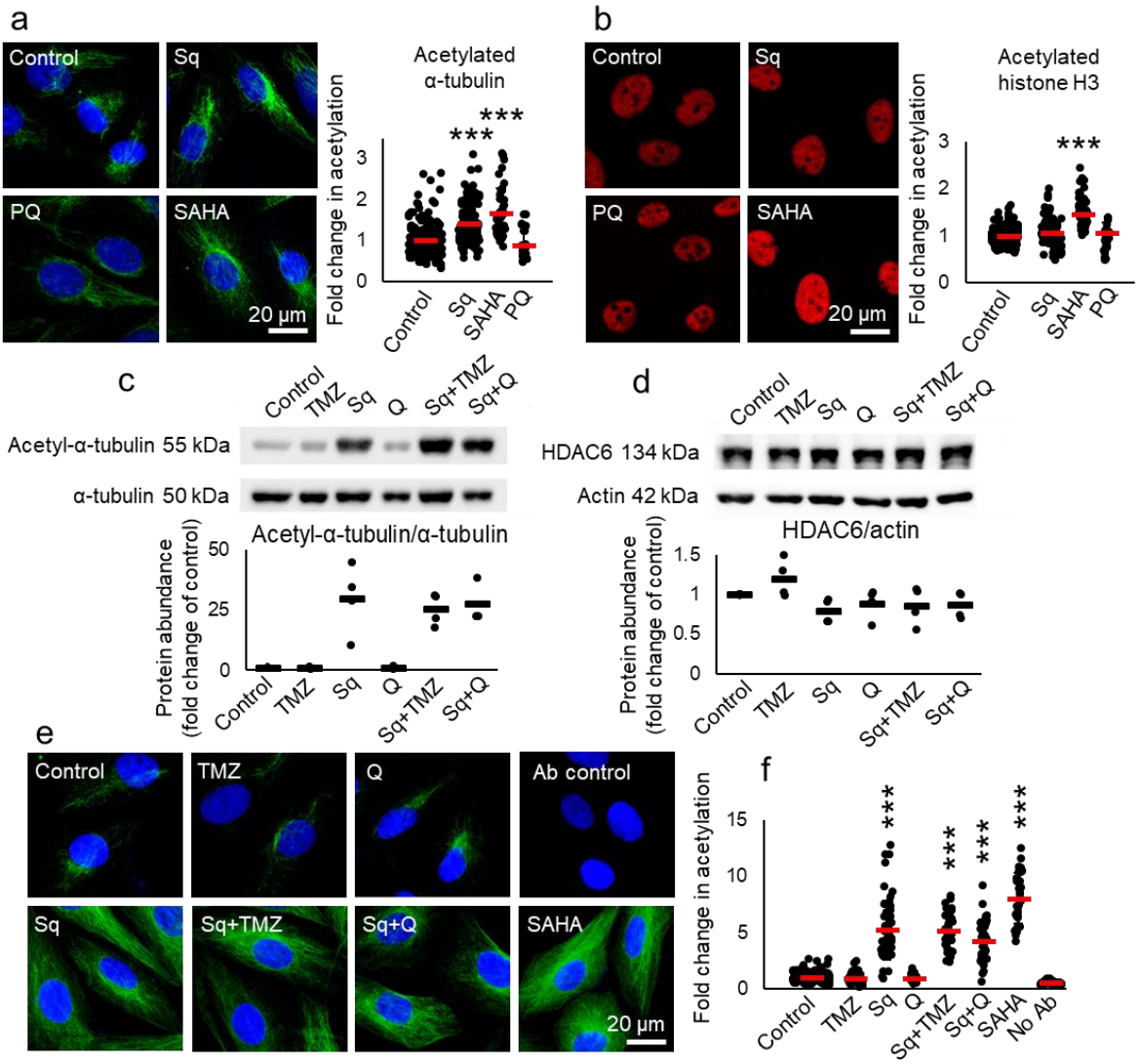
a
Control
Sq
PQ
SAHA
20 μm
Acetylated α-tubulin
Fold change in acetylation
***
***
Control
Sq
SAHA
PQ
b
Control
Sq
PQ
SAHA
20 μm
Acetylated histone H3
Fold change in acetylation
***
Control
Sq
SAHA
PQ
c
Control
TMZ
Sq
Q
Sq+TMZ
Sq+Q
Acetyl-α-tubulin 55 kDa
α-tubulin 50 kDa
Acetyl-α-tubulin/α-tubulin
Protein abundance (fold change of control)
d
HDAC6 134 kDa
Actin 42 kDa
HDAC6/actin
Protein abundance (fold change of control)
e
Control
TMZ
Q
Ab control
Sq
Sq+TMZ
Sq+Q
SAHA
20 μm
f
Fold change in acetylation
No Ab

Figure 2.5.

Figure 2.6. Sahaquine reduces EGFR abundance and AKT/ERK1/2 phosphorylation in human glioblastoma

(a) Representative fluorescence micrographs of human brain sections (GBM or healthy control) labeled for HDAC6, EGFR, phosphorylated AKT (p-AKT), or dually phosphorylated ERK1/2 (p-ERK1/2). Nuclei (blue) were labeled with Hoechst 33342. Cells were imaged using a fluorescence microscope and fluorescence was analyzed in ImageJ. (b) Horizontal bars represent averages of fluorescence per cell (SD) for HDAC6 (control, n = 181 cells, GBM, n = 272 cells), EGFR (control, n = 94 cells, GBM, n = 116 cells), p-AKT (control, n = 115 cells, GBM, n = 147 cells) and p-ERK1/2 (control, n = 35 cells, GBM, n = 104 cells). Each point represents a value normalized to the healthy control (set to 1) (***$p < 0.001$, Welch's ANOVA with Games–Howell post hoc test). (c) EGFR (TMZ, n = 4, Sq, n = 5, Q, n = 5, Sq + TMZ, n = 5, Sq + Q, n = 5), (d) phosphorylated AKT (n = 3), and (e) phosphorylated ERK1/2 (TMZ, n = 4, Sq, n = 4, Q, n = 4, Sq + TMZ, n = 4, Sq + Q, n = 3) protein abundances were measured in GBM cells treated with temozolomide (TMZ, 100 μM), sahaquine (Sq, 10 μM), or quercetin (Q, 100 μM) alone or in combination for 24 h, by Western blotting. EGFR protein abundance was normalized to the actin loading control. Phosphorylated AKT and ERK1/2 were normalized to total AKT and total ERK1/2, respectively. Each point represents a value normalized to the untreated control (set to 1). Horizontal bars represent means from at least three independent experiments.

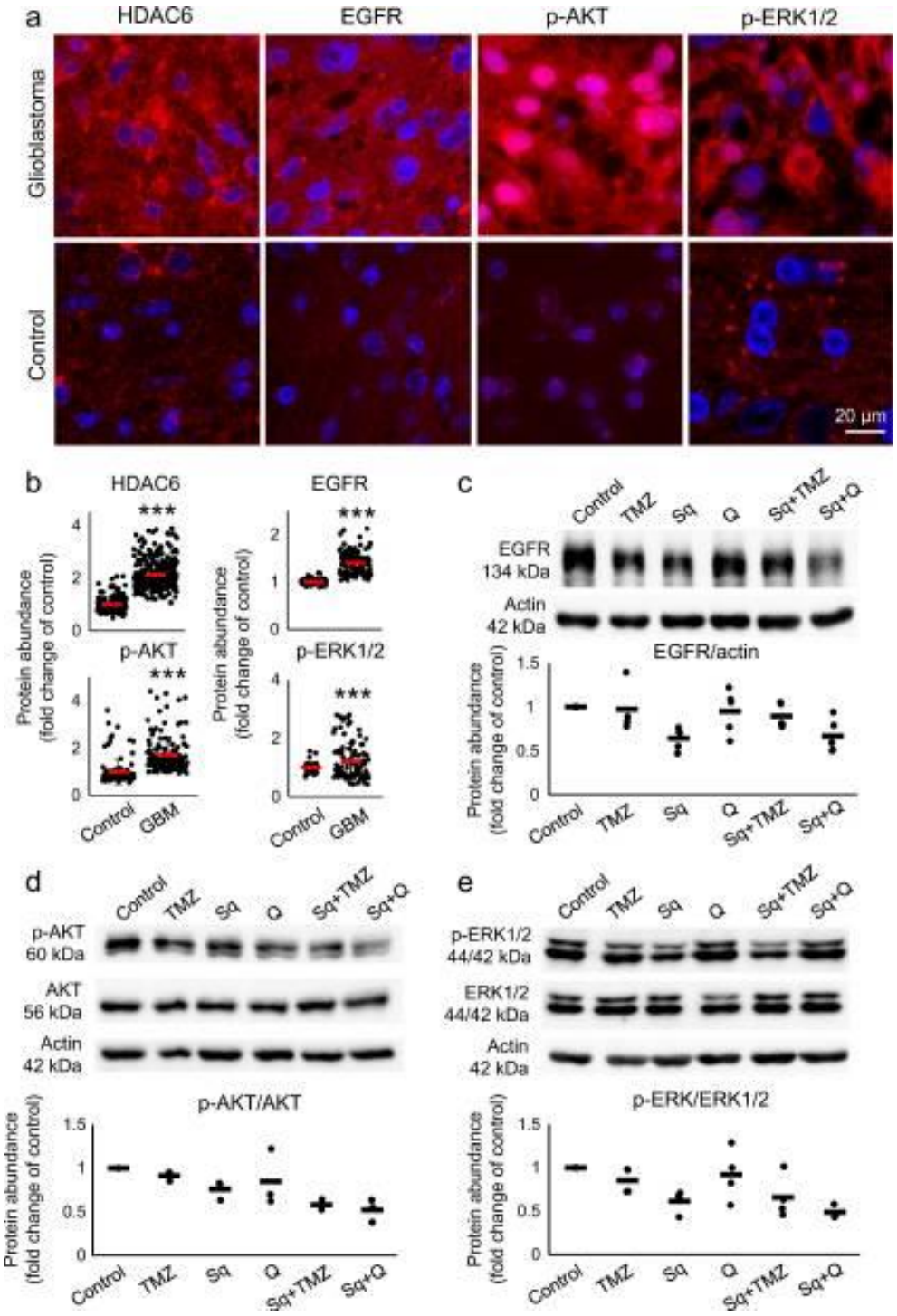
a
HDAC6
EGFR
p-AKT
p-ERK1/2
Glioblastoma
Control
20 μm
b
HDAC6
EGFR
p-AKT
p-ERK1/2
***
Protein abundance (fold change of control)
Control
GBM
c
Control
TMZ
Sq
Q
Sq+TMZ
Sq+Q
EGFR 134 kDa
Actin 42 kDa
EGFR/actin
d
p-AKT 60 kDa
AKT 56 kDa
Actin 42 kDa
p-AKT/AKT
e
p-ERK1/2 44/42 kDa
ERK1/2 44/42 kDa
Actin 42 kDa
p-ERK/ERK1/2

Figure 2.6.

Figure 2.7. Proposed mechanism of action of sahaquine and quercetin in GBM

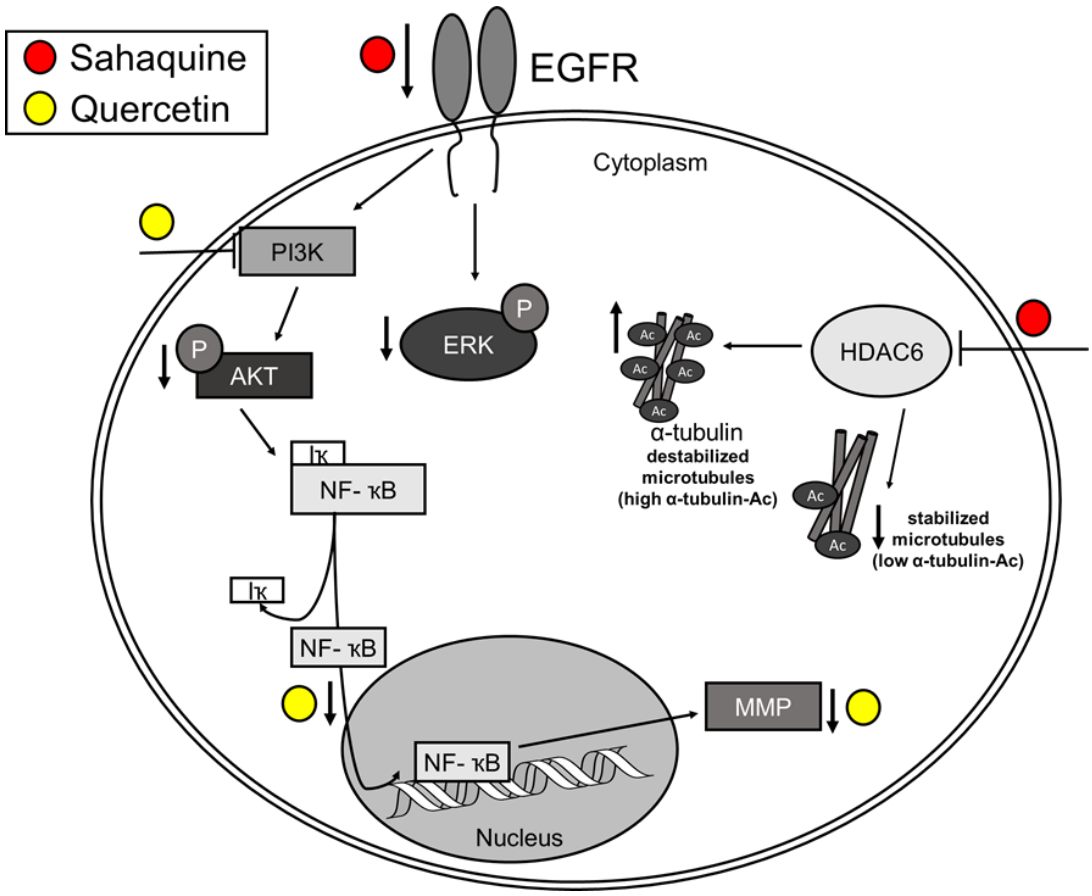
Sahaquine
Quercetin
EGFR
Cytoplasm
PI3K
P
AKT
P
ERK
Ac
Ac
Ac
Ac
Ac
HDAC6
α-tubulin
destabilized
microtubules
(high α-tubulin-Ac)
Ac
Ac
stabilized
microtubules
(low α-tubulin-Ac)
Iκ
NF- κB
Iκ
NF- κB
MMP
NF- κB
Nucleus

Figure 2.7.

Supplemental information

Chemistry

Melting points were measured on a Stuart Melting Point (SMP3) apparatus (Barloworld Scientific, UK) in open capillaries and are uncorrected. IR spectra were recorded on FTIR Perkin Elmer Paragon 500 and UV-Vis spectra on Lambda 20 double beam spectrophotometer (Perkin-Elmer, Waltham, MA, USA). All NMR (1H and 13C) spectra were recorded at 25°C on NMR Avance 600 (Bruker, Rheinstetten, Germany) and Varian Inova 400 spectrometers (Varian, Palo-Alto, CA, USA). Chemical shifts (δ) are reported in parts per million (ppm) using tetramethylsilane as reference in the 1H and the DMSO residual peak as reference in the 13C spectra (39.51 ppm). Coupling constants (J) are reported in Hertz (Hz). Mass spectra were recorded on HPLC-MS/MS (HPLC, Agilent Technologies 1200 Series; MS, Agilent Technologies 6410 Triple Quad, Santa Clara, CA, USA). Mass determination was realized using electron spray ionization (ESI) in positive mode. Elemental analyses were performed on a CHNS LECO analyzer (LECO Corporation, St. Joseph, MI, USA). Primaquine was prepared from primaquine diphosphate (Sigma Aldrich, St. Louis, MO, USA) prior the use. All reactions with primaquine were run light protected.

Synthesis of sahaquine

Compound 2

Mono-methyl glutarate 1 (0.206 g,0.0014 mol, Sigma-Aldrich, St. Louis, MO, USA), HATU (0.532 g, 0.0014 mol, Alfa Aesar, ThermoFisher, Kandel, Germany) and DIEA (0.362 g, 0.0028 mol, Alfa Aesar, ThermoFisher, Kandel, Germany) were dissolved and stirred in dichloromethane at room temperature. After 10 min, a solution of primaquine (0.401 g, 0.0015 mol, Sigma-Aldrich)

in dichloromethane was added. After 1h at room temperature, reaction mixture was evaporated under reduced pressure, dissolved in ethyl acetate and washed three times with brine. The organic layer was dried over sodium sulfate, filtered and evaporated under reduced pressure. The crude product was purified by column chromatography (dichloromethane/methanol 95:5) and crystallized from ether to give pure 2, yellow oil (0.439 g, 81%); IR: □max 3376, 3246, 3086, 2993, 2961, 2927, 1736, 1632, 1612, 1574, 1520, 1458, 1423, 1386, 1219, 1203, 1172, 1161, 1052, 992, 817, 788, 751, 720, 676 cm–1; 1H NMR (300 MHz, DMSO) δ 8.53(d, J = 2.6, 1H), 8.07 (d, J = 8.2, 1H), 7.78 (t, J = 3, 1H), 7.43-7.41 (m, 1H), 6.47 (d, J = 2.2, 1H), 6.26 (d, J = 2.2, 1H), 6.11 (d, J = 8.8, 1H), 3.82 (s, 3H), 3.64-3.60 (m, 1H), 3.57 (s, 3H), 3.05 (t, J = 6.0, 2H), 2.27 (t, J = 3.0, 2H), 2.07 (t, J = 7.3, 2H), 1.74-1.69 (m, 2H), 1.67-1.62, 1.54-1.44 (2m, 4H), 1.21(d, J = 6.2, 3H; 13C NMR (75 MHz, DMSO) δ 173.00, 171.18, 158.98, 144.60, 144.20, 134.76, 134.50, 129.55, 122.05, 96.08, 91.59, 54.95, 51.14, 46.97, 38.36, 34.28, 33.40, 32.64, 25.93, 20.62, 20.17; MS/MS (m/z): [M]+ calcd. for C21H29N3O4, 388.22; found, 388.3; analysis (calcd., found for C21H29N3O4): C (65.09, 65.35), H (7.54, (7.33), N (10.84, 10.99).

Compound 3

Lithium hydroxide monohydrate (0.126 g, 0.003 mol, Sigma-Aldrich, St. Louis, MO, USA) and ester 2 (0.323 g, 0.0006 mol) were stirred in a mixture of water and methanol for 1 h at room temperature. Methanol was evaporated under reduced pressure and the aqueous residue was neutralized with 10%-HCl and extracted three times with dichloromethane. The organic layer was dried over sodium sulfate, filtered and evaporated under reduced pressure. The crude product was crystallized from ether to give crude product 3 (0.186 g, 88%); pale yellow solid; mp 95–96 □C; IR: □max 3453, 3324, 2933, 1720, 1643, 1613, 1580, 1524, 1386, 1227, 1204, 1161, 1139, 1058,

822, 786, 675 cm–1; 1H NMR (300 MHz, DMSO) δ 12.00 (s, 1H), 8.55-8.53 (dd, J = 4.2, 1.6, 1H), 8.10-8.07 (dd, J = 8.3, 1.5, 1H), 7.80(t, J = 5.4, 1H), 7.45-7.41 (m, 1H), 6.48 (d, J = 2.4, 1H), 6.27 (d, J = 2.4, 1H), 6.13 (d, J = 8.7, 1H), 3.83 (s, 3H), 3.69-3.55 (m, 1H), 3.09-3.05 (m, 2H), 2.20 (t, J = 7.4, 2H), 2.08 (t, J = 7.4, 2H), 1.75-1.43 (m, 6H), 1.21 (d, J = 6.3, 3H); 13C NMR (75 MHz, DMSO) δ 147.15, 171.36, 159.00, 144.63, 144.23, 134.79, 134.53, 129.57, 122.09, 96.11, 91.60, 54.97, 46.98, 38.38, 34.46, 33.41, 33.04, 25.97, 20.71, 20.19; MS/MS (m/z): [M]+ calcd. for C20H27N3O4, 374.2; found, 374.2; analysis (calcd., found for C20H27N3O4): C (64.32, 64.21), H (7.29, 7.15), N (11.25, 11.48).

Compound 4

Solution of carboxylic acid 3 (0.224 g, 0.0006 mol), HATU (0.228 g, 0.0006 mol) and DIEA (0.155 g, 0.0012 mol) was stirred in dichloromethane at room temperature. After 10 min, O-benzylhydroxylamine hydrochloride (0.112 g, 0.0007 mol, Sigma-Aldrich, St. Louis, MO, USA) and triethylamine (0.071 g, 0.0007 mol, Sigma-Aldrich, St. Louis, MO, USA) were added. The reaction mixture was stirred for 2 h at room temperature, evaporated under reduced pressure, dissolved in ethyl acetate and washed three times with brine. The organic layer was dried over sodium sulfate, filtered and evaporated under reduced pressure. The crude product was purified by column chromatography (dichloromethane/methanol 95:5) and crystallized from ether/petroleum ether to give pure 4 (0.144 g, 50%); pale yellow solid; mp 84–85 □C; IR: □max 3367, 3325, 3187, 2960, 2931, 2857, 1738, 1677, 1634, 1614, 1518, 1455, 1387, 1219, 1203, 1170, 1157, 1052, 1033, 821, 790, 740, 696, 676 cm–1; 1H NMR (300 MHz, DMSO) δ 10.95 (s, 1H), 8.54-8.53 (dd, J = 4.1, 1.5, 1H), 8.09-8.06 (dd, J = 8.3, 1.4, 1H), 7.78 (t, J = 5.4, 1H), 7.44-7.33 (m, 6H), 6.47 (d, J = 2.4, 1H), 6.26 (d, J = 2.3, 1H), 6.13 (d, J = 8.8, 1H), 4.77 (s, 2H), 3.82 (s, 3H), 3.62-3.56 (m, 1H),

3.08-3.04 (m, 2H), 2.04 (t, J = 7.4, 2H), 1.95 (t, J = 7.3, 2H), 1.74-1.43 (m, 6H), 1.20 (d, J = 6.2, 3H); 13C NMR (75 MHz, DMSO) δ 171.32, 169.03, 159.00, 144.62, 144.23, 136.09, 134.79, 134.52, 129.57, 128.72, 128.26, 128.16, 122.09, 96.10, 91.59, 76.77, 54.97, 46.98, 38.41, 34.57, 33.43, 31.70, 25.99, 21.21, 20.19; MS/MS (m/z): [M]+ calcd. for C27H34N4O, 479.26; found 479.3; analysis (calcd., found for C27H34N4O): C (67.76, 67.59), H (7.16, 6.98), N (11.71, 12.04).

Compound 5 (sahaquine)

Suspension of O-benzylhydroxamic acid 4 (0,129 g, 0.00027 mol) and 20 mg 10% Pd/C (Sigma-Aldrich, St. Louis, MO, USA) in methanol was stirred for 2 h at room temperature under hydrogen atmosphere. The catalyst was filtered off and methanol was evaporated under reduced pressure. The crude product was crystallized from ether to give pure 5 (0.077g, 73%); pale yellow solid; mp 99–102 □C; IR: □max 3468, 3375, 3283, 3210, 3008, 2963, 2933, 1744, 1645, 1613, 1520, 1455, 1386, 1204, 1171, 1158, 1056, 821, 789, 677 cm–1; 1H NMR (300 MHz, DMSO) δ 10.32 (s, 1H), 8.63 (s, 1H), 8.55-8.52 (dd, J = 4.2, 1.6, 1H), 8.09-8.05 (dd, J = 8.3, 1.6, 1H), 7.76 (t, J = 5.3, 1H), 7.45-7.39 (m, 1H), 6.47 (d, J = 2.4, 1H), 6.26 (d, J = 2.4, 1H), 6.11 (d, J = 8.7, 1H), 3.82 (s, 3H), 3.68-3.56 (m, 1H), 3.05 (d, J = 5.6, 2H), 2.04 (t, J = 7.4, 2H), 1.94 (t, J = 7.4, 2H), 1.76-1.57, 1.57-1.40 (2m, 6H), 1.21 (d, J = 6.3, 3H); 13C NMR (75 MHz, DMSO) δ 171.37, 168.74, 158.98, 144.60, 144.20, 134.75, 134.50, 129.54, 122.05, 96.08, 91.61, 54.95, 46.98, 38.39, 34.73, 33.43, 31.75, 25.95, 21.42, 20.17; MS/MS (m/z): [M]+ calcd. for C20H28N4O4, 389.21; found 389.2; analysis (calcd., found for C20H28N4O4): C (61.84, 61.69), H (7.27, 7.03), N (14.42, 14.77).

Supplementary Table 2.1. Structures of sahaquine precursors with basic physicochemical properties, calculated with the Chemicalize.org program (Instant Cheminformatics Solutions. Available online: http://www.chemicalize.org/ (accessed on October 10th, 2017)).

Structure	IUPAC name	Molecular mass	log*P*	pI
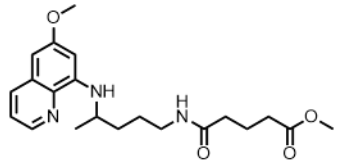	methyl 5-((4-((6-methoxyquinolin-8-yl)amino)pentyl)amino)-5-oxopentanoate	387.48	1.88	9.80
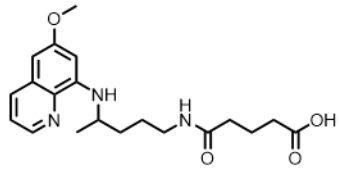	5-((4-((6-methoxyquinolin-8-yl)amino)pentyl)amino)-5-oxopentanoic acid	373.45	1.29	4.19
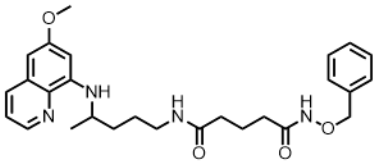	N^1-(benzyloxy)-N^5-(4-((6-methoxyquinolin-8-yl)amino)pentyl)glutaramide	478.58	3.02	6.18

Table S2.1.

Supplementary Figure 2.1. Spectra confirming the structure of sahaquine

(a) Annotated structure of sahaquine. (b) Mass spectra (MS) showing only one peak corresponding to [M+1]. MS was recorded on HPLC-MS/MS. Mass determination was performed using electron spray ionization (ESI) in positive mode. (c) 1H and (d) 13C NMR spectra with marked peaks. All NMR (1H and 13C) spectra were recorded at 25°C at 300, 400 and 600 MHz for 1H and 75, 100 and 150 MHz for 13C nuclei, respectively. Chemical shifts (δ) are reported in parts per million (ppm) using tetramethylsilane as reference in the 1H and the DMSO residual peak as reference in the 13C spectra (39.51 ppm).

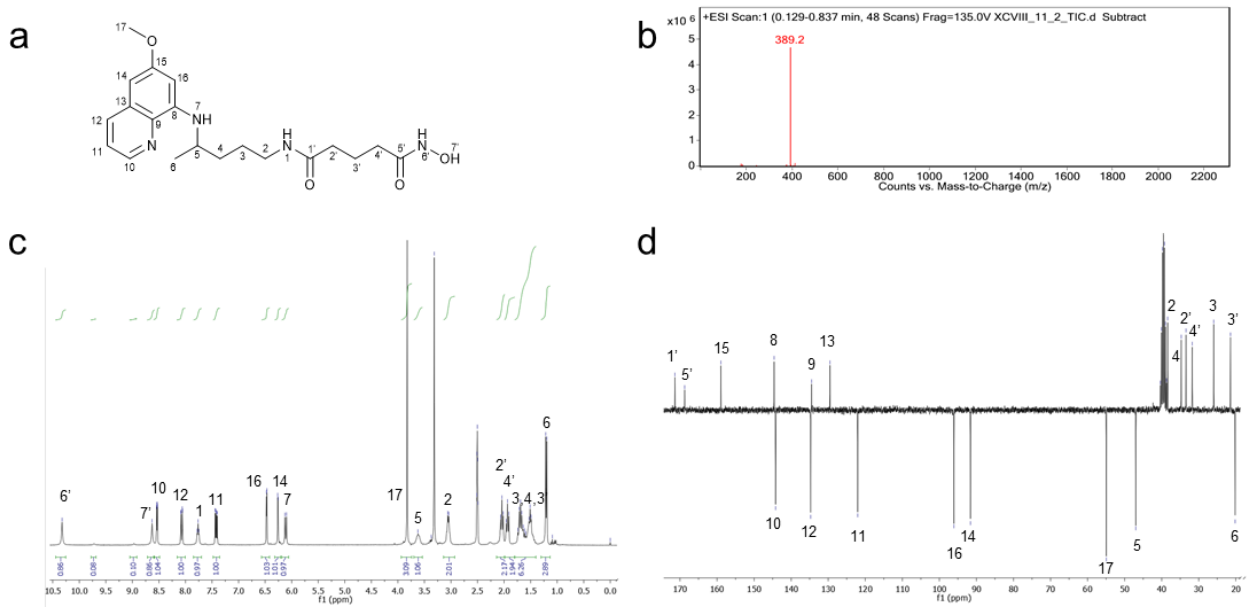
a
b
+ESI Scan:1 (0.129-0.837 min, 48 Scans) Frag=135.0V XCVIII_11_2_TIC.d Subtract
389.2
Counts vs. Mass-to-Charge (m/z)
c
f1 (ppm)
d
f1 (ppm)

Figure S2.1.

Supplementary Figure 2.2. Time-dependent decrease in cell viability with temozolomide combination treatments

GBM cells were treated for 24h or 72h with the combination of temozolomide (TMZ, 30 μM, 24 h n=21, 72 h n=22) and sahaquine (Sq, 10 μM, 24 h n=15, 72 h n=21; Sq+TMZ, 24 h n=21, 72 h n=21), quercetin (Q, 140 μM, 24 h n=21, 72 h n=22; Q+TMZ, 24 h n=21, 72 h n=21) or SAHA (1 μM, 24 h n=21, 72 h n=26; SAHA+TMZ, 24 h n=21, 72 h n=21) at IC50 concentrations. Cell viability was measured by counting Hoechst 33342-labeled nuclei imaged using a fluorescence microscope. Each point represents a percentage value normalized to the untreated control (24 h n=39, 72 h n=12). Horizontal bars represent the mean (SD) from at least three independent experiments (***$p<0.001$ compared to the untreated control; ##$p<0.01$, ###$p<0.001$ compared to TMZ; Welch's ANOVA with Games-Howell post hoc test).

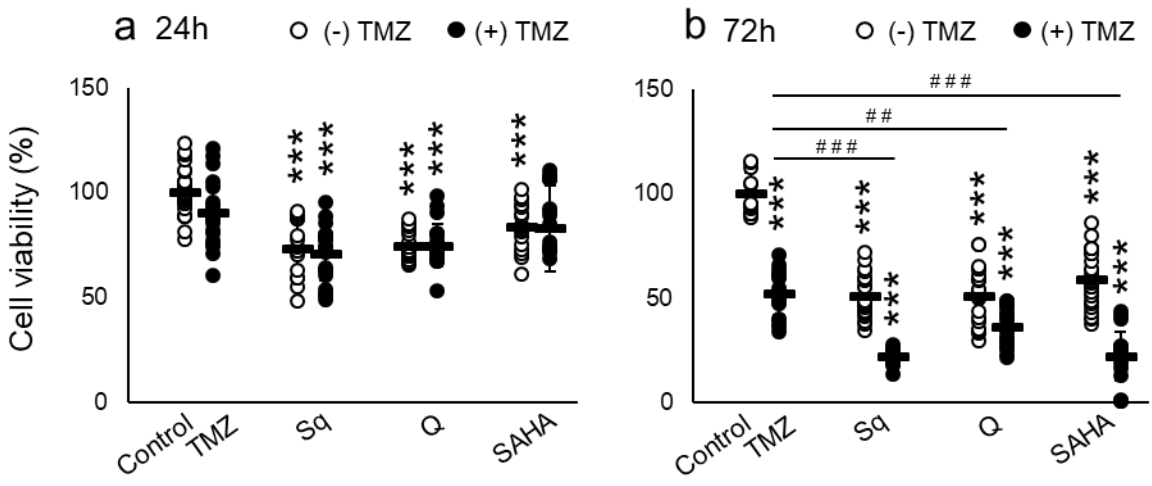
a 24h
(-) TMZ
(+) TMZ
Cell viability (%)
150
100
50
0
Control
TMZ
Sq
Q
SAHA
b 72h
(-) TMZ
(+) TMZ
###
##
###
150
100
50
0
Control
TMZ
Sq
Q
SAHA

Figure S2.2.

Supplementary Figure 2.3. Cytotoxic effects of selected drugs on human glioblastoma tumoroids

(a) Representative micrographs of GBM tumoroids exposed to temozolomide (TMZ, 100 μM, n=13), sahaquine (Sq, 10 μM, n=13) or quercetin (Q, 100 μM, n=17) for 7 days. (b) The size of the tumoroids was measured based on 2D micrographs. Each point represents a value normalized to the untreated control (set to 1, n=19). Horizontal bars represent the mean (SD) from at least three independent experiments (***$p<0.001$, one-way ANOVA with Tukey-Kramer's post hoc test).

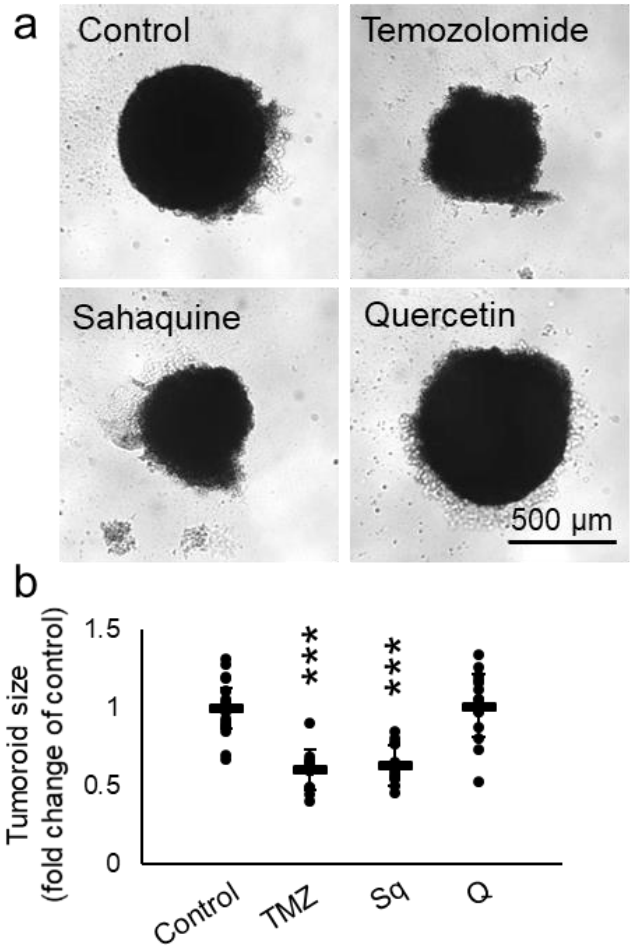
a
Control
Temozolomide
Sahaquine
Quercetin
500 μm
b
Tumoroid size
(fold change of control)
1.5
1
0.5
0
***
***
Control
TMZ
Sq
Q

Figure S2.3.

Supplementary Figure 2.4. The effect of select chemotherapeutic agents on the abundance of secreted MMP-2 and MMP-9 from human glioblastoma

Gelatin zymography of culture media from GBM cells treated with (a) temozolomide (TMZ, 100, 300, 500 μM), (b) sahaquine (Sq, 1, 10, 25 μM) or (c) quercetin (Q, 25, 50, 100 μM) for 24h. (d) Quantification of MMP-9 and MMP-2 from gelatin zymographs (TMZ, 100 μM, n=5; Sq, 10 μM, n=5; Q, 100 μM, n=3). Each point represents a value normalized to the untreated control (set to 1, n=7). Horizontal bars represent the mean from at least three independent experiments.

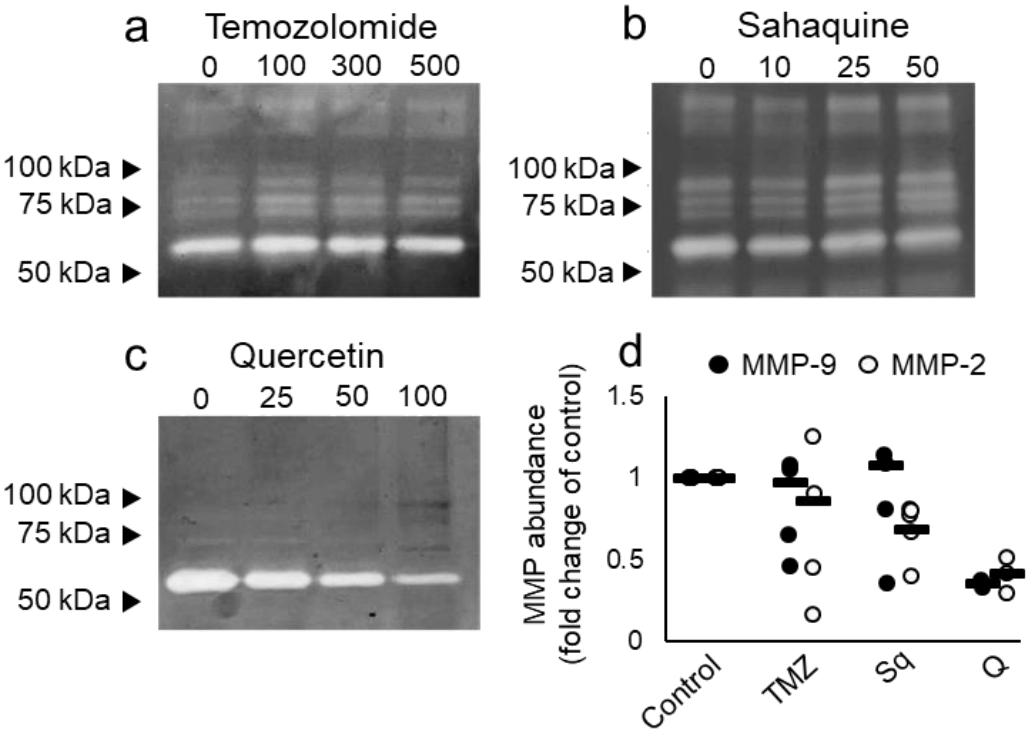
a
Temozolomide
0 100 300 500
100 kDa ▶
75 kDa ▶
50 kDa ▶
b
Sahaquine
0 10 25 50
100 kDa ▶
75 kDa ▶
50 kDa ▶
c
Quercetin
0 25 50 100
100 kDa ▶
75 kDa ▶
50 kDa ▶
d
MMP-9
MMP-2
MMP abundance
(fold change of control)
1.5
1
0.5
0
Control
TMZ
Sq
Q

Figure S2.4.

Supplementary Figure 2.5. Sahaquine inhibits P-glycoprotein activity

The intracellular accumulation of the P-glycoprotein substrate calcein-AM was measured in GBM cells treated with sahaquine (Sq, 10 μM, n=176 cells), primaquine (PQ, 10 μM n=182 cells, 60 μM n=218 cells) and SAHA (10 μM, n=192 cells) for 24h. Cyclosporine A (10 μM, 30 min, n=172 cells) was included as a positive control for the inhibition of P-glycoprotein. Cells were imaged using a fluorescence microscope and fluorescence was analyzed in ImageJ. Each point represents a value normalized to the untreated control (set to 1, n=310 cells). Horizontal bars represent the mean (SD) for control (1.00±0.24), Sq (1.28±0.27), PQ 10 μM (0.99±0.22), PQ 60 μM (1.35±0.29), SAHA (1.16±0.33) and cyclosporine A (1.29±0.28), from three independent experiments (***$p<0.001$, Welch's ANOVA with Games-Howell post hoc test).

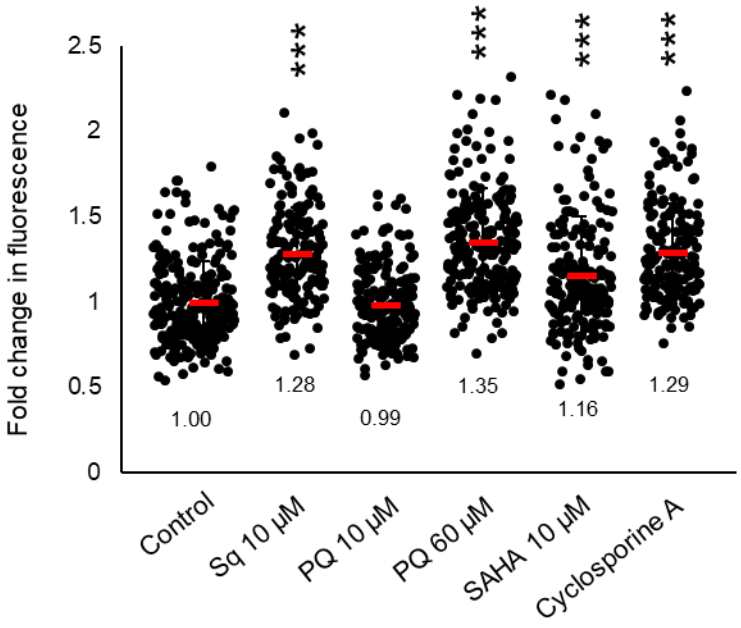
Fold change in fluorescence
2.5
2
1.5
1
0.5
0
***
***
***
***
1.00
1.28
0.99
1.35
1.16
1.29
Control
Sq 10 μM
PQ 10 μM
PQ 60 μM
SAHA 10 μM
Cyclosporine A

Figure S2.5.

Supplementary Figure 2.6. Selective HDAC6 inhibition with ACY-1215 and sahaquine-induced α-tubulin reorganization

Representative fluorescence micrographs of GBM a) α-tubulin acetylation (green) at lysine 40 and histone H3 acetylation (red) at lysine 9/lysine 14 in response to HDAC6-selective inhibitor ACY-1215 (100 nM) for 24h. b-c) Shown are means (SD) of fluorescence per cell for acetylated α-tubulin (n=32 cells) and acetylated histone H3 (n=110 cells) after treatment with ACY-1215 (100 nM) for 24h. Each point represents a value normalized to the untreated control (set to 1; acetylated α-tubulin n=197 cells; acetylated histone H3 n=158 cells) from at least three independent experiments (*$p<0.05$, ***$p<0.001$, Welch's ANOVA with Games-Howell post hoc test). Nuclei (blue) were labeled with Hoechst 33342. Cells were imaged using a fluorescence microscope and fluorescence was analyzed in ImageJ.

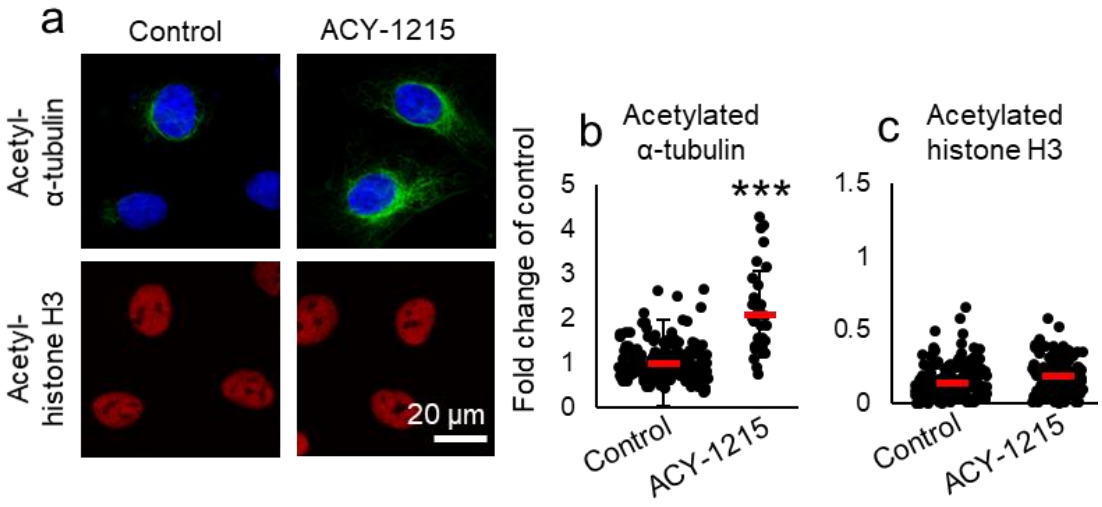
a
Control
ACY-1215
Acetyl-
α-tubulin
Acetyl-
histone H3
20 μm
b
Acetylated
α-tubulin
Fold change of control
5
4
3
2
1
0
***
Control
ACY-1215
c
Acetylated
histone H3
1.5
1
0.5
0
Control
ACY-1215

Figure S2.6.

Supplementary Figure 2.7. Sahaquine-induced α-tubulin reorganization

Representative fluorescence micrographs of GBM α-tubulin (red) reorganization in response to Sq (10 μM) after 24h treatment. Nuclei (blue) were labeled with Hoechst 33342. Cells were imaged using a fluorescence microscope. Inserts show the microtubule organizing center, where α-tubulin reorganization is observed.

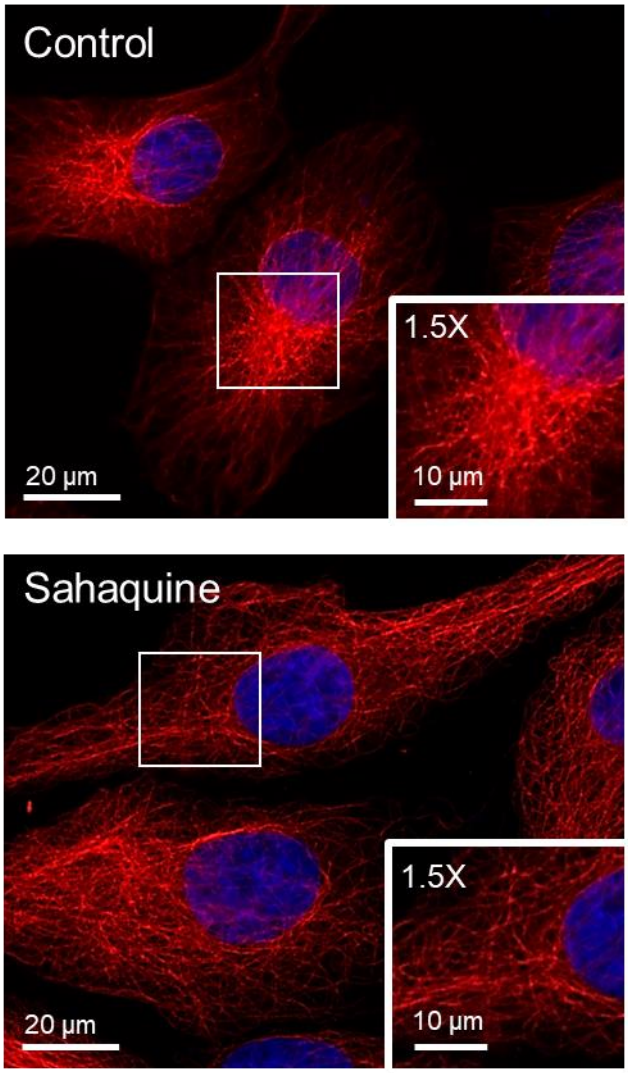

Figure S2.7.

Supplementary Figure 2.8. Sahaquine and quercetin decrease the abundance of Hsp70/Hsc70 in human glioblastoma

The abundance of heat shock proteins Hsp70 and Hsc70 was measured in GBM cells treated with temozolomide (TMZ, 100 μM), sahaquine (Sq, 10 μM) or quercetin (Q, 100 μM) alone or in combination for 24h, by Western blotting (n=4). Hsp70/Hsc70 protein abundance was normalized to the actin loading control. Each point represents a value normalized to the untreated control (set to 1). Horizontal bars represent means from four independent experiments.

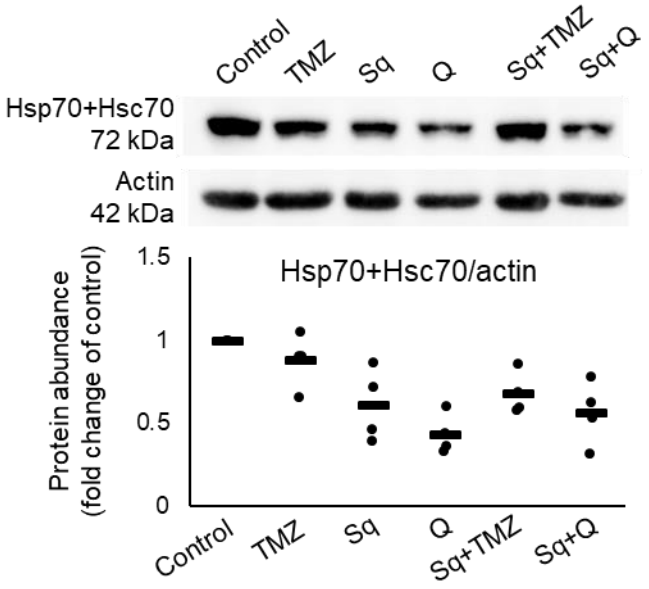
Control
TMZ
Sq
Q
Sq+TMZ
Sq+Q
Hsp70+Hsc70
72 kDa
Actin
42 kDa
Hsp70+Hsc70/actin
Protein abundance
(fold change of control)
1.5
1
0.5
0
Control
TMZ
Sq
Q
Sq+TMZ
Sq+Q

Figure S2.8.

Supplementary Figure 2.9. Buthionine sulfoximine enhances the cell killing effect of sahaquine in GBM

GBM cell viability following treatment with sahaquine (Sq, 10 μM, 24 h n=15, 72 h n=30), buthionine sulfoximine (BSO, 100 μM, 24 h n=32, 72 h n=18) or combination of sahaquine and buthionine sulfoximine (Sq + BSO, 24 h n=35, 72 h n=27) for 24h or 72h. Cell viability was measured by counting Hoechst 33342-labeled nuclei imaged using a fluorescence microscope. Shown are the average percentage cell viability (SD). Each point represents a value normalized to the untreated control (24 h n=33, 72 h n=18) from three independent experiments (***$p<0.001$, Welch's ANOVA with Games-Howell post hoc test).

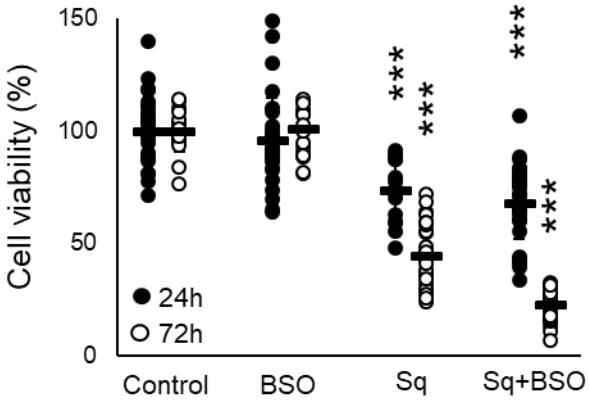

Figure S2.9.

Connecting Text

Glioblastoma multiforme is heterogeneous and can adapt to stressful stimuli, which is why combination treatments are crucial to overcome treatment resistance. In Chapter 2, we explored the effectiveness of the HDAC6 inhibitor sahaquine in monotherapy as well as in combination with the natural compound quercetin. Although natural compounds are attractive for heterogeneous tumors because of their multiple mechanisms of action and safe profile, they are often limited by their pharmacokinetic properties.

In Chapter 3, we investigated the role of lipid droplets in sequestering curcumin, a natural compound with promising anti-cancer properties. Lipid droplets are upregulated in glioblastoma (astrocytoma) compared to normal astrocytes and play an important role in supporting tumor growth and resistance. We show that the pharmacological inhibition of lipid droplet formation in glioblastoma increases cancer cell killing by curcumin. Using a dimerization-dependent biosensor for caspase-3 activity, we also shed light onto the mechanism of cell death induced by curcumin, as compared to that of the clinical standard temozolomide.

The results in Chapter 3 point to the importance of taking organellar adaptation into account when considering combination treatments for cancer. Lipid droplets are particularly interesting given their roles at the nexus of cell metabolism and inflammation, two key aspects in the glioblastoma microenvironment. In addition to these results published in the European Journal of Pharmaceutics and Biopharmaceutics, follow-up studies on the modulation of microglia and astrocytes activation in the tumor microenvironment using dendrimeric nanostructures are presented in Chapter 4.

Chapter 3. Pharmacological inhibition of lipid droplet formation enhances the effectiveness of curcumin in glioblastoma.

Zhang I, Cui Y, Amiri A, Ding Y, Campbell RE, Maysinger D. Eur J Pharm Biopharm. 2016; 100:66-76.

Abstract

Increased lipid droplet number and fatty acid synthesis allow glioblastoma multiforme, the most common and aggressive type of brain cancer, to withstand accelerated metabolic rates and resist therapeutic treatments. Lipid droplets are postulated to sequester hydrophobic therapeutic agents, thereby reducing drug effectiveness. We hypothesized that the inhibition of lipid droplet accumulation in glioblastoma cells using pyrrolidine-2, a cytoplasmic phospholipase A2 alpha inhibitor, can sensitize cancer cells to the killing effect of curcumin, a promising anticancer agent isolated from the turmeric spice. We observed that curcumin localized in the lipid droplets of human U251N glioblastoma cells. Reduction of lipid droplet number using pyrrolidine-2 drastically enhanced the therapeutic effect of curcumin in both 2D and 3D glioblastoma cell models. The mode of cell death involved was found to be mediated by caspase-3. Comparatively, the current clinical chemotherapeutic standard, temozolomide, was significantly less effective in inducing glioblastoma cell death. Together, our results suggest that the inhibition of lipid droplet accumulation is an effective way to enhance the chemotherapeutic effect of curcumin against glioblastoma multiforme.

Introduction

In cancers such as glioblastoma multiforme, enhanced fatty acid storage and synthesis provide the necessary resources for survival and rapid proliferation (K. Gupta et al., 2011). Although otherwise highly heterogeneous, most cancer types present a lipogenic phenotype characterized by the upregulation of key enzymes and transcriptional factors controlling lipid metabolism (e.g. Akt, fatty acid synthase, hypoxia-inducible factor 1-alpha, sterol regulatory element binding proteins, acetyl-CoA carboxylase alpha), and a boost in de novo lipogenesis (Baenke et al., 2013; Boroughs & DeBerardinis, 2015; Francis P. Kuhajda, 2006; Menendez & Lupu, 2007). In solid malignancies, the hypoxic conditions found at the core of the tumors induce adaptive pathways aimed at maintaining lipid synthesis, homeostatic pH and cell survival (Kamphorst et al., 2013). The resulting metabolic changes correlate with poor prognosis, poor treatment response and recurrence in diseases such as breast, liver and brain cancer (F. P. Kuhajda et al., 1994; Patterson et al., 2011; Prasanna et al., 1996; Renehan et al., 2015). Emerging therapeutic approaches have thus targeted lipid synthesis to counter the effects of metabolic reprogramming in cancer cells (Sounni et al., 2014; Umemura et al., 2014).

Aside from their increased de novo fatty acid synthesis, cancer cells are also characterized by their increased number of lipid droplets compared to normal tissues (Santos & Schulze, 2012; Swinnen et al., 2006). Lipid droplets are dynamic organelles that support cells with metabolic fuel, membrane biosynthesis, inflammatory intermediates and signaling mediators (Barbosa et al., 2015; Gross & Silver, 2014; Hashemi & Goodman, 2015). Although they can be found in almost all cell types, their increased biogenesis in neoplastic and inflammatory conditions defines them as targets for therapeutic intervention (Accioly et al., 2008). Aside from fueling the accelerated metabolism of cancer cells, lipid droplets also harbor numerous proteins and transcription factors critical to

lipid metabolism and related pathways (Welte, 2015). The hydrophobic core found in lipid droplets provides a favorable compartment to attract and sequester lipophilic proteins and compounds, fat-soluble vitamins, and even environmental pollutants (Thiam et al., 2013). As such, lipid droplets can sequester lipophilic drugs and prevent them from reaching their targets, thus decreasing drug effectiveness (Lagoutte et al., 2008; Rak et al., 2014). Therefore, it seems that inhibition by pharmacological or genetic means of enzymes necessary for lipid droplet formation could provide a way to reduce drug sequestration and improve drug effects. We tested this concept in glioblastoma cells treated with curcumin in combination with pyrrolidine-2, and inhibitor of cytosolic phospholipase A2 alpha (cPLA2α). Curcumin, a plant-derived polyphenol isolated from the turmeric spice, has been shown to be a safe, potent and effective anticancer agent both in vitro and *in vivo* (S. C. Gupta et al., 2013). It was found to affect multiple targets, leading to the inhibition of inflammation and cell proliferation (J.-K. Lin, 2007). Curcumin has a broad range of effects that are advantageous against multifactorial diseases such as cancer, and clinical trials have suggested biological activity in patients with colorectal and pancreatic cancer (Cheng et al., 2001; Dhillon et al., 2008). Despite being well-tolerated in humans, its poor bioavailability has limited prospects of broader clinical applications (Anand et al., 2007; Dhillon et al., 2008). Given its lipophilic properties, curcumin has been found to localize in lipid membranes and lipid droplets, thereby decreasing its availability at drug targets. Pyrrolidine-2, also known as pyrrophenone, is a potent and reversible inhibitor of cPLA2α, a key enzyme in the processes of arachidonic acid release, eicosanoid synthesis and lipid droplet formation (Gubern et al., 2008; Ono et al., 2002a). We hypothesize that pre-treatment of cancer cells with pyrrolidine-2 will enhance the cell killing effect of curcumin by reducing its sequestration in lipid droplets.

Glioblastoma multiforme is a highly aggressive and drug-resistant type of brain cancer which currently lacks effective treatments (Cohen & Colman, 2015; Cuddapah et al., 2014). Temozolomide, a DNA methylating agent, is the first-line drug used in concomitant and adjuvant radiochemotherapy against glioblastoma (Petrecca et al., 2013; Stupp et al., 2005; Weller et al., 2013). However, a large subset of patients is resistant to temozolomide due to the expression of the O6-methylguanine-DNA methyltransferase gene (MGMT), a DNA repair protein, and there is an urgent need for alternative mono- and combination therapies (Hegi et al., 2005c). We have investigated the susceptibility of human glioblastoma monolayer (2D) and spheroid (3D) cultures to curcumin and temozolomide used either individually or in combination with pyrrolidine-2. We also compared the effect of pyrrolidine-2 to that of buthionine sulfoximine (BSO), an irreversible inhibitor of gamma-glutamylcysteine synthetase, the rate-limiting enzyme in glutathione synthesis, found to be effective as a sensitizing agent in patient-derived neuroblastoma cell lines (Anderson & Reynolds, 2002; Griffith, 1982).

We further monitored the mode of cell death induced by these treatments using a newly developed, dimerization-based biosensor which provides a highly sensitive method to visualize and quantify caspase-dependent apoptotic activity in living cells (Ding et al., 2015). The cysteine protease caspase-3 is a main executioner caspase in the process of caspase-dependent apoptosis (Brown & Attardi, 2005; Kroemer et al., 2009). It was shown to be strongly activated in response to curcumin treatment in different cell lines (Anto et al., 2002; Gogada et al., 2011; Sikora et al., 2006). By investigating the activity of caspase-3 in cancer cells in response to chemotherapeutics and sensitizers, we can reveal drug efficacy and underlying mechanisms of cell death.

The objective of these studies was to investigate the sensitization of human glioblastoma cells in 2D and 3D cultures to caspase-3-mediated cell death induced by curcumin. We used the

pharmacological agent pyrrolidine-2 to manipulate lipid droplet number in glioblastoma cells and assessed caspase-3 activity in living cells using a recently developed biosensor. The results indicate a significant increase in caspase-3-mediated cell death induced by curcumin when lipid droplet formation is reduced.

Materials and methods

Materials

Curcumin (Sigma–Aldrich, Canada), pyrrolidine-2 (Calbiochem, United States), temozolomide (Sigma–Aldrich, Canada), buthionine sulfoximine (Sigma–Aldrich, Canada), staurosporine (Sigma–Aldrich, Canada), dimethyl sulfoxide (Sigma–Aldrich, Canada), Nile Red (Sigma–Aldrich, Canada), paraformaldehyde (Sigma–Aldrich, Canada), BODIPY 493/503 (Invitrogen, Canada), Hoechst 33342 (Sigma–Aldrich, Canada) and propidium iodide (Sigma–Aldrich, Canada) were used as received.

Cell culture

The U251N human glioblastoma cell line was originally obtained from the American Type Culture Collection. Unless otherwise specified, U251N cells were cultured in Dulbecco's Modified Eagle's Medium (DMEM; Invitrogen, Canada) containing 10% (v/v) fetal bovine serum (Invitrogen, Canada), 2 mM L-glutamine, 100 IU/mL penicillin, 100 μg/mL streptomycin (Invitrogen, Canada), and 1% non-essential amino acids. Cells were incubated at 37 °C with 5% CO2.

Spheroid preparation

Spheroid cultures were prepared using a protocol adapted from the previously established liquid overlay system: confluent U251N monolayer cell cultures were detached using 0.05% trypsin–EDTA (Invitrogen, Canada), and seeded at 5,000 cells per well in 96-well plates pre-coated with 2% agarose (Invitrogen, Canada) in serum-deprived DMEM (Dhanikula et al., 2008). Spheroids

were seeded and maintained in complete DMEM medium for four days before drug treatments. Spheroids expressing the caspase-3 biosensor were prepared following the same method, using transfected cells.

Cell treatment

Confluent monolayer cell cultures were detached using 0.05% trypsin–EDTA, seeded in 24-well or 96-well cell culture plates (Sarstedt, Canada) at 50,000 or 10,000 cells per well, respectively, and treated after 24 h. For 24 h dose–response experiments, drugs were administered in the following concentrations: curcumin (Cur; 5–100 μM); pyrrolidine-2 (Pyr-2; 1–5 μM). For 72 h dose–response experiments, curcumin was added at concentrations 5–30 μM. For pyrrolidine-2 (3 μM) and buthionine sulfoximine (BSO; 5 mM) pre-treatments, cells were treated for 24 h, after which the medium was refreshed. To establish the time course of drug effects in spheroid cultures, treatments were maintained for 24 h or 72 h. BSO stocks (200 mM) were prepared fresh in purified water. Stock solutions of temozolomide, curcumin, staurosporine and pyrrolidine-2 were prepared in dimethyl sulfoxide (DMSO), and added to cells for a final DMSO concentration <0.5%. Vehicle controls were included in each experiment.

Lipid droplet labeling, imaging and quantification

After treatment with curcumin (10–30 μM) for 24 h, the media were refreshed, and cells were incubated with Nile Red (2 μM; 10 min). Nile red is a commonly used fluorescent label for lipid droplets (Greenspan et al., 1985; Melo et al., 2011), but it can also bind to hydrophobic protein domains and be employed to probe hydrophobic pockets in purified native proteins (Sackett &

Wolff, 1987). Labeled cells were washed with phosphate buffered saline (PBS), and imaged using a fluorescence microscope (Leica, Canada). To quantify the number of lipid droplets per cell, U251N cells were fixed with paraformaldehyde (4%; 15 min) following treatment, labeled with BODIPY 493/503 (2 μM; 10 min), and then imaged using a fluorescence microscope.

Hoechst 33342 and propidium iodide labeling

In monolayer cultures, the culture medium was removed following treatment, and cells were fixed with paraformaldehyde (4%; 15 min). Cells were stained with Hoechst 33342 (10 μM; 10 min), and then washed and kept in PBS. Cell imaging was conducted using an automated microscopy platform (Operetta High Content Imaging System; Perkin Elmer, United States). Image analysis and cell counting were performed using the Columbus Image Data Storage and Analysis platform (Perkin Elmer, United States). In spheroid cultures, propidium iodide and Hoechst 33342 fluorescent dyes were added 3 h prior to measurements. At the end of treatment, individual spheroids were carefully transferred onto a microscope slide using a pipette, and flattened under a glass coverslip to facilitate imaging. Imaging was conducted using a fluorescence microscope, and fluorescence intensity was quantified using ImageJ.

Biosensor construction

The caspase-3 biosensor consists of two parts (Fig. 3). Plasmid 1 encodes the green dimerization-dependent fluorescent protein (GA) linked with a nuclear exclusion signal sequence (NES; LALKLAGLDIGS)(Alford et al., 2012; Wen et al., 1995), the caspase-3 substrate sequence (DEVD)(Xu et al., 1998), and a partner protein (B) linked to a nuclear localization signal (NLS;

DPKKKRKVDPKKKRKVDPKKKRKV)(Moreland et al., 1985). Plasmid 2 encodes the dimerization-dependent red fluorescent protein (RA) linked with a NLS. Expression and purification of constructs 1 and 2 were performed according to procedures previously described in detail (Ding et al., 2015). Details of the plasmid constructs are found in Table 1.

Plasmid preparation and transfection

Stocks of the caspase-3 biosensor plasmids (kindly provided by Dr. Robert E. Campbell, University of Alberta, Canada) were prepared in α-Select Escherichia coli (Bioline, United States) using a Miniprep Kit (Qiagen, Canada). DNA concentration was adjusted to 1 μg/μl in purified water, and plasmids were stored at -20 °C. For transfection, U251N cells were seeded in black 96-well plates (Corning, United States) at a density of 10,000 cells per well, and cultured for 24 h. Transfection was conducted in the absence of antibiotics, using Lipofectamine 2000 (Invitrogen, Canada), following the procedure recommended by the manufacturer. The transfection complexes were kept for 24 h, after which the medium was replaced by complete medium, and cells were treated.

Live cell imaging of the caspase-3 biosensor

Monolayer cells seeded in black 96-well cell culture plates were transfected with the biosensor, and treated for 24 h. Following treatment, cells were imaged using the Operetta High Content Imaging System to analyze green (eGFP) and red (Alexa 594) signals. Caspase-3 activity was quantified as the number of cells with red nuclei, and expressed as a percentage of total transfected cells (expressing green or red fluorescence). The absence of caspase-3 activity was quantified from

the number of cells with green cytoplasm, and expressed in the same manner. Eleven fields were analyzed per well, with six wells per treatment group. Negative controls were non-transfected cells in the presence or absence of drugs. Following treatment, transfected spheroids were transferred onto microscope slides, flattened under glass coverslips, and imaged using a fluorescence microscope. Full spheroids were imaged and the number of cells with green fluorescence in the cytoplasm or red fluorescence in the nucleus was counted.

Statistical analysis

Each experiment was independently performed at least two or three times. Each treatment was performed in three samples (24-well plates) or six samples (96-well plates). All data are expressed as mean ± SEM values. Statistical significance was calculated using one-way ANOVA, followed by the Student's t-test. For multiple comparisons, Bonferroni corrections were applied.

Results

Curcumin is sequestered in lipid droplets

Due to its fluorescent properties, curcumin's intracellular localization can be visualized using a fluorescence microscope (488/509 nm). After treating U251N glioblastoma cells with curcumin (10 μm) for 4 h, green fluorescence was found diffused throughout the cells, located at cell membranes, and concentrated in numerous punctate in the cytoplasm (Fig. 1A). Staining of curcumin-treated cells with Nile Red, a lipophilic stain for intracellular lipids, showed that curcumin co-localized with membrane lipids and lipid droplets. Given the importance of lipid droplets for cancer cells, we then employed pyrrolidine-2, an inhibitor of cPLA2α, to reduce lipid droplet number in glioblastoma cells. U251N cells normally contain lipid droplets and their number can be reduced using inhibitors of lipid droplet formation, or increased using fatty acids such as oleic acid (Fig. S1). Pyrrolidine-2 treatment (3 μM; 24 h) reduced lipid droplet number to 52 ± 5.7% of untreated control levels (Fig. 1C). Lipid droplet number in cells treated with both curcumin and pyrrolidine-2 was higher (82.3 ± 16.0%) than that of cells treated with pyrrolidine-2 alone.

Pyrrolidine-2 potentiates the cell killing effect of curcumin

We postulated that U251N glioblastoma cells would be more susceptible to the therapeutic effects of curcumin following the reduction of lipid droplet number by pyrrolidine-2. Cell viability measured by counting cell nuclei labeled with Hoechst 33342 showed that 25 μM of curcumin decreased cell number to 53.8 ± 2.8% after 24 h of treatment (Fig. 2A and B). In turn, pyrrolidine-2 alone did not induce any significant decrease in cell viability up to 4 μM (Fig. 2C). Pre-treatment

of U251N cells with pyrrolidine-2 potentiated the cell killing effect of curcumin. Notably, pre-treatment with pyrrolidine-2 (24 h) virtually abolished glioblastoma viability when followed by curcumin treatment (72 h) at concentrations above 20 μM (Fig. 2B). In comparison, pyrrolidine-2 modestly increased the effectiveness of temozolomide, which was included as a clinically relevant comparator (Fig. S2). The effect of pyrrolidine-2 as a sensitizer was compared to that of BSO. Although pre-treatment with BSO increased cell death at lower concentrations of curcumin, it did not substantially increase cell death at higher concentrations (Fig. S3).

Cell death induced by curcumin and pyrrolidine-2 is mediated by caspase-3

To investigate the mode of cell death induced by curcumin and pyrrolidine-2, we employed a newly developed biosensor for caspase-3 activation. This construct offers a highly sensitive method to detect caspase-3-mediated apoptosis in live cells. In the absence of caspase-3 activity, cells expressing the biosensor display green fluorescence in the cytoplasm. Following the activation of caspase-3, green fluorescence fades and red fluorescence increases in the cell nucleus. Thus, caspase-3 activity can be quantified by counting the number of cells with red fluorescence as a proportion of total transfected cells expressing either green or red fluorescence. Experiments showed that even under control conditions, a small proportion of cells (13.2 ± 1.4%) display caspase-3 activity. In turn, the positive control staurosporine, a potent activator of caspase-3, significantly increased the proportion of cells with a red nucleus (Fig. 3D).

To compare the mode of cell death induced by curcumin and pyrrolidine-2-sensitized curcumin treatments, U251N cells transfected with the caspase-3 biosensor were treated with mono- and combination therapies for 24 h. The results showed that although temozolomide,

curcumin and pyrrolidine-2-sensitized treatments all significantly reduced cell viability in U251N cells, only curcumin (alone or in combination) significantly induced caspase-3-mediated cell death (Fig. 4B and C).

Curcumin and pyrrolidine-2 are effective in glioblastoma spheroids

To further investigate the effectiveness of curcumin and pyrrolidine-2, we used glioblastoma spheroids cultures, which more closely represent brain tumors found *in vivo*. Following the preparation of U251N spheroids using cells transfected with the caspase-3 biosensor, spheroids were treated at drug concentrations found to be effective in monolayer experiments. Due to their 3D structure, spheroids were "squashed" between two glass surfaces in order to disperse the cells and facilitate their imaging (Fig. 5A). Both curcumin and curcumin combined with pyrrolidine-2 induced a time-dependent increase in caspase-3 activity. In contrast, cytotoxic concentrations of temozolomide did not induce caspase-3 activity, even after 72 h (Fig. 5B and C).

To relate caspase-3 activity to overall cell viability, we used Hoechst 33342 and propidium iodide labeling to examine the importance of necrotic cell death (Fig. 6). The results showed that a time-dependent increase in necrotic cell death was seen in response to temozolomide, curcumin and curcumin combined with pyrrolodine-2. Yet, the most dramatic increase was seen with the combination treatment, where the rate of necrotic cell death almost doubled from 24 h to 72 h of treatment (Fig. 6B and C).

Discussion

In the nervous system, the presence of lipid droplets in neurons is minimal, and is most noticeable in glia cells under physiological conditions. In many models of neurodegeneration, the excessive accumulation of lipid droplets in glial cells is a hallmark of disease and is linked to mitochondrial dysfunction (Welte, 2015). In glioblastoma multiforme, the accumulation of lipid droplets serves to fuel tumor growth and resist therapeutic treatments. Aside from providing energy to resist stress induced by chemotherapeutic drugs, it appears that lipid droplets can also directly decrease the amount of drugs available at targets by sequestering them inside the core of the lipid droplets. We hypothesized that the pharmacological inhibition of lipid droplet formation and the reduction of lipid droplet number in glioblastoma cells are viable strategies to increase the effectiveness of lipophilic chemotherapeutic drugs such as curcumin. The mechanisms involved are summarized in Fig. 7. Curcumin is a hydrophobic compound owing to its aromatic phenolic groups and methylene bridge (Aggarwal & Sung, 2009; Priyadarsini, 2013). The high lipophilicity of curcumin is indicated by its octanol–water partition coefficient of 2.5 × 104 M−1 (Heger et al., 2014; Kunwar et al., 2006). Curcumin's partition coefficient for 1,2-dioleoyl-sn-glycero-3-phosphocholine (DOPC) lipid bilayers and HEPES buffer was 2.4 × 104 M−1 (Hung et al., 2008). This high partition coefficient clearly indicates curcumin's preference for lipophilic cellular compartments. As such, it can rapidly cross cell membranes and localize in lipid droplets (Fig. 1A). In contrast, analysis using Time-of-Flight Secondary Ion Mass Spectrometry (TOF-SIMS) showed that temozolomide did not localize in lipid droplets (data not shown). The inhibition of lipid droplet formation can thus serve two purposes: (1) to lower the capacity of glioblastoma cells to withstand curcumin-induced stress by reducing their energy stores, and (2) to reduce the amount of compartments where curcumin can be sequestered, thereby increasing drug availability at

targets. Different kinds of delivery systems have been used to deliver curcumin to the brain and to glioblastoma *in vivo* (Xi Chen et al., 2013; Shinde et al., 2015; S. Wang et al., 2012). Polymeric carriers have the potential to improve the stability and solubility of curcumin(Naksuriya et al., 2015; Rabanel et al., 2015; X. Yang et al., 2015). Our research group has previously reported the incorporation of curcumin into A2B star polymer micelles and effectiveness of this preparation in glioblastoma (M Soliman, 2014; Moquin et al., 2015). A retention of curcumin's biological activity in nanocarriers, an enhanced permeability and retention (EPR) effect and diffusion of curcumin into the neighboring glioblastoma cells could provide an improved therapeutic intervention *in vivo* (Schütze et al., 2015).

Pyrrolidine-2 is an inhibitor of cPLA2α, a key rate limiting enzyme in the synthesis of eicosanoids and a necessary player in the formation of lipid droplets (Seno et al., 2000; Stephenson et al., 1994). In normal brain tissues, particularly in astrocytes and microglia, excessive PLA2 activation in response to stressors (e.g. glutamate excitotoxicity) can exacerbate inflammatory processes and oxidative stress. In turn, these can promote neurological disorders such as Alzheimer's disease, Parkinson's disease, and traumatic brain injuries (G. Y. Sun et al., 2010). In glioblastoma cells, cPLA2α activity is likely to be upregulated in response to chemotherapeutic intervention, allowing cancer cells to stock up in energy and adapt their metabolic pathways. Although pyrrolidine-2 treatment alone does not induce significant loss in cell viability in U251N glioblastoma cells up to 4 μM, its effect becomes apparent when followed by curcumin treatments. Our results show that pyrrolidine-2 pre-treatment dramatically increased the effectiveness of curcumin in U251N cells after 72 h, virtually abolishing cell viability at curcumin concentrations above 20 μM. Interestingly, the lipid droplet number of cells treated with curcumin following pyrrolidine-2 sensitization was higher than that of cells treated with curcumin alone – likely due

to the drug-induced cellular stress, previously reported to induce lipid droplet formation (Cabodevilla et al., 2013; Khatchadourian et al., 2012; Welte, 2015). Sensitization using BSO was comparatively less effective, likely due to the diversity of antioxidants and enzymes that can reduce ROS levels. Nevertheless, the depletion of glutathione by BSO increased curcumin-mediated cell death, possibly through the increased peroxidation of lipid droplets, and necrosis (Fig. 7)(L. Liu et al., 2015).

To investigate the mode of cell death induced by curcumin and pyrrolidine-2, we employed a highly sensitive biosensor to detect and measure caspase-3 activity in live cells (Ding et al., 2015). The mechanism of the biosensor relies on a bi-modular design, in which two fluorescent proteins with dimerization-dependent brightness are activated in a mutually-exclusive manner. When challenged with pro-apoptotic stimuli, cells transfected with the biosensor manifest a change in fluorescence color, from green to red, and in signal localization, from the cytosol to the nucleus. In the absence of caspase-3 activity, the green cytoplasmic protein is linked with a non-fluorescent partner protein which increases green fluorescence manyfolds. Following the activation of caspase-3 during apoptosis, the caspase-3 substrate (DEVD) contained in the linker region is cleaved, and green fluorescence is dramatically decreased. The partner protein then translocates into the nucleus and associates with high affinity to the red fluorescent protein, enhancing red fluorescence manyfold. Thus, the specificity of detection is based on (1) the caspase-3 substrate, (2) the change in the color of the signal, and (3) the change in the subcellular localization of the signal. It is to note that a small proportion of cells display caspase-3 activity under control conditions. Our results support previous findings stating that curcumin is a strong inducer of caspase-3-mediated apoptosis in cancer cells (Anto et al., 2002; Sikora et al., 2006). In contrast, temozolomide-induced cell death did not implicate caspase-3 activation, suggesting the

involvement of other modes of cell death, such as autophagy (Kanzawa et al., 2004). Autophagy is usually reduced in cells with a large number of lipid droplets, which could partly explain the limited effectiveness of temozolomide against glioblastoma tumors (Sesen et al., 2015; Z.-S. Zhang et al., 2015).

In normal brain tissues, it appears that cPLA2α and lipid droplets play protective roles, notably helping glia cells to support neurons and resist stressors. For example, cPLA2α (+/+) mice were found to be more resistant to hypoxic conditions resulting from brain ischemia than their null counterparts (Tabuchi et al., 2003). Excessive cPLA2α activity has also been involved in apoptosis, as it was found to drive arachidonic acid-mediated cytotoxicity and subsequent caspase-3 activation (Nakanishi & Rosenberg, 2006). On the other hand, the protective role of lipid droplets in glioblastoma cells is highly detrimental to cancer patients. The inhibition of cPLA2α is one of several approaches recently investigated to hinder lipid metabolism in cancer cells. Small molecules and gene silencing (e.g. acetyl-CoA carboxylase alpha) were shown to be effective in inhibiting cancer cell proliferation and viability *in vitro* (Cai et al., 2015; Hilvo et al., 2011; F. P. Kuhajda et al., 2000). However, most experiments performed in monolayer cancer cell cultures do not accurately reflect the conditions found in *in vivo*, where the intercellular contact, tumor dynamics and overall heterogeneous microenvironment found in tumors often heighten resistance to radiotherapy and chemotherapy (Håkanson et al., 2011; He et al., 2014; Zips et al., 2005). Glioblastoma spheroids harbor hypoxic cores where metabolic pathways, including those involving lipids, are changed (Ackerman & Simon, 2014; Baenke et al., 2013; Chinnaiyan et al., 2012; Kucharzewska et al., 2015). De novo lipogenesis, for instance, was shown to be bypassed in cancer cells in hypoxic conditions. Instead, cancer cells relied on extracellular lipid scavenging to supply for their needs (Kamphorst et al., 2013). Thus, we conducted experiments in 3D spheroid,

and confirmed that pyrrolidine-2 pre-treatment enhanced the cell killing effect of curcumin in a time- and caspase-3-dependent manner. In contrast, temozolomide alone was significantly less effective at inducing caspase-3 activation and glioblastoma cell death.

Because of the importance of cPLA2α in lipid metabolism and the production of pro-inflammatory mediators, its inhibition has also been studied in the context of inflammatory conditions such as arthritis (Balboa et al., 2003; Tai et al., 2010). The microenvironment of glioblastoma tumors is characterized by the infiltration of hyperactivated immune cells, which aggravate disease progression. Thus, it can be hypothesized that inhibition of lipid metabolism can also reduce inflammation at tumor sites (Desmarais et al., 2015; Sowers et al., 2014; Tafani et al., 2011). However, the potential side effects of pyrrolidine-2 deter its use *in vivo*. One of the best tolerated statins is simvastatin (Naci et al., 2013). Statins were tested in some CNS diseases and were suggested as supplemental anticancer agents (David Gaist et al., 2014; Menge et al., 2005). Thus, the administration of simvastatin in combination with curcumin might be a suitable therapeutic strategy for certain groups of glioblastoma patients.

Taken together, our results indicate that lipid droplets in glioblastoma cells play a protective role by sequestering drugs and promoting cell survival. Decreased lipid droplet formation using pyrrolidine-2 as a sensitizing agent significantly increases the cell killing effect of chemotherapeutic agents such as curcumin.

Acknowledgments

The present study was supported by CIHR (MOP-119425) and NSERC (RGPIN-2015-04994) grants. The authors have no conflicts of interest to declare.

Figure 3.1. Curcumin co-localizes with lipid droplets and pyrrolidine-2 reduces lipid droplet content in glioblastoma cells

(a) U251N glioblastoma cells treated with curcumin (10 μM; 4 h) show green fluorescence in the cytoplasm. Co-labeling with Nile Red (2 μM; 10 min) indicated that curcumin localizes in lipid droplets. Fluorescence micrograph overlays were prepared in ImageJ. Insets show details of curcumin co-localized with Nile Red-labeled lipid droplets. (b) Schematic representation of the status of lipid droplets (yellow), and curcumin localization (green) in U251N glioblastoma cells with or without pyrrolidine-2 treatment. Curcumin is sequestered in lipid droplets, and pyrrolidine-2 pre-treatment increases the availability of curcumin at its targets. (c) U251N glioblastoma cells treated with pyrrolidine-2 (3 μM; 24 h) show a significant reduction in lipid droplet content. Cells were labeled with Bodipy 493/503 (2 μM; 10 min) and imaged using a fluorescence microscope. The number of lipid droplets per cell was counted manually (250 cells were analyzed per treatment group). (∗∗∗ $p < 0.001$).

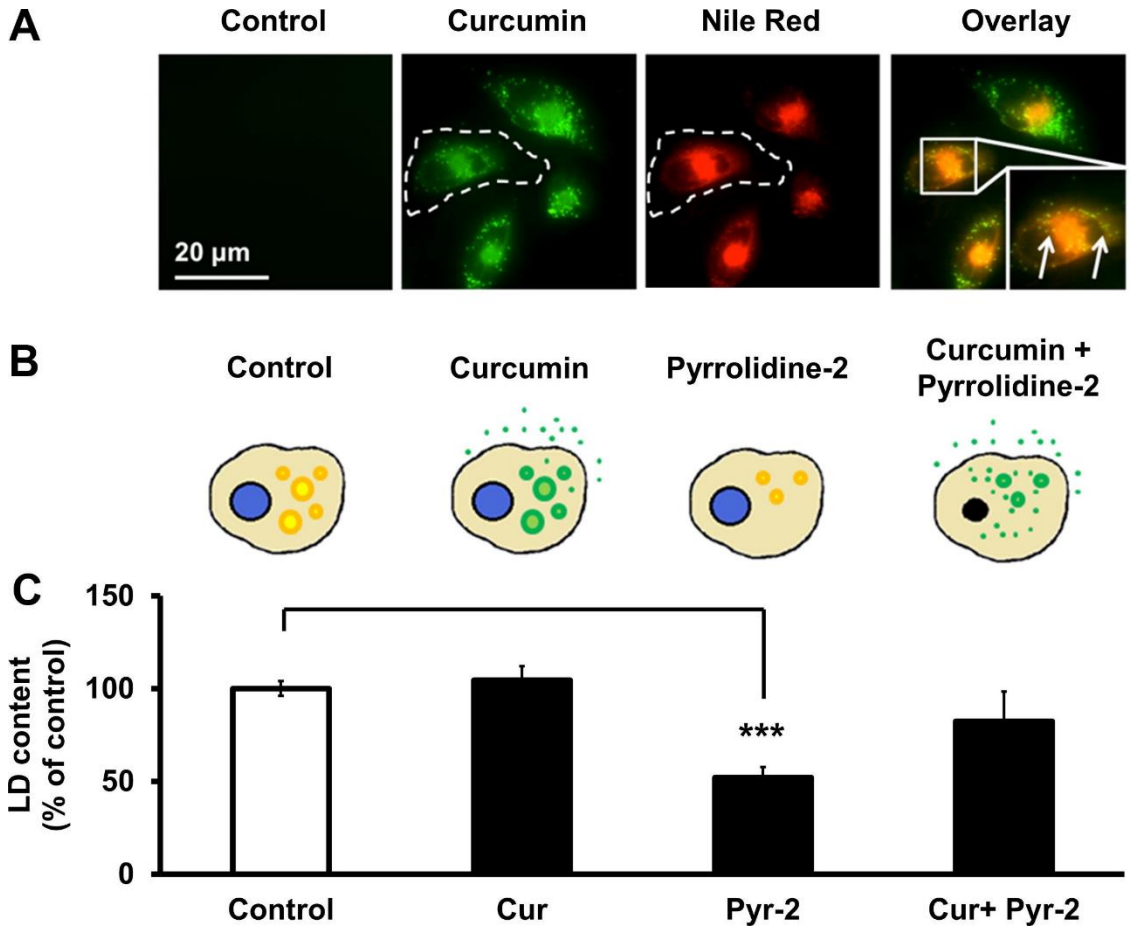
A
Control
Curcumin
Nile Red
Overlay
20 µm
B
Control
Curcumin
Pyrrolidine-2
Curcumin +
Pyrrolidine-2
C
LD content
(% of control)
150
100
50
0
***
Control
Cur
Pyr-2
Cur+ Pyr-2

Figure 3.1.

Figure 3.2. Sensitization with pyrrolidine-2 increased the cell killing effect of curcumin in U251N glioblastoma cells

(a) U251N glioblastoma cells treated with curcumin (5–100 μM) for 24 h were labeled with Hoechst 33342 and imaged using a high-throughput fluorescence microscope. Fluorescence micrographs show representative fields. (b) The cell viability of U251N glioblastoma cells treated with curcumin (5–100 μM) for 24 h was measured by counting the number of cell nuclei labeled with Hoechst 33342. Cells were imaged using a high-throughput microscope. Cell viability was significantly decreased at curcumin treatments above 25 μM. Shown are average percentage values ± SEM compared to untreated controls from three independent experiments. (∗∗∗ $p < 0.001$). (c) The cell viability of U251N glioblastoma cells treated with pyrrolidine-2 (1–5 μM) for 24 h was measured by counting the number of cell nuclei labeled with Hoechst 33342. Cells were imaged using a high-throughput microscope. Cell viability was significantly decreased at pyrrolidine-2 treatments above 4 μM. Shown are average percentage values ± SEM compared to untreated controls from three independent experiments. (∗∗∗ $p < 0.001$). (d) The cell viability of U251N glioblastoma cells treated with curcumin (5–30 μM; 72 h), with or without pyrrolidine-2 sensitization (3 μM; 24 h), was measured by counting the number of cell nuclei labeled with Hoechst 33342. Cells were imaged using a high-throughput microscope. Pyrrolidine-2 sensitization significantly increased cell death compared to treatment with curcumin alone. Shown are average percentage values ± SEM compared to untreated controls from three independent experiments. (∗∗∗ $p < 0.001$).

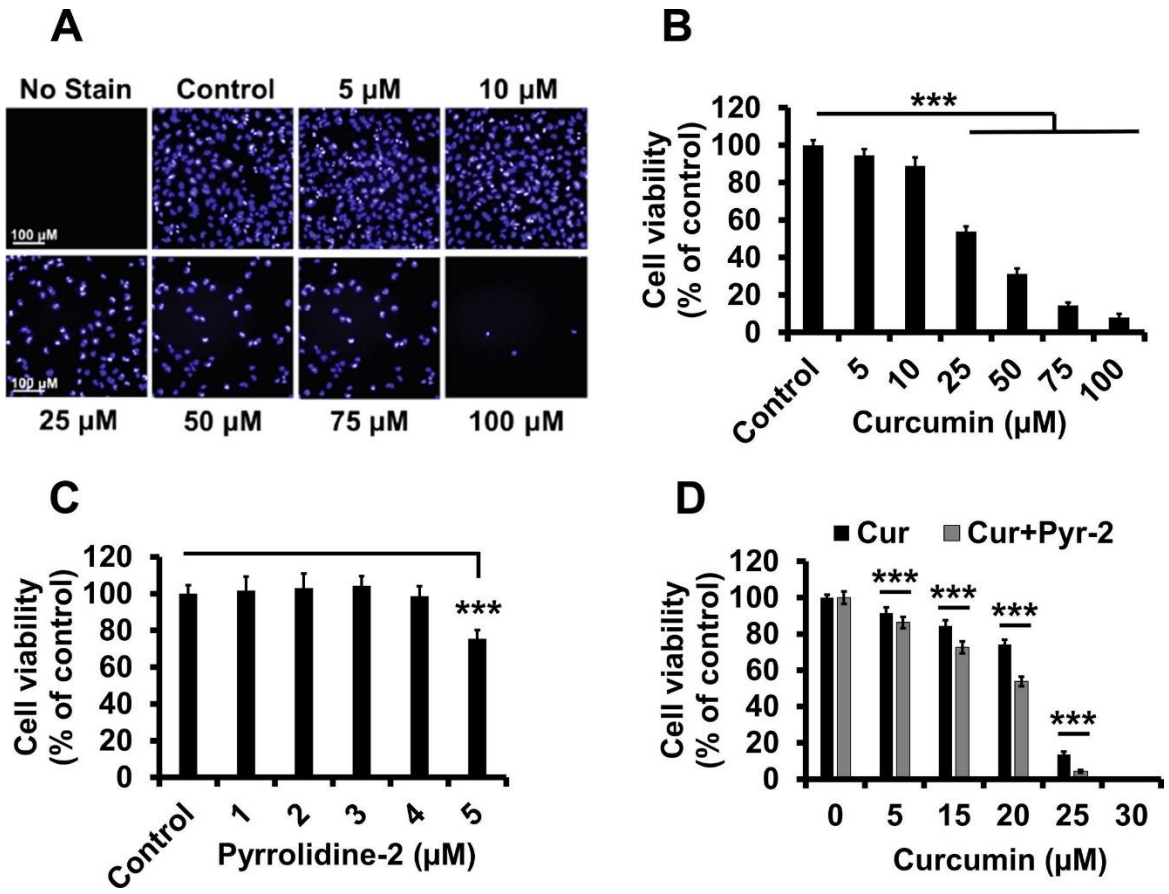
A
No Stain
Control
5 μM
10 μM
100 μM
100 μM
25 μM
50 μM
75 μM
100 μM
B
Cell viability (% of control)
120
100
80
60
40
20
0
***
Control
5
10
25
50
75
100
Curcumin (μM)
C
Cell viability (% of control)
120
100
80
60
40
20
0
***
Control
1
2
3
4
5
Pyrrolidine-2 (μM)
D
Cur
Cur+Pyr-2
Cell viability (% of control)
120
100
80
60
40
20
0
***
***
***
***
0
5
15
20
25
30
Curcumin (μM)

Figure 3.2.

Figure 3.3. Principle of caspase-3 detection using the dimerization-based biosensor and measurement of caspase-3 activity

(a) The caspase-3 biosensor is composed of two dimerization-dependent fluorescent proteins: (1) a red fluorescent protein (RA) with a nuclear localization signal (NLS), and (2) a green fluorescent protein (GA) with a nuclear exclusion signal (NES), heterodimerized with a non-fluorescent partner protein (b) through the caspase-3 substrate peptide (DEVD). Fluorescence micrographs show U251N cells with green cytoplasms when GA is heterodimerized with B (scale bar = 50 μm). (b) Upon caspase-3 activation, the caspase-3 substrate DEVD is cleaved, and green fluorescence signal from GA diminishes. (c) The partner protein B translocates into the nucleus by a NLS and heterodimerizes with RA, increasing red fluorescence in the nucleus manyfold. Fluorescence micrographs show U251N cells with red nuclei when RA is heterodimerized (scale bar = 50 μm). (d) Measurement of caspase-3 activity in U251N glioblastoma cells. Cells transfected with the biosensor were imaged using a fluorescence microscope following treatment with staurosporine (STS; 0.5 μM) for 24 h. Cells with active caspase-3 show an increase in red fluorescence (RFP) in the nucleus and a decrease in green fluorescence (GFP) in the cytoplasm. Mean percentage of total transfected cells expressing GFP or RFP ± SEM is shown for three independent experiments (∗∗∗ $p < 0.001$).

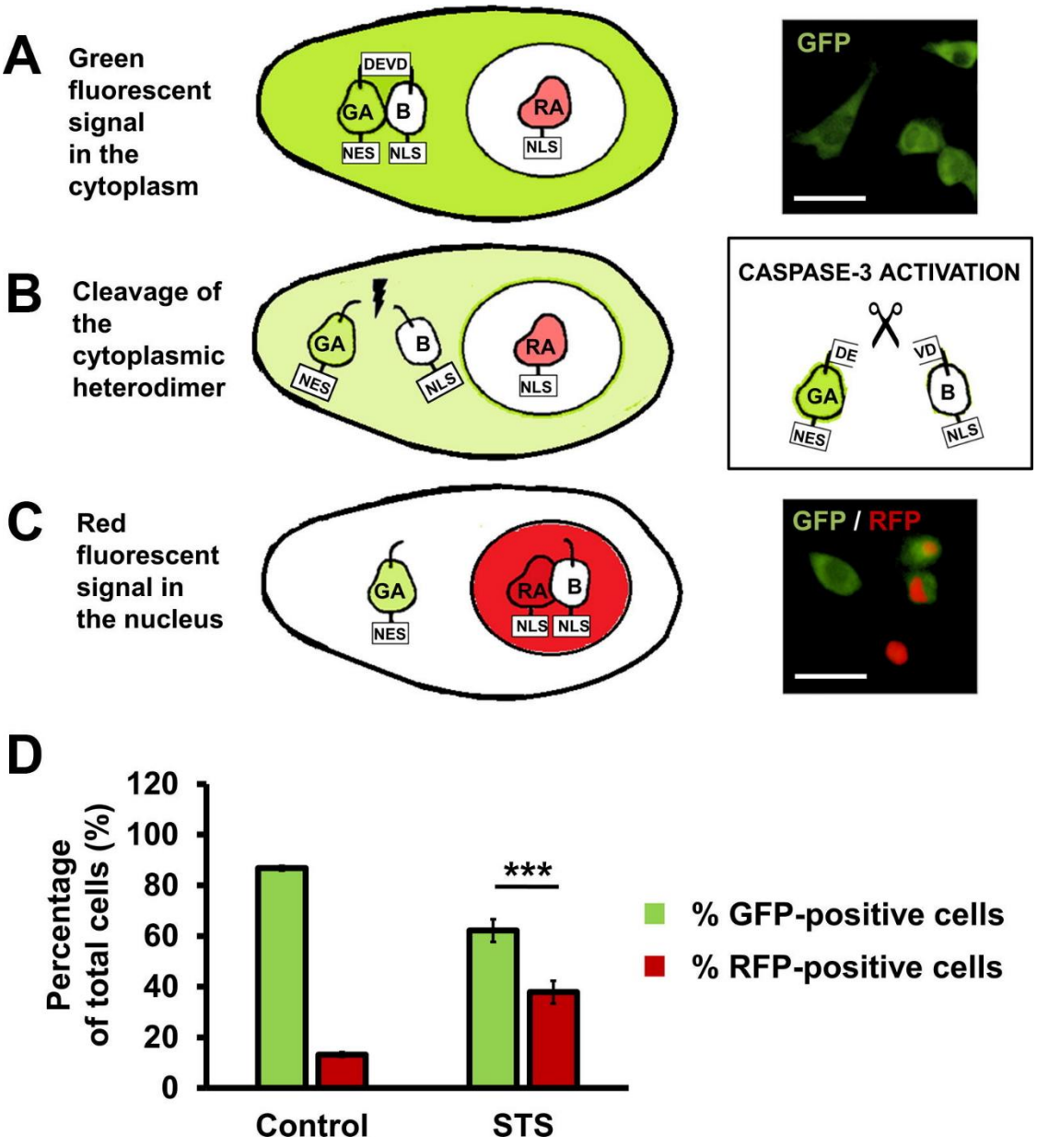
A
Green fluorescent signal in the cytoplasm
DEVD
GA
B
NES
NLS
RA
NLS
GFP
B
Cleavage of the cytoplasmic heterodimer
GA
NES
B
NLS
RA
NLS
CASPASE-3 ACTIVATION
DE
VD
GA
NES
B
NLS
C
Red fluorescent signal in the nucleus
GA
NES
RA
B
NLS
NLS
GFP / RFP
D
Percentage of total cells (%)
120
100
80
60
40
20
0
***
Control
STS
% GFP-positive cells
% RFP-positive cells

Figure 3.3.

Figure 3.4. Curcumin-mediated and pyrrolidine-2-sensitized cell deaths are mediated through caspase-3 activation

(a) Fluorescence micrographs of U251N cells transfected with the caspase-3 biosensor and treated with curcumin (25 μM; 24 h), with or without pyrrolidine-2 (Pyr-2; 3 μM; 24 h) pre-treatment. Temozolomide (TMZ; 400 μM; 24 h) was included as a clinically-relevant drug. Cells with green fluorescence in the cytoplasm express the caspase-3 biosensor, while those with a red nucleus present caspase-3 activity. (b) U251N cells transfected with the caspase-3 biosensor were treated with curcumin (Cur; 25 μM; 24 h), with or without pyrrolidine-2 (Pyr-2; 3 μM; 24 h) pre-treatment. Temozolomide (TMZ; 400 μM; 24 h) was included as a clinically-relevant drug. Caspase-3 activity was assessed using a fluorescence microscope. Mean percentage of total transfected cells expressing caspase-3 activity ± SEM is shown for three independent experiments. (∗∗∗ $p < 0.001$). (c) Cell viability of U251N cells treated with curcumin (Cur; 25 μM; 24 h), with or without pyrrolidine-2 (Pyr-2; 3 μM; 24 h) pre-treatment. Temozolomide (TMZ; 400 μM; 24 h) was included as a clinically-relevant drug. Cell viability was measured by counting the number of cell nuclei labeled with Hoechst 33342. Cells were imaged using a high-throughput microscope. Shown are average percentage values ± SEM compared to untreated controls from three independent experiments. (∗∗∗ $p < 0.001$).

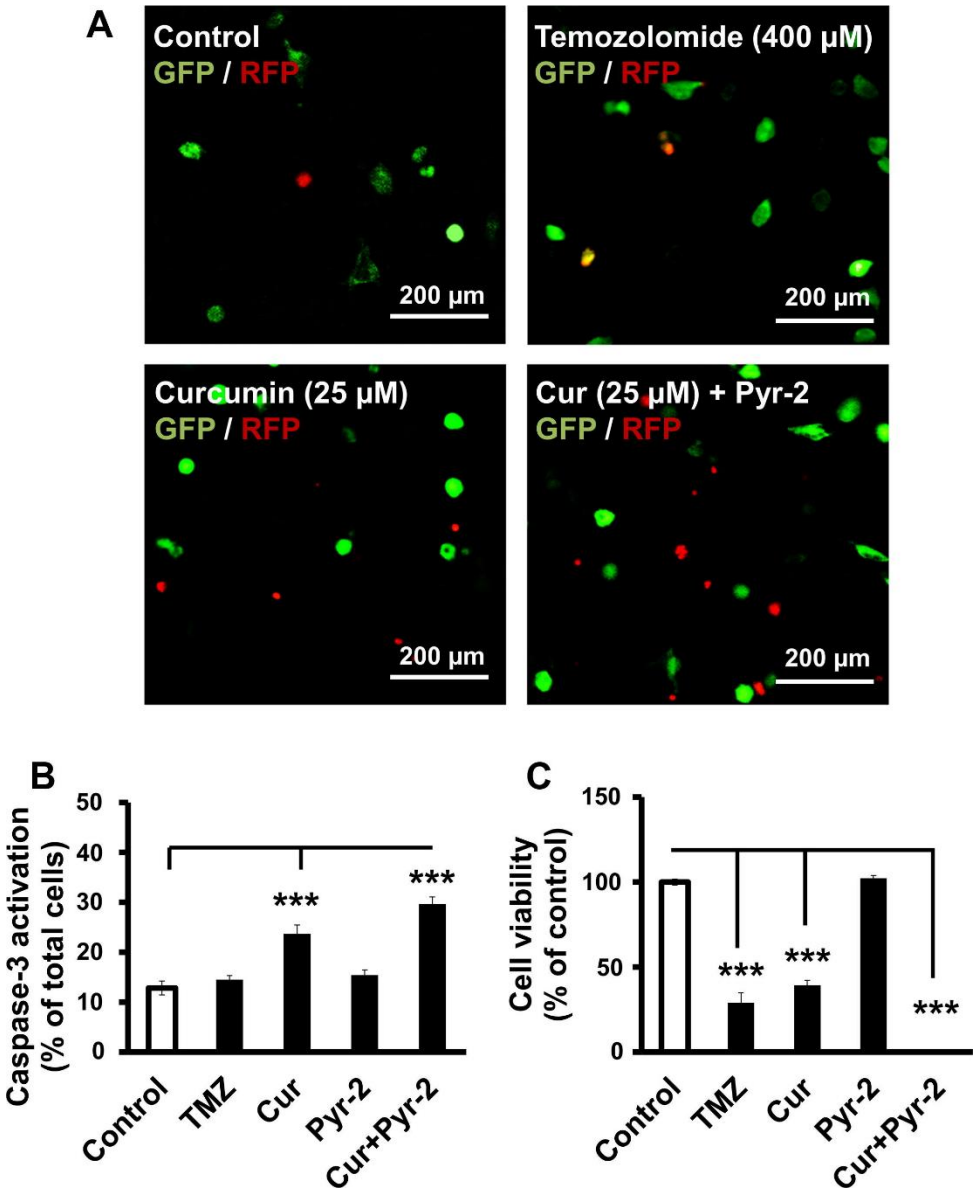
A
Control
GFP / RFP
200 μm
Temozolomide (400 μM)
GFP / RFP
200 μm
Curcumin (25 μM)
GFP / RFP
200 μm
Cur (25 μM) + Pyr-2
GFP / RFP
200 μm
B
Caspase-3 activation
(% of total cells)
50
40
30
20
10
0
***
***
Control
TMZ
Cur
Pyr-2
Cur+Pyr-2
C
Cell viability
(% of control)
150
100
50
0
***
***
***
Control
TMZ
Cur
Pyr-2
Cur+Pyr-2

Figure 3.4.

Figure 3.5. Curcumin and pyrrolidine-2-sensitization induce caspase-3-mediated cell death in glioblastoma spheroids

(a) U251N spheroids expressing the caspase-3 biosensor were prepared from U251N monolayer cells transfected with the caspase-3 biosensor. Transfected cells were collected and seeded in agarose-coated wells. The fluorescence micrograph shows cells expressing green and red fluorescence within the spheroid. U251N spheroids expressing the caspase-3 biosensor were squashed between a glass coverslip and a microscope slide to facilitate the quantification of cells expressing either green or red fluorescence. (b) U251N spheroids expressing the caspase-3 biosensor were treated with temozolomide (TMZ; 400 μM; 24 h) and curcumin (Cur; 25 μM; 24 h), with or without pre-treatment with pyrrolidine-2 (Pyr-2; 3 μM; 24 h). Following treatment, spheroids were squashed and imaged using a fluorescence microscope. The number of cells expressing either green or red fluorescence was counted. Caspase-3 activity was quantified as the number of cells expressing red fluorescence (the presence of caspase-3 activity) over the total number of transfected cells (cells with either green or red fluorescence). Mean percentage values ± SEM are shown from three independent experiments ran in triplicate. ∗∗∗($p < 0.001$). (c) U251N spheroids expressing the caspase-3 biosensor were treated with temozolomide (TMZ; 400 μM; 72 h) and curcumin (Cur, 25 μM; 72 h), with or without pre-treatment with pyrrolidine-2 (Pyr-2; 3 μM; 24 h). Following treatment, spheroids were imaged and caspase-3 activity was quantified as in (b). Mean percentage values ± SEM are shown from three independent experiments ran in triplicate. ∗∗∗($p < 0.001$).

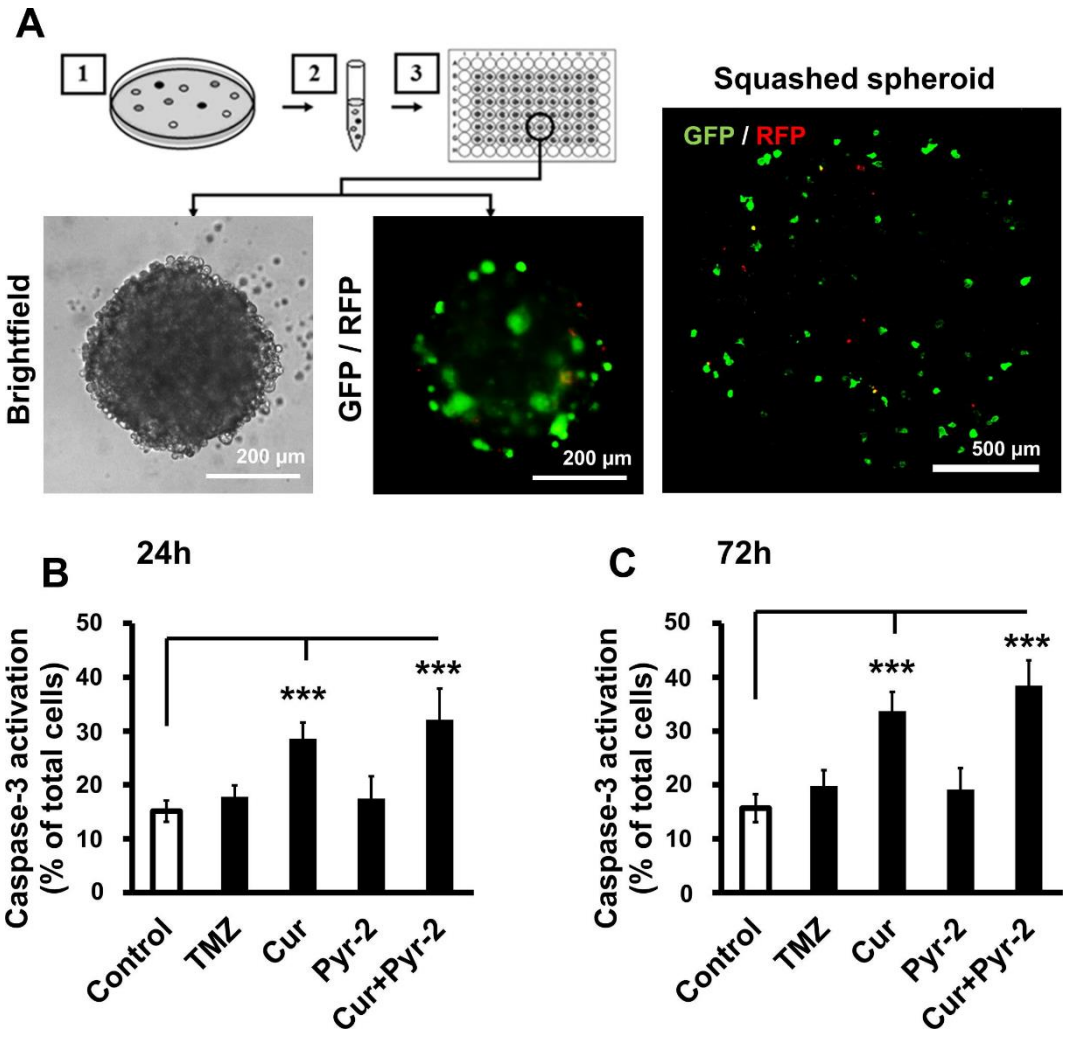
A
1
2
3
Squashed spheroid
GFP / RFP
Brightfield
200 µm
GFP / RFP
200 µm
500 µm
B
24h
Caspase-3 activation (% of total cells)
50
40
30
20
10
0
***
***
Control
TMZ
Cur
Pyr-2
Cur+Pyr-2
C
72h
Caspase-3 activation (% of total cells)
50
40
30
20
10
0
***
***
Control
TMZ
Cur
Pyr-2
Cur+Pyr-2

Figure 3.5.

Figure 3.6. Pyrrolidine-2-sensitization increases the killing effect of curcumin in glioblastoma spheroids

(a) Fluorescence micrographs of U251N spheroids treated with temozolomide (TMZ; 400 μM; 72 h) and curcumin (Cur; 25 μM; 72 h), with or without pre-treatment with pyrrolidine-2 (Pyr-2; 3 μM; 24 h). Cells were labeled with Hoechst 33342 and propidium iodide (PI) to quantify necrotic cell death. (b) U251N spheroids were treated with temozolomide (TMZ; 400 μM; 24 h) and curcumin (Cur; 25 μM; 24 h), with or without pre-treatment with pyrrolidine-2 (Pyr-2; 3 μM; 24 h). Following treatment, spheroids were imaged using a fluorescence microscope and cell death was quantified by calculating the ratio of propidium iodide to Hoechst 33342 fluorescence. Image analysis was carried out in ImageJ. Shown are mean fold increase values compared to the untreated control (set to 1), from three independent experiments. ***($p < 0.001$). (c) U251N spheroids were treated with temozolomide (TMZ; 400 μM; 72 h) and curcumin (Cur; 25 μM; 72 h), with or without pre-treatment with pyrrolidine-2 (Pyr-2; 3 μM; 24 h). Following treatment, spheroids were imaged using a fluorescence microscope and cell death was quantified by calculating the ratio of propidium iodide to Hoechst 33342 fluorescence. Image analysis was carried out in ImageJ. Shown are mean fold increase values compared to the untreated control (set to 1), from three independent experiments. **($p < 0.01$), ***($p < 0.001$).

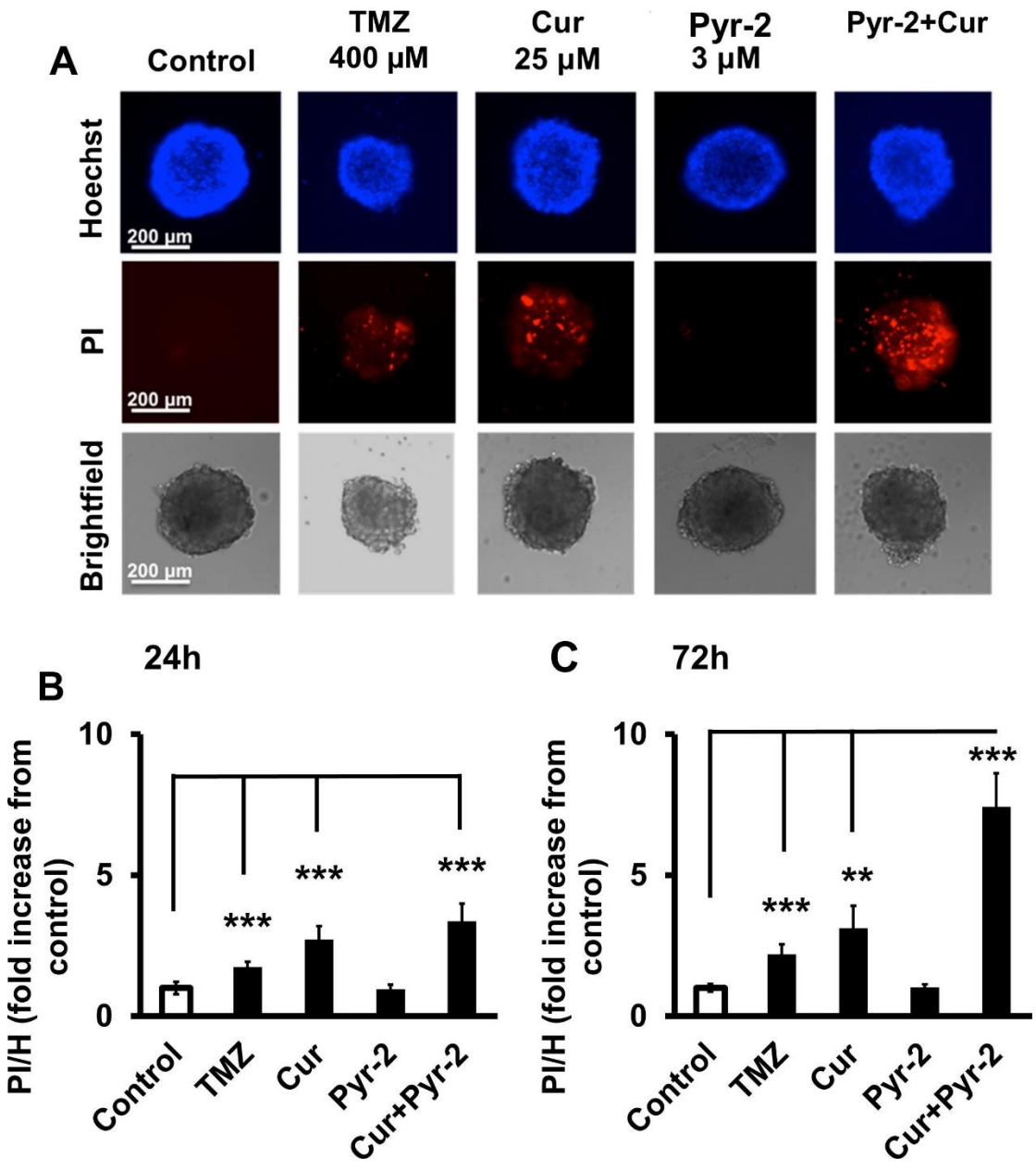
A
Control
TMZ
400 µM
Cur
25 µM
Pyr-2
3 µM
Pyr-2+Cur
Hoechst
PI
Brightfield
200 µm
B
24h
PI/H (fold increase from control)
10
5
0
***
***
***
Control
TMZ
Cur
Pyr-2
Cur+Pyr-2
C
72h
PI/H (fold increase from control)
10
5
0
***
**
***
Control
TMZ
Cur
Pyr-2
Cur+Pyr-2

Figure 3.6.

Figure 3.7. Proposed mechanisms of drug action for curcumin and pyrrolidine-2-sensitization

Curcumin is a pluripotent agent. It induces apoptosis mainly through the activation of caspase-3-mediated apoptosis. Lipid droplets (LD) can sequester curcumin, reducing the availability and effectiveness of the drug. Sensitization of glioblastoma cells with pyrrolidine-2, an inhibitor of cPLA2α and of lipid droplet formation, can increase curcumin's availability at targets and cell death. In combination with BSO, curcumin also induces necrosis by reducing the levels of the scavenger glutathione (GSH), thereby increasing reactive oxygen species (ROS), leakage of peroxidized lipids from lipid droplets, and cell death.

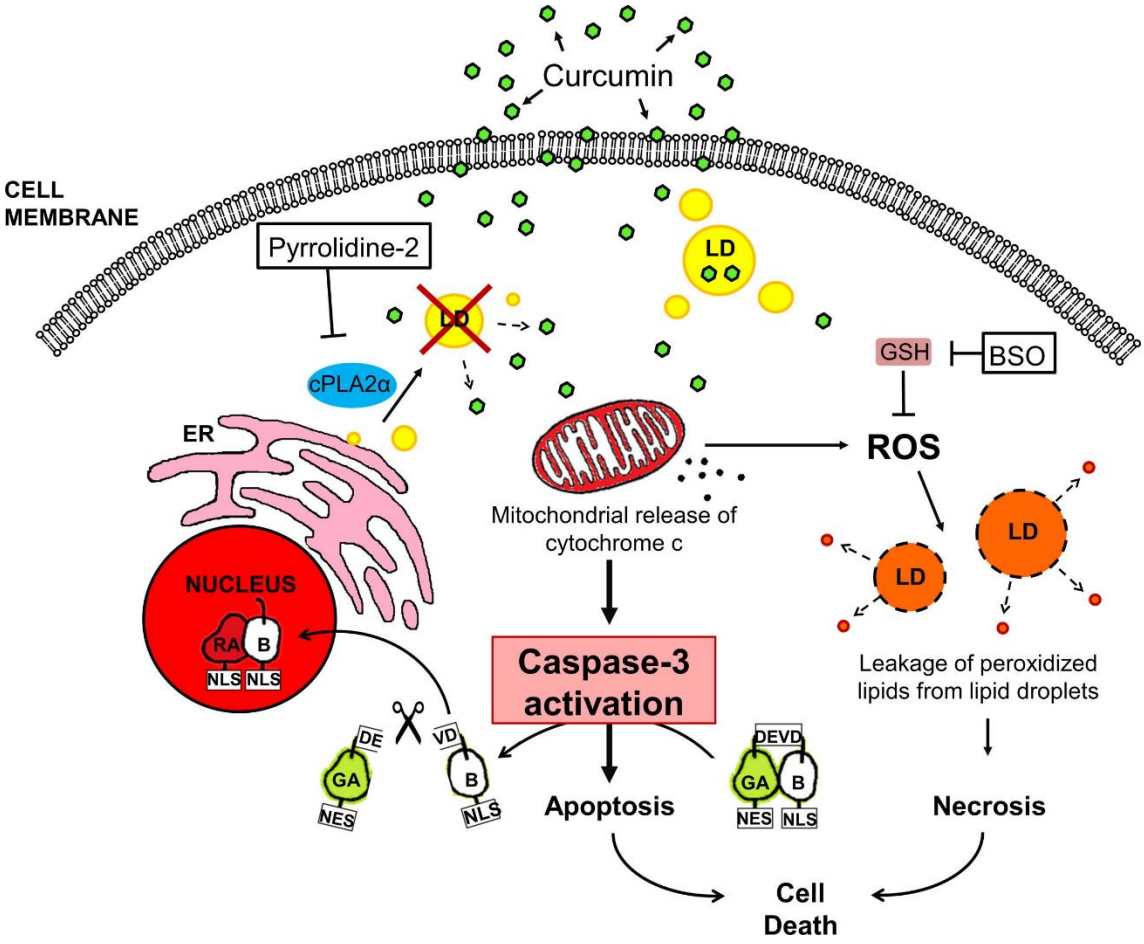
Curcumin
CELL MEMBRANE
Pyrrolidine-2
LD
LD
cPLA2α
ER
GSH
BSO
ROS
Mitochondrial release of cytochrome c
NUCLEUS
RA
B
NLS
NLS
LD
LD
Caspase-3 activation
Leakage of peroxidized lipids from lipid droplets
DE
VD
GA
B
NES
NLS
DEVD
GA
B
NES
NLS
Apoptosis
Necrosis
Cell Death

Figure 3.7.

Supplementary Figure 3.1. Pyrrolidine-2 decreases lipid droplet accumulation in U251N glioblastoma cells

Fluorescence micrographs of U251N cells labelled for nuclei (Hoechst 33342) and lipid droplets (Bodipy 493/503). Cells treated with pyrrolidine-2 (Pyr-2) for 24h show a dose-dependent decrease in lipid droplets numbers compared to untreated cells. Cells treated with oleic acid (OA) show increased lipid droplets numbers.

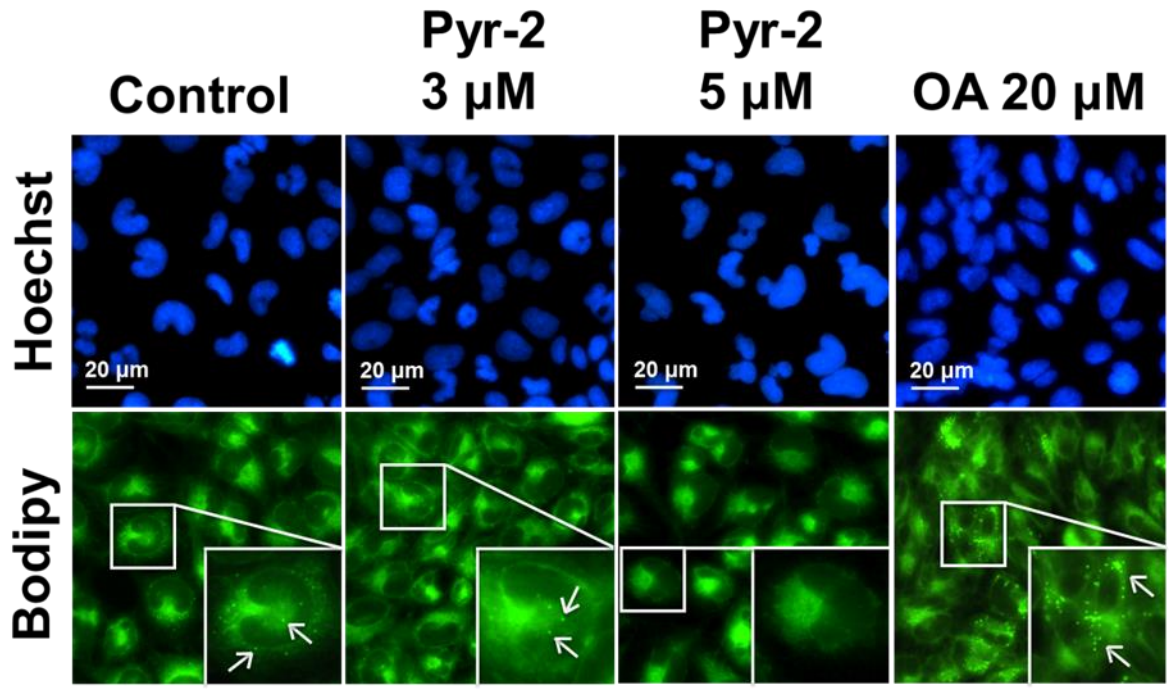
Control
Pyr-2
3 µM
Pyr-2
5 µM
OA 20 µM
Hoechst
Bodipy
20 µm
20 µm
20 µm
20 µm

Figure S3.1.

Supplementary Figure 3.2. Effect of pyrrolidine-2 on the cell killing effect of temozolomide in U251N glioblastoma cells

The cell viability of U251N glioblastoma cells treated with temozolomide (100-500 μM; 72h), with and without pyrrolidine-2 sensitization (3 μM; 24h), was measured by counting the number of cell nuclei labelled with Hoechst 33342. Cells were imaged using a high-throughput microscope. Shown are average percentage values ± SEM compared to untreated controls from two independent experiments. (**p<0.01; ***p<0.001)

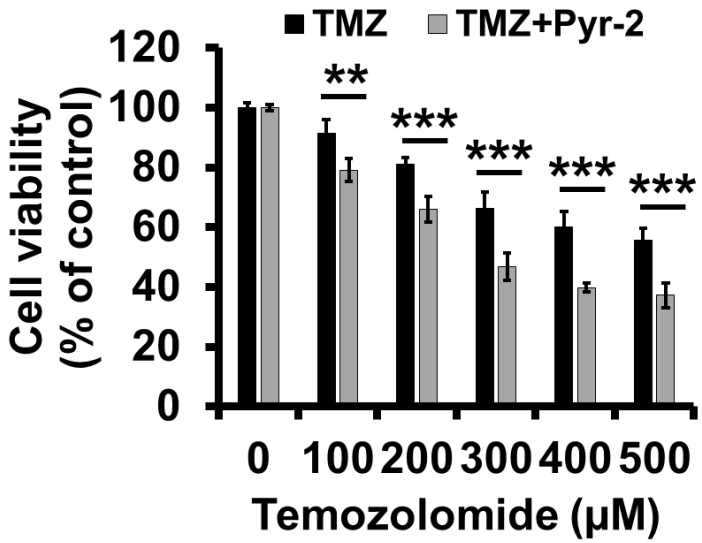
TMZ
TMZ+Pyr-2
Cell viability
(% of control)
120
100
80
60
40
20
0
**
***
***
***
***
0
100
200
300
400
500
Temozolomide (μM)

Figure S3.2.

Supplementary Figure 3.3. BSO modulates the cell killing effect of curcumin in U251N glioblastoma cells

Cell viability of U251N cells in response to curcumin (5-100 μM; 24h), in the presence or absence of buthionine sulfoximine (BSO; 5 mM; 24h) pre-treatment, was measured by counting the number of cell nuclei labelled with Hoechst 33342. Cells were imaged using a high-throughput microscope. Shown are mean percentage values ± SEM compared to untreated controls, from three independent experiments.

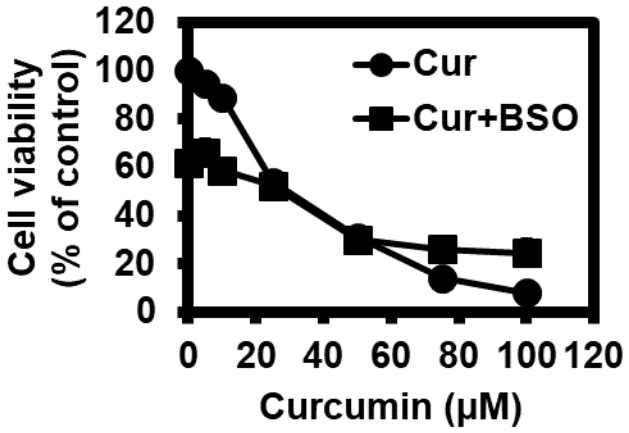
120
100
80
60
40
20
0
Cell viability
(% of control)
Cur
Cur+BSO
0
20
40
60
80
100
120
Curcumin (μM)

Figure S3.3.

Connecting Text

Glioblastoma cells of astrocytic origin are substantially different from normal astrocytes. In Chapter 3, we showed how adaptations at the organellar level can benefit cancer cell survival. Lipid droplets in GBM are larger and more numerous than in normal astrocytes, serving as an energy source and performing anti-oxidative functions. Such adaptative changes are not limited to the cancer cells. Normal neural cells respond to the presence of cancer cells and undergo changes that can ultimately contribute to disease progression.

Glial cells are particularly important in the tumor microenvironment; astrocytes and microglia secrete trophic factors that stimulate GBM survival and proliferation, as well as the recruitment of more immune cells from the periphery. There is great interest in modulating these cells to diminish their supportive role in the tumor stroma. In Chapter 4, we explore the use of dendritic polyglycerol sulfates, an anti-inflammatory nanotherapeutic that downregulates tumor-supportive secreted factors from glial cells, thereby limiting inflammatory processes and GBM invasiveness. We focused on the role of lipocalin-2, an acute phase protein with emerging roles in the brain. To adequately study the complex interactions between the different cell types of the brain, we employed human cerebral organoids to model neural cells in 3D.

Cerebral organoids are valuable tools to study the response of normal human brain cells. Chapter 4 discusses their use in the context of inflammation and the tumor microenvironment, which are aspects often neglected in GBM research. In addition, this chapter presents on the testing of nanotherapeutics in human neural cells, a topic of great interest given the ever-expanding potential nanostructures in medicine.

Chapter 4. Nanotherapeutic Modulation of Human Neural Cells and Glioblastoma in Organoids and Monocultures

Zhang I, Lépine P, Han C, Lacalle-Aurioles M, Chen C X C, Haag R, Durcan T M, Maysinger D. Cells. 2020l 9:2434.

Abstract

Inflammatory processes in the brain are orchestrated by microglia and astrocytes in response to activators such as pathogen-associated molecular patterns, danger-associated molecular patterns and some nanostructures. Microglia are the primary immune responders in the brain and initiate responses amplified by astrocytes through intercellular signaling. Intercellular communication between neural cells can be studied in cerebral organoids, co-cultures or *in vivo*. We used human cerebral organoids and glioblastoma co-cultures to study glia modulation by dendritic polyglycerol sulfate (dPGS). dPGS is an extensively studied nanostructure with inherent anti-inflammatory properties. Under inflammatory conditions, lipocalin-2 levels in astrocytes are markedly increased and indirectly enhanced by soluble factors released from hyperactive microglia. dPGS is an effective anti-inflammatory modulator of these markers. Our results show that dPGS can enter neural cells in cerebral organoids and glial cells in monocultures in a time-dependent manner. dPGS markedly reduces lipocalin-2 abundance in the neural cells. Glioblastoma tumoroids of astrocytic origin respond to activated microglia with enhanced invasiveness, whereas conditioned media from dPGS-treated microglia reduce tumoroid invasiveness. Considering that many nanostructures have only been tested in cancer cells and rodent models, experiments in human 3D cerebral organoids and co-cultures are complementary *in vitro* models to evaluate nanotherapeutics in the pre-clinical setting. Thoroughly characterized organoids and standardized procedures for their preparation are prerequisites to gain information of translational value in nanomedicine. This study provides data for a well-characterized dendrimer (dPGS) that modulates the activation state of human microglia implicated in brain tumor invasiveness.

Introduction

The brain is particularly challenging to model because of its complex structure and functions. Neural cells constantly interact with each other through signaling molecules as well as cell-cell contacts (Paolicelli et al., 2019; Pósfai et al., 2019; Simon et al., 2019). Monocultures are useful to answer cell type-specific questions, but processes involving multiple cell types benefit from the use of co-cultures and organoids (M. Li & Izpisua Belmonte, 2019; Rossi et al., 2018; Takebe & Wells, 2019).

Although primary dissociated and organotypic slice cultures are attractive models to investigate molecular mechanisms and functions, particularly for genetic knock-ins and knock-outs, key differences between human and mouse brains can impact the translational potential of experimental results (Breschi et al., 2017; Marshall & Mason, 2019). Primary human neural cells are valuable resources, but their use is often restrained by access or methodological limitations. Advances in stem cell research have led to the development of organoids as *in vitro* models resembling human tissues in structure and complexity (M. Li & Izpisua Belmonte, 2019; Rossi et al., 2018; Takebe & Wells, 2019). Cerebral organoids differentiated from induced pluripotent stem cells (iPSCs) show organized neurons and astrocytes in three-dimension (3D) (Xiuqing Chen et al., 2019; Lancaster & Knoblich, 2014).

Nanostructures have been extensively studied in different cell lines and rodents (Ioannidis et al., 2018), but limited amount of data is available in human primary cells and organoids. Rodent models were valuable for the assessment of absorption, distribution, elimination and metabolism of nanomedicines. They clearly showed problematic entry of some nanostructures into the cerebral parenchyma due to the blood-brain barrier (Aparicio-

Blanco et al., 2016; Jackson et al., 2019). Studies in rodents also provided information on how some nanostructures can be tuned in terms of size, shape and surface properties to facilitate brain entry. Similar studies are clearly not amenable in humans and are very sparse in non-human primates (e.g. Onpattro, Abraxane, BIND-014)(Akinc et al., 2019; Havel et al., 2016; Hrkach et al., 2012). Organoids therefore offer a valuable platform for the testing of organic and metallic nanostructures.

Among the nanostructures that have been studied in rodents and showed pronounced intrinsic anti-inflammatory properties are dendritic polyglycerol sulfates (dPGS) (Maysinger et al., 2015; Maysinger, Lalancette-Hébert, et al., 2019; Rades et al., 2018). Their structures with terminal sulfate groups resemble that of heparan sulfate, which exerts anti-coagulant effects (Dernedde et al., 2010; Parish, 2006; Rades et al., 2018). In contrast to heparan sulfate, dPGS show primarily anti-inflammatory activity with relatively weak anti-coagulant effects that are size- and charge-dependent. Earlier studies indicated that dPGS can effectively reduce hyperactivity of microglia stimulated by danger-associated molecular patterns and lipopolysaccharide (LPS) in mice (Maysinger et al., 2015; Maysinger, Ji, et al., 2018; Maysinger, Lalancette-Hébert, et al., 2019). Microglia are the resident immune cells of the central nervous system and constantly survey their surroundings under physiological conditions (Masuda et al., 2020; Prinz et al., 2019; Rodríguez-Gómez et al., 2020). Their morphology and phagocytic functions are elevated under many pathological conditions, making them attractive targets for nanotherapeutic interventions. Our previous studies showed that dPGS can modulate microglial activation in response to pathogen-associated molecular patterns and misfolded proteins (e.g. amyloid beta), thereby reducing losses in dendritic spine density of excitatory hippocampal neurons

in mouse organotypic slice cultures (Maysinger et al., 2015; Maysinger, Ji, et al., 2018; Maysinger, Lalancette-Hébert, et al., 2019). These studies also showed that hyperactive microglia generate reactive astrocytes through the release of acute-phase cytokines such as interleukin-6, tumor necrosis factor alpha and lipocalin-2 (LCN2). However, the abundance and release of LCN2 in human glial cells was not reported. We tested if dPGS can modulate LCN2 in a cerebral organoid model.

Aside from establishing human cerebral organoids, we also used glioblastoma tumoroids to investigate the effectiveness of nanotherapeutics in the brain tumor microenvironment. Glioblastoma are mainly astrocytomas characterized by their infiltrative nature (C. Li et al., 2019). Microglia in the glioblastoma environment promote disease progression by secreting cytokines and growth factors (Anfray et al., 2020; Broekman et al., 2018; Z. Chen & Hambardzumyan, 2018). By combining reconstituted 3D models of glioblastoma (tumoroids) with organoids and modulating the activity of microglia with dPGS, we demonstrate that dPGS is a powerful therapeutic agent that can reduce inflammatory markers and glioblastoma invasiveness.

Materials and methods

Generation of cerebral organoids from human iPSC

Procedures for culturing human iPSCs, embedding organoids in optimal cutting temperature (OCT) blocks, cryosectioning and immunostaining were all described previously (Xiuqing Chen et al., 2019)**.** The cell-line used was the NCRM1 iPSC line obtained from the National Institutes of Health. The method used to generate the 3D cerebral organoids was adapted from the protocol published by Lancaster and Knoblich in Nature Protocols (Lancaster & Knoblich, 2014)**.** Compositions of the different media are the same and reagents used are similar, except for: DMEM-F12 (Gibco, Ottawa, ON, Canada), human embryonic stem cell (hESC) quality fetal bovine serum (FBS) (Wisent, St-Bruno, QC, Canada), MEM Non-Essential Amino Acids Solution (MEM-NEAA) (Multicell, Montreal, QC, Canada), 2-mercaptoethanol (Millipore Sigma, Oakville, ON, Canada), Y27632 Rho-associated protein kinase (ROCK) inhibitor (Selleckchem, Burlington, ON, Canada), N2 supplement (Gibco) and Penicillin-Streptomycin (Multicell).

For the generation and maintenance of embryoid bodies (EBs, days 0-11), we started from a 100 mm dish with iPSCs at 70 % confluence with high quality (less than 10 % differentiated cells). Cells were washed with DMEM-F12 and dissociated with Accutase to generate a suspension of single cells. Cells were gently resuspended in hESC media containing ROCK inhibitor (Lancaster & Knoblich, 2014), FGF-b and plated at a density of 10 000 cells/well in a 96-well ultra-low attachment U-bottomed plate (Corning, Burlington, ON, Canada). Plates were centrifuged at 1 200 rpm for 10 min and incubated at 37 °C, 5 % CO_2 for 48 h. During day 2, a half media change was made, followed by a media change every other day up to day 11. Images of EBs were recorded with Evos XL Core Microscope (Thermo Fisher Scientific, Ottawa, ON, Canada) every 2 days during media changes to measure their diameter using the Image J software

(U. S. National Institutes of Health, Bethesda, Maryland, USA). Once EBs had reached ≥350 μm in diameter, hESC media was switched to be without ROCK inhibitor and FGF-b (Lancaster & Knoblich, 2014). When EBs were about 500-600 μm in diameter with smooth and bright edges, media was switched to neuronal induction media (NIM). EBs are maintained in NIM for 4-5 days until the outer surface is optically translucent and ready to be embedded in Matrigel® containing reduced growth factor droplets.

Matrigel® was thawed on ice. After media removal from each well containing the EBs, 30 μL of Matrigel® was added per well and incubated for 30 min at 37 °C. Next, 200 μL of final differentiation media without vitamin A (Lancaster & Knoblich, 2014) was added per well. Using a 1000 μL cut tip, the Matrigel®-embedded organoids were transferred into an uncoated 6-well ultra-low attachment plate (Corning) with 4 mL of final differentiation media without vitamin A per well. A maximum of five organoids were added and maintained per well to avoid fusion. Following transfer, plates were left for 48 h in stationary culture. After 48 h, media was changed to fresh final differentiation media without vitamin A, followed by a second 48 h incubation. Following the second media change, plates were transferred onto an orbital shaker set at 70 rpm (Scientific Industries Inc., Bohemia, NY, USA) housed within the 37 °C incubator. Media was changed every 3 days with fresh final differentiation media with vitamin A until the organoids were ready for analysis.

Immunofluorescence (IF) staining in organoids

Cerebral organoids were fixed with 4 % paraformaldehyde (overnight at 4 °C), washed in phosphate-buffered saline (PBS, Multicell), dehydrated in 20 % sucrose (1-3 days) and embedded in OCT Compound (Thermo Fisher Scientific). Blocks were kept at -80 °C until needed. For IF,

samples were sectioned (20 μm) in a cryostat (Cryostar NX70, Thermo Fisher Scientific), air dried at room temperature (RT), and kept at -20°C before IF staining. Cryosections were rehydrated in PBS (15 min) and permeabilized/blocked in blocking solution (1 h at RT) containing: 0.2 % Triton X-100 (Millipore Sigma), 0.05 % bovine serum albumin and 5 % normal donkey serum in PBS, before incubation (overnight at 4 °C) with primary antibodies. Antibodies used were as follows: mouse anti-Nestin (1:250, Developmental Studies Hybridoma Bank, Iowa City, IA, USA, rat-401), rabbit anti-SOX2 (1:500, Millipore, Oakville, ON, Canada, AB5603), chicken anti-MAP2 (1:1000, EnCor Biotechnology, Gainesville, FL, USA, CPCA-MAP2), rat anti-CTIP2 (1:500, Abcam, Toronto, ON, Canada, ab18465), rabbit anti-GFAP (1:250 Millipore, MAB144P), chicken anti-Beta III Tubulin (1:400, Millipore, AB9354), rabbit anti-Nestin (1:200, Abcam, ab92391) and rat anti-lipocalin-2 (1:500, R&D Systems, Toronto, ON, Canada, MAB1757). Sections were then washed in PBS (45 min) and incubated (1 h at RT) with secondary antibodies in blocking solution: goat anti-rat Dylight 488 (1:300, Abcam, ab96887), donkey anti-rabbit Dylight 594 (1:400, Abcam, ab96877), donkey anti-chicken Alexa 647 (1:500, Invitrogen, Ottawa, ON, Canada, A21447), donkey anti-mouse Dylight 550 (1:200, Abcam, ab96876), goat anti-chicken Dylight 650 (1:200, Abcam, ab96950), donkey anti-rabbit Dylight 550 (1:200, Abcam, ab96892) and goat anti-rat Alexa Fluor 647 (1:500, Thermo Fisher Scientific, A21247). Sections were washed (45 min) with PBS and incubated (10 min at RT) with Hoechst 33342 (1:5000, Thermo Fischer Scientific) in PBS, washed in PBS (10 min) and mounted using Aqua-Poly/Mount (Polysciences Inc.,Warrington, PA, USA). Samples were imaged on a Leica TCS SP8 confocal microscope (Leica, Richmond Hill, ON, Canada) at a 20X magnification.

Cell culture

U251N human glioblastoma cells and HMC3 human microglia were originally obtained from the American Type Culture Collection. Unless otherwise indicated, cells were maintained in Dulbecco's Modified Eagle Medium (DMEM, Thermo Fisher Scientific) supplemented with 5% fetal bovine serum (FBS, Wisent) and 1% Penicillin-Streptomycin (Thermo Fisher Scientific). Primary human astrocytes were obtained from Dr. Jack Antel's lab and maintained in DMEM supplemented with 5% FBS and 1% Penicillin-Streptomycin. Primary astrocytes were kept at passages below five. Conditioned media was obtained from cell cultures maintained in the exponential growth phase and used fresh at 50% (v/v) in fresh media following centrifugation (3,000 rpm, 5 min) to remove cell debris. When used for the treatment of cerebral organoids, conditioned media was prepared using organoid media.

Time-dependent dPG/dPGS internalization in organoids

Human cerebral organoids were treated with dPG-Cy5 (1 μM) or dPGS-Cy5 (1 μM) for 1 h, 4 h or 24 h, then used for IF staining or direct imaging. For direct imaging, organoids were fixed in 4% paraformaldehyde overnight and nuclei were labeled with Hoechst 33342 (10 μM, overnight). Organoids were washed in PBS and imaged using a fluorescence microscope. Fluorescence was analyzed in ImageJ. Glioblastoma tumoroids were treated with dPG-Cy5 (1 μM) or dPGS-Cy5 (1 μM) for 24 h, then washed twice with PBS before imaging using a fluorescence microscope.

Western blot

Western blot analysis followed published procedures (I. Zhang et al., 2018)**.** In brief, organoids were cut into small pieces using a razor blade and incubated in RIPA lysis buffer for 30 min on

ice. Lysates were vortexed for 10 sec every 10 min and lastly centrifuged for 30 min at 4 °C and 13,000 rpm. Lysates and media samples were separated by SDS-PAGE and blotted onto PVDF membranes (Bio-Rad, Mississauga, ON, Canada). Blocked membranes were probed with primary antibodies: rat anti-lipocalin-2 (1:500, R&D Systems, MAB1757), rabbit anti-NFκB p65 (1:1000, Abcam, ab16502), mouse anti-STAT3 (1:1000, Abcam, ab119352), mouse anti-actin (1:5000, Millipore Sigma, A5316) or mouse anti-alpha-tubulin (1:5000, Abcam, ab7291) overnight at 4 °C. Membranes were washed and incubated with secondary antibodies (goat anti-rat HRP, 1:1000, Thermo Fisher Scientific, 31470, goat anti-rabbit HRP, 1:1000, Bio-Rad, 1706515 and horse anti-mouse HRP, 1:5000, Cell Signaling, Burlington, ON, Canada, 7076S) for 1 h at RT. Membranes were washed and incubated with enhanced chemiluminescence substrate (Bio-Rad) for 5 min, signals were acquired with an Amersham 6000 imager (Amersham, Oakville, ON, Canada) or on film, and quantified in ImageJ.

Glioblastoma invasion assay

U251N tumoroids and human astrocyte spheroids were prepared using the hanging drop method (Del Duca et al., 2004)**.** Briefly, drops of 5,000 cells in 30 µl medium were pipetted onto the inner side of a 100 mm Petri dish (Thermo Fisher Scientific) lid. The lid was quickly flipped to cover the Petri dish filled with 20 mL PBS. Hanging drops were cultured at 37 °C for 48 h to allow tumoroids to form. Tumoroids were then gently scooped into a medium-filled Petri dish coated with 2% agarose (dissolved in PBS) and cultured for 48 h. Tumoroids were implanted in collagen gel (Advanced BioMatrix, San Diego, CA, USA), in the presence or absence of primary human astrocytes (7,000 cells) and human HMC3 microglia (3,000 cells) dispersed in 200 µL gel. Gels were covered with 200 µl DMEM with or without treatment. Tumoroids were imaged using light

microscopy immediately after implantation (time = 0 day) and after 6 days. The average length of cell outgrowth into the surrounding collagen was measured in ImageJ. For invasion assays of tumoroids into organoids, fluorescently-labeled tumoroids were prepared using U251N cells incubated with CellTracker Red (Thermo Fisher Scientific) following recommendations from the manufacturer. Tumoroids were placed in culture with organoids and observed to adhere after 24 h. Cultures were imaged using a fluorescence microscope over 6 days.

Immunocytochemistry

Cells were seeded at 5,000 cells/coverslip on glass coverslips (Merlan Scientific, Mississauga, ON, Canada) coated with poly-D-lysine (Millipore Sigma). Cells were cultured for 24 h (U251N and HMC3) or 48 h (primary human astrocytes) before treatment. Following treatment, cells were fixed in 4% paraformaldehyde (10 min), permeabilized with 0.1% Triton X-100 (10 min), blocked in 10% goat serum in PBS (Gibco) for 1 h and incubated with primary antibodies overnight at 4 °C: rabbit anti-GFAP (1:500, Abcam, ab7260), mouse anti-Lamp1 (1:500, Developmental Studies Hybridoma Bank, H4A3-c), rat anti-lipocalin-2 (1:500, R&D Systems, MAB1757), rabbit anti-NFkB p65 (1:500, Abcam, ab16502) or rabbit anti-phospho-STAT3 Y705 (1:500, Abcam, ab76315). Cells were washed in PBS three times and incubated with secondary antibodies for 1 h at RT: goat anti-rabbit Alexa Fluor 488 (1:1000, Thermo Fisher, Mississauga, ON, Canada, A27034), goat anti-rat Alexa Fluor 647 (1:500, Thermo Fisher, A21247) or goat anti-mouse Alexa Fluor 488 (1:1000, Thermo Fisher, A28175). Cells were washed with PBS and nuclei were labeled with Hoechst 33342 (10 μM, 10 min). After three more washings with PBS, coverslips were mounted on microscope slides (Diamed) using Aqua-Poly/Mount. Samples were imaged using a fluorescence microscope (Leica DMI4000B) and intracellular fluorescence was analyzed in

ImageJ. The nuclear and/or cytoplasmic fluorescence of NFκB, LCN2 and phosphor-STAT3 for each cell was measured and normalized to the nuclear or cytoplasmic area. The background fluorescence was subtracted.

Immunohistochemistry

Immunohistochemistry was performed as previously published (I. Zhang et al., 2018)**.** In brief, human brain sections were dewaxed in xylene and rehydrated in ethanol. Antigen retrieval was performed in citrate buffer. Following blocking, samples were incubated with primary antibodies: rat anti-lipocalin-2 (1:500, R&D Systems, MAB1757), mouse anti-IBA1 (1:300, Invitrogen, MA5-27726) or rabbit anti-GFAP (1:250 Millipore, MAB144P) overnight at 4 °C. Samples were washed and incubated with secondary antibodies: goat anti-rat Alexa Fluor 647 (1:500, Thermo Fisher Scientific, A21247), goat anti-mouse Alexa Fluor 647 (1:300, Thermo Fisher Scientific, A28181) or goat anti-rabbit Alexa Fluor 488 (1:500, Thermo Fisher, A27034) for 1 h at RT. Nuclei were labeled with DAPI (1 g/mL, 5 min, Molecular Probes, Ottawa, ON, Canada) and samples were mounted on microscope slides using Dako mounting medium (Dako, Burlington, ON, Canada). Samples were imaged using a fluorescence microscope. The samples were harvested under a protocol approved by the Montreal Neurological Hospital's research ethics board (NEU-10-066). Consent was given by all patients and controls (aged 55–76). Tissues were from the cerebral cortex.

Lipid droplet imaging

Cells seeded on glass coverslips at 5,000 cells/coverslip were cultured for 24 h before treatment. Following treatment, cells were washed twice with PBS and fixed in 4% paraformaldehyde (10 min). Cells were washed with PBS and incubated with BODIPY 493/503 (10 μM, Thermo Fisher)

and Hoechst 33342 (10 μM) for 10 min. Cells were washed with PBS four times, then mounted on microscope slides using EverBrite (Biotium, Burlington, ON, Canada). Samples were imaged using a fluorescence microscope.

MTT assay

Following treatment, organoids were washed in PBS twice and incubated in fresh media in the presence of 3-(4,5-dimethylthiazol-2-yl)-2,5-diphenyltetrazolium bromide (MTT) (0.5mg/mL, Millipore Sigma) for 1 h at 37 °C. The media was removed, and cells were lysed in 500 μL dimethyl sulfoxide (Santa Cruz, Dallas, TX, USA). Samples were measured at 595 nm in triplicate using a microplate reader (Spark 10M, Tecan, Männedorf, Switzerland). Measurements were normalized to the organoid weight.

Statistics

Statistical significance was determined using one-way ANOVA followed by the Student's t-test. p-values lesser than 0.05 were deemed significant. The Bonferroni correction was applied for multiple comparisons.

Results

dPGS are internalized in 3D cerebral organoids

Human cerebral organoids were generated from human iPSCs according to an established protocol (Lancaster & Knoblich, 2014)**.** A timeline of organoid formation and biomarkers used to delineate dynamic linage progression is illustrated in Figure S1. We used these organoids after a 100-day maturation to test dendritic polyglycerol sulfates (dPGS) as model nanostructures with anti-inflammatory properties in human neural cells, as well as other types of emerging nanostructures with biomedical applications, such as metallic gold nanoclusters (Bonačić-Koutecký & Antoine, 2019; J. Ji et al., 2019; Maysinger, Gran, et al., 2019)**.** Gold nanoclusters have been shown to affect cellular stress and organellar function thanks to their unique physicochemical properties, but little work was done in human neural cells. The nanostructures were screened for cytotoxic effects (Figure 1A and Figure S2) and results showed that they can be studied in human neural cells without jeopardizing the viability of the organoid cultures. This provides the basis for further investigations on nanomedical applications in a translationally-relevant model. The first step was to show if dPGS are internalized by neural cells within the organoids themselves. To this end, we treated organoids with fluorescently (Cy5)-labeled dPGS (Figure 1). Time-course experiments showed that dPGS-Cy5 was internalized within 1 h (12.8±2.2 SEM fold increase of baseline fluorescence), then progressively more over 24 h (64.5±11.4 SEM fold increase) (Figure 1B and C). Compared to dPGS, internalization of the non-sulfated dendritic polyglycerol (dPG) was low (8.7±2.1 SEM fold increase after 24 h)(Figure 1B and C), underlining the important role of the terminal sulfate groups to cell internalization. In the current study, we showed that GFAP-labeled astrocytes within the outermost layer (200-300 μm) of the cerebral organoids contain abundant amounts of dPGS (Figure 1D).

dPGS internalization in human microglia and normal astrocytes

Given the importance of glial cells in regulating inflammatory processes in the brain, we further studied the intracellular effects of dPGS in astrocytes and particularly microglia, which are absent from the cerebral organoids. We established in cell monolayer cultures that human microglia and astrocytes internalized comparable amounts of dPGS within 24 h of treatment (Figure 1E and F). Fluorescence imaging at the single cell level showed that dPGS-Cy5 accumulated in the perinuclear area (Figure 1E), and was partially co-localized with lysosomal compartments labeled with Lamp1 (Macairan et al., 2020). Given that microglia activated by pro-inflammagens (e.g. LPS) are associated with increased sequestration of neutral lipids into lipid droplets (LDs)(Marschallinger et al., 2020; Olzmann & Carvalho, 2019)(Figure S3B), we investigated if dPGS could have modulatory effects on lysosomes, which interact with LDs through lipophagy and other processes (Pu et al., 2016; Schulze et al., 2017)**.** This was suggested by changes in lysosomal positioning, with an increase in perinuclear lysosomes (Figure S3A). In turn, treatment with dPGS prevented LPS-induced lipid droplet accumulation (Figure S3C).

dPGS reduced microglia-stimulated lipocalin-2 in cerebral organoid models

Considering the importance of microglia-astrocyte crosstalk in rodent (Maysinger, Lalancette-Hébert, et al., 2019) and human neural cells (Paolicelli et al., 2019; Pósfai et al., 2019), we measured LCN2 abundance in human glial cells in response to LPS, a prototypical pro-inflammagen whose levels are exacerbated in endotoxemia and sepsis. The presence of microglia is required to stimulate the synthesis of LCN2 in neural cells, as levels in response to LPS remained comparable to that of the untreated control in the absence of microglia from the organoids (Figure

2A, B and Figure S4). In turn, conditioned media from LPS-stimulated microglia induced a significant increase in intracellular and extracellular LCN2 in the cerebral organoid cultures (Figure 3C-E), confirming that this upregulation is microglia-dependent in human neural cells. Given that astrocytes play a significant role in inflammatory processes in the brain, we investigated if there was increased LCN2 abundance in these cells in response to microglia activation.

Similarly to the results from cerebral organoids, direct stimulation of astrocytes with LPS did not have a significant effect (Figure 2F). In contrast, treatment with conditioned media from LPS-activated microglia increased LCN2 abundance, whereas the presence of dPGS returned LCN2 abundance to control levels (Figure 2F). dPGS alone and conditioned media from resting microglia did not have significant effects (Figure 3D-F). Finally, to show that dPGS is not cytotoxic to human neural cells, we measured mitochondrial metabolic activity using the MTT assay. Results from these studies showed that neither dPGS nor dPG affected mitochondrial metabolic activity in in 3D organoids for up to 72 h (Figure S2). Our earlier studies indicated that in rodent cells, concentrations of dPGS up to 100 μM did not cause any notable cytotoxicity (Maysinger et al., 2015)**.** These results encouraged us to investigate dPGS as a microglia modulator and indirect suppressor of glioblastoma invasiveness.

Microglia and dPGS modulate glioblastoma invasiveness

Glioblastoma multiforme is an aggressive brain tumor of astrocytic origin for which complete resection is often impossible due to its invasive nature (Mary Elizabeth Davis, 2016; C. Li et al., 2019). To model the impact of microglia and astrocytes on glioblastoma invasiveness, we designed a 3D invasion assay examining the propensity of the cancer cells to migrate into the surrounding collagen matrix. Human microglia and primary human astrocytes were embedded into the collagen

matrix, wherein a tumoroid was then implanted (Figure 3A). Over time, the normal neural cells extend their processes while cancer cells migrate radially from the tumoroid. Glioblastoma outgrowth from the tumoroid into the surrounding collagen was encouraged by the presence of microglia and astrocytes (Figure 3A and B), an effect replicated using microglia-conditioned media and inhibited by dPGS (Figure 3C and D). This indicates that neural cells secrete factors (extracellular matrix degradation enzymes, cytokines, growth factors) that can stimulate tumor invasiveness (Medema, 2013; Ramachandran et al., 2017; Vollmann-Zwerenz et al., 2020). In contrast, tumoroids grown in isolation or within cerebral organoids in the absence of microglia had comparatively less outgrowth over time (Figure 3A, 3B and Figure S5), and normal human astrocytes migrated in scattered pattern without radial outgrowth (Figure S6).

To characterize the effects of glioblastoma on its surrounding immune cells, glioblastoma cells were directly co-cultured with microglia cells and showed significantly higher LCN2 levels compared to glioblastoma cells in monoculture (Figure 3E). High LCN2 levels were also observed in tumor tissues from glioblastoma patients as compared to control brain tissues (Figure 3F). To investigate the mechanism behind LCN2 upregulation, microglia were stimulated with glioblastoma-conditioned media. This resulted in increased nuclear NFκB and STAT3 phosphorylation, two key transcription factors for immune activation (Figure 3G and H) that are also hyperactivated in glioblastoma. The protein levels of total NFκB and STAT3 in the cells remained comparable to the control (Figure 3I).

On the other hand, dPGS was internalized into glioblastoma tumoroids (Figure S7) and decreased LCN2 levels in glioblastoma cells *in vitro* (Figure 3E). This demonstrates proof of concept for using dPGS as a modulator of the tumor microenvironment (Figure 4).

Discussion

The key question addressed in this study is: can dendritic polyglycerol sulfates with intrinsic anti-inflammatory properties reduce inflammatory markers in cerebral organoids and glioblastoma invasiveness by modulating microglia activity? Mechanistic studies in 3D human neural cultures with new drugs or nanostructures are sparse due to the limited availability of neural tissues. To overcome such a problem, several protocols have been developed for the generation of 3D cerebral organoids and other types of organoids (Lancaster & Knoblich, 2014; M. Li & Izpisua Belmonte, 2019; Marshall & Mason, 2019; Rossi et al., 2018). Human cerebral organoids derived from iPSCs showing properties of different neural cell types are valuable models to study the interactions and effects of nanostructures in 3D. One of the most advanced organoids containing vasculature resembling that of the brain was recently proposed to investigate physiology and pathological changes in neurological disorders (Cakir et al., 2019). Although our organoids are not as complex as Cakir's, we took advantage of cerebral organoids to reveal how microglia exposed to the pro-inflammagen LPS and the dendritic nanostructure dPGS affect astrocyte reactivity. We show clear anti-inflammatory effects from dPGS and provide the first evidence for this in human brain cells. There are still several limitations to overcome: (1) the integration of resident and peripheral immune cells recruited chemotactically and (2) the contribution of endothelial cells in vasculature as part of the blood-brain barrier.

Our results in the organoid cultures showed that the presence of sulfate groups on dPGS was critical for the internalization of nanostructures, as it allowed binding to selectin receptors (Dernedde et al., 2010; Maysinger, Lalancette-Hébert, et al., 2019; Rades et al., 2018). Intracellular changes associated with dPGS included an increase in perinuclear lysosomes, which typically have lower luminal pH and increased degradation activity (D. E. Johnson et al., 2016; Pu et al., 2016),

functions often impaired in aging and neurodegenerative diseases. This is interesting given the role of lysosomes in processing LDs, which are upregulated in inflammation and cancer (Marschallinger et al., 2020; Olzmann & Carvalho, 2019). LDs are promiscuous organelles: depending on the cell type, cellular context and their intracellular location, they can play a protective role or become damaging to neural and other cells if peroxidized lipids are released. In aggressive tumors (e.g. glioblastoma and breast), they provide energy for cancer cells to thrive and can sequester lipophilic anticancer agents, reducing the rate at which they reach their desirable targets (Dubey et al., 2020; Treyer et al., 2018; I. Zhang et al., 2016). Their numbers are highly upregulated in glioblastoma compared to normal astrocytes (Figure S3C and D), and their inhibition was shown to enhance the effectiveness of pharmacological agents (I. Zhang et al., 2016).

As now shown in human neural cells, LCN2 is mainly produced by microglia-stimulated astrocytes. Microglia themselves are not significant contributors to LCN2 upregulation due to the LCN2 gene being suppressed by SRSF3 (Boutej et al., 2017). Instead, they secrete other cytokines (e.g. IL-6, TNFα) and alarmins under pro-inflammatory conditions that can activate astrocytes and other neural cells (Boutej et al., 2017; Liddelow et al., 2017). Several of these were shown to bind heparan sulfate (Mummery & Rider, 2000; Parish, 2006), suggesting that dPGS prevented microglia-mediated LCN2 production by blocking some soluble factors and preventing downstream signaling (Figure 2D and E). One of the candidate cytokines is interleukin-6 released from microglia, to which dPGS was shown to bind in our earlier studies using surface plasmon resonance (Maysinger, Lalancette-Hébert, et al., 2019).

Cytokines and alarmins play key roles in the tumor microenvironment (Conti et al., 2020; Matarredona & Pastor, 2020; Rapoport et al., 2020; Roesch et al., 2018; Sims et al., 2010). The

cancer cells secrete factors that actively recruit microglia and peripheral macrophages to the tumor site. In turn, these immune cells produce cytokine and growth factors that can promote cancer progression (Anfray et al., 2020). In this context, microglia-astrocyte crosstalk forms a positive feedback loop that maintains an unfavourable tumor microenvironment (Broekman et al., 2018; Gieryng et al., 2017). LCN2 is an acute-phase protein with emerging roles in the brain and in cancer. It was shown to complex with and enhance the activity of metalloproteinase-9, a protease secreted by cancer cells that breaks down the extracellular matrix and promotes invasiveness (Kobara et al., 2013; Y. Lin et al., 2014). This is significant given that dPGS can downregulate LCN2 in neural cells and decrease glioblastoma invasiveness. dPGS can bind P-selectin, which is expressed in the tumor endothelium and in glioblastoma cells. Because dPGS can also serve as nanocarrier, they have the potential to deliver anti-cancer agents (Ferber et al., 2017; Sousa-Herves et al., 2015). Nanocarriers such as functionalized dendrimers for siRNA and anti-cancer drug co-delivery (Mendes et al., 2019; Subhan & Torchilin, 2019) merit testing in human organoid models to reveal how combination therapy could affect interplay between cancer cells and the tumor microenvironment. The modulatory effect of dPGS on organelles could impact glioblastoma cells in several ways: 1) the increase in perinuclear lysosomes could decrease lysosomal exocytosis and the release of extracellular matrix-degrading enzymes (e.g. cathepsins)(Machado et al., 2015; Sundler, 1997), 2) a reduction in lipid droplet size and number (Kepsutlu et al., 2020) is an indicator of reduced microglia hyperactivity, thus fewer cytokines and trophic factors contributing to glioblastoma invasiveness, and 3) decreased lipid droplets prevents the sequestration of lipophilic anti-cancer agents, allowing them to reach their intracellular targets (e.g. curcumin)(I. Zhang et al., 2016).

Conclusions

Our results show that dPGS is an attractive candidate as an anti-inflammatory polyglycerol dendrimer able to modulate human microglia-astrocyte crosstalk. This dendrimer regulated lipocalin-2 abundance in human neural organoids. In the context of inflammation associated with glioblastoma multiforme, dPGS limited glioblastoma invasiveness by modulating microglial activation. Overall, these studies propose the evaluation of well-defined nanostructures in well-characterized human organoids and co-cultures. Cerebral organoids merit further studies as complementary 3D models in nanoscience, but they require rigorous characterization and application of standardized procedures to be widely used (Marx, 2020). Such three-dimensional systems together with co-cultures and *in vivo* experiments will provide a valuable evaluation platform for the internalization, cytotoxicity and modulatory effects of nanotherapeutics in human neural cells.

Acknowledgments

The authors would like to thank Nadine Rades for kindly providing dPG and dPGS nanostructures, Jack Antel for primary human astrocytes, Kevin Petrecca for human brain sections and Rodolphe Antoine for gold nanoclusters. T. M. Durcan and the EDDU acknowledge that funding for the generation of 3D cerebral organoids is through the Sebastian and Ghislaine Van Berkom Foundation, the Alain and Sandra Bouchard Foundation and the McGill Healthy Brains for Healthy Lives.

Figure 4.1. dPGS internalization in cerebral organoids and human neural cells

(a) Schematic representation of cerebral organoid usage for nanostructure screening. (b) Human cerebral organoids were treated with dendritic polyglycerol (dPG)-Cy5 (1 μM) or dendritic polyglycerol sulfate (dPGS)-Cy5 (1 μM) for 1 h, 4 h or 24 h. Nuclei were labeled with Hoechst 33342. Organoids were imaged using a fluorescence microscope. (c) Cy5 fluorescence in organoids was analyzed in ImageJ. Shown are the average fluorescence per condition ± SEM. At least 90 organoids were analyzed from three independent experiments. *** $p < 0.001$ (d) Fluorescence micrographs of human cerebral organoids treated with dPG-Cy5 (1 μM) or dPGS-Cy5 (1 μM) for 24 h and labeled for glial fibrillary acidic protein (GFAP). Nuclei were labeled with Hoechst 33342. (e) Primary human astrocytes and human HMC3 microglia internalization of dPGS-Cy5 (1 μM) after 24 h. dPGS-Cy5 (red) is partially co-localized with Lamp1-labeled lysosomal compartments (green). The negative control was prepared in the absence of dPGS-Cy5 and primary antibody to account for background fluorescence. Nuclei were labeled with Hoechst 33342 (blue). Cells were imaged using a fluorescence microscope. (f) Shown are the average intracellular Cy5 fluorescence per cell expressed as fold change from untreated cells ± SD. At least 90 cells were analyzed in two independent experiments. n.s. Non-significant.

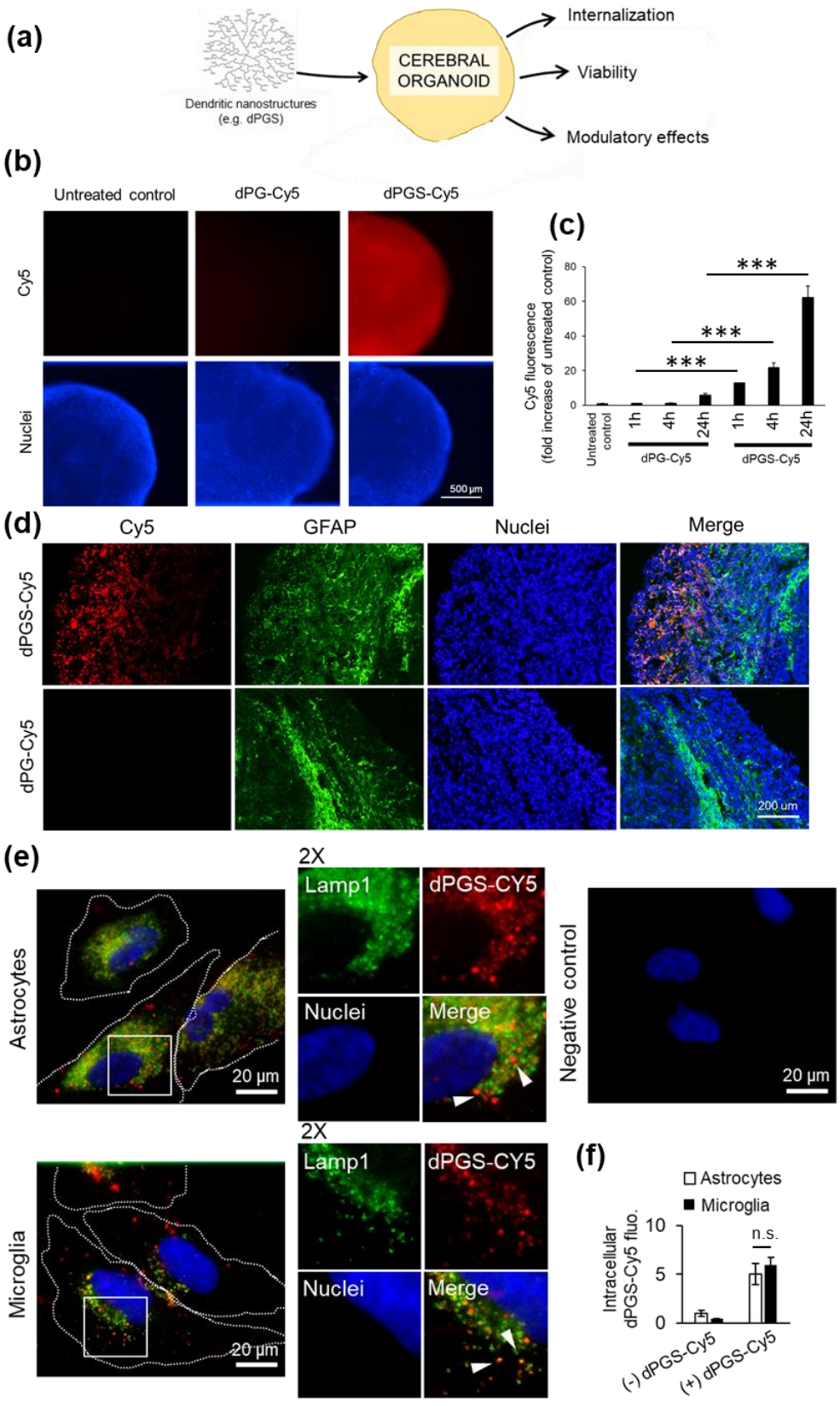
(a)
Dendritic nanostructures
(e.g. dPGS)
CEREBRAL
ORGANOID
Internalization
Viability
Modulatory effects
(b)
Untreated control
dPG-Cy5
dPGS-Cy5
Cy5
Nuclei
500 µm
(c)
Cy5 fluorescence
(fold increase of untreated control)
***
***
***
Untreated control
1h
4h
24h
1h
4h
24h
dPG-Cy5
dPGS-Cy5
(d)
Cy5
GFAP
Nuclei
Merge
dPGS-Cy5
dPG-Cy5
200 um
(e)
Astrocytes
20 µm
2X
Lamp1
dPGS-CY5
Nuclei
Merge
Negative control
20 µm
Microglia
20 µm
2X
Lamp1
dPGS-CY5
Nuclei
Merge
(f)
Astrocytes
Microglia
Intracellular
dPGS-Cy5 fluo.
n.s.
(-) dPGS-Cy5
(+) dPGS-Cy5

Figure 4.1.

Figure 4.2. Modulating lipocalin-2 levels in human cerebral organoids and neural cells

Lipocalin-2 levels in human cerebral organoids. (a) Micrographs of lipocalin-2 (LCN2) detected by immunofluorescence in organoid cryosections following treatment with LPS (10 ng/mL) for 24 h. Astrocytes were labeled with GFAP and nuclei with Hoechst 33342. The negative control was prepared in the absence of primary antibodies to account for background fluorescence. Samples were imaged using a fluorescence microscope. (b) LCN2 levels in organoids treated with lipopolysaccharide (LPS) (10 ng/mL) with or without dPG (1 μM) and dPGS (1 μM) for 24 h and measured by Western blot, with beta-actin as loading control. Quantification shown are the average intracellular LCN2 levels ± SD in organoids based on immunofluorescence images shown in (a). A total of 27 samples were analyzed from three independent experiments. (c) Schematic representation of media conditioning from microglia used for cerebral organoid treatment. (d) Representative fluorescence micrographs of intracellular LCN2 levels in organoids treated with conditioned media from microglia (MCM) treated with LPS (10 ng/mL), dPGS (1 μM) for 24 h. Quantifications show the average and single-cell levels of LCN2 fluorescence in cryosections. A total of 1017 cells were analyzed from independent experiments. *** $p < 0.001$ (e) LCN2 levels from organoids treated as in (d) and measured by Western blot, with alpha-tubulin as loading control. Shown are the average LCN2 levels from two independent experiments. * $p < 0.05$ (f) Fluorescence micrographs of LCN2 abundance in primary human astrocytes treated as in (d) and measured using immunocytochemistry. Shown are the average intracellular LCN2 levels in astrocytes as fold increase of the untreated control. A total of 477 cells from two independent experiments were analyzed. *** $p < 0.001$.

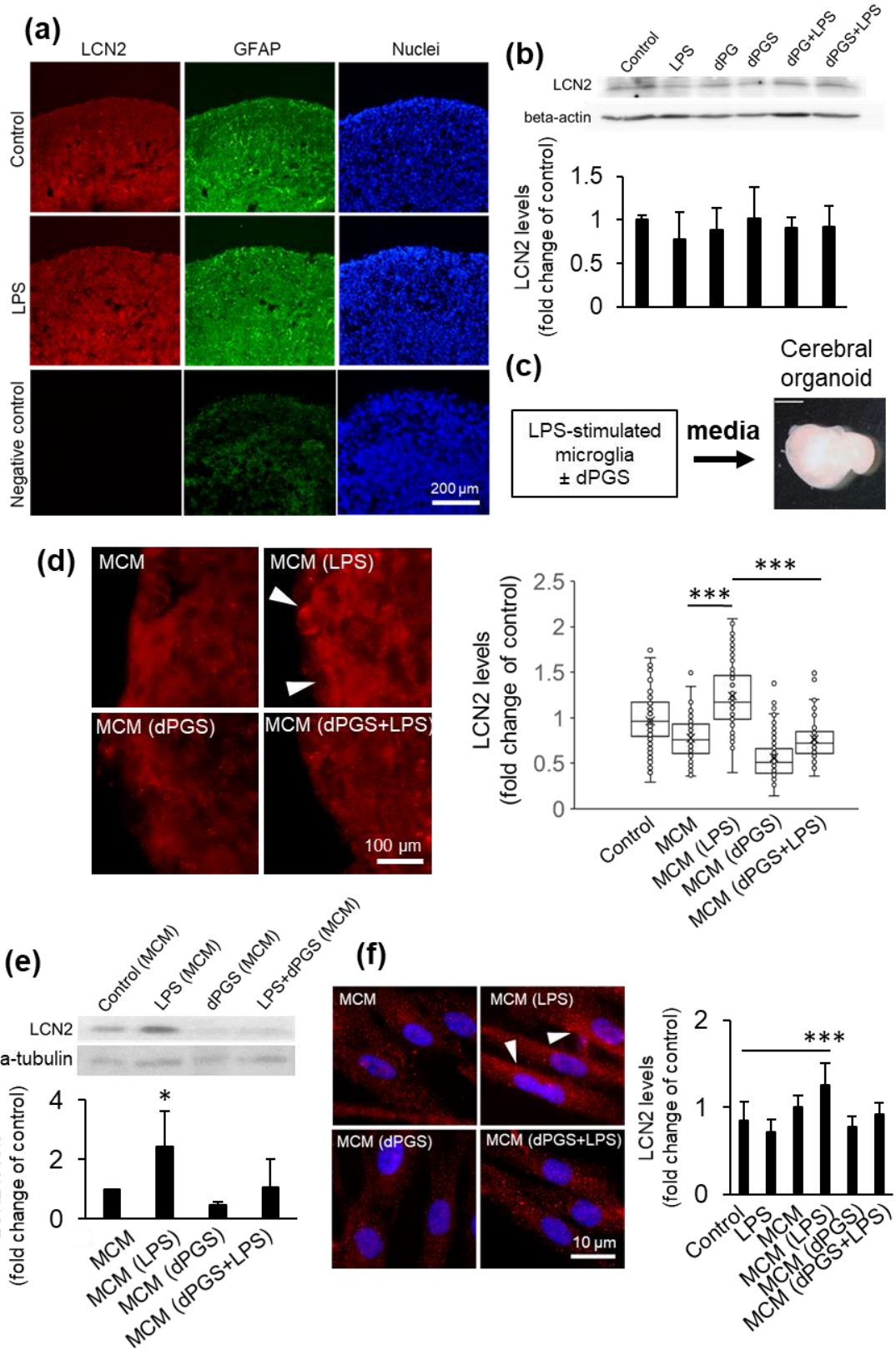
(a)
LCN2
GFAP
Nuclei
Control
LPS
Negative control
200 µm
(b)
Control
LPS
dPG
dPGS
dPG+LPS
dPGS+LPS
LCN2
beta-actin
LCN2 levels (fold change of control)
1.5
1
0.5
0
(c)
Cerebral organoid
LPS-stimulated microglia ± dPGS
media
(d)
MCM
MCM (LPS)
MCM (dPGS)
MCM (dPGS+LPS)
100 µm
LCN2 levels (fold change of control)
***
***
2.5
2
1.5
1
0.5
0
Control
MCM
MCM (LPS)
MCM (dPGS)
MCM (dPGS+LPS)
(e)
Control (MCM)
LPS (MCM)
dPGS (MCM)
LPS+dPGS (MCM)
LCN2
alpha-tubulin
LCN2 levels (fold change of control)
*
4
2
0
MCM
MCM (LPS)
MCM (dPGS)
MCM (dPGS+LPS)
(f)
MCM
MCM (LPS)
MCM (dPGS)
MCM (dPGS+LPS)
10 µm
LCN2 levels (fold change of control)
***
2
1
0
Control
LPS
MCM
MCM (LPS)
MCM (dPGS)
MCM (dPGS+LPS)

Figure 4.2.

Figure 4.3. Glioblastoma invasiveness in 3D co-cultures and the role of microglia

Glioblastoma (GBM) invasiveness in 3D co-cultures. (a) Collagen gels were seeded with human primary astrocytes and human HMC3 microglia in the presence or absence of a glioblastoma tumoroid. (b) Glioblastoma invasiveness in the presence or absence of microglia and astrocytes in 3D co-cultures after 6 days. Shown are the average distance of outgrowth from the tumoroid as a fold change of the tumoroid monoculture ± SEM. A total of 32 tumoroids were tested from at least three independent experiments. * $p < 0.05$ (c) Schematic representation of microglial conditioned media (MCM) used to treat collagen-embedded tumoroids. (d) Glioblastoma tumoroid outgrowth in the presence of conditioned media from microglia treated or not with dPGS (1 μM) after 6 days ± SEM. A total of 29 tumoroids were tested from at least four independent experiments. * $p < 0.05$ (e) Representative fluorescence micrographs showing intracellular LCN2 (red) in glioblastoma cells in the presence or absence of microglia cells in direct co-culture and dPGS (1 μM) for 24 h. LCN2 was fluorescently immunolabeled and cells were imaged using a fluorescence microscope. Quantifications show the average intracellular LCN2 levels ± SD per cell. At least 500 cells were analyzed from five independent experiments. *** $p < 0.001$; n.s. Non-significant. (f) Fluorescence micrographs of LCN2 (red) and GFAP (white) in human brain sections from non-cancerous brain or glioblastoma tumor tissues. LCN2 and GFAP were fluorescently labeled by immunohistochemistry and imaged using a fluorescence microscope. (g,h) Activation of transcription factors NFB and STAT3 in microglia in response to glioblastoma secreted factors. Human HMC3 microglia were treated with glioblastoma conditioned media (GCM) for 24 h, after which NFκB p65 and phosphorylated STAT3 Tyr705 were fluorescently immunolabeled (red) and cells were imaged using a fluorescence microscope. Shown are (g) the average nuclear NFκB p65

level per cell ± SEM (237 cells from three independent experiments) and (h) the average pSTAT3 Y705 level per cell SEM (317 cells from three independent experiments) *** $p < 0.001$. (i) Total NFκB p65 and STAT3 protein abundance in microglia treated as in (g,h). Protein levels were determined by measurements of immunopositive bands in Western blots. Alpha-tubulin was used as loading control. Shown are the average protein abundance of NFκB p65 and STAT3 from three independent experiments. n.s. Non-significant.

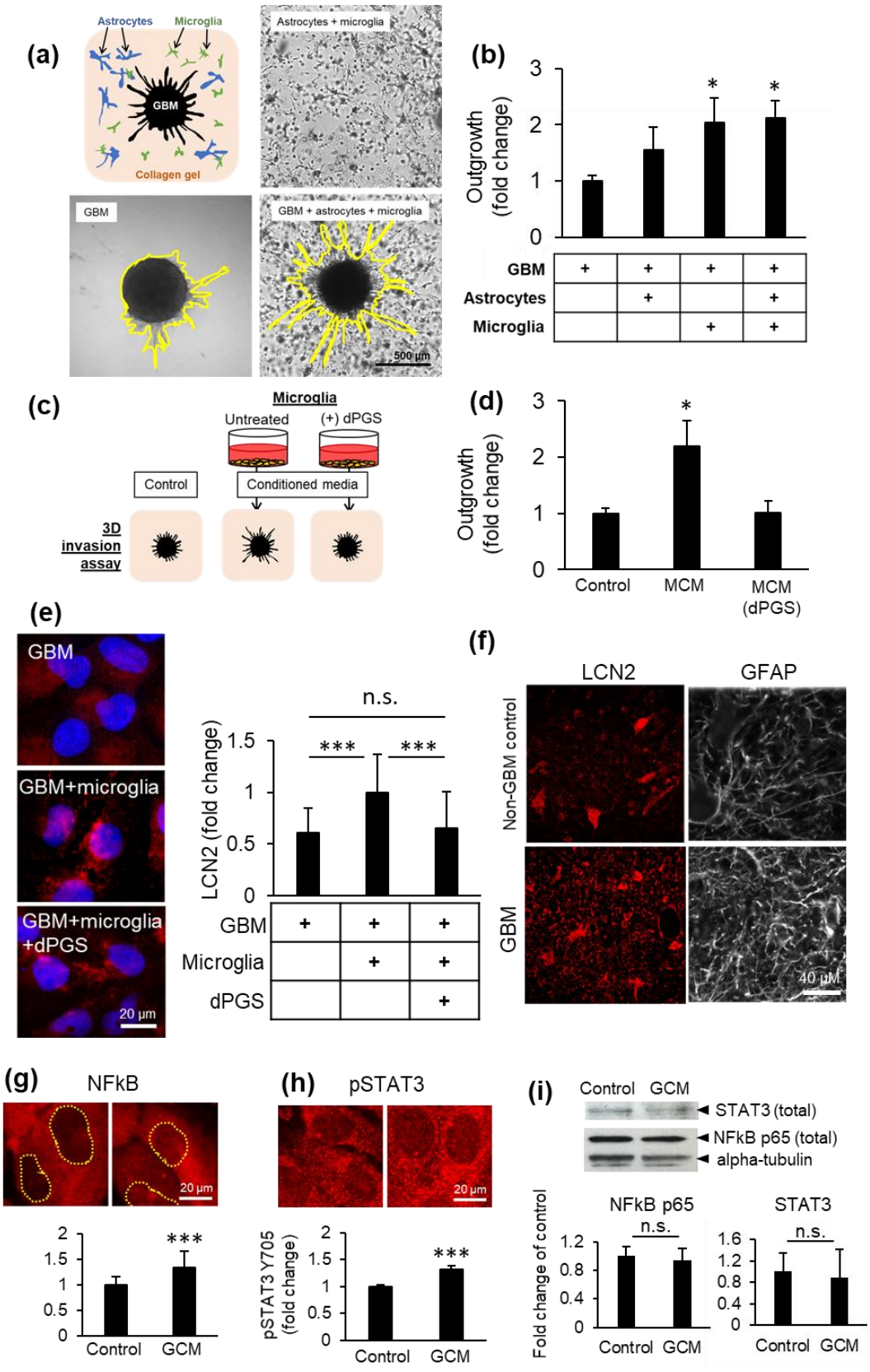
(a)
Astrocytes
Microglia
GBM
Collagen gel
Astrocytes + microglia
GBM
GBM + astrocytes + microglia
500 μm
(b)
Outgrowth (fold change)
GBM
Astrocytes
Microglia
(c)
Microglia
Untreated
(+) dPGS
Control
Conditioned media
3D invasion assay
(d)
Outgrowth (fold change)
Control
MCM
MCM (dPGS)
(e)
GBM
GBM+microglia
GBM+microglia +dPGS
20 μm
LCN2 (fold change)
n.s.
***
***
GBM
Microglia
dPGS
(f)
LCN2
GFAP
Non-GBM control
GBM
40 μM
(g)
NFkB
20 μm
***
Control
GCM
(h)
pSTAT3
20 μm
pSTAT3 Y705 (fold change)
***
Control
GCM
(i)
Control
GCM
STAT3 (total)
NFkB p65 (total)
alpha-tubulin
NFkB p65
STAT3
n.s.
n.s.
Fold change of control
Control
GCM
Control
GCM

Figure 4.3.

Figure 4.4. Schematic representation of the proposed modulatory effects of dPGS on microglia, astrocyte and glioblastoma crosstalk

(a) dPGS is internalized in cerebral organoids, and (b) downregulates LCN2 produced by microglia-induced astrocytes, thereby (c) reducing markers of inflammation (e.g., lipid droplets) and (d) glioblastoma invasiveness.

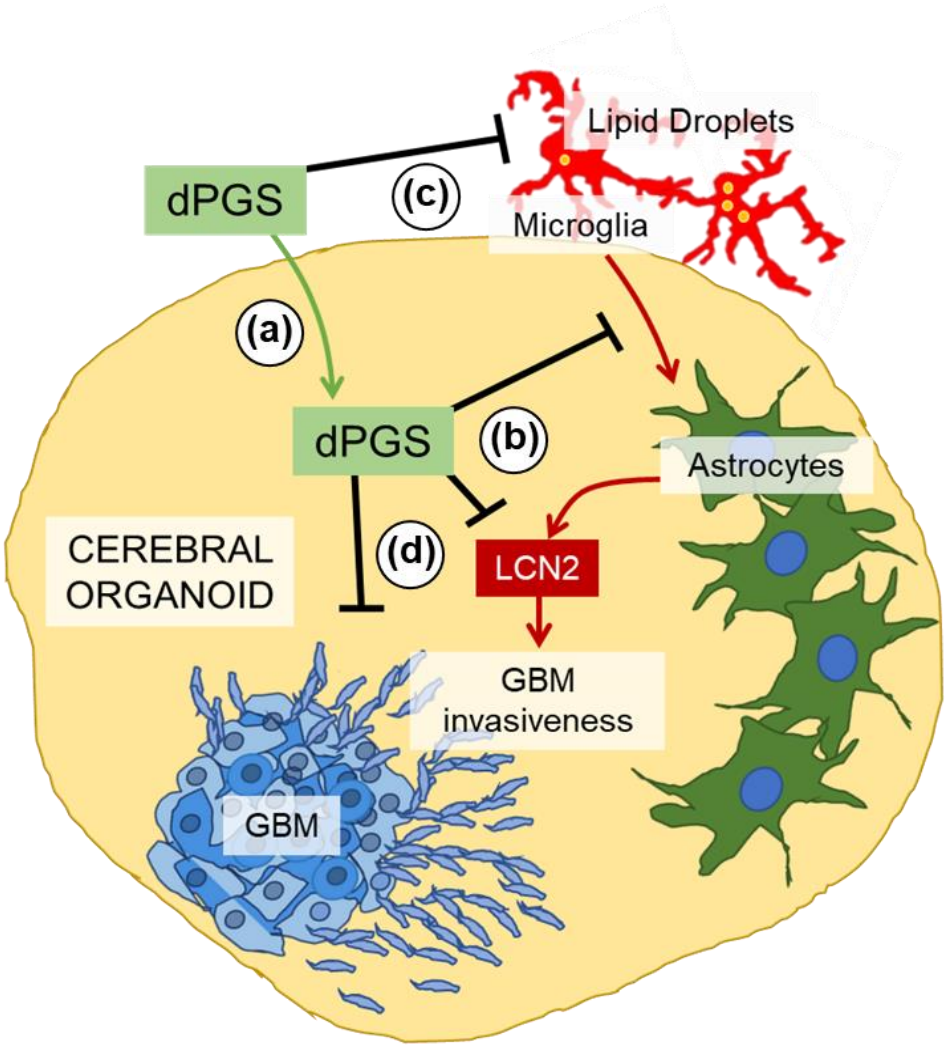
Lipid Droplets
dPGS
(c)
Microglia
(a)
dPGS
(b)
Astrocytes
CEREBRAL
ORGANOID
(d)
LCN2
GBM
invasiveness
GBM

Figure 4.4.

Supplementary Figure 4.1. Markers and development of cerebral organoids

(a) Expression of pluripotency markers in human iPSCs. Immunofluorescence images of NCRM1 cells labelled for the pluripotency markers SSEA-4, Oct3-4, Nanog and Tra-1-60 with nuclear staining (DAPI). Scale bar: 200 μm. (b) Timeline of cerebral organoid growth and development from iPSCs, over 100 days. (c,d) Stemness (SOX2, Nestin) and neural markers in cerebral organoids at day 60 and 100. Immunofluorescence staining for mature neurons expressing microtubule associated protein 2 (MAP2) and astrocytes expressing glial fibrillary acidic protein (GFAP). Staining of cell nuclei with Hoechst 33342. Scale bar: 200 μm (for higher magnification: scale bar: 25 μm).

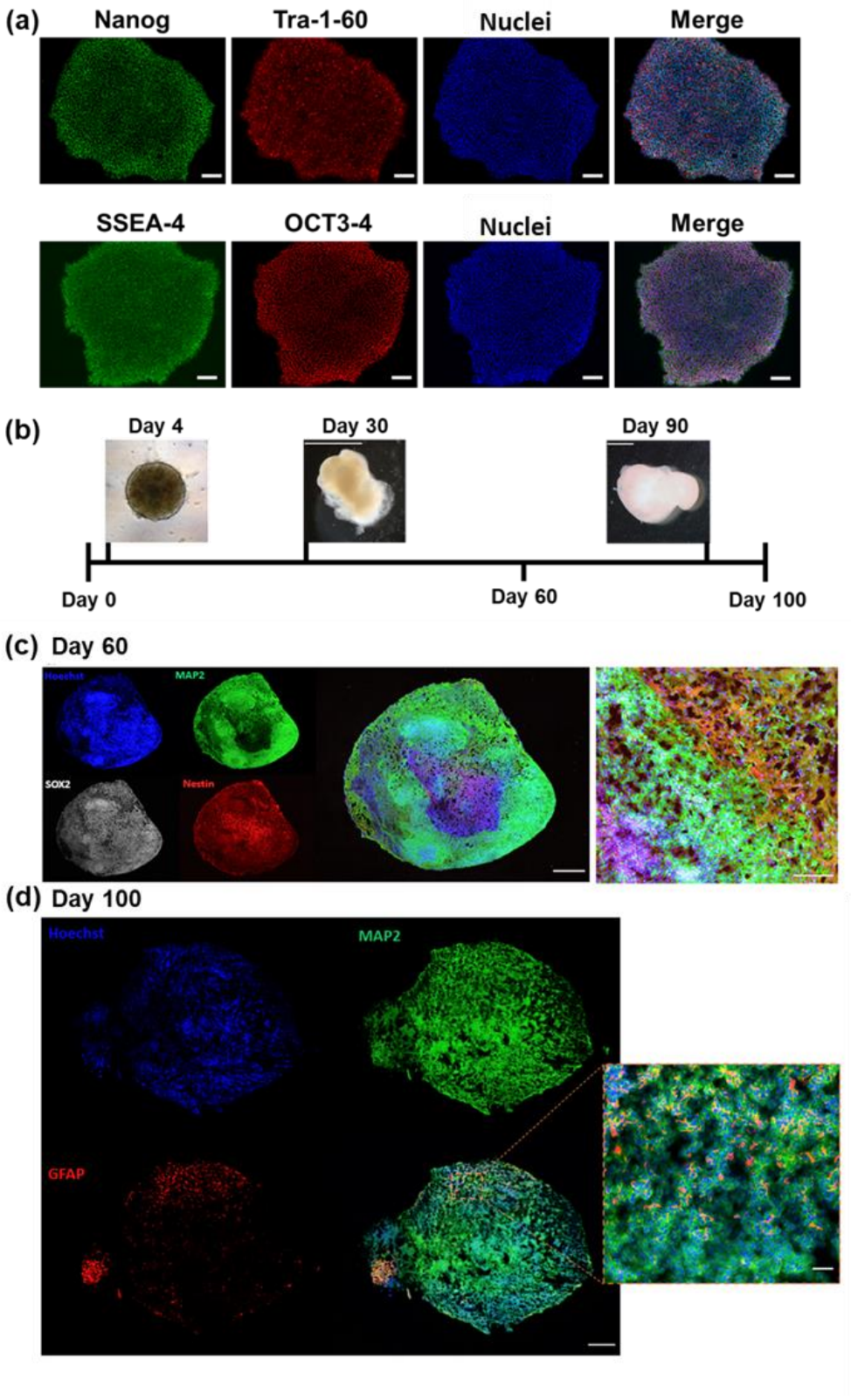
(a)
Nanog
Tra-1-60
Nuclei
Merge
SSEA-4
OCT3-4
Nuclei
Merge
(b)
Day 4
Day 30
Day 90
Day 0
Day 60
Day 100
(c) Day 60
Hoechst
MAP2
SOX2
Nestin
(d) Day 100
Hoechst
MAP2
GFAP

Figure S4.1.

Supplementary Figure 4.2. Mitochondrial activity in cerebral organoids exposed to nanostructures

(a) Mitochondrial metabolic activity in cerebral organoids following treatment with dPG and dPGS (1 μM, 72 h), using the MTT assay. Shown are the average percentage mitochondrial metabolic activity ±SD. (b) Mitochondrial metabolic activity in cerebral organoids following treatment with gold nanoclusters Au15SG and Au15PEG (1 μM, 72 h), using the MTT assay. Shown are the average percentage mitochondrial metabolic activity ± SD.

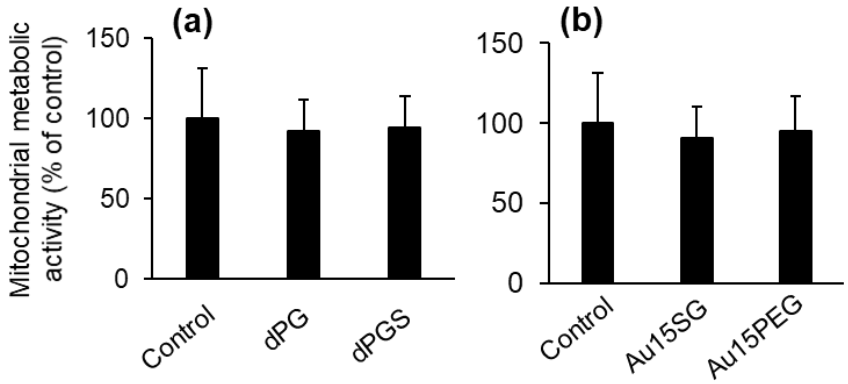
(a)
(b)
Mitochondrial metabolic activity (% of control)
150
100
50
0
Control
dPG
dPGS
Au15SG
Au15PEG

Figure S4.2.

Supplementary Figure 4.3. Lysosome and lipid droplet adaptation in microglia and GBM

(a) Increase in microglial perinuclear lysosomal marker Lamp1 in response to dPGS treatment. Human HMC3 microglia were treated with dPGS (1 μM) for 2 h or 24 h, then Lamp1 was fluorescently labeled by immunocytochemistry. Cells were imaged using a fluorescent microscope and perinuclear signal (within 5 μm of the nucleus) was measured in ImageJ. Shown are the average perinuclear Lamp1 signal per cell ±SEM. 356 cells were analyzed from two independent experiments. ***$p<0.001$ (b) Increase in microglial lipid droplet numbers in response to LPS and normalization of lipid droplet numbers with dPGS. Human HMC3 microglia were treated with LPS (10 ng/mL) with or without dPGS (1 μM) for 24 h, after which lipid droplets were fluorescently labeled with BODIPY 493/503 and imaged using a fluorescence microscope. The number of lipid droplets per cell was counted manually. Shown are the average number of lipid droplets per cell ±SEM. At least 250 cells from three independent experiments were analyzed. ***$p<0.001$ (c) Fluorescence micrographs of lipid droplets in human primary astrocytes and U251N glioblastoma (astrocytoma) cells. Lipid droplets were labelled as in (b) and imaged using a fluorescence microscope. (d) Shown are the average number of lipid droplets in human primary astrocytes and glioblastoma cells ±SD. 51 cells were analyzed from two independent experiments. ***$p<0.001$

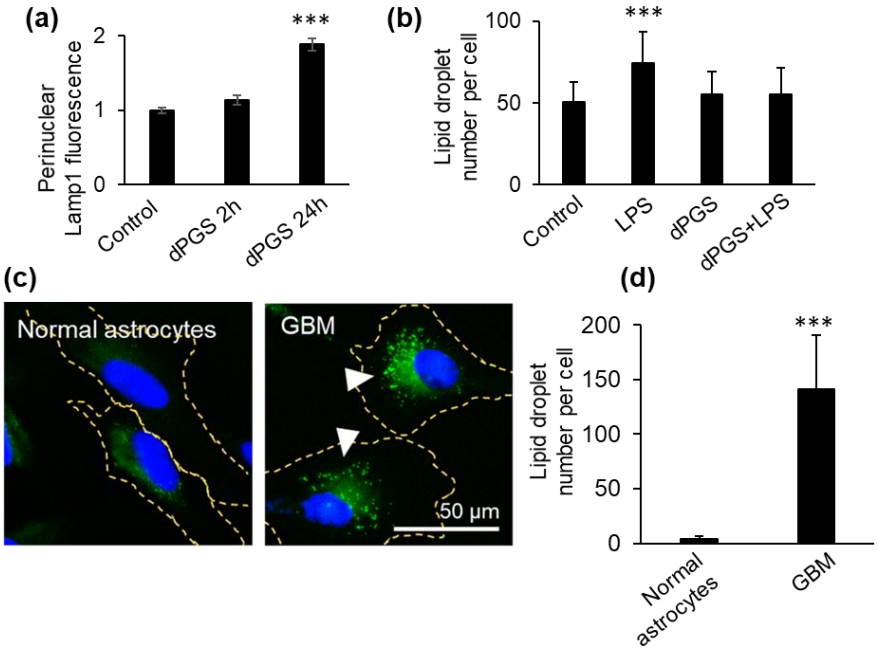
(a)
Perinuclear Lamp1 fluorescence
2
1
0
***
Control
dPGS 2h
dPGS 24h
(b)
Lipid droplet number per cell
100
50
0
***
Control
LPS
dPGS
dPGS+LPS
(c)
Normal astrocytes
GBM
50 μm
(d)
Lipid droplet number per cell
200
150
100
50
0
***
Normal astrocytes
GBM

Figure S4.3.

Supplementary Figure 4.4. Absence of microglia from cerebral organoids

Absence of microglia from the cerebral organoids, as shown by IBA1 labeling. Immunofluorescence staining for astrocytes with GFAP and microglia with IBA1. Staining of cell nuclei with Hoechst 33342.

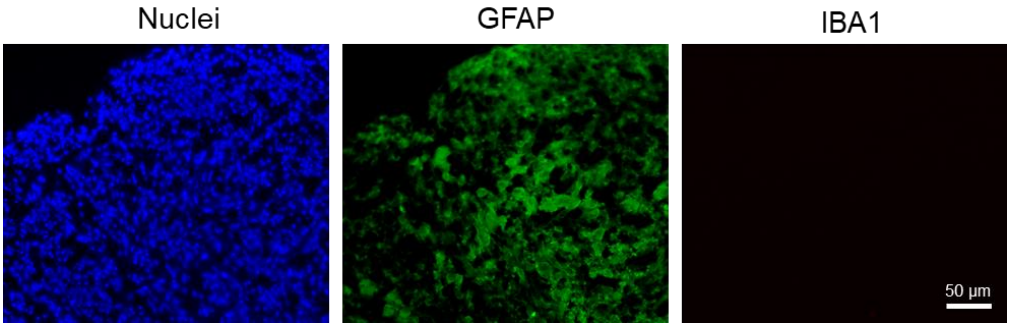

Figure S4.4.

Supplementary Figure 4.5. Glioblastoma invasiveness in cerebral organoids in the absence of microglia

Glioblastoma tumoroid has limited invasiveness in cerebral organoids in the absence of microglia cells. Fluorescently-labeled glioblastoma tumoroids were implanted in cerebral organoids and imaged after 6 days for infiltrative invasiveness using a fluorescence microscope.

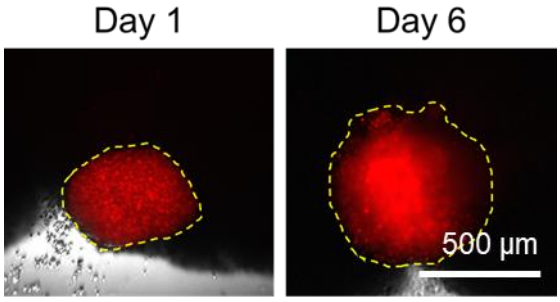

Figure S4.5.

Supplementary Figure 4.6. Movement of normal human astrocytes in 3D culture

Human astrocyte spheroids were implanted into collagen gels and cultured for 6 days. Spheroids were imaged using brightfield.

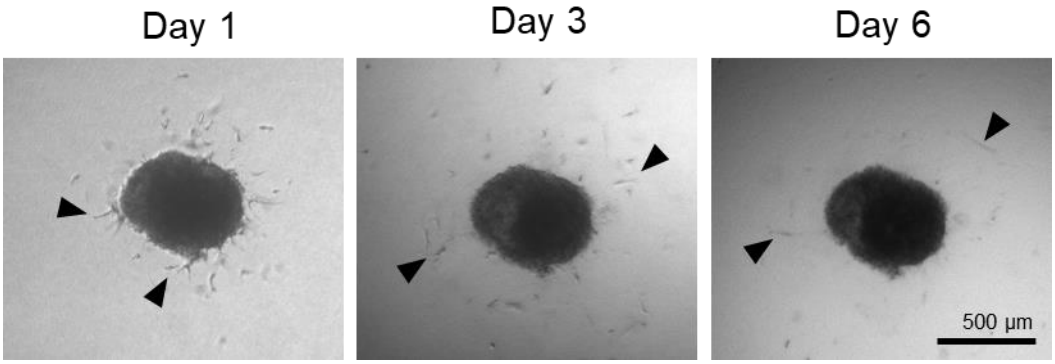

Figure S4.6.

Supplementary Figure 4.7. Internalization of fluorescent dPGS-Cy5 in glioblastoma tumoroids

Shown are representative fluorescence micrographs of glioblastoma tumoroids treated with dPGS-CY5 (red) or dPG-Cy5 for 24h at 1 μM. Nuclei were labeled with Hoechst 33342 (blue). Tumoroids were imaged using a fluorescence microscope.

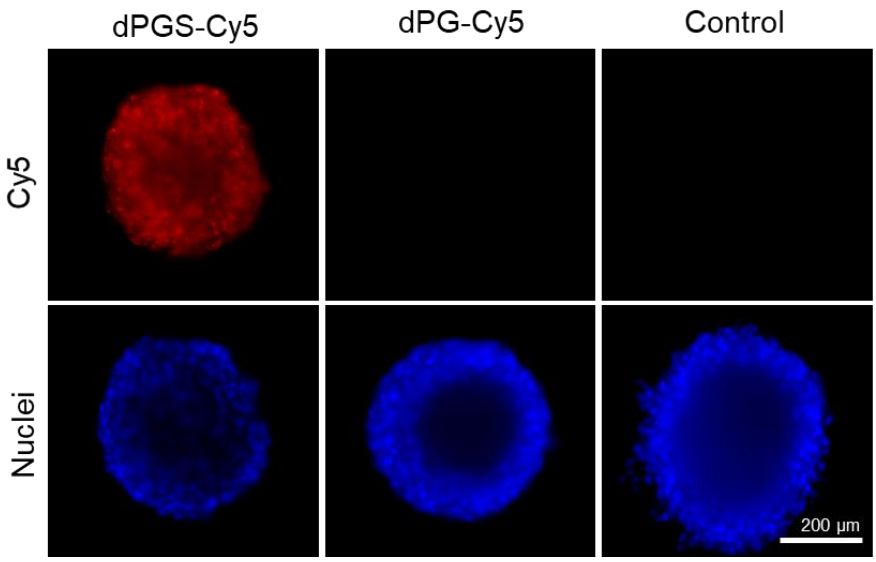

Figure S4.7.

Chapter 5. General Discussion

This manuscript-based thesis has two main goals. (1) To provide and interpret new data related to glioblastoma treatment with HDAC6 inhibitors starting from simple monolayer culture systems and leading to more complex 3D models such as tumoroids and cerebral organoids. These systems were used to test mono- and combination therapies as well as to show the role of several signal transduction mechanisms. (2) To show how cells in the glioblastoma microenvironment can be modulated to reduce the negative impact of neuroinflammation. In this context, the role of lipid droplets is highlighted and new therapeutic approaches based on nanomedicine are proposed.

Glioblastoma multiforme is a challenging disease for which current treatments are often ineffective due to different mechanisms of resistance (Erasimus et al., 2016a; S. Y. Lee, 2016a; Weller et al., 2013). These include the prevalence of upregulated DNA repair mechanisms in the nucleus, which result in resistance to the first-line treatment temozolomide, and warranted our interest in sahaquine, a new pharmacological agent targeting the cytoplasmic protein HDAC6. Particularly, the selectivity of sahaquine for HDAC6 was deemed to be an advantage due to the pre-clinically and clinically observed toxicity of non-selective HDAC inhibitors such as SAHA (Subramanian et al., 2010).

Other less understood mechanisms of resistance involve lipid droplets, cytosolic organelles that not only store lipids and serve as energy sources for GBM but can also entrap and prevent the pharmacological effect of lipophilic compounds such as curcumin. Beyond their role in GBM cells, lipid droplets also participate in the inflammatory processes that involve cells of the tumor microenvironment, particularly normal astrocytes and microglia (Barber & Raben, 2019; Marschallinger et al., 2020; Olzmann & Carvalho, 2019). These cells can significantly contribute to GBM progression, which is why nanostructures such as dendritic polyglycerol sulfates are so interesting as inflammatory modulators (Abels et al., 2019; Matias et al., 2018; Roesch et al., 2018).

5.1. Advantages and considerations of HDAC6 inhibition in GBM

5.1.1. Role of HDAC6 in signalling pathways

Previous reports have related increased levels of HDAC6 with worse prognosis in different types of cancers, including GBM (S. Li et al., 2015; T. Li et al., 2018; Yano et al., 2018; S.-L. Zhang et al., 2019). HDAC6 plays several roles in GBM, as well as normal cells. It regulates the acetylation of several client proteins, such as the cytoskeletal component α-tubulin and heat shock protein 90 (HSP90), among others. In turn, acetylation of these proteins regulates their function (e.g. α-tubulin stability, HSP90 binding to its client proteins). In cancer, high levels of HDAC6 was shown to be important for the hyperactivation of proliferative pathways involving kinases such as Akt and Erk1/2, and is linked to worse prognosis in patients. Upstream of these kinases is EGFR, perhaps the best characterized receptor in GBM whose amplification contributes to tumor growth and survival. Although several strategies and pharmaceutical agents (e.g. monoclonal antibodies, tyrosine kinase inhibitors) have been developed over the years to target EGFR and downregulate its signalling, little progress has been achieved in clinical trials (Ayati et al., 2020; Bhullar et al., 2018, p.). This is in part due to genetic variability in EGFR, which compromises the effectiveness of EGFR-binding agents, and in part due to the severity of side effects from broad spectrum agents such as tyrosine kinase inhibitors. In contrast, HDAC6 was not reported to be often mutated in GBM or other cancers, and thus has a lower risk of resistance to its inhibitors. We hypothesized that sahaquine could downregulate EGFR levels – as well as the activation of downstream kinases Akt and Erk1/2 – by its inhibition of HDAC6. Our results showed that selective HDAC6 inhibition with sahaquine significantly decreased EGFR levels in GBM cells, in monolayer cultures as well as three dimensional tumoroids (Chapter 4)(I. Zhang et al., 2018). This is likely due to the role of

HDAC6 in regulating microtubule trafficking, which impacts EGFR cell surface expression and subsequent degradation (W. Liu et al., 2012).

5.1.2. Role of HDAC6 in cancer invasiveness

Through its effect on α-tubulin and microtubule stability, HDAC6 also regulates cell motility (Boyault et al., 2007, p. 6). In the context of GBM, this implies that HDAC6 regulates the invasiveness of cancer cells into the surrounding brain tissues. GBM invasiveness is a main reason why surgery is ineffective, since tumor cells infiltrate the normal tissues extensively, preventing the possibility of full resection. Cancer cells left behind are then susceptible to initiate recurrent tumors, which are usually more resistant to treatment. Studies on compounds targeting microtubules have yielded several successful anti-cancer drugs (Dumontet & Jordan, 2010). Paclitaxel – the first of the taxane family to be used in anti-cancer therapy – stabilizes microtubules and prevents cell cycle progression past the G2/M phase. This not only prevents fast-growing cancer cells from proliferating, but also limits tumor invasiveness and metastasis. Paclitaxel has been widely used in clinics for several types of cancers (ovarian, breast, non-small cell lung cancer, etc.) since 1993, but also has a well-described toxicity profile (Camidge, 2001; Marupudi et al., 2007). Significant side effects include myelosuppression, neuropathy and hair loss, which are typical of agents affecting all rapidly dividing cells of the body (bone marrow, hair follicles). Clinical trials with the pan-HDAC inhibitor SAHA showed several grade 3 and 4 adverse effects, including thrombocytopenia, fatigue and dehydration (Subramanian et al., 2010).

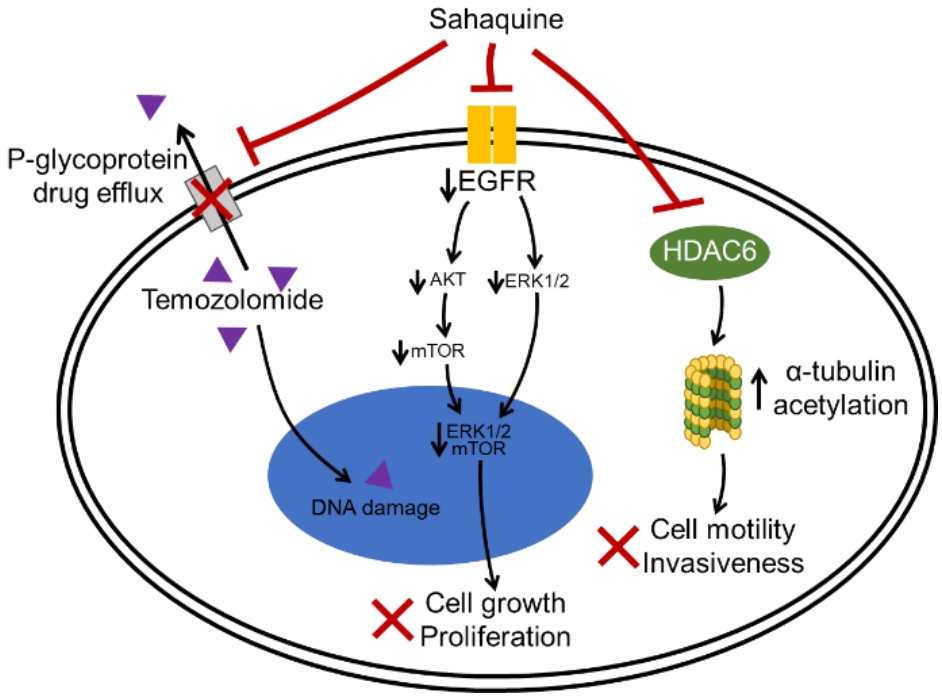

Figure 5.1. Proposed mechanisms of action of sahaquine in GBM

More worrying are reports of electrocardiogram changes, which warranted close monitoring of potential cardiac arrhythmias (Subramanian et al., 2010).

5.1.3. Side effects of HDAC6 inhibition

Although inhibition of HDAC6 results in the hyperacetylation α-tubulin, side effects observed in clinical trials with ACY-1215, a HDAC6-selective inhibitor, were very different from that of paclitaxel or SAHA. The drug was overall well tolerated, with grade 1 and 2 side effects (nausea, fatigue) in dose-finding studies. The most notable side effect at higher doses is thrombocytopenia, which is present with both HDAC6-selective and non-selective HDAC inhibitors (Subramanian et al., 2010) This was suggested to be caused by the role played by HDAC6 in the maturation of megakaryocytes. Interestingly, HDAC6 knock-out mice are viable, fertile and develop normally, although α-tubulin is globally hyperacetylated in their body. This suggests that although HDAC6 is found in all cells, inhibition of its activity is unlikely to results in severe side effects. In contrast, HDAC1 knock-out mice are embryonic lethal due to severe development defects stemming from impaired cell proliferation (Y. Zhang et al., 2008).

5.1.4. Properties of HDAC inhibitors for the brain

Both SAHA and ACY-1215 are available as oral drugs. ACY-1215 was the first in-class orally available HDAC6-selective inhibitor to be tested in clinical trials (Vogl et al., 2017). However, both drugs have been mostly studied for diseases outside of the central nervous system and there is limited data on blood brain barrier (BBB) permeability. Studies done in nude mice showed that SAHA crossed the BBB, as evidenced by increased levels of acetylated histone H3 and H4 in the

brain (Yin et al., 2007b). Mice studies with ACY-1215 showed that the compound had lower brain permeability compared to same-family molecules such as ACY-1083, although both compounds can exert significant effects in the brain (D. Wang et al., 2019; L. Zhang et al., 2014). Both molecules contain hydroxamic acid as the active HDAC-inhibiting moiety, yet other properties (e.g. lipophilicity, size) differ.

Different conformations in the L1 loops of HDAC6 and Class I HDACs can explain the selectivity of ACY-1215 and sahaquine. These two compounds have capping groups larger than that of pan-inhibitor SAHA, causing steric hindrance that prevents interaction with the active site of Class I HDACs. In particular, it is the L1 loop of Class I HDACs which constricts their active site in a manner that prevents HDAC6-selective compounds like ACY-1215 and sahaquine from reaching in (Porter, Osko, et al., 2018; Porter, Shen, et al., 2018).

Because the main mechanism of action of sahaquine is the same as that of ACY-1215, it likely has commonalities with this drug, including potential side effects in humans. However, sahaquine is different is some aspects. It is smaller (388.47 g/mol for sahaquine; 433.512 g/mol for ACY-1215) and its log*P* is very close to that of SAHA, which is brain permeable (0.92 for sahaquine; 1.0 for SAHA). Importantly, recent reports have shown that ACY-1215 was susceptible to an acquired mechanism of drug resistance mediated by human ATP-binding cassette transporters ABCB1 and ABCG2 (Wu et al., 2018), which are enriched at the BBB. These transporters are thought to be responsible for the lower effectiveness of several drugs – including tyrosine kinase inhibitors such as ibrutinib – *in vivo* compared to their predicted effect based on *in vitro* studies (Amengual et al., 2017; van Hoppe et al., 2018).

On the other hand, primaquine – and primaquine-containing compounds like sahaquine – can inhibit efflux pumps responsible for multidrug resistance (Wu et al., 2008), and thus are

attractive to overcome one of the most common issues related to cancer drugs. As a hybrid molecule, sahaquine not only merges two different drugs into one, but the effects of one drug positively impacts the effect of the other: primaquine provides the bulkiness necessary for the capping group to cause steric hindrance with the active site of Class I HDACs, thereby giving sahaquine HDAC6 selectivity, and inhibits efflux pumps that might otherwise result in poor BBB permeability or drug resistance.

Another common issue related to cancer chemotherapy is peripheral neuropathy, a serious adverse effect observed with drugs such as paclitaxel, cisplatin and pan-HDAC inhibitors like SAHA (Starobova & Vetter, 2017; Subramanian et al., 2010). In contrast, HDAC6-selective inhibitors were found to reverse neuropathy by improving mitochondrial and axonal transport through tubulin stabilization. The positive results in mice led to clinical trials for ACY-1215 to benefit patients with diabetic neuropathy (D. Wang et al., 2019). In the future, such studies are planned for neuropathies secondary to chemotherapy and Charcot–Marie–Tooth disease, supporting the use of HDAC6 inhibitors for combination therapy in cancer and other diseases (Shukla & Tekwani, 2020). One example is Alzheimer's disease, where ACY-1215 was found to improve autophagic clearance of amyloid-β and hyperphosphorylated tau in mouse brains (L. Zhang et al., 2014) through the modulation of intracellular transport along microtubules and organellar function.

5.2. Role and inhibition of lipid droplets in GBM

5.2.1. Lipid droplets in astrocytes and GBM

GBM cells easily adapt to stressful stimuli (Colwell et al., 2017; Shen et al., 2019). In response to hypoxia in the GBM microenvironment, the cancer cells stimulate angiogenesis to increase oxygen supply to the tumor core. To support its growth, GBM obtains energy from different sources, including lipids. In contrast with normal astrocytes, which have few, very small lipid droplets, GBM typically have numerous LDs that can serve several purposes (Geng & Guo, 2017; Taïb et al., 2019; I. Zhang et al., 2016).

LDs are primarily storage sites for lipids, but participate extensively in cellular processes such as signal transduction, membrane synthesis, etc. LDs can form to store fatty acids internalized by the cell or from *de novo* fatty acid synthesis (Olzmann & Carvalho, 2019). In turn, LDs provide fatty acids for functions such as β-oxidation in mitochondria, membrane repair, prostaglandin synthesis, etc. For a long time, the role of β-oxidation in the brain was unclear, as glucose was well described as the main source of energy for neural cells. GBM was also described as reliant on glucose, which is why the ketogenic diet was proposed to deprive tumors from their preferred source of energy (Schwartz et al., 2018; van der Louw et al., 2019). However, several issues arose. Firstly, some patients would not tolerate well the drastic changes imposed by a ketogenic diet. Secondly, GBM is not solely dependent on glucose and can use fatty acids as an energy source (Kant et al., 2020; Strickland & Stoll, 2017). In fact, brain tumors are often iso-metabolic compared to normal gray matter when detected by positron emission tomography with 2-deoxy-2-[fluorine-18]fluoro- D-glucose, rendering the method ineffective in differentiating cancer tissue from the normal brain (Y. Yang et al., 2019). Lastly and most importantly, several factors upregulated in GBM actually promote fatty acid synthesis and usage, particularly under the hypoxic and low pH

conditions of the tumor core. One example is EGFR, which is upregulated in more than 40% of GBM tumors, promotes the activation of sterol regulatory element-binding transcription factor 1c (SREBP-1c), a master regulator of lipogenesis (Sperry et al., 2019). Some of the fatty acid synthesis rate-limiting enzymes upregulated by transcription factors in the SREBP family are fatty acid synthetase and acetyl-CoA carboxylases, among others.

5.2.2. Lipid droplet functions in GBM

Besides serving as energy sources, LDs can also prevent oxidative damage and lipotoxicity by serving as buffer systems (Olzmann & Carvalho, 2019; Taïb et al., 2019). They prevent peroxidation reactions that might otherwise damage cellular membranes; store excess lipids to avoid cytosolic overload, provide repair material for membranes damaged by oxidative stress, etc. LD homeostasis is different dependent on the cell type, and neither too few nor too many is beneficial in the long term. If LDs are overloaded in cells other than adipose cells, there is a risk of leakage and lipotoxicity. On the other hand, too few LDs in cells that normally require them may result in energy shortage and starvation. In GBM, LDs serve as energy source as well as defence against oxidative stress resulting from their high metabolic activity. Under hypoxic conditions, hypoxia inducible factors HIF-1α and HIF-2α upregulate glucose and glutamine import, along with SREBP activation. These mechanisms of adaptation result in increased lipid droplets under hypoxic conditions (Koizume & Miyagi, 2016).

Another function of LDs in GBM explored in Chapter 3 is their role in trapping lipophilic agents such as curcumin, modifying their pharmacokinetic and pharmacodynamic profiles (i.e. effectiveness, duration, metabolism, etc.). This trapping can be observed at the systemic level for

lipophilic drugs that significantly partition into adipose tissues. This is particularly important for the drug-dosing of lipophilic anesthetics (e.g. diazepam), while that of agents with low lipophilicity (e.g. sevoflurane, desflurane) is less impacted (Casati & Putzu, 2005). Furthermore, compounds accumulating in LDs are susceptible to be further processed by several lipases and other enzymes associated with these organelles, thus affecting drug metabolism. For example, lasonolide A, a lipophilic macrolide with anti-cancer properties, is cleaved by lipid droplet-associated hydrolase into a toxic metabolite that can significantly increase adverse effects (Dubey et al., 2020).

5.2.3. Inhibiting lipid droplet formation in GBM

Our results demonstrated that inhibiting of LDs increases the cell killing effect of curcumin in GBM. Pyrrolidine-2, an inhibitor of cytoplasmic phospholipase A2, was a potent pharmacological tool to demonstrate the importance of LDs in supporting GBM function (Ono et al., 2002b). Although effective *in vitro*, pyrrolidine-2 has not progressed into clinical trials so far; it was shown to have off-target effects, namely the blocking of calcium release from the ER and of calcium increases in mitochondria (Yun et al., 2016). Furthermore, cPLA2 is necessary for lipid release from normal astrocytes, which mediates signalling between neural cells (F. Wang et al., 2020, p.). Due to the important role of cPLA2 in normal cells, its adverse effects are likely to be significant in humans. Interestingly, long-term treatment with curcumin itself was found to improve triglyceride and cholesterol levels in humans, and was used to promote glycemic control in patients with diabetes, the metabolic syndrome and related conditions (Tabrizi et al., 2018). In hepatocytes, curcumin was shown to regulate endoplasmic reticulum stress, thereby lowering stress-induced LD formation (H.-Y. Lee et al., 2017).

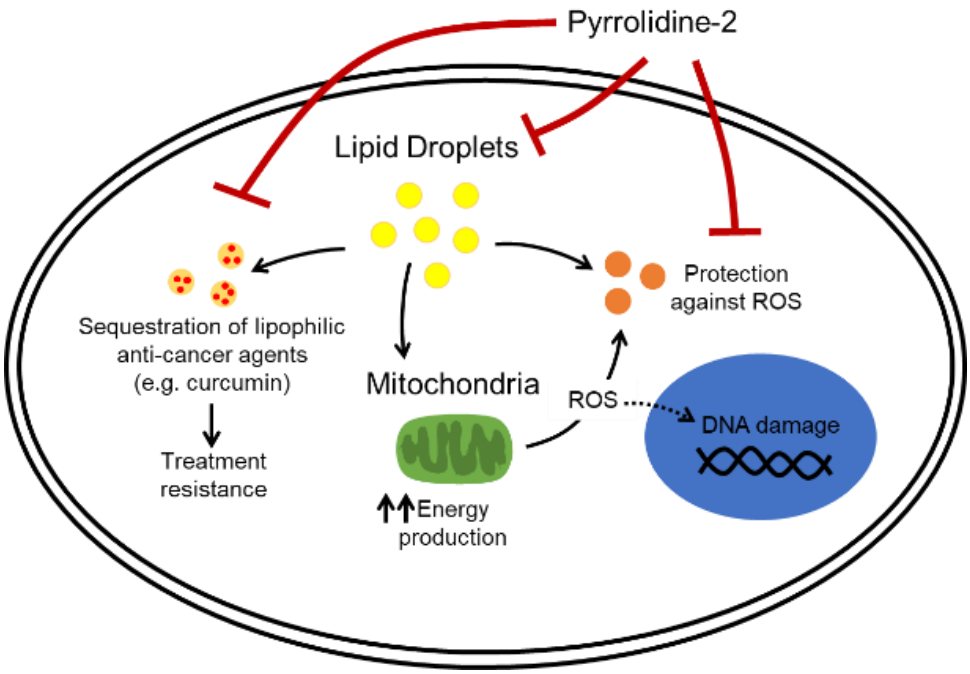

Figure 5.2. Roles of lipid droplets in GBM

However, many phytochemicals that reached clinical trials have shown limited effectiveness, often due to low bioavailability and stability *in vivo*. Although curcumin is well tolerated even at high doses (12 g/day), it is poorly water-soluble and was barely detected in the serum at doses below 4-8g/day (Lao et al., 2006). Even compounds like genistein that comply to Lipinski's 'rule of five' do not necessarily have good absorptive properties; they are susceptible to other factors such as metabolism (gastric pH, first-pass effect, gut microbiome, etc.) and rate of absorption in the intestines (Aqil et al., 2013).

5.3. Nanostructures as pharmacological modulators of the brain

5.3.1. Nanodelivery systems for natural compounds and lipophilic drugs

Despite the detrimental effect of lipid droplets in reducing the effectiveness of curcumin, the concept of "entrapping" lipophilic compounds is not necessarily always disadvantageous and has been exploited for the delivery of therapeutic agents that would otherwise lack the bioavailability or stability to be effective *in vivo*. For instance, these compounds can be loaded inside nanostructured carriers with a hydrophobic interior and a hydrophilic exterior, which protects the agent and improves solubility. In turn, this lengthens the half-life of the compound while retaining its biological effect.

Numerous types of nanocarriers have been explored over the years. Micellar structures made of block copolymers simulate endogenous micelles (e.g. lipoproteins) and are readily internalized by cells along with their cargo (Savić et al., 2006). Telodendrimeric self-assembly systems made of amphiphilic polymers preserve the biological activity of curcumin, reducing neurite loss in a model of cisplatin-mediated neuropathy (Moquin et al., 2019). Release of the drug

is determined by the stability of the nanostructures, which depends on the critical aggregation concentration (CAC) of the nanomaterial. When the nanostructures reach cells and their concentration becomes lower than that of the CAC, the nanocarrier unravels and releases the cargo.

5.3.2. Nanostructures for the brain

Although numerous types of nanostructures have been studied in animal models, their effects *in vivo* greatly differ depending on their size, shape and surface properties (Sitharaman, 2016). Despite these differences, most nanostructures tend to accumulate in well vascularized organs (e.g. liver and kidneys), then are cleared over time. The BBB remains the greatest challenge for drug delivery to the brain, as tight junctions restrict passage for most blood-borne substances (Villabona-Rueda et al., 2019).

However, the BBB undergoes important changes under pathological conditions (e.g. GBM, inflammation)(Arvanitis et al., 2020; Shigemoto-Mogami et al., 2018). Tight junctions are disrupted from the pressure of the growing tumor and from the activation and recruitment of immune cells at the tumor site. These disruptions make the BBB more permeable, allowing for nanostructures and drugs to enter the brain. Furthermore, tumor neovasculature is more "leaky" than established vessels, allowing for nanostructures to seep out and accumulate at the tumor site – an effect termed enhanced permeability and retention (Fang et al., 2011; Greish, 2010).

Nanoconstructs can also be designed to bind tumor cells, for instance with delivery systems specifically targeting EGFRvIII, a constitutively active EGFR variant commonly found in GBM. They can also be recruited by interacting with factors upregulated at the tumor site. The microenvironment of GBM is infiltrated with resident and peripheral immune cells, predominantly

microglia and macrophages. These cells are activated by factors released from the tumor and express high levels of selectins (L/P) on their surface (Siew & Chern, 2018). Dendritic polyglycerol sulfates (dPGS) are polymeric nanostructures that are particularly interesting in this context. dPGS can cross the BBB and binds to selectins on the surface of activated immune cells (Barthel et al., 2007). Furthermore, it was shown that these selectins are enriched on GBM cells and the tumor endothelium, thus making dPGS interesting targeted nanostructures (Ferber et al., 2017).

5.3.3. dPGS as modulators of inflammation

Dendritic polyglycerol sulfates were originally synthesized from the sulfation of dendritic polyglycerols (dPG)(Sandler & Berg, 1966) to serve as synthetic alternatives to heparin. Heparin is still commonly used as an anti-coagulant, but the need to isolate it from animal sources means higher risks of contamination from pathogens. Although similar in structure to heparin, dPGS showed significantly lower anti-coagulant properties and its hydroxylated analog dPG had none (Türk et al., 2004). dPGS binds to P-selectin on leukocytes with high affinity; this data and experimental work in immune cells suggested dPGS as anti-inflammatory nanostructures (Dernedde et al., 2010; Rades et al., 2018; Türk et al., 2004).

The evidence the anti-inflammatory properties of dPGS was provided in several studies by our group in mice, using dissociated primary neural cells as well as organotypic slice cultures. dPGS blunted the upregulation in cytokines and alarmins (e.g. IL-6, TNF-α, lipocalin-2) in response to LPS and amyloid-β, thus reducing impairments in morphological plasticity in hippocampal excitatory neurons, and reducing the loss of dendritic spines in the hippocampus

(Maysinger et al., 2015; Maysinger, Ji, et al., 2018; Maysinger, Lalancette-Hébert, et al., 2019). Studies described in Chapter 4 capitalize on these findings and expand the investigations of dPGS in human neural cells, both in the simple dissociated human glial cells and in human cerebral organoids (I. Zhang et al., 2020). Although human and mouse neural cells share a number of common features, they also have considerable differences. For instance, the mouse and human brains are similar in structure, but great differences exist in the way pathways and genes are activated (Breschi et al., 2017; Hodge et al., 2019; Kalmbach et al., 2018). Expression in glial cells diverge significantly, with more than 3 500 genes showing at least a ten-fold difference between the two species (Hodge et al., 2019). This is particularly important for microglia, as subtypes with distinct transcriptional profiles can emerge depending on the pathology (Masuda et al., 2019) and astrocytes depend on microglia to shape their own response (Bellver-Landete et al., 2019; Maysinger, Lalancette-Hébert, et al., 2019; Nichols et al., 2019; Tremblay et al., 2016).

5.3.4. Cerebral organoids as 3D brain models

The development of human cerebral organoids was of great significance for the study of the brain, as it allowed to examine crosstalk between neural cells in 3D (Eiraku & Sasai, 2012; Lancaster & Knoblich, 2014). There are several advantages to cerebral organoids compared to dispersed neural cells from human donors. Apart from practical or technical perks such as availability and reproducibility, organoids are also attractive for modelling complex disorders (e.g. microencephaly, Alzheimer's, autism etc.)(Lancaster et al., 2013; Mariani et al., 2015; Nascimento et al., 2019; Raja et al., 2016) and for avoiding phenotypic changes associated with culture in monolayers. Nevertheless, studies employing human cerebral organoids to test nanostructures such

as dPGS remain rare despite the fast growing field of nanomedicine and few reviews cover the subject (Abdel Fattah & Ranga, 2020; Q. Zhang et al., 2019).

A limitation to most models of cerebral organoids is the lack of vasculature. Endothelial cells forming the blood brain barrier regulate brain entry for immune cells and therapeutic agents (Daneman & Prat, 2015; Sweeney et al., 2019). The extent to which these elements can enter the brain depends on changes in the blood brain barrier in pathological conditions. Systemic inflammation can cause transient or permanent loss of integrity in the tight junctions, damage to endothelial cells and breakdown of the glia limitans (Varatharaj & Galea, 2017). Furthermore, endothelial cells themselves can exacerbate injury by increasing vascular permeability, leading to edema and excessive inflammation (Daneman & Prat, 2015; Varatharaj & Galea, 2017). The inhibition of P-selectin on endothelial cells has been proposed to reduce brain injury, and dPGS is an interesting candidate given its P-selectin binding properties (Ferber et al., 2017; Ishikawa et al., 2004; Ruehl et al., 2002). Because peripheral immune cells bind P-selectin prior to extravasation, dPGS could also reduce migration of peripheral macrophages through the blood brain barrier toward inflamed or tumor tissues (Mayadas et al., 1993). In GBM, pressure from the growing tumor can physically disrupt the blood brain barrier and vasculature at the tumor site tends to be leakier than elsewhere (Arvanitis et al., 2020). This led to the assumption that pharmacological agents and nanotherapeutical constructs can accumulate homogeneously at the tumor site of all GBM patients, which is not the case. There is a significant proportion of GBM patients with parts or most of the blood brain barrier intact, especially in the early stages of the pathology (Sarkaria et al., 2018). Thus, organoids which can include or model the blood brain barrier are advantageous (Bergmann et al., 2018; Cakir et al., 2019).

Another important limitation to most cerebral organoids is the absence of microglia. Microglia originate from erythro-myeloid progenitors in the yolk sac then migrate to the brain, and therefore are not differentiated from the neuroectoderm along with other neural cells (Alliot et al., 1999; Menassa & Gomez-Nicola, 2018). Although this absence prevents the study of immune and neural cell interactions in the brain, it can be useful for experiments requiring microglial depletion. In primary mixed neural cultures, depletion is usually achieved by mechanical, genetic or pharmacologic manipulations, but there is often a small percentage (<5%) of microglia that could still make astrocytes significantly reactive. In experiments where microglia are required, efforts were made to develop cerebral organoids containing microglia, either by differentiating them along with neural cells or by subsequent addition (Ormel et al., 2018; Song et al., 2019). However, these models came with their own limitations, the most important being high variability in the distribution and number of microglia within and across individual organoids (Ormel et al., 2018; Song et al., 2019). As the immune surveyors and phagocytes of the brain, microglia are the most capable brain cells to internalize nanostructures compared to astrocytes and neurons. Nanomedicines are thus particularly attractive as modulators of microglia plasticity and activity (D. M. and J. Ji, 2019; Maysinger & Zhang, 2016; Rodell et al., 2018).

5.3.5. Role and modulation of the tumor microenvironment

The tumor microenvironment has received considerable attention in recent years. Its importance was shown in different types of cancer and several features remained consistent: alternations to the tumor stroma in terms of 1) signalling molecules (e.g. cytokines, alarmins) and 2) cell types (e.g. endothelial cells, immune cells)(Brandao et al., 2019; Quail & Joyce, 2017; Roesch et al., 2018). Although the specifics of these alterations can differ, their contribution to disease

progression are such that immune checkpoints inhibitors (e.g. monoclonal antibodies against PD-L1) are now considered landmark interventions (Chamoto et al., 2020).

The brain, however, has long been considered an immune privileged organ and does not follow the same regulations as peripheral organs. As opposed to "hot" tumors (e.g. kidney cancer, melanoma), GBM has very low T-cell infiltration and is an unlikely candidate for checkpoint inhibitors targeting effector T-cells (Duan et al., 2020). Although T-cell infiltration into "cold" tumors can be stimulated using vaccines (Bonaventura et al., 2019; Hilf et al., 2019; Keskin et al., 2019), the effectiveness *in situ* is compromised by the tumor microenvironment itself. The GBM microenvironment is rich in transforming growth factor beta (TGF-β) and interleukin-10 (IL-10), which would largely suppress the anti-cancer activity of cytotoxic T-cells (Ye et al., 2007).

GBM tumors are massively infiltrated by microglia and peripheral macrophages (Hambardzumyan et al., 2016), which are collectively termed tumor-associated macrophages (TAMs)(Pathria et al., 2019; Roesch et al., 2018; Zhou et al., 2020). These cells are the source of most cytokines upregulated in the tumor microenvironment and are receptive to immunomodulatory agents. For instance, the antibiotic minocycline reduced microglial-secreted factors and tumor growth (Markovic et al., 2011), whereas the antifungal amphotericin B enhanced microglial activation and subsequent cancer killing (Sarkar & Yong, 2014). These two seemingly opposing approaches share the same goal: to shift the polarization of TAMs away from tumor-supportive functions.

Apart from promoting GBM proliferation, invasiveness and angiogenesis, TAMs-secreted factors (e.g. TGF-β, IL-6 and IL-10) also maintain stemness in brain tumor stem cells through the activation of STAT3 (Almiron Bonnin et al., 2018; Galoczova et al., 2018, p. 3). Brain tumor stem cells are central to tumor recurrence due to their resistance to conventional radiotherapy and

chemotherapy. Their self-renewal properties are dependant on STAT3 and can be abolished using STAT3 inhibitors (Han et al., 2019). The ideal path to achieving STAT3 inhibition remains a matter of debate, given the essential roles played by this transcription factor throughout the body. STAT3 has no enzymatic pocket to target, and upstream kinases (JAK1/2) are too promiscuous to inhibit without significant side effects (Yue & Turkson, 2009). Many approaches have been tested for direct STAT3 inhibition (e.g. peptides, small molecules, siRNA), yielding so far no outstanding candidates in clinical trials (Gelain et al., 2019; Yue & Turkson, 2009). STAT3 is rarely mutated in cancer, being instead hyperactively driven by the tumor microenvironment (Dasgupta et al., 2015). As such, it would be susceptible to indirect inhibitors (e.g. dPGS) acting at the source of its activation, i.e. by downregulating TAMs-secreted factors (Huynh et al., 2019).

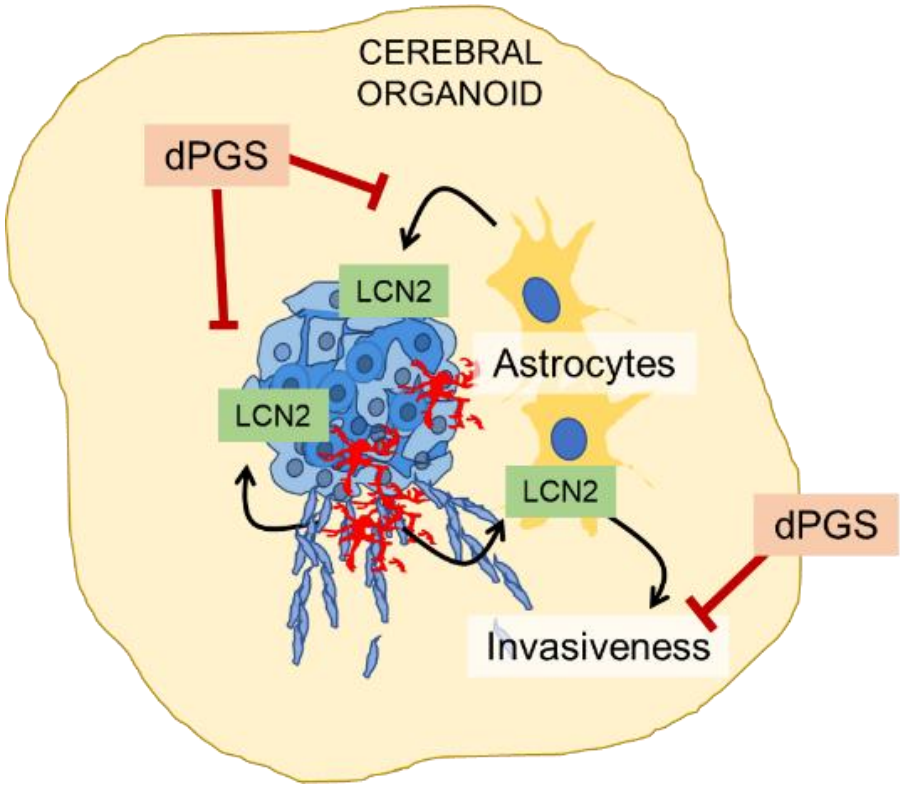

Figure 5.3. Mechanisms of action of dPGS on the GBM microenvironment

5.3.6. Nanotherapeutic and pharmacological modulators of the glioblastoma microenvironment

Due to the complexity of GBM, monotherapies are likely to fail. It is essential to consider the tumor microenvironment in pre-clinical research to avoid oversimplifying the disease and overestimating treatment effectiveness. The main objectives are to 1) kill GBM cells, 2) kill or differentiate brain tumor stem cells, 3) limit tumor invasiveness and 4) interrupt tumor-supporting functions in cells of the tumor stroma. Achieving objective #4 would greatly contribute to progress toward the other three objectives, which is why immunomodulatory agents such as dPGS are of interest.

dPGS does not directly kill cancer cells but could significantly enhance GBM killing in combination with anti-cancer drugs with low cancer resistance potential (e.g. sahaquine). Due to their effects on different elements of the GBM microenvironment, synergistic effects between dPGS and sahaquine would only be apparent in complex 3D models, which are still under-represented in screening experiments for combination therapies. Our studies have revealed synergistic effects between sahaquine and temozolomide, as the combination index (CI) was < 1 (I. Zhang et al., 2018). CI is a useful quantifier which clearly shows the biological outcome when two therapeutics are combined: if $CI = 1$, there is an additive effect, if $CI < 1$, there is synergism, and if $CI > 1$, antagonism (Chou, 2018). Combination treatment focusing on different aspects of the disease is important given the heterogeneity of GBM. Apart from intratumoral heterogeneity, there is also differences between patients (e.g. sex, age, health) that can significantly impact treatment response. Women tend to respond better than men, and younger patients, better than older ones (Ostrom et al., 2018; Trifiletti et al., 2017; W. Yang et al., 2019). Medical history can also matter: the chronic use of certain drugs, such as statins, is associated with lower GBM risk

and better prognostic (B. K. Chen et al., 2016; D. Gaist et al., 2013; Lu & McDonald, 2017). This particular association reflects the findings of Chapter 2, where combination therapy with temozolomide and pyrrolidine-2 increased GBM killing through the inhibition of lipid droplets (I. Zhang et al., 2016).

Ongoing progress toward a better understanding of GBM as a disease and development of new therapeutic agents as well as human brain models are converging to advance translational research. Most exciting are emerging nanotherapeutic agents such as dPGS that could serve both as targeted drug carriers for anti-cancer agents (e.g. sahaquine, temozolomide) and as modulators of TAMs.

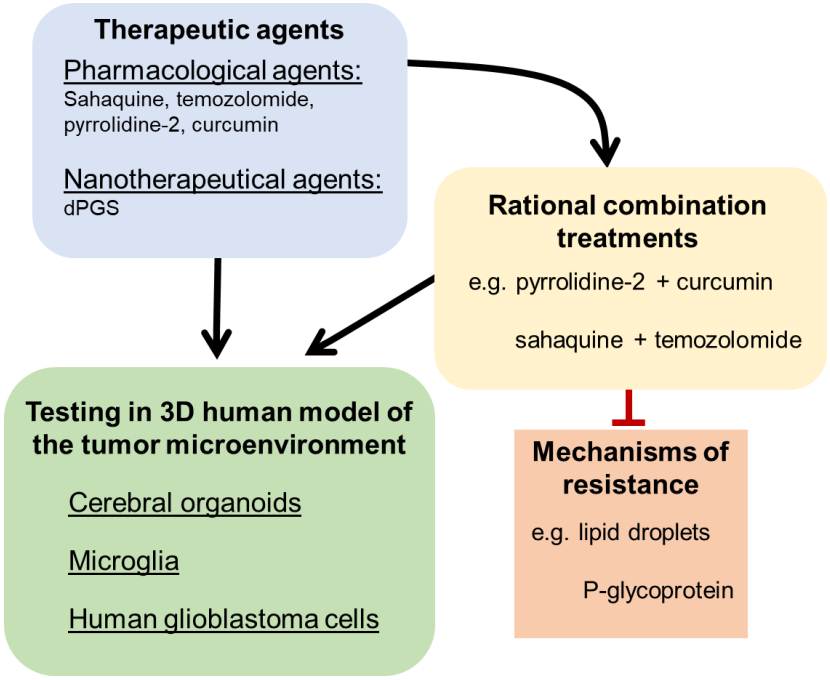

Figure 5.4. Integration of therapeutic and technical advancements for GBM

Conclusions

This thesis presents current therapeutic challenges and corresponding advances for glioblastoma multiforme, a devastating disease for which treatments consistently fail. The urgent need for new therapeutics was a main motive for investigating the novel hybrid molecule sahaquine. The observation that some lipophilic anti-cancer agents are sequestered in fat cells and organelles led to studies on lipid droplets, which were largely unexplored in brain tumors. We hypothesized that better understanding of their role in cancer resistance will lead to the selection of more effective combination treatments. Finally, considering the limitations of 2D glioblastoma models, we established complex *in vitro* brain models in 3D to study inflammation in the glioblastoma microenvironment using human neural cells.

Chapter 2 of the thesis presents direct and indirect effects of targeting the uniquely cytoplasmic HDAC6 using sahaquine, an anti-cancer hybrid molecule that also inhibits P-glycoprotein-mediated drug efflux. Additionally, sahaquine kills brain tumor stem cells and minimizes hyperactivation of pro-survival pathways. Importantly, combination treatments presented in Chapter 2 were superior to monotherapies in tackling glioblastoma heterogeneity and adaptability.

Chapter 3 focused on the effectiveness of combination treatment with pyrrolidine-2, an inhibitor of lipid droplet formation, and curcumin, a natural compound previously suggested for cancer treatments. Results from this chapter clearly show the contribution of lipid droplets to glioblastoma resistance. The extensive organellar and functional changes in glioblastoma were also observed in cells of the tumor stroma.

In Chapter 4, we capitalize on human neural cells forming organoids to test anti-inflammatory effects in the glioblastoma microenvironment. Results in Chapter 4 reveal the contribution of normal astrocytes and microglia to cancer progression. We used dendritic polyglycerol sulfates as anti-inflammatory nanostructures to normalize glial functions in the tumor microenvironment in 3D.

Taken together, this thesis joined pharmacological and nanomedical advances with emerging pre-clinical tools and biological models. Results from this thesis should provide the basis for future studies with combination therapies *in vivo* by combining metabolomic, proteomic and lipidomic approaches. Ultimately, this thesis strives to advance patient prospects beyond the Hobson's choice currently available in clinics.

References

Abdel Fattah, A. R., & Ranga, A. (2020). Nanoparticles as Versatile Tools for Mechanotransduction in Tissues and Organoids. *Frontiers in Bioengineering and Biotechnology*, *8*, 240. https://doi.org/10.3389/fbioe.2020.00240

Abels, E. R., Maas, S. L. N., Nieland, L., Wei, Z., Cheah, P. S., Tai, E., Kolsteeg, C.-J., Dusoswa, S. A., Ting, D. T., Hickman, S., El Khoury, J., Krichevsky, A. M., Broekman, M. L. D., & Breakefield, X. O. (2019). Glioblastoma-Associated Microglia Reprogramming Is Mediated by Functional Transfer of Extracellular miR-21. *Cell Reports*, *28*(12), 3105-3119.e7. https://doi.org/10.1016/j.celrep.2019.08.036

Accioly, M. T., Pacheco, P., Maya-Monteiro, C. M., Carrossini, N., Robbs, B. K., Oliveira, S. S., Kaufmann, C., Morgado-Diaz, J. A., Bozza, P. T., & Viola, J. P. B. (2008). Lipid bodies are reservoirs of cyclooxygenase-2 and sites of prostaglandin-E2 synthesis in colon cancer cells. *Cancer Research*, *68*(6), 1732–1740. https://doi.org/10.1158/0008-5472.CAN-07-1999

Ackerman, D., & Simon, M. C. (2014). Hypoxia, lipids, and cancer: Surviving the harsh tumor microenvironment. *Trends in Cell Biology*, *24*(8), 472–478. https://doi.org/10.1016/j.tcb.2014.06.001

ACY-1215 (Ricolinostat) in Combination With Pomalidomide and Low-dose Dex in Relapsed-and-Refractory Multiple Myeloma—Full Text View—ClinicalTrials.gov. (n.d.). Retrieved May 31, 2018, from https://clinicaltrials.gov/ct2/show/NCT01997840

Aggarwal, B. B., & Sung, B. (2009). Pharmacological basis for the role of curcumin in chronic diseases: An age-old spice with modern targets. *Trends in Pharmacological Sciences*, *30*(2), 85–94. https://doi.org/10.1016/j.tips.2008.11.002

Aizawa, F., Nishinaka, T., Yamashita, T., Nakamoto, K., Koyama, Y., Kasuya, F., & Tokuyama, S. (2016). Astrocytes Release Polyunsaturated Fatty Acids by Lipopolysaccharide Stimuli. *Biological & Pharmaceutical Bulletin*, *39*(7), 1100–1106. https://doi.org/10.1248/bpb.b15-01037

Akinc, A., Maier, M. A., Manoharan, M., Fitzgerald, K., Jayaraman, M., Barros, S., Ansell, S., Du, X., Hope, M. J., Madden, T. D., Mui, B. L., Semple, S. C., Tam, Y. K., Ciufolini, M., Witzigmann, D., Kulkarni, J. A., van der Meel, R., & Cullis, P. R. (2019). The Onpattro story and the clinical translation of nanomedicines containing nucleic acid-based drugs. *Nature Nanotechnology*, *14*(12), 1084–1087. https://doi.org/10.1038/s41565-019-0591-y

Alaseem, A., Alhazzani, K., Dondapati, P., Alobid, S., Bishayee, A., & Rathinavelu, A. (2017). Matrix Metalloproteinases: A challenging paradigm of cancer management. *Seminars in Cancer Biology*. https://doi.org/10.1016/j.semcancer.2017.11.008

Alford, S. C., Abdelfattah, A. S., Ding, Y., & Campbell, R. E. (2012). A fluorogenic red fluorescent protein heterodimer. *Chemistry & Biology*, *19*(3), 353–360. https://doi.org/10.1016/j.chembiol.2012.01.006

Alliot, F., Godin, I., & Pessac, B. (1999). Microglia derive from progenitors, originating from the yolk sac, and which proliferate in the brain. *Developmental Brain Research*, *117*(2), 145–152. https://doi.org/10.1016/S0165-3806(99)00113-3

Almiron Bonnin, D. A., Havrda, M. C., Lee, M. C., Liu, H., Zhang, Z., Nguyen, L. N., Harrington, L. X., Hassanpour, S., Cheng, C., & Israel, M. A. (2018). Secretion-mediated STAT3 activation promotes self-renewal of glioma stem-like cells during hypoxia. *Oncogene*, *37*(8), 1107–1118. https://doi.org/10.1038/onc.2017.404

Amengual, J. E., Prabhu, S. A., Lombardo, M., Zullo, K., Johannet, P. M., Gonzalez, Y., Scotto, L., Serrano, X. J., Wei, Y., Duong, J., Nandakumar, R., Cremers, S., Verma, A., Elemento, O., & O'Connor, O. A. (2017). Mechanisms of Acquired Drug Resistance to the HDAC6 Selective Inhibitor Ricolinostat Reveals Rational Drug: Drug Combination with Ibrutinib. *Clinical Cancer Research : An Official Journal of the American Association for Cancer Research*, *23*(12), 3084–3096. https://doi.org/10.1158/1078-0432.CCR-16-2022

Anand, P., Kunnumakkara, A. B., Newman, R. A., & Aggarwal, B. B. (2007). Bioavailability of curcumin: Problems and promises. *Molecular Pharmaceutics*, *4*(6), 807–818. https://doi.org/10.1021/mp700113r

Anderson, C. P., & Reynolds, C. P. (2002). Synergistic cytotoxicity of buthionine sulfoximine (BSO) and intensive melphalan (L-PAM) for neuroblastoma cell lines established at relapse after myeloablative therapy. *Bone Marrow Transplantation*, *30*(3), 135–140. https://doi.org/10.1038/sj.bmt.1703605

Andres, S., Pevny, S., Ziegenhagen, R., Bakhiya, N., Schäfer, B., Hirsch-Ernst, K. I., & Lampen, A. (2018). Safety Aspects of the Use of Quercetin as a Dietary Supplement. *Molecular Nutrition & Food Research*, *62*(1). https://doi.org/10.1002/mnfr.201700447

Anfray, C., Ummarino, A., Andón, F. T., & Allavena, P. (2020). Current Strategies to Target Tumor-Associated-Macrophages to Improve Anti-Tumor Immune Responses. *Cells*, *9*(1), 46. https://doi.org/10.3390/cells9010046

Anselmo, A. C., & Mitragotri, S. (2016). Nanoparticles in the clinic. *Bioengineering & Translational Medicine*, *1*(1), 10–29. https://doi.org/10.1002/btm2.10003

Anto, R. J., Mukhopadhyay, A., Denning, K., & Aggarwal, B. B. (2002). Curcumin (diferuloylmethane) induces apoptosis through activation of caspase-8, BID cleavage and cytochrome c release: Its suppression by ectopic expression of Bcl-2 and Bcl-xl. *Carcinogenesis*, *23*(1), 143–150. https://doi.org/10.1093/carcin/23.1.143

Aparicio-Blanco, J., Martín-Sabroso, C., & Torres-Suárez, A.-I. (2016). In vitro screening of nanomedicines through the blood brain barrier: A critical review. *Biomaterials*, *103*, 229–255. https://doi.org/10.1016/j.biomaterials.2016.06.051

Aqil, F., Munagala, R., Jeyabalan, J., & Vadhanam, M. V. (2013). Bioavailability of phytochemicals and its enhancement by drug delivery systems. *Cancer Letters*, *334*(1), 133–141. https://doi.org/10.1016/j.canlet.2013.02.032

Arvanitis, C. D., Ferraro, G. B., & Jain, R. K. (2020). The blood–brain barrier and blood–tumour barrier in brain tumours and metastases. *Nature Reviews Cancer*, *20*(1), 26–41. https://doi.org/10.1038/s41568-019-0205-x

Ayati, A., Moghimi, S., Salarinejad, S., Safavi, M., Pouramiri, B., & Foroumadi, A. (2020). A review on progression of epidermal growth factor receptor (EGFR) inhibitors as an efficient approach in cancer targeted therapy. *Bioorganic Chemistry*, *99*, 103811. https://doi.org/10.1016/j.bioorg.2020.103811

Baenke, F., Peck, B., Miess, H., & Schulze, A. (2013). Hooked on fat: The role of lipid synthesis in cancer metabolism and tumour development. *Disease Models & Mechanisms*, *6*(6), 1353–1363. https://doi.org/10.1242/dmm.011338

Balboa, M. A., Pérez, R., & Balsinde, J. (2003). Amplification mechanisms of inflammation: Paracrine stimulation of arachidonic acid mobilization by secreted phospholipase A2 is regulated by cytosolic phospholipase A2-derived hydroperoxyeicosatetraenoic acid. *Journal of Immunology (Baltimore, Md.: 1950)*, *171*(2), 989–994. https://doi.org/10.4049/jimmunol.171.2.989

Bao, S., Wu, Q., Sathornsumetee, S., Hao, Y., Li, Z., Hjelmeland, A. B., Shi, Q., McLendon, R. E., Bigner, D. D., & Rich, J. N. (2006). Stem cell-like glioma cells promote tumor angiogenesis through vascular endothelial growth factor. *Cancer Research*, *66*(16), 7843–7848. https://doi.org/10.1158/0008-5472.CAN-06-1010

Barber, C. N., & Raben, D. M. (2019). Lipid Metabolism Crosstalk in the Brain: Glia and Neurons. *Frontiers in Cellular Neuroscience*, *13*. https://doi.org/10.3389/fncel.2019.00212

Barbosa, A. D., Savage, D. B., & Siniossoglou, S. (2015). Lipid droplet-organelle interactions: Emerging roles in lipid metabolism. *Current Opinion in Cell Biology*, *35*, 91–97. https://doi.org/10.1016/j.ceb.2015.04.017

Barry, J., Fritz, M., Brender, J. R., Smith, P. E. S., Lee, D.-K., & Ramamoorthy, A. (2009). Determining the effects of lipophilic drugs on membrane structure by solid-state NMR spectroscopy: The case

of the antioxidant curcumin. *Journal of the American Chemical Society*, *131*(12), 4490–4498. https://doi.org/10.1021/ja809217u

Barthel, S. R., Gavino, J. D., Descheny, L., & Dimitroff, C. J. (2007). Targeting selectins and selectin ligands in inflammation and cancer. *Expert Opinion on Therapeutic Targets*, *11*(11), 1473–1491. https://doi.org/10.1517/14728222.11.11.1473

Bellver-Landete, V., Bretheau, F., Mailhot, B., Vallières, N., Lessard, M., Janelle, M.-E., Vernoux, N., Tremblay, M.-È., Fuehrmann, T., Shoichet, M. S., & Lacroix, S. (2019). Microglia are an essential component of the neuroprotective scar that forms after spinal cord injury. *Nature Communications*, *10*(1), 518. https://doi.org/10.1038/s41467-019-08446-0

Bergmann, S., Lawler, S. E., Qu, Y., Fadzen, C. M., Wolfe, J. M., Regan, M. S., Pentelute, B. L., Agar, N. Y. R., & Cho, C.-F. (2018). Blood–brain-barrier organoids for investigating the permeability of CNS therapeutics. *Nature Protocols*, *13*(12), 2827–2843. https://doi.org/10.1038/s41596-018-0066-x

Bertrand, S., Hélesbeux, J.-J., Larcher, G., & Duval, O. (2013). Hydroxamate, a key pharmacophore exhibiting a wide range of biological activities. *Mini Reviews in Medicinal Chemistry*, *13*(9), 1311–1326.

Bhullar, K. S., Lagarón, N. O., McGowan, E. M., Parmar, I., Jha, A., Hubbard, B. P., & Rupasinghe, H. P. V. (2018). Kinase-targeted cancer therapies: Progress, challenges and future directions. *Molecular Cancer*, *17*. https://doi.org/10.1186/s12943-018-0804-2

Bieliauskas, A. V., & Pflum, M. K. H. (2008). Isoform-selective histone deacetylase inhibitors. *Chemical Society Reviews*, *37*(7), 1402–1413. https://doi.org/10.1039/b703830p

Bleau, A.-M., Hambardzumyan, D., Ozawa, T., Fomchenko, E. I., Huse, J. T., Brennan, C. W., & Holland, E. C. (2009). PTEN/PI3K/Akt pathway regulates the side population phenotype and ABCG2 activity in glioma tumor stem-like cells. *Cell Stem Cell*, *4*(3), 226–235. https://doi.org/10.1016/j.stem.2009.01.007

Bonačić-Koutecký, V., & Antoine, R. (2019). Enhanced two-photon absorption of ligated silver and gold nanoclusters: Theoretical and experimental assessments. *Nanoscale*, *11*(26), 12436–12448. https://doi.org/10.1039/C9NR01826C

Bonaventura, P., Shekarian, T., Alcazer, V., Valladeau-Guilemond, J., Valsesia-Wittmann, S., Amigorena, S., Caux, C., & Depil, S. (2019). Cold Tumors: A Therapeutic Challenge for Immunotherapy. *Frontiers in Immunology*, *10*. https://doi.org/10.3389/fimmu.2019.00168

Bond, M., Chase, A. J., Baker, A. H., & Newby, A. C. (2001). Inhibition of transcription factor NF-kappaB reduces matrix metalloproteinase-1, -3 and -9 production by vascular smooth muscle cells. *Cardiovascular Research*, *50*(3), 556–565.

Boridy, S., Le, P. U., Petrecca, K., & Maysinger, D. (2014). Celastrol targets proteostasis and acts synergistically with a heat-shock protein 90 inhibitor to kill human glioblastoma cells. *Cell Death & Disease*, *5*, e1216. https://doi.org/10.1038/cddis.2014.182

Boroughs, L. K., & DeBerardinis, R. J. (2015). Metabolic pathways promoting cancer cell survival and growth. *Nature Cell Biology*, *17*(4), 351–359. https://doi.org/10.1038/ncb3124

Boutej, H., Rahimian, R., Thammisetty, S. S., Béland, L.-C., Lalancette-Hébert, M., & Kriz, J. (2017). Diverging mRNA and Protein Networks in Activated Microglia Reveal SRSF3 Suppresses Translation of Highly Upregulated Innate Immune Transcripts. *Cell Reports*, *21*(11), 3220–3233. https://doi.org/10.1016/j.celrep.2017.11.058

Boyault, C., Sadoul, K., Pabion, M., & Khochbin, S. (2007). HDAC6, at the crossroads between cytoskeleton and cell signaling by acetylation and ubiquitination. *Oncogene*, *26*(37), 5468–5476. https://doi.org/10.1038/sj.onc.1210614

Brandao, M., Simon, T., Critchley, G., & Giamas, G. (2019). Astrocytes, the rising stars of the glioblastoma microenvironment. *Glia*, *67*(5), 779–790. https://doi.org/10.1002/glia.23520

Breschi, A., Gingeras, T. R., & Guigó, R. (2017). Comparative transcriptomics in human and mouse. *Nature Reviews Genetics*, *18*(7), 425–440. https://doi.org/10.1038/nrg.2017.19

Broekman, M. L., Maas, S. L. N., Abels, E. R., Mempel, T. R., Krichevsky, A. M., & Breakefield, X. O. (2018). Multidimensional communication in the microenvirons of glioblastoma. *Nature Reviews Neurology*, *14*(8), 482–495. https://doi.org/10.1038/s41582-018-0025-8

Brown, J. M., & Attardi, L. D. (2005). The role of apoptosis in cancer development and treatment response. *Nature Reviews. Cancer*, *5*(3), 231–237. https://doi.org/10.1038/nrc1560

Cabodevilla, A. G., Sánchez-Caballero, L., Nintou, E., Boiadjieva, V. G., Picatoste, F., Gubern, A., & Claro, E. (2013). Cell survival during complete nutrient deprivation depends on lipid droplet-fueled β-oxidation of fatty acids. *The Journal of Biological Chemistry*, *288*(39), 27777–27788. https://doi.org/10.1074/jbc.M113.466656

Cai, X., Hu, X., Tan, X., Cheng, W., Wang, Q., Chen, X., Guan, Y., Chen, C., & Jing, X. (2015). Metformin Induced AMPK Activation, G0/G1 Phase Cell Cycle Arrest and the Inhibition of Growth of Esophageal Squamous Cell Carcinomas In Vitro and In Vivo. *PloS One*, *10*(7), e0133349. https://doi.org/10.1371/journal.pone.0133349

Cakir, B., Xiang, Y., Tanaka, Y., Kural, M. H., Parent, M., Kang, Y.-J., Chapeton, K., Patterson, B., Yuan, Y., He, C.-S., Raredon, M. S. B., Dengelegi, J., Kim, K.-Y., Sun, P., Zhong, M., Lee, S., Patra, P., Hyder, F., Niklason, L. E., … Park, I.-H. (2019). Engineering of human brain organoids with a functional vascular-like system. *Nature Methods*, *16*(11), 1169–1175. https://doi.org/10.1038/s41592-019-0586-5

Calgarotto, A. K., Maso, V., Junior, G. C. F., Nowill, A. E., Filho, P. L., Vassallo, J., & Saad, S. T. O. (2018). Antitumor activities of Quercetin and Green Tea in xenografts of human leukemia HL60 cells. *Scientific Reports*, *8*(1), 3459. https://doi.org/10.1038/s41598-018-21516-5

Camidge, R. (2001). The Story of Taxol: Nature and Politics in the Pursuit of an Anti-Cancer Drug. *BMJ : British Medical Journal*, *323*(7304), 115.

Cancer Genome Atlas Research Network. (2008). Comprehensive genomic characterization defines human glioblastoma genes and core pathways. *Nature*, *455*(7216), 1061–1068. https://doi.org/10.1038/nature07385

Caporali, S., Falcinelli, S., Starace, G., Russo, M. T., Bonmassar, E., Jiricny, J., & D'Atri, S. (2004). DNA damage induced by temozolomide signals to both ATM and ATR: Role of the mismatch repair system. *Molecular Pharmacology*, *66*(3), 478–491. https://doi.org/10.1124/mol.66.3.

Casati, A., & Putzu, M. (2005). Anesthesia in the obese patient: Pharmacokinetic considerations. *Journal of Clinical Anesthesia*, *17*(2), 134–145. https://doi.org/10.1016/j.jclinane.2004.01.009

Cavalli, F. M. G., Remke, M., Rampasek, L., Peacock, J., Shih, D. J. H., Luu, B., Garzia, L., Torchia, J., Nor, C., Morrissy, A. S., Agnihotri, S., Thompson, Y. Y., Kuzan-Fischer, C. M., Farooq, H., Isaev, K., Daniels, C., Cho, B.-K., Kim, S.-K., Wang, K.-C., … Taylor, M. D. (2017). Intertumoral Heterogeneity within Medulloblastoma Subgroups. *Cancer Cell*, *31*(6), 737-754.e6. https://doi.org/10.1016/j.ccell.2017.05.005

Chamoto, K., Hatae, R., & Honjo, T. (2020). Current issues and perspectives in PD-1 blockade cancer immunotherapy. *International Journal of Clinical Oncology*. https://doi.org/10.1007/s10147-019-01588-7

Chemicalize—Instant Cheminformatics Solutions. (n.d.). Retrieved May 31, 2018, from https://chemicalize.com/

Chen, B. K., Chiu, H.-F., & Yang, C.-Y. (2016). Statins are Associated With a Reduced Risk of Brain Cancer: A Population-Based Case–Control Study. *Medicine*, *95*(17), e3392. https://doi.org/10.1097/MD.0000000000003392

Chen, J., McKay, R. M., & Parada, L. F. (2012). Malignant Glioma: Lessons from Genomics, Mouse Models, and Stem Cells. *Cell*, *149*(1), 36–47. https://doi.org/10.1016/j.cell.2012.03.009

Chen, S.-F., Chang, Y.-C., Nieh, S., Liu, C.-L., Yang, C.-Y., & Lin, Y.-S. (2012). Nonadhesive Culture System as a Model of Rapid Sphere Formation with Cancer Stem Cell Properties. *PLoS ONE*, *7*(2). https://doi.org/10.1371/journal.pone.0031864

Chen, Xi, Zhi, F., Jia, X., Zhang, X., Ambardekar, R., Meng, Z., Paradkar, A. R., Hu, Y., & Yang, Y. (2013). Enhanced brain targeting of curcumin by intranasal administration of a thermosensitive

poloxamer hydrogel. *The Journal of Pharmacy and Pharmacology*, *65*(6), 807–816. https://doi.org/10.1111/jphp.12043

Chen, Xiuqing, Rocha, C., Rao, T., & Durcan, T. M. (2019). *NeuroEDDU protocols_iPSC culture*. https://doi.org/10.5281/zenodo.3337402

Chen, Z., & Hambardzumyan, D. (2018). Immune Microenvironment in Glioblastoma Subtypes. *Frontiers in Immunology*, *9*, 1004. https://doi.org/10.3389/fimmu.2018.01004

Cheng, A. L., Hsu, C. H., Lin, J. K., Hsu, M. M., Ho, Y. F., Shen, T. S., Ko, J. Y., Lin, J. T., Lin, B. R., Ming-Shiang, W., Yu, H. S., Jee, S. H., Chen, G. S., Chen, T. M., Chen, C. A., Lai, M. K., Pu, Y. S., Pan, M. H., Wang, Y. J., … Hsieh, C. Y. (2001). Phase I clinical trial of curcumin, a chemopreventive agent, in patients with high-risk or pre-malignant lesions. *Anticancer Research*, *21*(4B), 2895–2900.

Chinnaiyan, P., Kensicki, E., Bloom, G., Prabhu, A., Sarcar, B., Kahali, S., Eschrich, S., Qu, X., Forsyth, P., & Gillies, R. (2012). The metabolomic signature of malignant glioma reflects accelerated anabolic metabolism. *Cancer Research*, *72*(22), 5878–5888. https://doi.org/10.1158/0008-5472.CAN-12-1572-T

Choi, A.-R., Kim, J.-H., Woo, Y. H., Kim, H. S., & Yoon, S. (2016). Anti-malarial Drugs Primaquine and Chloroquine Have Different Sensitization Effects with Anti-mitotic Drugs in Resistant Cancer Cells. *Anticancer Research*, *36*(4), 1641–1648.

Choi, J., Moquin, A., Bomal, E., Na, L., Maysinger, D., & Kakkar, A. (2017). Telodendrimers for Physical Encapsulation and Covalent Linking of Individual or Combined Therapeutics. *Molecular Pharmaceutics*, *14*(8), 2607–2615. https://doi.org/10.1021/acs.molpharmaceut.7b00019

Chou, T.-C. (2018). The combination index (CI < 1) as the definition of synergism and of synergy claims. *Synergy*, *7*, 49–50. https://doi.org/10.1016/j.synres.2018.04.001

Claes, A., Idema, A. J., & Wesseling, P. (2007). Diffuse glioma growth: A guerilla war. *Acta Neuropathologica*, *114*(5), 443–458. https://doi.org/10.1007/s00401-007-0293-7

Cohen, A. L., & Colman, H. (2015). Glioma biology and molecular markers. *Cancer Treatment and Research*, *163*, 15–30. https://doi.org/10.1007/978-3-319-12048-5_2

Colwell, N., Larion, M., Giles, A. J., Seldomridge, A. N., Sizdahkhani, S., Gilbert, M. R., & Park, D. M. (2017). Hypoxia in the glioblastoma microenvironment: Shaping the phenotype of cancer stem-like cells. *Neuro-Oncology*, *19*(7), 887–896. https://doi.org/10.1093/neuonc/now258

Combs, S. E., Heeger, S., Haselmann, R., Edler, L., Debus, J., & Schulz-Ertner, D. (2006). Treatment of primary glioblastoma multiforme with cetuximab, radiotherapy and temozolomide (GERT) – phase I/II trial: Study protocol. *BMC Cancer*, *6*, 133. https://doi.org/10.1186/1471-2407-6-133

Conti, I., Varano, G., Simioni, C., Laface, I., Milani, D., Rimondi, E., & Neri, L. M. (2020). MiRNAs as Influencers of Cell–Cell Communication in Tumor Microenvironment. *Cells*, *9*(1), 220. https://doi.org/10.3390/cells9010220

Corbet, C., & Feron, O. (2017). Tumour acidosis: From the passenger to the driver's seat. *Nature Reviews. Cancer*, *17*(10), 577–593. https://doi.org/10.1038/nrc.2017.77

Cuddapah, V. A., Robel, S., Watkins, S., & Sontheimer, H. (2014). A neurocentric perspective on glioma invasion. *Nature Reviews. Neuroscience*, *15*(7), 455–465. https://doi.org/10.1038/nrn3765

Dagogo-Jack, I., & Shaw, A. T. (2018). Tumour heterogeneity and resistance to cancer therapies. *Nature Reviews. Clinical Oncology*, *15*(2), 81–94. https://doi.org/10.1038/nrclinonc.2017.166

Daneman, R., & Prat, A. (2015). The Blood–Brain Barrier. *Cold Spring Harbor Perspectives in Biology*, *7*(1). https://doi.org/10.1101/cshperspect.a020412

Dasgupta, M., Dermawan, J. K. T., Willard, B., & Stark, G. R. (2015). STAT3-driven transcription depends upon the dimethylation of K49 by EZH2. *Proceedings of the National Academy of Sciences*, *112*(13), 3985–3990. https://doi.org/10.1073/pnas.1503152112

Davis, Mark E., Chen, Z. (Georgia), & Shin, D. M. (2008). Nanoparticle therapeutics: An emerging treatment modality for cancer. *Nature Reviews Drug Discovery*, *7*(9), 771–782. https://doi.org/10.1038/nrd2614

Davis, Mary Elizabeth. (2016). Glioblastoma: Overview of Disease and Treatment. *Clinical Journal of Oncology Nursing*, *20*(5), S2–S8. https://doi.org/10.1188/16.CJON.S1.2-8

Del Duca, D., Werbowetski, T., & Del Maestro, R. F. (2004). Spheroid preparation from hanging drops: Characterization of a model of brain tumor invasion. *Journal of Neuro-Oncology*, *67*(3), 295–303. https://doi.org/10.1023/b:neon.0000024220.07063.70

Dernedde, J., Rausch, A., Weinhart, M., Enders, S., Tauber, R., Licha, K., Schirner, M., Zügel, U., Bonin, A. von, & Haag, R. (2010). Dendritic polyglycerol sulfates as multivalent inhibitors of inflammation. *Proceedings of the National Academy of Sciences*, *107*(46), 19679–19684. https://doi.org/10.1073/pnas.1003103107

Desmarais, G., Charest, G., Fortin, D., Bujold, R., Mathieu, D., & Paquette, B. (2015). Cyclooxygenase-2 inhibitor prevents radiation-enhanced infiltration of F98 glioma cells in brain of Fischer rat. *International Journal of Radiation Biology*, *91*(8), 624–633. https://doi.org/10.3109/09553002.2015.1043756

Dhanikula, R. S., Argaw, A., Bouchard, J.-F., & Hildgen, P. (2008). Methotrexate loaded polyether-copolyester dendrimers for the treatment of gliomas: Enhanced efficacy and intratumoral transport capability. *Molecular Pharmaceutics*, *5*(1), 105–116. https://doi.org/10.1021/mp700086j

Dhillon, N., Aggarwal, B. B., Newman, R. A., Wolff, R. A., Kunnumakkara, A. B., Abbruzzese, J. L., Ng, C. S., Badmaev, V., & Kurzrock, R. (2008). Phase II trial of curcumin in patients with advanced pancreatic cancer. *Clinical Cancer Research: An Official Journal of the American Association for Cancer Research*, *14*(14), 4491–4499. https://doi.org/10.1158/1078-0432.CCR-08-0024

Ding, Y., Li, J., Enterina, J. R., Shen, Y., Zhang, I., Tewson, P. H., Mo, G. C. H., Zhang, J., Quinn, A. M., Hughes, T. E., Maysinger, D., Alford, S. C., Zhang, Y., & Campbell, R. E. (2015). Ratiometric biosensors based on dimerization-dependent fluorescent protein exchange. *Nature Methods*, *12*(3), 195–198. https://doi.org/10.1038/nmeth.3261

Dirkse, A., Golebiewska, A., Buder, T., Nazarov, P. V., Muller, A., Poovathingal, S., Brons, N. H. C., Leite, S., Sauvageot, N., Sarkisjan, D., Seyfrid, M., Fritah, S., Stieber, D., Michelucci, A., Hertel, F., Herold-Mende, C., Azuaje, F., Skupin, A., Bjerkvig, R., … Niclou, S. P. (2019). Stem cell-associated heterogeneity in Glioblastoma results from intrinsic tumor plasticity shaped by the microenvironment. *Nature Communications*, *10*(1), 1–16. https://doi.org/10.1038/s41467-019-09853-z

Donson, A. M., Addo-Yobo, S. O., Handler, M. H., Gore, L., & Foreman, N. K. (2007). MGMT promoter methylation correlates with survival benefit and sensitivity to temozolomide in pediatric glioblastoma. *Pediatric Blood & Cancer*, *48*(4), 403–407. https://doi.org/10.1002/pbc.20803

Driever, P. H., Knüpfer, M. M., Cinatl, J., & Wolff, J. E. (1999). Valproic acid for the treatment of pediatric malignant glioma. *Klinische Padiatrie*, *211*(4), 323–328. https://doi.org/10.1055/s-2008-1043809

Du, M., Zhang, L., Scorsone, K. A., Woodfield, S. E., & Zage, P. E. (2016). Nifurtimox Is Effective Against Neural Tumor Cells and Is Synergistic with Buthionine Sulfoximine. *Scientific Reports*, *6*. https://doi.org/10.1038/srep27458

Duan, Q., Zhang, H., Zheng, J., & Zhang, L. (2020). Turning Cold into Hot: Firing up the Tumor Microenvironment. *Trends in Cancer*, *0*(0). https://doi.org/10.1016/j.trecan.2020.02.022

Dubey, R., Stivala, C. E., Nguyen, H. Q., Goo, Y.-H., Paul, A., Carette, J. E., Trost, B. M., & Rohatgi, R. (2020). Lipid droplets can promote drug accumulation and activation. *Nature Chemical Biology*, *16*(2), 206–213. https://doi.org/10.1038/s41589-019-0447-7

Dumontet, C., & Jordan, M. A. (2010). Microtubule-binding agents: A dynamic field of cancer therapeutics. *Nature Reviews. Drug Discovery*, *9*(10), 790–803. https://doi.org/10.1038/nrd3253

Eiraku, M., & Sasai, Y. (2012). Self-formation of layered neural structures in three-dimensional culture of ES cells. *Current Opinion in Neurobiology*, *22*(5), 768–777. https://doi.org/10.1016/j.conb.2012.02.005

Emrich, J. G., Brady, L. W., Quang, T. S., Class, R., Miyamoto, C., Black, P., & Rodeck, U. (2002). Radioiodinated (I-125) monoclonal antibody 425 in the treatment of high grade glioma patients: Ten-year synopsis of a novel treatment. *American Journal of Clinical Oncology*, *25*(6), 541–546. https://doi.org/10.1097/01.COC.0000041009.06780.E5

Erasimus, H., Gobin, M., Niclou, S., & Van Dyck, E. (2016a). DNA repair mechanisms and their clinical impact in glioblastoma. *Mutation Research/Reviews in Mutation Research*, *769*, 19–35. https://doi.org/10.1016/j.mrrev.2016.05.005

Erasimus, H., Gobin, M., Niclou, S., & Van Dyck, E. (2016b). DNA repair mechanisms and their clinical impact in glioblastoma. *Mutation Research. Reviews in Mutation Research*, *769*, 19–35. https://doi.org/10.1016/j.mrrev.2016.05.005

Fang, J., Nakamura, H., & Maeda, H. (2011). The EPR effect: Unique features of tumor blood vessels for drug delivery, factors involved, and limitations and augmentation of the effect. *Advanced Drug Delivery Reviews*, *63*(3), 136–151. https://doi.org/10.1016/j.addr.2010.04.009

Ferber, S., Tiram, G., Sousa-Herves, A., Eldar-Boock, A., Krivitsky, A., Scomparin, A., Yeini, E., Ofek, P., Ben-Shushan, D., Vossen, L. I., Licha, K., Grossman, R., Ram, Z., Henkin, J., Ruppin, E., Auslander, N., Haag, R., Calderón, M., & Satchi-Fainaro, R. (2017). Co-targeting the tumor endothelium and P-selectin-expressing glioblastoma cells leads to a remarkable therapeutic outcome. *ELife*, *6*. https://doi.org/10.7554/eLife.25281

Fouse, S. D., Nakamura, J. L., James, C. D., Chang, S., & Costello, J. F. (2014). Response of primary glioblastoma cells to therapy is patient specific and independent of cancer stem cell phenotype. *Neuro-Oncology*, *16*(3), 361–371. https://doi.org/10.1093/neuonc/not223

Fukumoto, T., Fatkhutdinov, N., Zundell, J. A., Tcyganov, E. N., Nacarelli, T., Karakashev, S., Wu, S., Liu, Q., Gabrilovich, D. I., & Zhang, R. (2019). HDAC6 inhibition synergizes with anti-PD-L1 therapy in ARID1A-inactivated ovarian cancer. *Cancer Research*. https://doi.org/10.1158/0008-5472.CAN-19-1302

Gaist, D., Andersen, L., Hallas, J., Toft Sørensen, H., Schrøder, H. D., & Friis, S. (2013). Use of statins and risk of glioma: A nationwide case–control study in Denmark. *British Journal of Cancer*, *108*(3), 715–720. https://doi.org/10.1038/bjc.2012.536

Gaist, David, Hallas, J., Friis, S., Hansen, S., & Sørensen, H. T. (2014). Statin use and survival following glioblastoma multiforme. *Cancer Epidemiology*, *38*(6), 722–727. https://doi.org/10.1016/j.canep.2014.09.010

Galanis, E., Anderson, S. K., Miller, C. R., Sarkaria, J. N., Jaeckle, K., Buckner, J. C., Ligon, K. L., Ballman, K. V., Moore, D. F., Nebozhyn, M., Loboda, A., Schiff, D., Ahluwalia, M. S., Lee, E. Q., Gerstner, E. R., Lesser, G. J., Prados, M., Grossman, S. A., Cerhan, J., … Alliance for Clinical Trials in Oncology and ABTC. (2018). Phase I/II trial of vorinostat combined with temozolomide and radiation therapy for newly diagnosed glioblastoma: Results of Alliance N0874/ABTC 02. *Neuro-Oncology*, *20*(4), 546–556. https://doi.org/10.1093/neuonc/nox161

Galanis, E., Jaeckle, K. A., Maurer, M. J., Reid, J. M., Ames, M. M., Hardwick, J. S., Reilly, J. F., Loboda, A., Nebozhyn, M., Fantin, V. R., Richon, V. M., Scheithauer, B., Giannini, C., Flynn, P. J., Moore, D. F., Zwiebel, J., & Buckner, J. C. (2009). Phase II trial of vorinostat in recurrent glioblastoma multiforme: A north central cancer treatment group study. *Journal of Clinical Oncology: Official Journal of the American Society of Clinical Oncology*, *27*(12), 2052–2058. https://doi.org/10.1200/JCO.2008.19.0694

Galli, R., Binda, E., Orfanelli, U., Cipelletti, B., Gritti, A., De Vitis, S., Fiocco, R., Foroni, C., Dimeco, F., & Vescovi, A. (2004). Isolation and characterization of tumorigenic, stem-like neural precursors from human glioblastoma. *Cancer Research*, *64*(19), 7011–7021. https://doi.org/10.1158/0008-5472.CAN-04-1364

Galoczova, M., Coates, P., & Vojtesek, B. (2018). STAT3, stem cells, cancer stem cells and p63. *Cellular & Molecular Biology Letters*, *23*. https://doi.org/10.1186/s11658-018-0078-0

Gelain, A., Mori, M., Meneghetti, F., & Villa, S. (2019). Signal Transducer and Activator of Transcription Protein 3 (STAT3): An Update on its Direct Inhibitors as Promising Anticancer

Agents. *Current Medicinal Chemistry*, *26*(27), 5165–5206. https://doi.org/10.2174/0929867325666180719122729

Geng, F., & Guo, D. (2017). Lipid droplets, potential biomarker and metabolic target in glioblastoma. *Internal Medicine Review (Washington, D.C. : Online)*, *3*(5). https://www.ncbi.nlm.nih.gov/pmc/articles/PMC5639724/

Gialeli, C., Theocharis, A. D., & Karamanos, N. K. (2011). Roles of matrix metalloproteinases in cancer progression and their pharmacological targeting. *The FEBS Journal*, *278*(1), 16–27. https://doi.org/10.1111/j.1742-4658.2010.07919.x

Gieryng, A., Pszczolkowska, D., Walentynowicz, K. A., Rajan, W. D., & Kaminska, B. (2017). Immune microenvironment of gliomas. *Laboratory Investigation*, *97*(5), 498–518. https://doi.org/10.1038/labinvest.2017.19

Glozak, M. A., & Seto, E. (2007). Histone deacetylases and cancer. *Oncogene*, *26*(37), 5420–5432. https://doi.org/10.1038/sj.onc.1210610

Gogada, R., Amadori, M., Zhang, H., Jones, A., Verone, A., Pitarresi, J., Jandhyam, S., Prabhu, V., Black, J. D., & Chandra, D. (2011). Curcumin induces Apaf-1-dependent, p21-mediated caspase activation and apoptosis. *Cell Cycle (Georgetown, Tex.)*, *10*(23), 4128–4137. https://doi.org/10.4161/cc.10.23.18292

Grant, S., Easley, C., & Kirkpatrick, P. (2007). Vorinostat. *Nature Reviews. Drug Discovery*, *6*(1), 21–22. https://doi.org/10.1038/nrd2227

Greenspan, P., Mayer, E. P., & Fowler, S. D. (1985). Nile red: A selective fluorescent stain for intracellular lipid droplets. *The Journal of Cell Biology*, *100*(3), 965–973. https://doi.org/10.1083/jcb.100.3.965

Greish, K. (2010). Enhanced permeability and retention (EPR) effect for anticancer nanomedicine drug targeting. *Methods in Molecular Biology (Clifton, N.J.)*, *624*, 25–37. https://doi.org/10.1007/978-1-60761-609-2_3

Griffith, O. W. (1982). Mechanism of action, metabolism, and toxicity of buthionine sulfoximine and its higher homologs, potent inhibitors of glutathione synthesis. *The Journal of Biological Chemistry*, *257*(22), 13704–13712.

Gross, D. A., & Silver, D. L. (2014). Cytosolic lipid droplets: From mechanisms of fat storage to disease. *Critical Reviews in Biochemistry and Molecular Biology*, *49*(4), 304–326. https://doi.org/10.3109/10409238.2014.931337

Gubern, A., Casas, J., Barceló-Torns, M., Barneda, D., de la Rosa, X., Masgrau, R., Picatoste, F., Balsinde, J., Balboa, M. A., & Claro, E. (2008). Group IVA phospholipase A2 is necessary for the biogenesis of lipid droplets. *The Journal of Biological Chemistry*, *283*(41), 27369–27382. https://doi.org/10.1074/jbc.M800696200

Gupta, K., Kalra, I., Salunke, P., & Vasishta, R. K. (2011). Lipidized glioblastoma: A rare differentiation pattern. *Neuropathology: Official Journal of the Japanese Society of Neuropathology*, *31*(1), 93–97. https://doi.org/10.1111/j.1440-1789.2010.01141.x

Gupta, S. C., Patchva, S., & Aggarwal, B. B. (2013). Therapeutic roles of curcumin: Lessons learned from clinical trials. *The AAPS Journal*, *15*(1), 195–218. https://doi.org/10.1208/s12248-012-9432-8

Håkanson, M., Textor, M., & Charnley, M. (2011). Engineered 3D environments to elucidate the effect of environmental parameters on drug response in cancer. *Integrative Biology: Quantitative Biosciences from Nano to Macro*, *3*(1), 31–38. https://doi.org/10.1039/c0ib00074d

Hambardzumyan, D., & Bergers, G. (2015). Glioblastoma: Defining Tumor Niches. *Trends in Cancer*, *1*(4), 252–265. https://doi.org/10.1016/j.trecan.2015.10.009

Hambardzumyan, D., Gutmann, D. H., & Kettenmann, H. (2016). The role of microglia and macrophages in glioma maintenance and progression. *Nature Neuroscience*, *19*(1), 20–27. https://doi.org/10.1038/nn.4185

Han, D., Yu, T., Dong, N., Wang, B., Sun, F., & Jiang, D. (2019). Napabucasin, a novel STAT3 inhibitor suppresses proliferation, invasion and stemness of glioblastoma cells. *Journal of Experimental & Clinical Cancer Research: CR*, *38*(1), 289. https://doi.org/10.1186/s13046-019-1289-6

Hashemi, H. F., & Goodman, J. M. (2015). The life cycle of lipid droplets. *Current Opinion in Cell Biology*, *33*, 119–124. https://doi.org/10.1016/j.ceb.2015.02.002

Havel, H., Finch, G., Strode, P., Wolfgang, M., Zale, S., Bobe, I., Youssoufian, H., Peterson, M., & Liu, M. (2016). Nanomedicines: From Bench to Bedside and Beyond. *The AAPS Journal*, *18*(6), 1373–1378. https://doi.org/10.1208/s12248-016-9961-7

He, W., Kuang, Y., Xing, X., Simpson, R. J., Huang, H., Yang, T., Chen, J., Yang, L., Liu, E., He, W., & Gu, J. (2014). Proteomic comparison of 3D and 2D glioma models reveals increased HLA-E expression in 3D models is associated with resistance to NK cell-mediated cytotoxicity. *Journal of Proteome Research*, *13*(5), 2272–2281. https://doi.org/10.1021/pr500064m

Heger, M., van Golen, R. F., Broekgaarden, M., & Michel, M. C. (2014). The molecular basis for the pharmacokinetics and pharmacodynamics of curcumin and its metabolites in relation to cancer. *Pharmacological Reviews*, *66*(1), 222–307. https://doi.org/10.1124/pr.110.004044

Hegi, M. E., Diserens, A.-C., Gorlia, T., Hamou, M.-F., de Tribolet, N., Weller, M., Kros, J. M., Hainfellner, J. A., Mason, W., Mariani, L., Bromberg, J. E. C., Hau, P., Mirimanoff, R. O., Cairncross, J. G., Janzer, R. C., & Stupp, R. (2005a). MGMT Gene Silencing and Benefit from Temozolomide in Glioblastoma. *New England Journal of Medicine*, *352*(10), 997–1003. https://doi.org/10.1056/NEJMoa043331

Hegi, M. E., Diserens, A.-C., Gorlia, T., Hamou, M.-F., de Tribolet, N., Weller, M., Kros, J. M., Hainfellner, J. A., Mason, W., Mariani, L., Bromberg, J. E. C., Hau, P., Mirimanoff, R. O., Cairncross, J. G., Janzer, R. C., & Stupp, R. (2005b). MGMT gene silencing and benefit from temozolomide in glioblastoma. *The New England Journal of Medicine*, *352*(10), 997–1003. https://doi.org/10.1056/NEJMoa043331

Hegi, M. E., Diserens, A.-C., Gorlia, T., Hamou, M.-F., de Tribolet, N., Weller, M., Kros, J. M., Hainfellner, J. A., Mason, W., Mariani, L., Bromberg, J. E. C., Hau, P., Mirimanoff, R. O., Cairncross, J. G., Janzer, R. C., & Stupp, R. (2005c). MGMT Gene Silencing and Benefit from Temozolomide in Glioblastoma. *New England Journal of Medicine*, *352*(10), 997–1003. https://doi.org/10.1056/NEJMoa043331

Hilf, N., Kuttruff-Coqui, S., Frenzel, K., Bukur, V., Stevanović, S., Gouttefangeas, C., Platten, M., Tabatabai, G., Dutoit, V., van der Burg, S. H., Thor Straten, P., Martínez-Ricarte, F., Ponsati, B., Okada, H., Lassen, U., Admon, A., Ottensmeier, C. H., Ulges, A., Kreiter, S., … Wick, W. (2019). Actively personalized vaccination trial for newly diagnosed glioblastoma. *Nature*, *565*(7738), 240–245. https://doi.org/10.1038/s41586-018-0810-y

Hilvo, M., Denkert, C., Lehtinen, L., Müller, B., Brockmöller, S., Seppänen-Laakso, T., Budczies, J., Bucher, E., Yetukuri, L., Castillo, S., Berg, E., Nygren, H., Sysi-Aho, M., Griffin, J. L., Fiehn, O., Loibl, S., Richter-Ehrenstein, C., Radke, C., Hyötyläinen, T., … Oresic, M. (2011). Novel theranostic opportunities offered by characterization of altered membrane lipid metabolism in breast cancer progression. *Cancer Research*, *71*(9), 3236–3245. https://doi.org/10.1158/0008-5472.CAN-10-3894

Hodge, R. D., Bakken, T. E., Miller, J. A., Smith, K. A., Barkan, E. R., Graybuck, L. T., Close, J. L., Long, B., Johansen, N., Penn, O., Yao, Z., Eggermont, J., Höllt, T., Levi, B. P., Shehata, S. I., Aevermann, B., Beller, A., Bertagnolli, D., Brouner, K., … Lein, E. S. (2019). Conserved cell types with divergent features in human versus mouse cortex. *Nature*, *573*(7772), 61–68. https://doi.org/10.1038/s41586-019-1506-7

Holland, E. C. (2000). Glioblastoma multiforme: The terminator. *Proceedings of the National Academy of Sciences of the United States of America*, *97*(12), 6242–6244.

Hrkach, J., Hoff, D. V., Ali, M. M., Andrianova, E., Auer, J., Campbell, T., Witt, D. D., Figa, M., Figueiredo, M., Horhota, A., Low, S., McDonnell, K., Peeke, E., Retnarajan, B., Sabnis, A., Schnipper, E., Song, J. J., Song, Y. H., Summa, J., … Zale, S. (2012). Preclinical Development

and Clinical Translation of a PSMA-Targeted Docetaxel Nanoparticle with a Differentiated Pharmacological Profile. *Science Translational Medicine*, *4*(128), 128ra39-128ra39. https://doi.org/10.1126/scitranslmed.3003651

Hummel, T. R., Wagner, L., Ahern, C., Fouladi, M., Reid, J. M., McGovern, R. M., Ames, M. M., Gilbertson, R. J., Horton, T., Ingle, A. M., Weigel, B., & Blaney, S. M. (2013a). A pediatric phase 1 trial of vorinostat and temozolomide in relapsed or refractory primary brain or spinal cord tumors: A Children's Oncology Group phase 1 consortium study. *Pediatric Blood & Cancer*, *60*(9), 1452–1457. https://doi.org/10.1002/pbc.24541

Hummel, T. R., Wagner, L., Ahern, C., Fouladi, M., Reid, J. M., McGovern, R. M., Ames, M. M., Gilbertson, R. J., Horton, T., Ingle, A. M., Weigel, B., & Blaney, S. M. (2013b). A Pediatric Phase 1 Trial Of Vorinostat And Temozolomide In Relapsed Or Refractory Primary Brain Or Spinal Cord Tumors: A Children's Oncology Group Phase 1 Consortium Study. *Pediatric Blood & Cancer*, *60*(9), 1452–1457. https://doi.org/10.1002/pbc.24541

Hung, W.-C., Chen, F.-Y., Lee, C.-C., Sun, Y., Lee, M.-T., & Huang, H. W. (2008). Membrane-thinning effect of curcumin. *Biophysical Journal*, *94*(11), 4331–4338. https://doi.org/10.1529/biophysj.107.126888

Hunter, K. W., Amin, R., Deasy, S., Ha, N.-H., & Wakefield, L. (2018). Genetic insights into the morass of metastatic heterogeneity. *Nature Reviews. Cancer*, *18*(4), 211–223. https://doi.org/10.1038/nrc.2017.126

Huynh, J., Chand, A., Gough, D., & Ernst, M. (2019). Therapeutically exploiting STAT3 activity in cancer—Using tissue repair as a road map. *Nature Reviews Cancer*, *19*(2), 82–96. https://doi.org/10.1038/s41568-018-0090-8

Iaconelli, J., Lalonde, J., Watmuff, B., Liu, B., Mazitschek, R., Haggarty, S. J., & Karmacharya, R. (2017). Lysine Deacetylation by HDAC6 Regulates the Kinase Activity of AKT in Human Neural Progenitor Cells. *ACS Chemical Biology*, *12*(8), 2139–2148. https://doi.org/10.1021/acschembio.6b01014

Ioannidis, J. P. A., Kim, B. Y. S., & Trounson, A. (2018). How to design preclinical studies in nanomedicine and cell therapy to maximize the prospects of clinical translation. *Nature Biomedical Engineering*, *2*(11), 797–809. https://doi.org/10.1038/s41551-018-0314-y

Ioannou, M. S., Jackson, J., Sheu, S.-H., Chang, C.-L., Weigel, A. V., Liu, H., Pasolli, H. A., Xu, C. S., Pang, S., Matthies, D., Hess, H. F., Lippincott-Schwartz, J., & Liu, Z. (2019). Neuron-Astrocyte Metabolic Coupling Protects against Activity-Induced Fatty Acid Toxicity. *Cell*, *177*(6), 1522-1535.e14. https://doi.org/10.1016/j.cell.2019.04.001

Ishikawa, M., Cooper, D., Arumugam, T. V., Zhang, J. H., Nanda, A., & Granger, D. N. (2004). Platelet–Leukocyte–Endothelial Cell Interactions after Middle Cerebral Artery Occlusion and Reperfusion. *Journal of Cerebral Blood Flow & Metabolism*, *24*(8), 907–915. https://doi.org/10.1097/01.WCB.0000132690.96836.7F

Jackson, S., Meeks, C., Vézina, A., Robey, R. W., Tanner, K., & Gottesman, M. M. (2019). Model systems for studying the blood-brain barrier: Applications and challenges. *Biomaterials*, *214*, 119217. https://doi.org/10.1016/j.biomaterials.2019.05.028

Jacobsen, J. A., Major Jourden, J. L., Miller, M. T., & Cohen, S. M. (2010). To bind zinc or not to bind zinc: An examination of innovative approaches to improved metalloproteinase inhibition. *Biochimica et Biophysica Acta (BBA) - Molecular Cell Research*, *1803*(1), 72–94. https://doi.org/10.1016/j.bbamcr.2009.08.006

Ji, D. M. and J. (2019, September 30). *Nanostructured Modulators of Neuroglia*. Current Pharmaceutical Design. http://www.eurekaselect.com/174843/article

Ji, J., Moquin, A., Bertorelle, F., Ky Chang, P., Antoine, R., Luo, J., McKinney, R. A., & Maysinger, D. (2019). Organotypic and primary neural cultures as models to assess effects of different gold nanostructures on glia and neurons. *Nanotoxicology*, *13*(3), 285–304. https://doi.org/10.1080/17435390.2018.1543468

Johnson, B. E., Mazor, T., Hong, C., Barnes, M., Aihara, K., McLean, C. Y., Fouse, S. D., Yamamoto, S., Ueda, H., Tatsuno, K., Asthana, S., Jalbert, L. E., Nelson, S. J., Bollen, A. W., Gustafson, W. C.,

Charron, E., Weiss, W. A., Smirnov, I. V., Song, J. S., … Costello, J. F. (2014). Mutational Analysis Reveals the Origin and Therapy-driven Evolution of Recurrent Glioma. *Science (New York, N.Y.)*, *343*(6167), 189–193. https://doi.org/10.1126/science.1239947

Johnson, D. E., Ostrowski, P., Jaumouillé, V., & Grinstein, S. (2016). The position of lysosomes within the cell determines their luminal pH. *The Journal of Cell Biology*, *212*(6), 677–692. https://doi.org/10.1083/jcb.201507112

Johnstone, R. W. (2002). Histone-deacetylase inhibitors: Novel drugs for the treatment of cancer. *Nature Reviews. Drug Discovery*, *1*(4), 287–299. https://doi.org/10.1038/nrd772

Kalmbach, B. E., Buchin, A., Long, B., Close, J., Nandi, A., Miller, J. A., Bakken, T. E., Hodge, R. D., Chong, P., Frates, R. de, Dai, K., Maltzer, Z., Nicovich, P. R., Keene, C. D., Silbergeld, D. L., Gwinn, R. P., Cobbs, C., Ko, A. L., Ojemann, J. G., … Ting, J. T. (2018). H-Channels Contribute to Divergent Intrinsic Membrane Properties of Supragranular Pyramidal Neurons in Human versus Mouse Cerebral Cortex. *Neuron*, *100*(5), 1194-1208.e5. https://doi.org/10.1016/j.neuron.2018.10.012

Kamphorst, J. J., Cross, J. R., Fan, J., Stanchina, E. de, Mathew, R., White, E. P., Thompson, C. B., & Rabinowitz, J. D. (2013). Hypoxic and Ras-transformed cells support growth by scavenging unsaturated fatty acids from lysophospholipids. *Proceedings of the National Academy of Sciences*, *110*(22), 8882–8887. https://doi.org/10.1073/pnas.1307237110

Kant, S., Kesarwani, P., Prabhu, A., Graham, S. F., Buelow, K. L., Nakano, I., & Chinnaiyan, P. (2020). Enhanced fatty acid oxidation provides glioblastoma cells metabolic plasticity to accommodate to its dynamic nutrient microenvironment. *Cell Death & Disease*, *11*(4), 1–13. https://doi.org/10.1038/s41419-020-2449-5

Kanzawa, T., Germano, I. M., Komata, T., Ito, H., Kondo, Y., & Kondo, S. (2004). Role of autophagy in temozolomide-induced cytotoxicity for malignant glioma cells. *Cell Death and Differentiation*, *11*(4), 448–457. https://doi.org/10.1038/sj.cdd.4401359

Kekatpure, V. D., Dannenberg, A. J., & Subbaramaiah, K. (2009). HDAC6 Modulates Hsp90 Chaperone Activity and Regulates Activation of Aryl Hydrocarbon Receptor Signaling. *The Journal of Biological Chemistry*, *284*(12), 7436–7445. https://doi.org/10.1074/jbc.M808999200

Kepsutlu, B., Wycisk, V., Achazi, K., Kapishnikov, S., Pérez-Berná, A. J., Guttmann, P., Cossmer, A., Pereiro, E., Ewers, H., Ballauff, M., Schneider, G., & McNally, J. G. (2020). Cells Undergo Major Changes in the Quantity of Cytoplasmic Organelles after Uptake of Gold Nanoparticles with Biologically Relevant Surface Coatings. *ACS Nano*, *14*(2), 2248–2264. https://doi.org/10.1021/acsnano.9b09264

Keskin, D. B., Anandappa, A. J., Sun, J., Tirosh, I., Mathewson, N. D., Li, S., Oliveira, G., Giobbie-Hurder, A., Felt, K., Gjini, E., Shukla, S. A., Hu, Z., Li, L., Le, P. M., Allesøe, R. L., Richman, A. R., Kowalczyk, M. S., Abdelrahman, S., Geduldig, J. E., … Reardon, D. A. (2019). Neoantigen vaccine generates intratumoral T cell responses in phase Ib glioblastoma trial. *Nature*, *565*(7738), 234–239. https://doi.org/10.1038/s41586-018-0792-9

Khatchadourian, A., Bourque, S. D., Richard, V. R., Titorenko, V. I., & Maysinger, D. (2012). Dynamics and regulation of lipid droplet formation in lipopolysaccharide (LPS)-stimulated microglia. *Biochimica Et Biophysica Acta*, *1821*(4), 607–617. https://doi.org/10.1016/j.bbalip.2012.01.007

Kim, J.-H., Choi, A.-R., Kim, Y. K., & Yoon, S. (2013). Co-treatment with the anti-malarial drugs mefloquine and primaquine highly sensitizes drug-resistant cancer cells by increasing P-gp inhibition. *Biochemical and Biophysical Research Communications*, *441*(3), 655–660. https://doi.org/10.1016/j.bbrc.2013.10.095

Kobara, H., Miyamoto, T., Suzuki, A., Asaka, R., Yamada, Y., Ishikawa, K., Kikuchi, N., Ohira, S., & Shiozawa, T. (2013). Lipocalin2 enhances the matrix metalloproteinase-9 activity and invasion of extravillous trophoblasts under hypoxia. *Placenta*, *34*(11), 1036–1043. https://doi.org/10.1016/j.placenta.2013.08.004

Koizume, S., & Miyagi, Y. (2016). Lipid Droplets: A Key Cellular Organelle Associated with Cancer Cell Survival under Normoxia and Hypoxia. *International Journal of Molecular Sciences*, *17*(9). https://doi.org/10.3390/ijms17091430

Kroemer, G., Galluzzi, L., Vandenabeele, P., Abrams, J., Alnemri, E. S., Baehrecke, E. H., Blagosklonny, M. V., El-Deiry, W. S., Golstein, P., Green, D. R., Hengartner, M., Knight, R. A., Kumar, S., Lipton, S. A., Malorni, W., Nuñez, G., Peter, M. E., Tschopp, J., Yuan, J., … Nomenclature Committee on Cell Death 2009. (2009). Classification of cell death: Recommendations of the Nomenclature Committee on Cell Death 2009. *Cell Death and Differentiation*, *16*(1), 3–11. https://doi.org/10.1038/cdd.2008.150

Kucharzewska, P., Christianson, H. C., & Belting, M. (2015). Global profiling of metabolic adaptation to hypoxic stress in human glioblastoma cells. *PloS One*, *10*(1), e0116740. https://doi.org/10.1371/journal.pone.0116740

Kuhajda, F. P., Jenner, K., Wood, F. D., Hennigar, R. A., Jacobs, L. B., Dick, J. D., & Pasternack, G. R. (1994). Fatty acid synthesis: A potential selective target for antineoplastic therapy. *Proceedings of the National Academy of Sciences of the United States of America*, *91*(14), 6379–6383. https://doi.org/10.1073/pnas.91.14.6379

Kuhajda, F. P., Pizer, E. S., Li, J. N., Mani, N. S., Frehywot, G. L., & Townsend, C. A. (2000). Synthesis and antitumor activity of an inhibitor of fatty acid synthase. *Proceedings of the National Academy of Sciences of the United States of America*, *97*(7), 3450–3454. https://doi.org/10.1073/pnas.050582897

Kuhajda, Francis P. (2006). Fatty acid synthase and cancer: New application of an old pathway. *Cancer Research*, *66*(12), 5977–5980. https://doi.org/10.1158/0008-5472.CAN-05-4673

Kunwar, A., Barik, A., Pandey, R., & Priyadarsini, K. I. (2006). Transport of liposomal and albumin loaded curcumin to living cells: An absorption and fluorescence spectroscopic study. *Biochimica Et Biophysica Acta*, *1760*(10), 1513–1520. https://doi.org/10.1016/j.bbagen.2006.06.012

Lagoutte, D., Nicolas, V., Poupon, E., Fournet, A., Hocquemiller, R., Libong, D., Chaminade, P., & Loiseau, P. M. (2008). Antifungal canthin-6-one series accumulate in lipid droplets and affect fatty acid metabolism in Saccharomyces cerevisiae. *Biomedicine & Pharmacotherapy = Biomedecine & Pharmacotherapie*, *62*(2), 99–103. https://doi.org/10.1016/j.biopha.2007.07.014

Lancaster, M. A., & Knoblich, J. A. (2014). Generation of cerebral organoids from human pluripotent stem cells. *Nature Protocols*, *9*(10), 2329–2340. https://doi.org/10.1038/nprot.2014.158

Lancaster, M. A., Renner, M., Martin, C.-A., Wenzel, D., Bicknell, L. S., Hurles, M. E., Homfray, T., Penninger, J. M., Jackson, A. P., & Knoblich, J. A. (2013). Cerebral organoids model human brain development and microcephaly. *Nature*, *501*(7467), 373–379. https://doi.org/10.1038/nature12517

Lao, C. D., Ruffin, M. T., Normolle, D., Heath, D. D., Murray, S. I., Bailey, J. M., Boggs, M. E., Crowell, J., Rock, C. L., & Brenner, D. E. (2006). Dose escalation of a curcuminoid formulation. *BMC Complementary and Alternative Medicine*, *6*, 10. https://doi.org/10.1186/1472-6882-6-10

Lee, D. H., Ryu, H.-W., Won, H.-R., & Kwon, S. H. (2017). Advances in epigenetic glioblastoma therapy. *Oncotarget*, *8*(11), 18577–18589. https://doi.org/10.18632/oncotarget.14612

Lee, E. Q., Puduvalli, V. K., Reid, J. M., Kuhn, J. G., Lamborn, K. R., Cloughesy, T. F., Chang, S. M., Drappatz, J., Yung, W. K. A., Gilbert, M. R., Robins, H. I., Lieberman, F. S., Lassman, A. B., McGovern, R. M., Xu, J., Desideri, S., Ye, X., Ames, M. M., Espinoza-Delgado, I., … Wen, P. Y. (2012). Phase I Study of Vorinostat in Combination with Temozolomide in Patients with High-Grade Gliomas: North American Brain Tumor Consortium Study 04-03. *Clinical Cancer Research : An Official Journal of the American Association for Cancer Research*, *18*(21), 6032–6039. https://doi.org/10.1158/1078-0432.CCR-12-1841

Lee, H.-Y., Kim, S.-W., Lee, G.-H., Choi, M.-K., Chung, H.-W., Lee, Y.-C., Kim, H.-R., Kwon, H. J., & Chae, H.-J. (2017). Curcumin and Curcuma longa L. extract ameliorate lipid accumulation through the regulation of the endoplasmic reticulum redox and ER stress. *Scientific Reports*, *7*(1), 1–14. https://doi.org/10.1038/s41598-017-06872-y

Lee, J., Kotliarova, S., Kotliarov, Y., Li, A., Su, Q., Donin, N. M., Pastorino, S., Purow, B. W., Christopher, N., Zhang, W., Park, J. K., & Fine, H. A. (2006). Tumor stem cells derived from glioblastomas cultured in bFGF and EGF more closely mirror the phenotype and genotype of primary tumors than do serum-cultured cell lines. *Cancer Cell*, *9*(5), 391–403. https://doi.org/10.1016/j.ccr.2006.03.030

Lee, J.-H., Mahendran, A., Yao, Y., Ngo, L., Venta-Perez, G., Choy, M. L., Kim, N., Ham, W.-S., Breslow, R., & Marks, P. A. (2013). Development of a histone deacetylase 6 inhibitor and its biological effects. *Proceedings of the National Academy of Sciences of the United States of America*, *110*(39), 15704–15709. https://doi.org/10.1073/pnas.1313893110

Lee, S. W., Fraass, B. A., Marsh, L. H., Herbort, K., Gebarski, S. S., Martel, M. K., Radany, E. H., Lichter, A. S., & Sandler, H. M. (1999). Patterns of failure following high-dose 3-D conformal radiotherapy for high-grade astrocytomas: A quantitative dosimetric study. *International Journal of Radiation Oncology, Biology, Physics*, *43*(1), 79–88. https://doi.org/10.1016/s0360-3016(98)00266-1

Lee, S. Y. (2016a). Temozolomide resistance in glioblastoma multiforme. *Genes & Diseases*, *3*(3), 198–210. https://doi.org/10.1016/j.gendis.2016.04.007

Lee, S. Y. (2016b). Temozolomide resistance in glioblastoma multiforme. *Genes & Diseases*, *3*(3), 198–210. https://doi.org/10.1016/j.gendis.2016.04.007

Li, C., Wang, S., Yan, J.-L., Piper, R. J., Liu, H., Torheim, T., Kim, H., Zou, J., Boonzaier, N. R., Sinha, R., Matys, T., Markowetz, F., & Price, S. J. (2019). Intratumoral Heterogeneity of Glioblastoma Infiltration Revealed by Joint Histogram Analysis of Diffusion Tensor Imaging. *Neurosurgery*, *85*(4), 524–534. https://doi.org/10.1093/neuros/nyy388

Li, M., & Izpisua Belmonte, J. C. (2019). Organoids—Preclinical Models of Human Disease. *New England Journal of Medicine*, *380*(6), 569–579. https://doi.org/10.1056/NEJMra1806175

Li, S., Liu, X., Chen, X., Zhang, L., & Wang, X. (2015). Histone deacetylase 6 promotes growth of glioblastoma through inhibition of SMAD2 signaling. *Tumor Biology*, *36*(12), 9661–9665. https://doi.org/10.1007/s13277-015-3747-x

Li, T., Zhang, C., Hassan, S., Liu, X., Song, F., Chen, K., Zhang, W., & Yang, J. (2018). Histone deacetylase 6 in cancer. *Journal of Hematology & Oncology*, *11*(1), 111. https://doi.org/10.1186/s13045-018-0654-9

Li, Y., & Seto, E. (2016). HDACs and HDAC Inhibitors in Cancer Development and Therapy. *Cold Spring Harbor Perspectives in Medicine*, *6*(10). https://doi.org/10.1101/cshperspect.a026831

Liddelow, S. A., Guttenplan, K. A., Clarke, L. E., Bennett, F. C., Bohlen, C. J., Schirmer, L., Bennett, M. L., Münch, A. E., Chung, W.-S., Peterson, T. C., Wilton, D. K., Frouin, A., Napier, B. A., Panicker, N., Kumar, M., Buckwalter, M. S., Rowitch, D. H., Dawson, V. L., Dawson, T. M., … Barres, B. A. (2017). Neurotoxic reactive astrocytes are induced by activated microglia. *Nature*, *541*(7638), 481–487. https://doi.org/10.1038/nature21029

Lin, C.-C. J., Yu, K., Hatcher, A., Huang, T.-W., Lee, H. K., Carlson, J., Weston, M. C., Chen, F., Zhang, Y., Zhu, W., Mohila, C. A., Ahmed, N., Patel, A. J., Arenkiel, B. R., Noebels, J. L., Creighton, C. J., & Deneen, B. (2017). Identification of diverse astrocyte populations and their malignant analogs. *Nature Neuroscience*, *20*(3), 396–405. https://doi.org/10.1038/nn.4493

Lin, J.-K. (2007). Molecular targets of curcumin. *Advances in Experimental Medicine and Biology*, *595*, 227–243. https://doi.org/10.1007/978-0-387-46401-5_10

Lin, Y., Ren, J., & Qu, X. (2014). Catalytically active nanomaterials: A promising candidate for artificial enzymes. *Accounts of Chemical Research*, *47*(4), 1097–1105. https://doi.org/10.1021/ar400250z

Liu, G., Yuan, X., Zeng, Z., Tunici, P., Ng, H., Abdulkadir, I. R., Lu, L., Irvin, D., Black, K. L., & Yu, J. S. (2006). Analysis of gene expression and chemoresistance of CD133+ cancer stem cells in glioblastoma. *Molecular Cancer*, *5*, 67. https://doi.org/10.1186/1476-4598-5-67

Liu, L., Zhang, K., Sandoval, H., Yamamoto, S., Jaiswal, M., Sanz, E., Li, Z., Hui, J., Graham, B. H., Quintana, A., & Bellen, H. J. (2015). Glial lipid droplets and ROS induced by mitochondrial

defects promote neurodegeneration. *Cell*, *160*(1–2), 177–190. https://doi.org/10.1016/j.cell.2014.12.019

Liu, W., Fan, L. X., Zhou, X., Sweeney, W. E., Avner, E. D., & Li, X. (2012). HDAC6 Regulates Epidermal Growth Factor Receptor (EGFR) Endocytic Trafficking and Degradation in Renal Epithelial Cells. *PLoS ONE*, *7*(11). https://doi.org/10.1371/journal.pone.0049418

Lu, V. M., & McDonald, K. L. (2017). The current evidence of statin use affecting glioblastoma prognosis. *Journal of Clinical Neuroscience*, *42*, 196–197. https://doi.org/10.1016/j.jocn.2017.04.036

M Soliman, G. (2014). Miktoarm Star Micelles Containing Curcumin Reduce Cell Viability of Sensitized Glioblastoma. *Journal of Nanomedicine & Biotherapeutic Discovery*, *04*(02). https://doi.org/10.4172/2155-983X.1000124

Macairan, J.-R., Zhang, I., Clermont-Paquette, A., Naccache, R., & Maysinger, D. (2020). Optical Sensing: Ratiometric pH Sensing in Living Cells Using Carbon Dots (Part. Part. Syst. Charact. 1/2020). *Particle & Particle Systems Characterization*, *37*(1), 2070002. https://doi.org/10.1002/ppsc.202070002

Machado, E., White-Gilbertson, S., Vlekkert, D. van de, Janke, L., Moshiach, S., Campos, Y., Finkelstein, D., Gomero, E., Mosca, R., Qiu, X., Morton, C. L., Annunziata, I., & d'Azzo, A. (2015). Regulated lysosomal exocytosis mediates cancer progression. *Science Advances*, *1*(11), e1500603. https://doi.org/10.1126/sciadv.1500603

Mahoney, B. P., Raghunand, N., Baggett, B., & Gillies, R. J. (2003). Tumor acidity, ion trapping and chemotherapeutics. I. Acid pH affects the distribution of chemotherapeutic agents in vitro. *Biochemical Pharmacology*, *66*(7), 1207–1218.

Mariani, J., Coppola, G., Zhang, P., Abyzov, A., Provini, L., Tomasini, L., Amenduni, M., Szekely, A., Palejev, D., Wilson, M., Gerstein, M., Grigorenko, E. L., Chawarska, K., Pelphrey, K. A., Howe, J. R., & Vaccarino, F. M. (2015). FOXG1-Dependent Dysregulation of GABA/Glutamate Neuron

Differentiation in Autism Spectrum Disorders. *Cell*, *162*(2), 375–390. https://doi.org/10.1016/j.cell.2015.06.034

Markovic, D. S., Vinnakota, K., van Rooijen, N., Kiwit, J., Synowitz, M., Glass, R., & Kettenmann, H. (2011). Minocycline reduces glioma expansion and invasion by attenuating microglial MT1-MMP expression. *Brain, Behavior, and Immunity*, *25*(4), 624–628. https://doi.org/10.1016/j.bbi.2011.01.015

Marschallinger, J., Iram, T., Zardeneta, M., Lee, S. E., Lehallier, B., Haney, M. S., Pluvinage, J. V., Mathur, V., Hahn, O., Morgens, D. W., Kim, J., Tevini, J., Felder, T. K., Wolinski, H., Bertozzi, C. R., Bassik, M. C., Aigner, L., & Wyss-Coray, T. (2020). Lipid-droplet-accumulating microglia represent a dysfunctional and proinflammatory state in the aging brain. *Nature Neuroscience*, *23*(2), 194–208. https://doi.org/10.1038/s41593-019-0566-1

Marshall, J. J., & Mason, J. O. (2019). Mouse vs man: Organoid models of brain development & disease. *Brain Research*, *1724*, 146427. https://doi.org/10.1016/j.brainres.2019.146427

Marupudi, N. I., Han, J. E., Li, K. W., Renard, V. M., Tyler, B. M., & Brem, H. (2007). Paclitaxel: A review of adverse toxicities and novel delivery strategies. *Expert Opinion on Drug Safety*, *6*(5), 609–621. https://doi.org/10.1517/14740338.6.5.609

Marx, V. (2020). Reality check for organoids in neuroscience. *Nature Methods*, *17*(10), 961–964. https://doi.org/10.1038/s41592-020-0964-z

Masuda, T., Sankowski, R., Staszewski, O., Böttcher, C., Amann, L., Sagar, Scheiwe, C., Nessler, S., Kunz, P., van Loo, G., Coenen, V. A., Reinacher, P. C., Michel, A., Sure, U., Gold, R., Grün, D., Priller, J., Stadelmann, C., & Prinz, M. (2019). Spatial and temporal heterogeneity of mouse and human microglia at single-cell resolution. *Nature*, *566*(7744), 388–392. https://doi.org/10.1038/s41586-019-0924-x

Masuda, T., Sankowski, R., Staszewski, O., & Prinz, M. (2020). Microglia Heterogeneity in the Single-Cell Era. *Cell Reports*, *30*(5), 1271–1281. https://doi.org/10.1016/j.celrep.2020.01.010

Matarredona, E. R., & Pastor, A. M. (2020). Extracellular Vesicle-Mediated Communication between the Glioblastoma and Its Microenvironment. *Cells*, *9*(1), 96. https://doi.org/10.3390/cells9010096

Matias, D., Balça-Silva, J., da Graça, G. C., Wanjiru, C. M., Macharia, L. W., Nascimento, C. P., Roque, N. R., Coelho-Aguiar, J. M., Pereira, C. M., Dos Santos, M. F., Pessoa, L. S., Lima, F. R. S., Schanaider, A., Ferrer, V. P., Spohr, T. C. L. de S. e, & Moura-Neto, V. (2018). Microglia/Astrocytes–Glioblastoma Crosstalk: Crucial Molecular Mechanisms and Microenvironmental Factors. *Frontiers in Cellular Neuroscience*, *12*. https://doi.org/10.3389/fncel.2018.00235

Mayadas, T. N., Johnson, R. C., Rayburn, H., Hynes, R. O., & Wagner, D. D. (1993). Leukocyte rolling and extravasation are severely compromised in P selectin-deficient mice. *Cell*, *74*(3), 541–554. https://doi.org/10.1016/0092-8674(93)80055-J

Maysinger, D., Gran, E. R., Bertorelle, F., Fakhouri, H., Antoine, R., Kaul, E. S., Samhadaneh, D. A., & Stochaj, U. (2019). Gold nanoclusters elicit homeostatic perturbations in glioblastoma cells and adaptive changes of lysosomes. *Theranostics*. https://doi.org/10.7150/thno.37674

Maysinger, D., Groger, D., Lake, A., Licha, K., Weinhart, M., Chang, P. K.-Y., Mulvey, R., Haag, R., & McKinney, R. A. (2015). Dendritic Polyglycerol Sulfate Inhibits Microglial Activation and Reduces Hippocampal CA1 Dendritic Spine Morphology Deficits. *Biomacromolecules*, *16*(9), 3073–3082. https://doi.org/10.1021/acs.biomac.5b00999

Maysinger, D., Ji, J., Moquin, A., Hossain, S., Hancock, M. A., Zhang, I., Chang, P. K. Y., Rigby, M., Anthonisen, M., Grutter, P., Breitner, J., McKinney, R. A., Reimann, S., Haag, R., & Multhaup, G. (2018). Dendritic Polyglycerol Sulfates in the Prevention of Synaptic Loss and Mechanism of Action on Glia. *ACS Chemical Neuroscience*, *9*(2), 260–271. https://doi.org/10.1021/acschemneuro.7b00301

Maysinger, D., Lalancette-Hébert, M., Ji, J., Jabbour, K., Dernedde, J., Silberreis, K., Haag, R., & Kriz, J. (2019). Dendritic polyglycerols are modulators of microglia-astrocyte crosstalk. *Future Neurology*, *14*(4), FNL31. https://doi.org/10.2217/fnl-2019-0008

Maysinger, D., Moquin, A., Choi, J., Kodiha, M., & Stochaj, U. (2018). Gold nanourchins and celastrol reorganize the nucleo- and cytoskeleton of glioblastoma cells. *Nanoscale*, *10*(4), 1716–1726. https://doi.org/10.1039/c7nr07833a

Maysinger, D., & Zhang, I. (2016). Nutritional and Nanotechnological Modulators of Microglia. *Frontiers in Immunology*, *7*, 270. https://doi.org/10.3389/fimmu.2016.00270

Meacham, C. E., & Morrison, S. J. (2013). Tumour heterogeneity and cancer cell plasticity. *Nature*, *501*(7467), 328–337. https://doi.org/10.1038/nature12624

Medema, J. P. (2013). Cancer stem cells: The challenges ahead. *Nature Cell Biology*, *15*(4), 338–344. https://doi.org/10.1038/ncb2717

Melo, R. C. N., D'Ávila, H., Bozza, P. T., & Weller, P. F. (2011). Imaging Lipid Bodies Within Leukocytes with Different Light Microscopy Techniques. *Methods in Molecular Biology (Clifton, N.J.)*, *689*, 149–161. https://doi.org/10.1007/978-1-60761-950-5_9

Menassa, D. A., & Gomez-Nicola, D. (2018). Microglial Dynamics During Human Brain Development. *Frontiers in Immunology*, *9*. https://doi.org/10.3389/fimmu.2018.01014

Mendes, L. P., Sarisozen, C., Luther, E., Pan, J., & Torchilin, V. P. (2019). Surface-engineered polyethyleneimine-modified liposomes as novel carrier of siRNA and chemotherapeutics for combination treatment of drug-resistant cancers. *Drug Delivery*, *26*(1), 443–458. https://doi.org/10.1080/10717544.2019.1574935

Menendez, J. A., & Lupu, R. (2007). Fatty acid synthase and the lipogenic phenotype in cancer pathogenesis. *Nature Reviews. Cancer*, *7*(10), 763–777. https://doi.org/10.1038/nrc2222

Menge, T., Hartung, H.-P., & Stüve, O. (2005). Statins—A cure-all for the brain? *Nature Reviews. Neuroscience*, *6*(4), 325–331. https://doi.org/10.1038/nrn1652

Meunier, B. (2008). Hybrid Molecules with a Dual Mode of Action: Dream or Reality? *Accounts of Chemical Research*, *41*(1), 69–77. https://doi.org/10.1021/ar7000843

Moquin, A., Sharma, A., Cui, Y., Lau, A., Maysinger, D., & Kakkar, A. (2015). Asymmetric AB3 Miktoarm Star Polymers: Synthesis, Self-Assembly, and Study of Micelle Stability Using AF4

for Efficient Drug Delivery. *Macromolecular Bioscience*, *15*(12), 1744–1754. https://doi.org/10.1002/mabi.201500186

Moquin, A., Sturn, J., Zhang, I., Ji, J., von Celsing, R., Vali, H., Maysinger, D., & Kakkar, A. (2019). Unraveling Aqueous Self-Assembly of Telodendrimers to Shed Light on Their Efficacy in Drug Encapsulation. *ACS Applied Bio Materials*, *2*(10), 4515–4526. https://doi.org/10.1021/acsabm.9b00643

Moreland, R. B., Nam, H. G., Hereford, L. M., & Fried, H. M. (1985). Identification of a nuclear localization signal of a yeast ribosomal protein. *Proceedings of the National Academy of Sciences of the United States of America*, *82*(19), 6561–6565. https://doi.org/10.1073/pnas.82.19.6561

Morrissy, A. S., Cavalli, F. M. G., Remke, M., Ramaswamy, V., Shih, D. J. H., Holgado, B. L., Farooq, H., Donovan, L. K., Garzia, L., Agnihotri, S., Kiehna, E. N., Mercier, E., Mayoh, C., Papillon-Cavanagh, S., Nikbakht, H., Gayden, T., Torchia, J., Picard, D., Merino, D. M., … Taylor, M. D. (2017). Spatial heterogeneity in medulloblastoma. *Nature Genetics*, *49*(5), 780–788. https://doi.org/10.1038/ng.3838

Mummery, R. S., & Rider, C. C. (2000). Characterization of the heparin-binding properties of IL-6. *Journal of Immunology (Baltimore, Md.: 1950)*, *165*(10), 5671–5679. https://doi.org/10.4049/jimmunol.165.10.5671

Naci, H., Brugts, J., & Ades, T. (2013). Comparative tolerability and harms of individual statins: A study-level network meta-analysis of 246 955 participants from 135 randomized, controlled trials. *Circulation. Cardiovascular Quality and Outcomes*, *6*(4), 390–399. https://doi.org/10.1161/CIRCOUTCOMES.111.000071

Nakada, M., Okada, Y., & Yamashita, J. (2003). The role of matrix metalloproteinases in glioma invasion. *Frontiers in Bioscience: A Journal and Virtual Library*, *8*, e261-269.

Nakanishi, M., & Rosenberg, D. W. (2006). Roles of cPLA2α and Arachidonic Acid in Cancer. *Biochimica et Biophysica Acta*, *1761*(11), 1335–1343. https://doi.org/10.1016/j.bbalip.2006.09.005

Naksuriya, O., Shi, Y., van Nostrum, C. F., Anuchapreeda, S., Hennink, W. E., & Okonogi, S. (2015). HPMA-based polymeric micelles for curcumin solubilization and inhibition of cancer cell growth. *European Journal of Pharmaceutics and Biopharmaceutics: Official Journal of Arbeitsgemeinschaft Fur Pharmazeutische Verfahrenstechnik e.V*, *94*, 501–512. https://doi.org/10.1016/j.ejpb.2015.06.010

Narayana, A., Yamada, J., Berry, S., Shah, P., Hunt, M., Gutin, P. H., & Leibel, S. A. (2006). Intensity-modulated radiotherapy in high-grade gliomas: Clinical and dosimetric results. *International Journal of Radiation Oncology, Biology, Physics*, *64*(3), 892–897. https://doi.org/10.1016/j.ijrobp.2005.05.067

Nascimento, J. M., Saia-Cereda, V. M., Sartore, R. C., da Costa, R. M., Schitine, C. S., Freitas, H. R., Murgu, M., de Melo Reis, R. A., Rehen, S. K., & Martins-de-Souza, D. (2019). Human Cerebral Organoids and Fetal Brain Tissue Share Proteomic Similarities. *Frontiers in Cell and Developmental Biology*, *7*. https://doi.org/10.3389/fcell.2019.00303

Nichols, M. R., St-Pierre, M.-K., Wendeln, A.-C., Makoni, N. J., Gouwens, L. K., Garrad, E. C., Sohrabi, M., Neher, J. J., Tremblay, M.-E., & Combs, C. K. (2019). Inflammatory mechanisms in neurodegeneration. *Journal of Neurochemistry*, *149*(5), 562–581. https://doi.org/10.1111/jnc.14674

Olzmann, J. A., & Carvalho, P. (2019). Dynamics and functions of lipid droplets. *Nature Reviews Molecular Cell Biology*, *20*(3), 137–155. https://doi.org/10.1038/s41580-018-0085-z

ONC201 in Adults With Recurrent H3 K27M-mutant Glioma—Full Text View—ClinicalTrials.gov. (n.d.). Retrieved May 31, 2018, from https://clinicaltrials.gov/ct2/show/NCT03295396

Ono, T., Yamada, K., Chikazawa, Y., Ueno, M., Nakamoto, S., Okuno, T., & Seno, K. (2002a). Characterization of a novel inhibitor of cytosolic phospholipase A2alpha, pyrrophenone. *The Biochemical Journal*, *363*(Pt 3), 727–735. https://doi.org/10.1042/0264-6021:3630727

Ono, T., Yamada, K., Chikazawa, Y., Ueno, M., Nakamoto, S., Okuno, T., & Seno, K. (2002b). Characterization of a novel inhibitor of cytosolic phospholipase A2α, pyrrophenone. *Biochemical Journal*, *363*(3), 727–735. https://doi.org/10.1042/bj3630727

Ormel, P. R., Vieira de Sá, R., van Bodegraven, E. J., Karst, H., Harschnitz, O., Sneeboer, M. A. M., Johansen, L. E., van Dijk, R. E., Scheefhals, N., Berdenis van Berlekom, A., Ribes Martínez, E., Kling, S., MacGillavry, H. D., van den Berg, L. H., Kahn, R. S., Hol, E. M., de Witte, L. D., & Pasterkamp, R. J. (2018). Microglia innately develop within cerebral organoids. *Nature Communications*, *9*(1), 4167. https://doi.org/10.1038/s41467-018-06684-2

Ostrom, Q. T., Rubin, J. B., Lathia, J. D., Berens, M. E., & Barnholtz-Sloan, J. S. (2018). Females have the survival advantage in glioblastoma. *Neuro-Oncology*, *20*(4), 576–577. https://doi.org/10.1093/neuonc/noy002

Paolicelli, R. C., Bergamini, G., & Rajendran, L. (2019). Cell-to-cell Communication by Extracellular Vesicles: Focus on Microglia. *Neuroscience*, *405*, 148–157. https://doi.org/10.1016/j.neuroscience.2018.04.003

Parish, C. R. (2006). The role of heparan sulphate in inflammation. *Nature Reviews Immunology*, *6*(9), 633–643. https://doi.org/10.1038/nri1918

Parveen, S., Misra, R., & Sahoo, S. K. (2012). Nanoparticles: A boon to drug delivery, therapeutics, diagnostics and imaging. *Nanomedicine: Nanotechnology, Biology and Medicine*, *8*(2), 147–166. https://doi.org/10.1016/j.nano.2011.05.016

Patel, A. P., Tirosh, I., Trombetta, J. J., Shalek, A. K., Gillespie, S. M., Wakimoto, H., Cahill, D. P., Nahed, B. V., Curry, W. T., Martuza, R. L., Louis, D. N., Rozenblatt-Rosen, O., Suvà, M. L., Regev, A., & Bernstein, B. E. (2014). Single-cell RNA-seq highlights intratumoral heterogeneity in primary glioblastoma. *Science (New York, N.Y.)*, *344*(6190), 1396–1401. https://doi.org/10.1126/science.1254257

Pathria, P., Louis, T. L., & Varner, J. A. (2019). Targeting Tumor-Associated Macrophages in Cancer. *Trends in Immunology*, *40*(4), 310–327. https://doi.org/10.1016/j.it.2019.02.003

Patterson, A. D., Maurhofer, O., Beyoglu, D., Lanz, C., Krausz, K. W., Pabst, T., Gonzalez, F. J., Dufour, J.-F., & Idle, J. R. (2011). Aberrant lipid metabolism in hepatocellular carcinoma revealed by plasma metabolomics and lipid profiling. *Cancer Research*, *71*(21), 6590–6600. https://doi.org/10.1158/0008-5472.CAN-11-0885

Peters, K. B., Lipp, E. S., Miller, E., Herndon, J. E., McSherry, F., Desjardins, A., Reardon, D. A., & Friedman, H. S. (2018). Phase I/II trial of vorinostat, bevacizumab, and daily temozolomide for recurrent malignant gliomas. *Journal of Neuro-Oncology*, *137*(2), 349–356. https://doi.org/10.1007/s11060-017-2724-1

Petrecca, K., Guiot, M.-C., Panet-Raymond, V., & Souhami, L. (2013). Failure pattern following complete resection plus radiotherapy and temozolomide is at the resection margin in patients with glioblastoma. *Journal of Neuro-Oncology*, *111*(1), 19–23. https://doi.org/10.1007/s11060-012-0983-4

Porter, N. J., Osko, J. D., Diedrich, D., Kurz, T., Hooker, J. M., Hansen, F. K., & Christianson, D. W. (2018). Histone Deacetylase 6-Selective Inhibitors and the Influence of Capping Groups on Hydroxamate-Zinc Denticity. *Journal of Medicinal Chemistry*, *61*(17), 8054–8060. https://doi.org/10.1021/acs.jmedchem.8b01013

Porter, N. J., Shen, S., Barinka, C., Kozikowski, A. P., & Christianson, D. W. (2018). Molecular Basis for the Selective Inhibition of Histone Deacetylase 6 by a Mercaptoacetamide Inhibitor. *ACS Medicinal Chemistry Letters*, *9*(12), 1301–1305. https://doi.org/10.1021/acsmedchemlett.8b00487

Pósfai, B., Cserép, C., Orsolits, B., & Dénes, Á. (2019). New Insights into Microglia–Neuron Interactions: A Neuron's Perspective. *Neuroscience*, *405*, 103–117. https://doi.org/10.1016/j.neuroscience.2018.04.046

Prasanna, P., Thibault, A., Liu, L., & Samid, D. (1996). Lipid metabolism as a target for brain cancer therapy: Synergistic activity of lovastatin and sodium phenylacetate against human glioma cells. *Journal of Neurochemistry*, *66*(2), 710–716. https://doi.org/10.1046/j.1471-4159.1996.66020710.x

Prinz, M., Jung, S., & Priller, J. (2019). Microglia Biology: One Century of Evolving Concepts. *Cell*, *179*(2), 292–311. https://doi.org/10.1016/j.cell.2019.08.053

Priyadarsini, K. I. (2013). Chemical and structural features influencing the biological activity of curcumin. *Current Pharmaceutical Design*, *19*(11), 2093–2100. https://doi.org/10.2174/138161213805289228

Pu, J., Guardia, C. M., Keren-Kaplan, T., & Bonifacino, J. S. (2016). Mechanisms and functions of lysosome positioning. *Journal of Cell Science*, *129*(23), 4329–4339. https://doi.org/10.1242/jcs.196287

Quail, D. F., & Joyce, J. A. (2017). The Microenvironmental Landscape of Brain Tumors. *Cancer Cell*, *31*(3), 326–341. https://doi.org/10.1016/j.ccell.2017.02.009

Quang, T. S., & Brady, L. W. (2004). Radioimmunotherapy as a novel treatment regimen: 125I-labeled monoclonal antibody 425 in the treatment of high-grade brain gliomas. *International Journal of Radiation Oncology, Biology, Physics*, *58*(3), 972–975. https://doi.org/10.1016/j.ijrobp.2003.09.096

Rabanel, J.-M., Faivre, J., Paka, G. D., Ramassamy, C., Hildgen, P., & Banquy, X. (2015). Effect of polymer architecture on curcumin encapsulation and release from PEGylated polymer nanoparticles: Toward a drug delivery nano-platform to the CNS. *European Journal of Pharmaceutics and Biopharmaceutics: Official Journal of Arbeitsgemeinschaft Fur Pharmazeutische Verfahrenstechnik e.V*, *96*, 409–420. https://doi.org/10.1016/j.ejpb.2015.09.004

Rades, N., Licha, K., & Haag, R. (2018). Dendritic Polyglycerol Sulfate for Therapy and Diagnostics. *Polymers*, *10*(6). https://doi.org/10.3390/polym10060595

Rahman, R., Hempfling, K., Norden, A. D., Reardon, D. A., Nayak, L., Rinne, M. L., Beroukhim, R., Doherty, L., Ruland, S., Rai, A., Rifenburg, J., LaFrankie, D., Alexander, B. M., Huang, R. Y., Wen, P. Y., & Lee, E. Q. (2014). Retrospective study of carmustine or lomustine with bevacizumab in recurrent glioblastoma patients who have failed prior bevacizumab. *Neuro-Oncology*, *16*(11), 1523–1529. https://doi.org/10.1093/neuonc/nou118

Raja, W. K., Mungenast, A. E., Lin, Y.-T., Ko, T., Abdurrob, F., Seo, J., & Tsai, L.-H. (2016). Self-Organizing 3D Human Neural Tissue Derived from Induced Pluripotent Stem Cells Recapitulate Alzheimer's Disease Phenotypes. *PloS One*, *11*(9), e0161969. https://doi.org/10.1371/journal.pone.0161969

Rak, S., De Zan, T., Stefulj, J., Kosović, M., Gamulin, O., & Osmak, M. (2014). FTIR spectroscopy reveals lipid droplets in drug resistant laryngeal carcinoma cells through detection of increased ester vibrational bands intensity. *The Analyst*, *139*(13), 3407–3415. https://doi.org/10.1039/c4an00412d

Ramachandran, R. K., Sørensen, M. D., Aaberg-Jessen, C., Hermansen, S. K., & Kristensen, B. W. (2017). Expression and prognostic impact of matrix metalloproteinase-2 (MMP-2) in astrocytomas. *PLoS ONE*, *12*(2). https://doi.org/10.1371/journal.pone.0172234

Rapoport, B. L., Steel, H. C., Theron, A. J., Heyman, L., Smit, T., Ramdas, Y., & Anderson, R. (2020). High Mobility Group Box 1 in Human Cancer. *Cells*, *9*(7), 1664. https://doi.org/10.3390/cells9071664

Renehan, A. G., Zwahlen, M., & Egger, M. (2015). Adiposity and cancer risk: New mechanistic insights from epidemiology. *Nature Reviews. Cancer*, *15*(8), 484–498. https://doi.org/10.1038/nrc3967

Rodell, C. B., Arlauckas, S. P., Cuccarese, M. F., Garris, C. S., Li, R., Ahmed, M. S., Kohler, R. H., Pittet, M. J., & Weissleder, R. (2018). TLR7/8-agonist-loaded nanoparticles promote the polarization of tumour-associated macrophages to enhance cancer immunotherapy. *Nature Biomedical Engineering*, *2*(8), 578–588. https://doi.org/10.1038/s41551-018-0236-8

Rodríguez-Gómez, J. A., Kavanagh, E., Engskog-Vlachos, P., Engskog, M. K. R., Herrera, A. J., Espinosa-Oliva, A. M., Joseph, B., Hajji, N., Venero, J. L., & Burguillos, M. A. (2020). Microglia: Agents of the CNS Pro-Inflammatory Response. *Cells*, *9*(7). https://doi.org/10.3390/cells9071717

Roesch, S., Rapp, C., Dettling, S., & Herold-Mende, C. (2018). When Immune Cells Turn Bad—Tumor-Associated Microglia/Macrophages in Glioma. *International Journal of Molecular Sciences*, *19*(2). https://doi.org/10.3390/ijms19020436

Rossi, G., Manfrin, A., & Lutolf, M. P. (2018). Progress and potential in organoid research. *Nature Reviews Genetics*, *19*(11), 671–687. https://doi.org/10.1038/s41576-018-0051-9

Ruehl, M. L., Orozco, J. A., Stoker, M. B., McDonagh, P. F., Coull, B. M., & Ritter, L. S. (2002). Protective effects of inhibiting both blood and vascular selectins after stroke and reperfusion. *Neurological Research*, *24*(3), 226–232. https://doi.org/10.1179/016164102101199738

Sackett, D. L., & Wolff, J. (1987). Nile red as a polarity-sensitive fluorescent probe of hydrophobic protein surfaces. *Analytical Biochemistry*, *167*(2), 228–234. https://doi.org/10.1016/0003-2697(87)90157-6

Sanchez-Vega, F., Mina, M., Armenia, J., Chatila, W. K., Luna, A., La, K. C., Dimitriadoy, S., Liu, D. L., Kantheti, H. S., Saghafinia, S., Chakravarty, D., Daian, F., Gao, Q., Bailey, M. H., Liang, W.-W., Foltz, S. M., Shmulevich, I., Ding, L., Heins, Z., … Schultz, N. (2018). Oncogenic Signaling Pathways in The Cancer Genome Atlas. *Cell*, *173*(2), 321-337.e10. https://doi.org/10.1016/j.cell.2018.03.035

Sandler, S. R., & Berg, F. R. (1966). Room temperature polymerization of glycidol. *Journal of Polymer Science A Polymer Chemistry*, *4*, 1253–1259. https://doi.org/10.1002/pol.1966.150040523

Santo, L., Hideshima, T., Kung, A. L., Tseng, J.-C., Tamang, D., Yang, M., Jarpe, M., van Duzer, J. H., Mazitschek, R., Ogier, W. C., Cirstea, D., Rodig, S., Eda, H., Scullen, T., Canavese, M., Bradner, J., Anderson, K. C., Jones, S. S., & Raje, N. (2012). Preclinical activity, pharmacodynamic, and pharmacokinetic properties of a selective HDAC6 inhibitor, ACY-1215, in combination with bortezomib in multiple myeloma. *Blood*, *119*(11), 2579–2589. https://doi.org/10.1182/blood-2011-10-387365

Santos, C. R., & Schulze, A. (2012). Lipid metabolism in cancer. *The FEBS Journal*, *279*(15), 2610–2623. https://doi.org/10.1111/j.1742-4658.2012.08644.x

Sarkar, S., & Yong, V. W. (2014). The battle for the brain. *Oncoimmunology*, *3*. https://doi.org/10.4161/onci.28047

Sarkaria, J. N., Hu, L. S., Parney, I. F., Pafundi, D. H., Brinkmann, D. H., Laack, N. N., Giannini, C., Burns, T. C., Kizilbash, S. H., Laramy, J. K., Swanson, K. R., Kaufmann, T. J., Brown, P. D., Agar, N. Y. R., Galanis, E., Buckner, J. C., & Elmquist, W. F. (2018). Is the blood-brain barrier really disrupted in all glioblastomas? A critical assessment of existing clinical data. *Neuro-Oncology*, *20*(2), 184–191. https://doi.org/10.1093/neuonc/nox175

Savić, R., Eisenberg, A., & Maysinger, D. (2006). Block copolymer micelles as delivery vehicles of hydrophobic drugs: Micelle-cell interactions. *Journal of Drug Targeting*, *14*(6), 343–355. https://doi.org/10.1080/10611860600874538

Schäfer, S., Saunders, L., Eliseeva, E., Velena, A., Jung, M., Schwienhorst, A., Strasser, A., Dickmanns, A., Ficner, R., Schlimme, S., Sippl, W., Verdin, E., & Jung, M. (2008). Phenylalanine-containing hydroxamic acids as selective inhibitors of class IIb histone deacetylases (HDACs). *Bioorganic & Medicinal Chemistry*, *16*(4), 2011–2033. https://doi.org/10.1016/j.bmc.2007.10.092

Schulze, R. J., Sathyanarayan, A., & Mashek, D. G. (2017). Breaking fat: The regulation and mechanisms of lipophagy. *Biochimica et Biophysica Acta*, *1862*(10 Pt B), 1178–1187. https://doi.org/10.1016/j.bbalip.2017.06.008

Schütze, F., Röhrig, F., Vorlová, S., Gätzner, S., Kuhn, A., Ergün, S., & Henke, E. (2015). Inhibition of Lysyl Oxidases Improves Drug Diffusion and Increases Efficacy of Cytotoxic Treatment in 3D Tumor Models. *Scientific Reports*, *5*, 17576. https://doi.org/10.1038/srep17576

Schwartz, K. A., Noel, M., Nikolai, M., & Chang, H. T. (2018). Investigating the Ketogenic Diet As Treatment for Primary Aggressive Brain Cancer: Challenges and Lessons Learned. *Frontiers in Nutrition*, *5*. https://doi.org/10.3389/fnut.2018.00011

Senapati, S., Mahanta, A. K., Kumar, S., & Maiti, P. (2018). Controlled drug delivery vehicles for cancer treatment and their performance. *Signal Transduction and Targeted Therapy*, *3*(1), 1–19. https://doi.org/10.1038/s41392-017-0004-3

Seno, K., Okuno, T., Nishi, K., Murakami, Y., Watanabe, F., Matsuura, T., Wada, M., Fujii, Y., Yamada, M., Ogawa, T., Okada, T., Hashizume, H., Kii, M., Hara, S., Hagishita, S., Nakamoto, S., Yamada, K., Chikazawa, Y., Ueno, M., … Ohtani, M. (2000). Pyrrolidine inhibitors of human cytosolic phospholipase A(2). *Journal of Medicinal Chemistry*, *43*(6), 1041–1044. https://doi.org/10.1021/jm9905155

Sesen, J., Dahan, P., Scotland, S. J., Saland, E., Dang, V.-T., Lemarié, A., Tyler, B. M., Brem, H., Toulas, C., Cohen-Jonathan Moyal, E., Sarry, J.-E., & Skuli, N. (2015). Metformin inhibits growth of human glioblastoma cells and enhances therapeutic response. *PloS One*, *10*(4), e0123721. https://doi.org/10.1371/journal.pone.0123721

Sharma, P., Wagner, K., Wolchok, J. D., & Allison, J. P. (2011). Novel cancer immunotherapy agents with survival benefit: Recent successes and next steps. *Nature Reviews. Cancer*, *11*(11), 805–812. https://doi.org/10.1038/nrc3153

Shen, Y., Grisdale, C. J., Islam, S. A., Bose, P., Lever, J., Zhao, E. Y., Grinshtein, N., Ma, Y., Mungall, A. J., Moore, R. A., Lun, X., Senger, D. L., Robbins, S. M., Wang, A. Y., MacIsaac, J. L., Kobor, M. S., Luchman, H. A., Weiss, S., Chan, J. A., … Jones, S. J. M. (2019). Comprehensive genomic profiling of glioblastoma tumors, BTICs, and xenografts reveals stability and adaptation to growth environments. *Proceedings of the National Academy of Sciences of the United States of America*, *116*(38), 19098–19108. https://doi.org/10.1073/pnas.1813495116

Shergalis, A., Bankhead, A., Luesakul, U., Muangsin, N., & Neamati, N. (2018). Current Challenges and Opportunities in Treating Glioblastoma. *Pharmacological Reviews*, *70*(3), 412–445. https://doi.org/10.1124/pr.117.014944

Shigemoto-Mogami, Y., Hoshikawa, K., & Sato, K. (2018). Activated Microglia Disrupt the Blood-Brain Barrier and Induce Chemokines and Cytokines in a Rat in vitro Model. *Frontiers in Cellular Neuroscience*, *12*. https://doi.org/10.3389/fncel.2018.00494

Shinde, R. L., Bharkad, G. P., & Devarajan, P. V. (2015). Intranasal microemulsion for targeted nose to brain delivery in neurocysticercosis: Role of docosahexaenoic acid. *European Journal of*

Pharmaceutics and Biopharmaceutics: Official Journal of Arbeitsgemeinschaft Fur Pharmazeutische Verfahrenstechnik e.V, *96*, 363–379. https://doi.org/10.1016/j.ejpb.2015.08.008

Shinojima, N., Tada, K., Shiraishi, S., Kamiryo, T., Kochi, M., Nakamura, H., Makino, K., Saya, H., Hirano, H., Kuratsu, J.-I., Oka, K., Ishimaru, Y., & Ushio, Y. (2003). Prognostic value of epidermal growth factor receptor in patients with glioblastoma multiforme. *Cancer Research*, *63*(20), 6962–6970.

Shukla, S., & Tekwani, B. L. (2020). Histone Deacetylases Inhibitors in Neurodegenerative Diseases, Neuroprotection and Neuronal Differentiation. *Frontiers in Pharmacology*, *11*. https://doi.org/10.3389/fphar.2020.00537

Siew, J. J., & Chern, Y. (2018). Microglial Lectins in Health and Neurological Diseases. *Frontiers in Molecular Neuroscience*, *11*. https://doi.org/10.3389/fnmol.2018.00158

Sikora, E., Bielak-Zmijewska, A., Magalska, A., Piwocka, K., Mosieniak, G., Kalinowska, M., Widlak, P., Cymerman, I. A., & Bujnicki, J. M. (2006). Curcumin induces caspase-3-dependent apoptotic pathway but inhibits DNA fragmentation factor 40/caspase-activated DNase endonuclease in human Jurkat cells. *Molecular Cancer Therapeutics*, *5*(4), 927–934. https://doi.org/10.1158/1535-7163.MCT-05-0360

Simon, E., Obst, J., & Gomez-Nicola, D. (2019). The Evolving Dialogue of Microglia and Neurons in Alzheimer's Disease: Microglia as Necessary Transducers of Pathology. *Neuroscience*, *405*, 24–34. https://doi.org/10.1016/j.neuroscience.2018.01.059

Sims, G. P., Rowe, D. C., Rietdijk, S. T., Herbst, R., & Coyle, A. J. (2010). HMGB1 and RAGE in Inflammation and Cancer. *Annual Review of Immunology*, *28*(1), 367–388. https://doi.org/10.1146/annurev.immunol.021908.132603

Singh, S. K., Hawkins, C., Clarke, I. D., Squire, J. A., Bayani, J., Hide, T., Henkelman, R. M., Cusimano, M. D., & Dirks, P. B. (2004). Identification of human brain tumour initiating cells. *Nature*, *432*(7015), 396–401. https://doi.org/10.1038/nature03128

Sitharaman, B. (2016). *Nanobiomaterials Handbook*. CRC Press.

Song, L., Yuan, X., Jones, Z., Vied, C., Miao, Y., Marzano, M., Hua, T., Sang, Q.-X. A., Guan, J., Ma, T., Zhou, Y., & Li, Y. (2019). Functionalization of Brain Region-specific Spheroids with Isogenic Microglia-like Cells. *Scientific Reports*, *9*. https://doi.org/10.1038/s41598-019-47444-6

Sottoriva, A., Spiteri, I., Piccirillo, S. G. M., Touloumis, A., Collins, V. P., Marioni, J. C., Curtis, C., Watts, C., & Tavaré, S. (2013). Intratumor heterogeneity in human glioblastoma reflects cancer evolutionary dynamics. *Proceedings of the National Academy of Sciences of the United States of America*, *110*(10), 4009–4014. https://doi.org/10.1073/pnas.1219747110

Soubannier, V., & Stifani, S. (2017). NF-κB Signalling in Glioblastoma. *Biomedicines*, *5*(2). https://doi.org/10.3390/biomedicines5020029

Sounni, N. E., Cimino, J., Blacher, S., Primac, I., Truong, A., Mazzucchelli, G., Paye, A., Calligaris, D., Debois, D., De Tullio, P., Mari, B., De Pauw, E., & Noel, A. (2014). Blocking lipid synthesis overcomes tumor regrowth and metastasis after antiangiogenic therapy withdrawal. *Cell Metabolism*, *20*(2), 280–294. https://doi.org/10.1016/j.cmet.2014.05.022

Sousa-Herves, A., Würfel, P., Wegner, N., Khandare, J., Licha, K., Haag, R., Welker, P., & Calderón, M. (2015). Dendritic polyglycerol sulfate as a novel platform for paclitaxel delivery: Pitfalls of ester linkage. *Nanoscale*, *7*(9), 3923–3932. https://doi.org/10.1039/C4NR04428B

Sowers, J. L., Johnson, K. M., Conrad, C., Patterson, J. T., & Sowers, L. C. (2014). The Role of Inflammation in Brain Cancer. In B. B. Aggarwal, B. Sung, & S. C. Gupta (Eds.), *Inflammation and Cancer* (pp. 75–105). Springer. https://doi.org/10.1007/978-3-0348-0837-8_4

Sperry, J., Belle, J. E. L., Condro, M. C., Guo, L., Braas, D., Vanderveer-Harris, N., Kim, K. K. O., Pope, W. B., Divakaruni, A. S., Lai, A., Christofk, H., & Kornblum, H. I. (2019). Metabolism of fatty acids and ketone bodies for glioblastoma growth: Implications for Ketogenic Diet Therapy. *BioRxiv*, 659474. https://doi.org/10.1101/659474

Srivastava, S., Somasagara, R. R., Hegde, M., Nishana, M., Tadi, S. K., Srivastava, M., Choudhary, B., & Raghavan, S. C. (2016). Quercetin, a Natural Flavonoid Interacts with DNA, Arrests Cell Cycle

and Causes Tumor Regression by Activating Mitochondrial Pathway of Apoptosis. *Scientific Reports*, *6*, 24049. https://doi.org/10.1038/srep24049

Starobova, H., & Vetter, I. (2017). Pathophysiology of Chemotherapy-Induced Peripheral Neuropathy. *Frontiers in Molecular Neuroscience*, *10*. https://doi.org/10.3389/fnmol.2017.00174

Stephenson, D. T., Manetta, J. V., White, D. L., Chiou, X. G., Cox, L., Gitter, B., May, P. C., Sharp, J. D., Kramer, R. M., & Clemens, J. A. (1994). Calcium-sensitive cytosolic phospholipase A2 (cPLA2) is expressed in human brain astrocytes. *Brain Research*, *637*(1–2), 97–105. https://doi.org/10.1016/0006-8993(94)91221-1

Strickland, M., & Stoll, E. A. (2017). Metabolic Reprogramming in Glioma. *Frontiers in Cell and Developmental Biology*, *5*. https://doi.org/10.3389/fcell.2017.00043

Stupp, R., Mason, W. P., van den Bent, M. J., Weller, M., Fisher, B., Taphoorn, M. J. B., Belanger, K., Brandes, A. A., Marosi, C., Bogdahn, U., Curschmann, J., Janzer, R. C., Ludwin, S. K., Gorlia, T., Allgeier, A., Lacombe, D., Cairncross, J. G., Eisenhauer, E., & Mirimanoff, R. O. (2005). Radiotherapy plus Concomitant and Adjuvant Temozolomide for Glioblastoma. *New England Journal of Medicine*, *352*(10), 987–996. https://doi.org/10.1056/NEJMoa043330

Stupp, R., Taillibert, S., Kanner, A., Read, W., Steinberg, D. M., Lhermitte, B., Toms, S., Idbaih, A., Ahluwalia, M. S., Fink, K., Meco, F. D., Lieberman, F., Zhu, J.-J., Stragliotto, G., Tran, D. D., Brem, S., Hottinger, A. F., Kirson, E. D., Lavy-Shahaf, G., … Ram, Z. (2017). Effect of Tumor-Treating Fields Plus Maintenance Temozolomide vs Maintenance Temozolomide Alone on Survival in Patients With Glioblastoma: A Randomized Clinical Trial. *JAMA*, *318*(23), 2306–2316. https://doi.org/10.1001/jama.2017.18718

Subhan, M. A., & Torchilin, V. P. (2019). Efficient nanocarriers of siRNA therapeutics for cancer treatment. *Translational Research: The Journal of Laboratory and Clinical Medicine*, *214*, 62–91. https://doi.org/10.1016/j.trsl.2019.07.006

Subramanian, S., Bates, S. E., Wright, J. J., Espinoza-Delgado, I., & Piekarz, R. L. (2010). Clinical Toxicities of Histone Deacetylase Inhibitors. *Pharmaceuticals*, *3*(9), 2751–2767. https://doi.org/10.3390/ph3092751

Sun, G. Y., Shelat, P. B., Jensen, M. B., He, Y., Sun, A. Y., & Simonyi, A. (2010). Phospholipases A2 and inflammatory responses in the central nervous system. *Neuromolecular Medicine*, *12*(2), 133–148. https://doi.org/10.1007/s12017-009-8092-z

Sun, S., Gong, F., Liu, P., & Miao, Q. (2018). Metformin combined with quercetin synergistically repressed prostate cancer cells via inhibition of VEGF/PI3K/Akt signaling pathway. *Gene*, *664*, 50–57. https://doi.org/10.1016/j.gene.2018.04.045

Sundler, R. (1997). Lysosomal and cytosolic pH as regulators of exocytosis in mouse macrophages. *Acta Physiologica Scandinavica*, *161*(4), 553–556. https://doi.org/10.1046/j.1365-201X.1997.00262.x

Suraweera, A., O'Byrne, K. J., & Richard, D. J. (2018). Combination Therapy With Histone Deacetylase Inhibitors (HDACi) for the Treatment of Cancer: Achieving the Full Therapeutic Potential of HDACi. *Frontiers in Oncology*, *8*. https://doi.org/10.3389/fonc.2018.00092

Sweeney, M. D., Zhao, Z., Montagne, A., Nelson, A. R., & Zlokovic, B. V. (2019). Blood-Brain Barrier: From Physiology to Disease and Back. *Physiological Reviews*, *99*(1), 21–78. https://doi.org/10.1152/physrev.00050.2017

Swinnen, J. V., Brusselmans, K., & Verhoeven, G. (2006). Increased lipogenesis in cancer cells: New players, novel targets. *Current Opinion in Clinical Nutrition and Metabolic Care*, *9*(4), 358–365. https://doi.org/10.1097/01.mco.0000232894.28674.30

Tabrizi, R., Vakili, S., Lankarani, K. B., Akbari, M., Mirhosseini, N., Ghayour-Mobarhan, M., Ferns, G., Karamali, F., Karamali, M., Taghizadeh, M., Kouchaki, E., & Asemi, Z. (2018). The Effects of Curcumin on Glycemic Control and Lipid Profiles Among Patients with Metabolic Syndrome and Related Disorders: A Systematic Review and Metaanalysis of Randomized Controlled Trials. *Current Pharmaceutical Design*, *24*(27), 3184–3199. https://doi.org/10.2174/1381612824666180828162053

Tabuchi, S., Uozumi, N., Ishii, S., Shimizu, Y., Watanabe, T., & Shimizu, T. (2003). Mice deficient in cytosolic phospholipase A2 are less susceptible to cerebral ischemia/reperfusion injury. *Acta Neurochirurgica. Supplement*, *86*, 169–172. https://doi.org/10.1007/978-3-7091-0651-8_36

Tafani, M., Di Vito, M., Frati, A., Pellegrini, L., De Santis, E., Sette, G., Eramo, A., Sale, P., Mari, E., Santoro, A., Raco, A., Salvati, M., De Maria, R., & Russo, M. A. (2011). Pro-inflammatory gene expression in solid glioblastoma microenvironment and in hypoxic stem cells from human glioblastoma. *Journal of Neuroinflammation*, *8*, 32. https://doi.org/10.1186/1742-2094-8-32

Tai, N., Kuwabara, K., Kobayashi, M., Yamada, K., Ono, T., Seno, K., Gahara, Y., Ishizaki, J., & Hori, Y. (2010). Cytosolic phospholipase A2 alpha inhibitor, pyrroxyphene, displays anti-arthritic and anti-bone destructive action in a murine arthritis model. *Inflammation Research: Official Journal of the European Histamine Research Society ... [et Al.]*, *59*(1), 53–62. https://doi.org/10.1007/s00011-009-0069-8

Taïb, B., Aboussalah, A. M., Moniruzzaman, M., Chen, S., Haughey, N. J., Kim, S. F., & Ahima, R. S. (2019). Lipid accumulation and oxidation in glioblastoma multiforme. *Scientific Reports*, *9*(1), 1–14. https://doi.org/10.1038/s41598-019-55985-z

Takebe, T., & Wells, J. M. (2019). Organoids by design. *Science*, *364*(6444), 956–959. https://doi.org/10.1126/science.aaw7567

Thiam, A. R., Farese Jr, R. V., & Walther, T. C. (2013). The biophysics and cell biology of lipid droplets. *Nature Reviews Molecular Cell Biology*, *14*(12), 775–786. https://doi.org/10.1038/nrm3699

Tremblay, M.-E., Zhang, I., Bisht, K., Savage, J. C., Lecours, C., Parent, M., Titorenko, V., & Maysinger, D. (2016). Remodeling of lipid bodies by docosahexaenoic acid in activated microglial cells. *Journal of Neuroinflammation*, *13*(1), 116. https://doi.org/10.1186/s12974-016-0580-0

Treyer, A., Mateus, A., Wiśniewski, J. R., Boriss, H., Matsson, P., & Artursson, P. (2018). Intracellular Drug Bioavailability: Effect of Neutral Lipids and Phospholipids. *Molecular Pharmaceutics*, *15*(6), 2224–2233. https://doi.org/10.1021/acs.molpharmaceut.8b00064

Trifiletti, D. M., Alonso, C., Grover, S., Fadul, C. E., Sheehan, J. P., & Showalter, T. N. (2017). Prognostic Implications of Extent of Resection in Glioblastoma: Analysis from a Large Database. *World Neurosurgery*, *103*, 330–340. https://doi.org/10.1016/j.wneu.2017.04.035

Türk, H., Haag, R., & Alban, S. (2004). Dendritic Polyglycerol Sulfates as New Heparin Analogues and Potent Inhibitors of the Complement System. *Bioconjugate Chemistry*, *15*(1), 162–167. https://doi.org/10.1021/bc034044j

Umemura, A., Park, E. J., Taniguchi, K., Lee, J. H., Shalapour, S., Valasek, M. A., Aghajan, M., Nakagawa, H., Seki, E., Hall, M. N., & Karin, M. (2014). Liver damage, inflammation, and enhanced tumorigenesis after persistent mTORC1 inhibition. *Cell Metabolism*, *20*(1), 133–144. https://doi.org/10.1016/j.cmet.2014.05.001

van der Louw, E. J. T. M., Olieman, J. F., van den Bemt, P. M. L. A., Bromberg, J. E. C., Oomen-de Hoop, E., Neuteboom, R. F., Catsman-Berrevoets, C. E., & Vincent, A. J. P. E. (2019). Ketogenic diet treatment as adjuvant to standard treatment of glioblastoma multiforme: A feasibility and safety study. *Therapeutic Advances in Medical Oncology*, *11*. https://doi.org/10.1177/1758835919853958

van Hoppe, S., Rood, J. J. M., Buil, L., Wagenaar, E., Sparidans, R. W., Beijnen, J. H., & Schinkel, A. H. (2018). P-Glycoprotein (MDR1/ABCB1) Restricts Brain Penetration of the Bruton's Tyrosine Kinase Inhibitor Ibrutinib, While Cytochrome P450-3A (CYP3A) Limits Its Oral Bioavailability. *Molecular Pharmaceutics*, *15*(11), 5124–5134. https://doi.org/10.1021/acs.molpharmaceut.8b00702

van Weert, A. W., Geuze, H. J., Groothuis, B., & Stoorvogel, W. (2000). Primaquine interferes with membrane recycling from endosomes to the plasma membrane through a direct interaction with endosomes which does not involve neutralisation of endosomal pH nor osmotic swelling of endosomes. *European Journal of Cell Biology*, *79*(6), 394–399. https://doi.org/10.1078/0171-9335-00062

Varatharaj, A., & Galea, I. (2017). The blood-brain barrier in systemic inflammation. *Brain, Behavior, and Immunity*, *60*, 1–12. https://doi.org/10.1016/j.bbi.2016.03.010

Verhaak, R. G. W., Hoadley, K. A., Purdom, E., Wang, V., Qi, Y., Wilkerson, M. D., Miller, C. R., Ding, L., Golub, T., Mesirov, J. P., Alexe, G., Lawrence, M., O'Kelly, M., Tamayo, P., Weir, B. A., Gabrie, S., Winckler, W., Gupta, S., Jakkula, L., … Hayes, D. N. (2010). An integrated genomic analysis identifies clinically relevant subtypes of glioblastoma characterized by abnormalities in PDGFRA, IDH1, EGFR and NF1. *Cancer Cell*, *17*(1), 98. https://doi.org/10.1016/j.ccr.2009.12.020

Villabona-Rueda, A., Erice, C., Pardo, C. A., & Stins, M. F. (2019). The Evolving Concept of the Blood Brain Barrier (BBB): From a Single Static Barrier to a Heterogeneous and Dynamic Relay Center. *Frontiers in Cellular Neuroscience*, *13*. https://doi.org/10.3389/fncel.2019.00405

Vogl, D. T., Raje, N., Jagannath, S., Richardson, P., Hari, P., Orlowski, R., Supko, J. G., Tamang, D., Yang, M., Jones, S. S., Wheeler, C., Markelewicz, R. J., & Lonial, S. (2017). Ricolinostat, the first selective histone deacetylase 6 inhibitor, in combination with bortezomib and dexamethasone for relapsed or refractory multiple myeloma. *Clinical Cancer Research : An Official Journal of the American Association for Cancer Research*, *23*(13), 3307–3315. https://doi.org/10.1158/1078-0432.CCR-16-2526

Vollmann-Zwerenz, A., Leidgens, V., Feliciello, G., Klein, C. A., & Hau, P. (2020). Tumor Cell Invasion in Glioblastoma. *International Journal of Molecular Sciences*, *21*(6). https://doi.org/10.3390/ijms21061932

Vorinostat and Radiation Therapy Followed by Maintenance Therapy With Vorinostat in Treating Younger Patients With Newly Diagnosed Diffuse Intrinsic Pontine Glioma—Full Text View—ClinicalTrials.gov. (n.d.). Retrieved May 31, 2018, from https://clinicaltrials.gov/ct2/show/NCT01189266

Wang, D., Wang, B., Liu, Y., Dong, X., Su, Y., & Li, S. (2019). Protective Effects of ACY-1215 Against Chemotherapy-Related Cognitive Impairment and Brain Damage in Mice. *Neurochemical Research*, *44*(11), 2460–2469. https://doi.org/10.1007/s11064-019-02882-6

Wang, F., Bradshaw, H. B., Pena, S., Jablonska, B., Xavier, J., Gong, S., Li, B., Chandler-Militello, D., Bekar, L. K., & Smith, N. A. (2020). Calcium-independent astrocytic lipid release modulates neuronal activity through Kv channels. *BioRxiv*, 2020.01.12.903393. https://doi.org/10.1101/2020.01.12.903393

Wang, L., Leite de Oliveira, R., Huijberts, S., Bosdriesz, E., Pencheva, N., Brunen, D., Bosma, A., Song, J.-Y., Zevenhoven, J., Los-de Vries, G. T., Horlings, H., Nuijen, B., Beijnen, J. H., Schellens, J. H. M., & Bernards, R. (2018). An Acquired Vulnerability of Drug-Resistant Melanoma with Therapeutic Potential. *Cell*, *173*(6), 1413-1425.e14. https://doi.org/10.1016/j.cell.2018.04.012

Wang, S., Chen, P., Zhang, L., Yang, C., & Zhai, G. (2012). Formulation and evaluation of microemulsion-based in situ ion-sensitive gelling systems for intranasal administration of curcumin. *Journal of Drug Targeting*, *20*(10), 831–840. https://doi.org/10.3109/1061186X.2012.719230

Weathers, S.-P., & Gilbert, M. R. (2014). Advances in treating glioblastoma. *F1000prime Reports*, *6*, 46. https://doi.org/10.12703/P6-46

Weller, M., Cloughesy, T., Perry, J. R., & Wick, W. (2013). Standards of care for treatment of recurrent glioblastoma—Are we there yet? *Neuro-Oncology*, *15*(1), 4–27. https://doi.org/10.1093/neuonc/nos273

Weller, M., Stupp, R., Reifenberger, G., Brandes, A. A., van den Bent, M. J., Wick, W., & Hegi, M. E. (2010). MGMT promoter methylation in malignant gliomas: Ready for personalized medicine? *Nature Reviews. Neurology*, *6*(1), 39–51. https://doi.org/10.1038/nrneurol.2009.197

Weller, M., van den Bent, M., Tonn, J. C., Stupp, R., Preusser, M., Cohen-Jonathan-Moyal, E., Henriksson, R., Le Rhun, E., Balana, C., Chinot, O., Bendszus, M., Reijneveld, J. C., Dhermain, F., French, P., Marosi, C., Watts, C., Oberg, I., Pilkington, G., Baumert, B. G., … European

Association for Neuro-Oncology (EANO) Task Force on Gliomas. (2017). European Association for Neuro-Oncology (EANO) guideline on the diagnosis and treatment of adult astrocytic and oligodendroglial gliomas. *The Lancet. Oncology*, *18*(6), e315–e329. https://doi.org/10.1016/S1470-2045(17)30194-8

Welte, M. A. (2015). Expanding roles for lipid droplets. *Current Biology: CB*, *25*(11), R470-481. https://doi.org/10.1016/j.cub.2015.04.004

Wen, W., Meinkoth, J. L., Tsien, R. Y., & Taylor, S. S. (1995). Identification of a signal for rapid export of proteins from the nucleus. *Cell*, *82*(3), 463–473. https://doi.org/10.1016/0092-8674(95)90435-2

Wu, C.-P., Calcagno, A. M., & Ambudkar, S. V. (2008). Reversal of ABC drug transporter-mediated multidrug resistance in cancer cells: Evaluation of current strategies. *Current Molecular Pharmacology*, *1*(2), 93–105.

Wu, C.-P., Hsieh, Y.-J., Murakami, M., Vahedi, S., Hsiao, S.-H., Yeh, N., Chou, A.-W., Li, Y.-Q., Wu, Y.-S., Yu, J.-S., & Ambudkar, S. V. (2018). Human ATP-binding cassette transporters ABCB1 and ABCG2 confer resistance to histone deacetylase 6 inhibitor ricolinostat (ACY-1215) in cancer cell lines. *Biochemical Pharmacology*, *155*, 316–325. https://doi.org/10.1016/j.bcp.2018.07.018

Xu, X., Gerard, A. L., Huang, B. C., Anderson, D. C., Payan, D. G., & Luo, Y. (1998). Detection of programmed cell death using fluorescence energy transfer. *Nucleic Acids Research*, *26*(8), 2034–2035. https://doi.org/10.1093/nar/26.8.2034

Yang, W., Warrington, N. M., Taylor, S. J., Whitmire, P., Carrasco, E., Singleton, K. W., Wu, N., Lathia, J. D., Berens, M. E., Kim, A. H., Barnholtz-Sloan, J. S., Swanson, K. R., Luo, J., & Rubin, J. B. (2019). Sex differences in GBM revealed by analysis of patient imaging, transcriptome, and survival data. *Science Translational Medicine*, *11*(473). https://doi.org/10.1126/scitranslmed.aao5253

Yang, X., Li, Z., Wang, N., Li, L., Song, L., He, T., Sun, L., Wang, Z., Wu, Q., Luo, N., Yi, C., & Gong, C. (2015). Curcumin-encapsulated polymeric micelles suppress the development of colon cancer in vitro and in vivo. *Scientific Reports*, *5*, 10322. https://doi.org/10.1038/srep10322

Yang, Y., He, M. Z., Li, T., & Yang, X. (2019). MRI combined with PET-CT of different tracers to improve the accuracy of glioma diagnosis: A systematic review and meta-analysis. *Neurosurgical Review*, *42*(2), 185–195. https://doi.org/10.1007/s10143-017-0906-0

Yang, Z. J., Chee, C. E., Huang, S., & Sinicrope, F. A. (2011). The role of autophagy in cancer: Therapeutic implications. *Molecular Cancer Therapeutics*, *10*(9), 1533–1541. https://doi.org/10.1158/1535-7163.MCT-11-0047

Yano, M., Yasuda, M., Sakaki, M., Nagata, K., Fujino, T., Arai, E., Hasebe, T., Miyazawa, M., Miyazawa, M., Ogane, N., Hasegawa, K., & Narahara, H. (2018). Association of histone deacetylase expression with histology and prognosis of ovarian cancer. *Oncology Letters*, *15*(3), 3524–3531. https://doi.org/10.3892/ol.2018.7726

Ye, Z., Huang, H., Hao, S., Xu, S., Yu, H., Van Den Hurk, S., & Xiang, J. (2007). IL-10 has a distinct immunoregulatory effect on naive and active T cell subsets. *Journal of Interferon & Cytokine Research: The Official Journal of the International Society for Interferon and Cytokine Research*, *27*(12), 1031–1038. https://doi.org/10.1089/jir.2006.0144

Yin, D., Ong, J. M., Hu, J., Desmond, J. C., Kawamata, N., Konda, B. M., Black, K. L., & Koeffler, H. P. (2007a). Suberoylanilide hydroxamic acid, a histone deacetylase inhibitor: Effects on gene expression and growth of glioma cells in vitro and in vivo. *Clinical Cancer Research: An Official Journal of the American Association for Cancer Research*, *13*(3), 1045–1052. https://doi.org/10.1158/1078-0432.CCR-06-1261

Yin, D., Ong, J. M., Hu, J., Desmond, J. C., Kawamata, N., Konda, B. M., Black, K. L., & Koeffler, H. P. (2007b). Suberoylanilide hydroxamic acid, a histone deacetylase inhibitor: Effects on gene expression and growth of glioma cells in vitro and in vivo. *Clinical Cancer Research: An Official*

Journal of the American Association for Cancer Research, *13*(3), 1045–1052. https://doi.org/10.1158/1078-0432.CCR-06-1261

Yue, P., & Turkson, J. (2009). Targeting STAT3 in cancer: How successful are we? *Expert Opinion on Investigational Drugs*, *18*(1), 45–56. https://doi.org/10.1517/13543780802565791

Yun, B., Lee, H., Ewing, H., Gelb, M. H., & Leslie, C. C. (2016). Off-target effect of the cPLA2α inhibitor pyrrophenone: Inhibition of calcium release from the endoplasmic reticulum. *Biochemical and Biophysical Research Communications*, *479*(1), 61–66. https://doi.org/10.1016/j.bbrc.2016.09.033

Zanini, C., Giribaldi, G., Mandili, G., Carta, F., Crescenzio, N., Bisaro, B., Doria, A., Foglia, L., di Montezemolo, L. C., Timeus, F., & Turrini, F. (2007). Inhibition of heat shock proteins (HSP) expression by quercetin and differential doxorubicin sensitization in neuroblastoma and Ewing's sarcoma cell lines. *Journal of Neurochemistry*, *103*(4), 1344–1354. https://doi.org/10.1111/j.1471-4159.2007.04835.x

Zhang, I., Beus, M., Stochaj, U., Le, P. U., Zorc, B., Rajic, Z., Petrecca, K., & Maysinger, D. (2018). Inhibition of glioblastoma cell proliferation, invasion, and mechanism of action of a novel hydroxamic acid hybrid molecule. *Cell Death Discovery*, *4*, 41. https://doi.org/10.1038/s41420-018-0103-0

Zhang, I., Cui, Y., Amiri, A., Ding, Y., Campbell, R. E., & Maysinger, D. (2016). Pharmacological inhibition of lipid droplet formation enhances the effectiveness of curcumin in glioblastoma. *European Journal of Pharmaceutics and Biopharmaceutics : Official Journal of Arbeitsgemeinschaft Fur Pharmazeutische Verfahrenstechnik e.V*, *100*, 66–76. https://doi.org/10.1016/j.ejpb.2015.12.008

Zhang, I., Lépine, P., Han, C., Lacalle-Aurioles, M., Chen, C. X.-Q., Haag, R., Durcan, T. M., & Maysinger, D. (2020). Nanotherapeutic Modulation of Human Neural Cells and Glioblastoma in Organoids and Monocultures. *Cells*, *9*(11). https://doi.org/10.3390/cells9112434

Zhang, L., Liu, C., Wu, J., Tao, J.-J., Sui, X.-L., Yao, Z.-G., Xu, Y.-F., Huang, L., Zhu, H., Sheng, S.-L., & Qin, C. (2014). Tubastatin A/ACY-1215 improves cognition in Alzheimer's disease transgenic mice. *Journal of Alzheimer's Disease: JAD*, *41*(4), 1193–1205. https://doi.org/10.3233/JAD-140066

Zhang, Q., Higginbotham, J. N., Jeppesen, D. K., Yang, Y.-P., Li, W., McKinley, E. T., Graves-Deal, R., Ping, J., Britain, C. M., Dorsett, K. A., Hartman, C. L., Ford, D. A., Allen, R. M., Vickers, K. C., Liu, Q., Franklin, J. L., Bellis, S. L., & Coffey, R. J. (2019). Transfer of Functional Cargo in Exomeres. *Cell Reports*, *27*(3), 940-954.e6. https://doi.org/10.1016/j.celrep.2019.01.009

Zhang, S.-L., Zhu, H.-Y., Zhou, B.-Y., Chu, Y., Huo, J.-R., Tan, Y.-Y., & Liu, D.-L. (2019). Histone deacetylase 6 is overexpressed and promotes tumor growth of colon cancer through regulation of the MAPK/ERK signal pathway. *OncoTargets and Therapy*, *12*, 2409–2419. https://doi.org/10.2147/OTT.S194986

Zhang, Xian, Guo, Q., Chen, J., & Chen, Z. (2015). Quercetin Enhances Cisplatin Sensitivity of Human Osteosarcoma Cells by Modulating microRNA-217-KRAS Axis. *Molecules and Cells*, *38*(7), 638–642. https://doi.org/10.14348/molcells.2015.0037

Zhang, Xuan, Zhang, J., Tong, L., Luo, Y., Su, M., Zang, Y., Li, J., Lu, W., & Chen, Y. (2013). The discovery of colchicine-SAHA hybrids as a new class of antitumor agents. *Bioorganic & Medicinal Chemistry*, *21*(11), 3240–3244. https://doi.org/10.1016/j.bmc.2013.03.049

Zhang, Y., Kwon, S., Yamaguchi, T., Cubizolles, F., Rousseaux, S., Kneissel, M., Cao, C., Li, N., Cheng, H.-L., Chua, K., Lombard, D., Mizeracki, A., Matthias, G., Alt, F. W., Khochbin, S., & Matthias, P. (2008). Mice lacking histone deacetylase 6 have hyperacetylated tubulin but are viable and develop normally. *Molecular and Cellular Biology*, *28*(5), 1688–1701. https://doi.org/10.1128/MCB.01154-06

Zhang, Z.-S., Wang, J., Shen, Y.-B., Guo, C.-C., Sai, K. E., Chen, F.-R., Mei, X., Han, F. U., & Chen, Z.-P. (2015). Dihydroartemisinin increases temozolomide efficacy in glioma cells by inducing autophagy. *Oncology Letters*, *10*(1), 379–383. https://doi.org/10.3892/ol.2015.3183

Zhitomirsky, B., & Assaraf, Y. G. (2017). Lysosomal accumulation of anticancer drugs triggers lysosomal exocytosis. *Oncotarget*, *8*(28), 45117–45132. https://doi.org/10.18632/oncotarget.15155

Zhou, J., Tang, Z., Gao, S., Li, C., Feng, Y., & Zhou, X. (2020). Tumor-Associated Macrophages: Recent Insights and Therapies. *Frontiers in Oncology*, *10*. https://doi.org/10.3389/fonc.2020.00188

Zips, D., Thames, H. D., & Baumann, M. (2005). New anticancer agents: In vitro and in vivo evaluation. *In Vivo (Athens, Greece)*, *19*(1), 1–7.

Appendices

Rights and permissions

Zhang et al. *Cell Death Discovery* (2018)4:41
DOI 10.1038/s41420-018-0103-0

Cell Death Discovery

ARTICLE Open Access

Inhibition of glioblastoma cell proliferation, invasion, and mechanism of action of a novel hydroxamic acid hybrid molecule

Issan Zhang[1], Maja Beus[1,2], Ursula Stochaj[3], Phuong Uyen Le[4], Branka Zorc[2], Zrinka Rajić[2], Kevin Petrecca[4] and Dusica Maysinger[1]

Abstract

Glioblastoma multiforme is one of the most aggressive brain tumors and current therapies with temozolomide or suberoylanilide hydroxamic acid (SAHA, vorinostat) show considerable limitations. SAHA is a histone deacetylase (HDAC) inhibitor that can cause undesirable side effects due to the lack of selectivity. We show here properties of a novel hybrid molecule, sahaquine, which selectively inhibits cytoplasmic HDAC6 at nanomolar concentrations without markedly suppressing class I HDACs. Inhibition of HDAC6 leads to significant α-tubulin acetylation, thereby impairing cytoskeletal organization in glioblastoma cells. The primaquine moiety of sahaquine reduced the activity of P-glycoprotein, which contributes to glioblastoma multiforme drug resistance. We propose the mechanism of action of sahaquine to implicate HDAC6 inhibition together with suppression of epidermal growth factor receptor and downstream kinase activity, which are prominent therapeutic targets in glioblastoma multiforme. Sahaquine significantly reduces the viability and invasiveness of glioblastoma tumoroids, as well as brain tumor stem cells, which are key to tumor survival and recurrence. These effects are augmented with the combination of sahaquine with temozolomide, the natural compound quercetin or buthionine sulfoximine, an inhibitor of glutathione biosynthesis. Thus, a combination of agents disrupting glioblastoma and brain tumor stem cell homeostasis provides an effective anti–cancer intervention.

Introduction

Glioblastoma multiforme (GBM) is the most common and aggressive form of brain cancer, with limited treatment options and dismal survival rates. Current treatment involves surgical resection followed by radiotherapy and chemotherapy with temozolomide (TMZ)[1]. However, more than half of GBM patients do not respond to TMZ due to the overexpression of DNA repair enzymes, notably O^6-methylguanine transferase[2–4].

Histone deacetylase (HDAC) inhibitors exert anticancer effects by inducing cell differentiation, cell cycle arrest, and apoptotic cell death through the upregulation of tumor suppressor and cell cycle-regulatory genes[5]. Suberoylanilide hydroxamic acid (SAHA, vorinostat) is a Food and Drug Administration-approved drug for the treatment of cutaneous T cell lymphoma. It is currently in clinical trials for GBM as monotherapy and combined with radiotherapy[6–9]. Despite advancements in treatments, the median survival rate for GBM remains low (14–16 months) and new therapeutic options are urgently needed[3,10].

In this study, we combined hydroxamic acid—the active moiety of SAHA exerting biological effects in cancer cells—with primaquine to generate a new class of hybrid anticancer agents: sahaquines. Hydroxamic acid inhibits HDACs;

Correspondence: Dusica Maysinger (dusica.maysinger@mcgill.ca)
[1]Department of Pharmacology and Therapeutics, McGill University, Montreal, QC, Canada
[2]Faculty of Pharmacy and Biochemistry, University of Zagreb, Zagreb, Croatia
Full list of author information is available at the end of the article.
These authors contributed equally: Issan Zhang, Maja Beus
Edited by M.V. Niklison Chirou

SPRINGER NATURE CDDpress

these enzymes are overexpressed in many cancers, including GBM[11,12]. The hydroxamic acid pharmacophore of SAHA chelates metal ions, thereby inhibiting metalloenzymes such as HDACs and matrix metalloproteinases (MMPs), which promote cancer growth and invasiveness[13–15]. Hydroxamic acid is a weak acid, which is favorable in the acidic tumor microenvironment as weak bases become protonated, resulting in ion trapping, lysosomal accumulation, elimination by lysosomal exocytosis, and overall decreased biological activity[16–18]. Primaquine can directly interfere with endosomal trafficking to the plasma membrane[19], inhibit the multidrug resistance transporter P-glycoprotein, and autophagy, thereby sensitizing cancer cells to anti-mitotic drugs[20,21]. Considering that monotherapies have limited effectiveness in GBM, we tested sahaquine in combination with TMZ, the standard of care for GBM, quercetin, and buthionine sulfoxamine. Quercetin is an abundant flavonoid found in fruits and vegetables, such as apples and onions. Its estimated daily intake ranges from 3–40 mg, but supplements up to 1000 mg per day are considered safe[22]. Although it shows no toxicity in normal cells, several studies have shown that quercetin has anticancer effects. Its mechanism of action involves the upregulation of pro-apoptotic and downregulation of anti-apoptotic factors, cell cycle arrest, and DNA intercalation, resulting in DNA damage, activation of apoptosis, and cell death[23]. In animal studies, quercetin inhibited tumor growth and improved the lifespan of tumor-bearing mice[23,24]. Furthermore, the anticancer effects of quercetin are enhanced in combination with chemotherapeutic agents or other drugs[25–27].

We investigated the loss of cell viability and invasiveness in GBM as functional read-outs of the effects of sahaquine alone or in combination with TMZ and quercetin. Sahaquine was tested in both differentiated GBM cells and brain tumor stem cells (BTSCs), which are key to tumor survival and recurrence[28–31]. Our study supports the model that sahaquine-induced cell death of GBM is mediated through multiple pathways, including inhibition of HDAC6, reduction of epidermal growth factor receptor (EGFR) protein abundance, and decreased activation of downstream kinases AKT and ERK1/2. The primaquine moiety of sahaquine contributes to the inhibition of P-glycoprotein. Considering that sahaquine significantly reduced BTSC viability and markedly inhibited GBM invasion by disruption of GBM homeostasis, further systematic studies are warranted in patient-derived organoids.

Results

Sahaquine synthesis and physicochemical properties of the selected anticancer agents

Sahaquine is a primaquine and hydroxamic acid derivative linked with glutaric acid. It is synthesized in four steps (Fig. 1). The pharmacophore, hydroxamic acid, was introduced in the last step. Yields were good to excellent (50–88%). Sahaquine was fully characterized by conventional spectroscopic and analytical methods (melting point, IR, MS, ^{1}H-NMR, ^{13}C-NMR), and the data were consistent with the proposed structure (Supplementary Fig. S1). The quinoline ring of sahaquine acts as the capping group and the hydroxamic acid binds zinc. Calculations of physicochemical properties showed that TMZ is a hydrophilic compound ($\log P = -0.28$), whereas sahaquine and particularly quercetin are more lipophilic ($\log P = 0.92$ and 2.16, respectively) (Table 1). The isoelectric point (pI) values of these compounds vary from 2.9 (quercetin) to 9.2 (SAHA)[32].

Sahaquine is more potent than TMZ for killing human glioblastoma and BTSCs

The half maximal inhibitory concentration (IC_{50}) value of sahaquine (10 μM) was about threefold lower than that

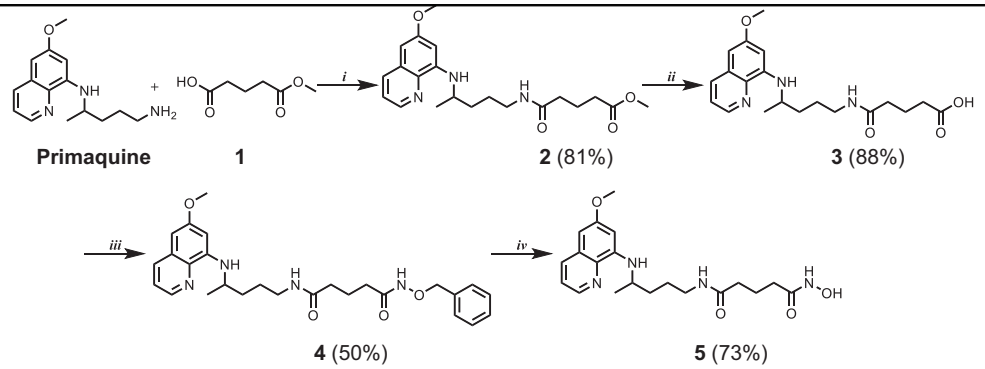

Figure 1 Synthesis of sahaquine and its precursors. Reagents and conditions: (i) HATU, DIEA, dichloromethane, 1 h, (ii) LiOH, methanol, H_2O, 1 h, (iii) *O*-benzylhydroxylamine, HATU, DIEA, dichloromethane, 2 h, (iv) H_2, 10% Pd/C, methanol, 4 h. All reactions were performed at room temperature. Yields are shown in brackets. HATU 1-[*bis*(dimethylamino)methylene]-1*H*-1,2,3-triazolo[4,5-*b*]pyridinium 3-oxid hexafluorophosphate, DIEA *N*,*N*-diisopropylethylamine, LiOH lithium hydroxide)

Table 1 Structures of sahaquine, temozolomide, quercetin, and SAHA with basic physicochemical properties

Structure	IUPAC name	Molecular mass	log*P*	pI
Sahaquine 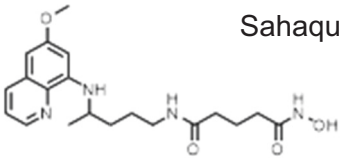	*N*-hydroxy-*N*'-{4-[(6-methoxyquinolin-8-yl)amino]pentyl}pentanediamide	388.47	0.92	6.48
Temozolomide 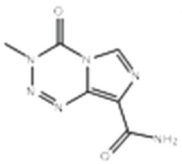	3-methyl-4-oxo-3*H*,4*H*-imidazo[4,3-*d*][1,2,3,5]tetrazine-8-carboxamide	194.15	-0.28	7.1
Quercetin 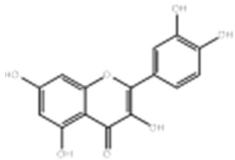	2-(3,4-dihydroxyphenyl)-3,5,7-trihydroxy-4*H*-chromen-4-one	302.24	2.16	2.9
SAHA 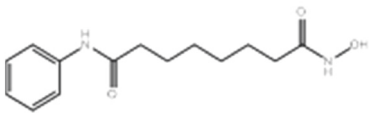	*N*'-hydroxy-*N*-phenyloctanediamide	264.33	1.0	9.2

The physicochemical properties are calculated with the Chemicalize.org program (Instant Cheminformatics Solutions. Available online at http://www.chemicalize.org/ (accessed on 10 October 2017))

of TMZ (31 μM), whereas it was less potent than its parent compound SAHA after 72 h incubation (Fig. 2). Sahaquine precursors were also tested, but because of the relatively high IC_{50} values (>50 μM), further experiments were not pursued (Supplementary Table S1). Enhanced cell killing was achieved by combining quercetin with sahaquine in a dose-dependent manner, although quercetin alone showed limited cytotoxicity ($IC_{50} = 140$ μM after 72 h) (Fig. 2e). Combination of TMZ with sahaquine, quercetin, or SAHA at IC_{50} concentrations was more effective than any of the compounds alone (Supplementary Fig. S2). Similar results were obtained by measurements of mitochondrial metabolic activity using the MTT (3-[4,5-dimethylthiazol-2-yl]-2,5-diphenyl tetrazolium bromide) assay (Supplementary Fig. S3).

We further tested the selected compounds on GBM tumoroids, which are more drug-resistant and representative models of brain tumors in vivo. Sahaquine and TMZ reduced tumoroid sizes by 37 and 40%, respectively, while quercetin did not have a significant effect after 7 days (Supplementary Fig. S4).

Based on the results shown in Fig. 2, we investigated the cytotoxic effects of the selected compounds on BTSCs. BTSCs are a key subpopulation of GBM tumors implicated in tumor initiation, propagation and recurrence[28,30]. In vitro BTSC cultures spontaneously formed neurospheres of approximately 100 μm in diameter within 7 days. Sahaquine and quercetin were most effective at reducing the size of BTSC aggregates and abolishing the formation of neurospheres (Fig. 3).

Sahaquine inhibits GBM invasion and P-glycoprotein activity

GBM is characterized by a diffuse brain tissue distribution[33]. Tumors commonly reoccur within a few centimeters of the original lesion, making surgical resection difficult[33]. We tested the effect of sahaquine and quercetin on GBM migration using a scratch assay, and invasion using a three-dimensional (3D) collagen matrix. Sahaquine did not significantly inhibit cell migration over 24 h, while quercetin reduced cell migration by 20% (Fig. 4a). The combination of sahaquine with quercetin

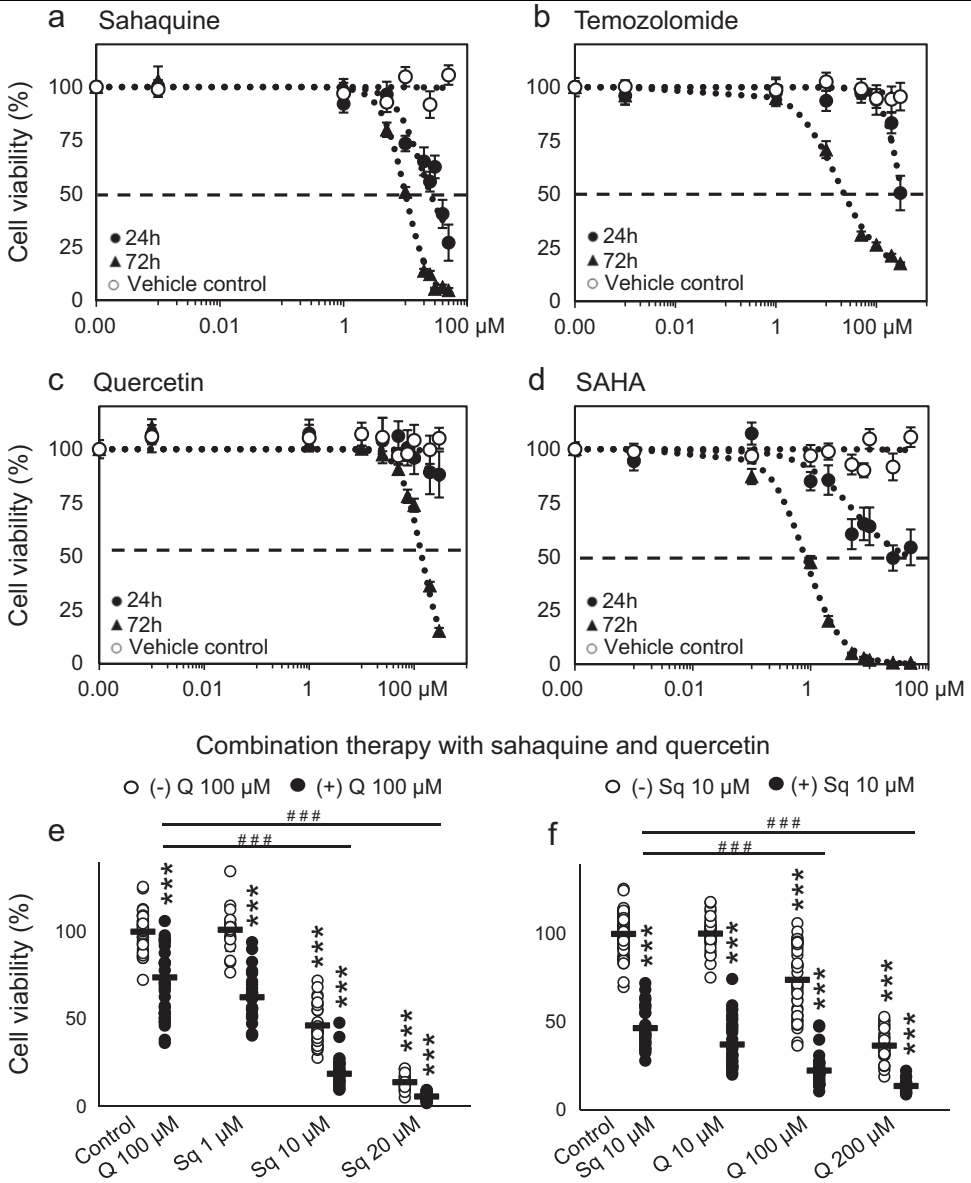

Figure 2 Sahaquine kills human glioblastoma cells in a dose-dependent and time-dependent manner. GBM cell viability ($n = 9$) following treatment with **a** sahaquine (Sq, 0.001–50 μM), **b** temozolomide (TMZ, 0.001–500 μM), **c** quercetin (Q, 0.001–300 μM), and **d** SAHA (0.001–50 μM) for 24 or 72 h. Shown is the mean (SEM) percentage cell viability compared to untreated controls from three independent experiments. **e**, **f** Dose-dependent decrease in cell viability (72 h) with the combination of either a fixed concentration of quercetin (100 μM, n = 41) and increasing concentrations of sahaquine (Sq 1 μM, $n = 21$, Sq 10 μM, $n = 30$, Sq 20 μM, $n = 21$, Sq 1 μM + Q, $n = 25$, Sq 10 μM + Q, $n = 29$, Sq 20 μM + Q, $n = 27$), or a fixed concentration of sahaquine (10 μM $n = 30$) and increasing concentrations of quercetin (Q 10 μM, $n = 37$, Q 100 μM, $n = 41$, Q 200 μM, $n = 28$, Q 10 μM + Sq, $n = 34$, Q 100 μM + Sq, $n = 35$, Q 200 μM + Sq, $n = 21$). Each point represents a percentage value normalized to the untreated control (**e** $n = 47$, **f** $n = 125$). Horizontal bars represent the mean (SD) from at least three independent experiments (***$p < 0.001$ compared to the untreated control; $^{###}p < 0.001$ compared to **e** Q 100 μM alone or **f** Sq 10 μM alone; Welch's ANOVA with Games–Howell post hoc test). Cell viability was measured by counting Hoechst 33342-labeled nuclei imaged using a fluorescence microscope

was most effective, reducing migration by 42%. This effect was not observed when combining sahaquine with TMZ. In contrast, sahaquine significantly inhibited GBM invasiveness, whereas quercetin and TMZ reduced cell invasion by 35 and 45% after 4 days, respectively (Fig. 4c). GBM invasiveness is enabled by MMP degradation of the extracellular matrix and basement membranes[34,35]. We investigated the effect of the selected compounds on the abundance of secreted MMPs using gelatin zymography and showed that quercetin decreases MMP abundance in a dose-dependent manner (Supplementary Fig. S5). Neither sahaquine nor TMZ reduced MMP concentrations,

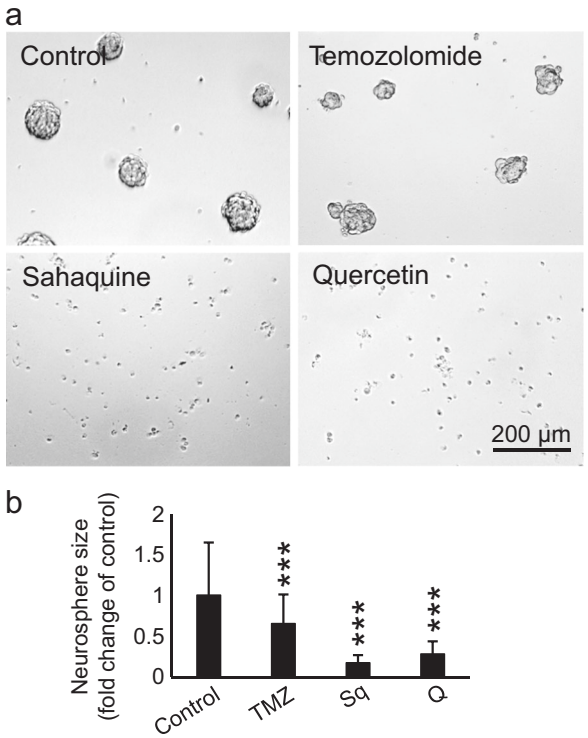

Figure 3 Sahaquine and quercetin are most effective in killing human brain cancer stem cells. a Representative micrographs of BTSCs treated with temozolomide (100 µM, $n = 99$), sahaquine (10 µM, $n = 183$) or quercetin (100 µM, $n = 264$) for 7 days. **b** The surface area of neurospheres was measured based on 2D micrographs from three independent experiments. Shown are average values (SD) normalized to the untreated controls (set to 1, $n = 334$) (***$p < 0.001$, Welch's ANOVA with Games–Howell post hoc test)

although the hydroxamic acid moiety in sahaquine can bind zinc within the MMP structure[36]. The primaquine moiety of sahaquine contributed to the inhibition of P-glycoprotein, as assessed by intracellular retention of calcein-AM (Supplementary Fig. S6). The primaquine concentration within sahaquine (10 µM) effectively inhibited P-glycoprotein activity, whereas 60 µM of unincorporated primaquine was required to achieve a comparable effect. A smaller extent of P-glycoprotein inhibition by SAHA was obtained with equimolar sahaquine concentrations (10 µM) (Supplementary Fig. S6).

Sahaquine selectively inhibits HDAC6

We further examined the HDAC inhibitory activity of sahaquine compared to its parent compound SAHA. SAHA is a pan-HDAC inhibitor that caused an increase in both acetylated α-tubulin (K40) and acetylated histone H3 (K9/K14) (Fig. 5). We hypothesized sahaquine to be selective toward HDAC6, because its bulky capping group would fit better into the wide binding site of the enzyme[37,38]. Nanomolar concentrations (100 nM) of sahaquine resulted in a 1.5-fold increase in acetylated α-tubulin compared to the untreated control, but did not affect histone acetylation (Fig. 5a). Similar results were obtained with the HDAC6-selective inhibitor ACY-1215 (Supplementary Fig. S7). TMZ and quercetin did not inhibit HDAC6. These results were supported by Western blot analyses (Fig. 5c). HDAC6 abundance was comparable following all treatments, suggesting that sahaquine inhibited the enzyme activity without affecting its protein levels (Fig. 5d).

Sahaquine reduces EGFR abundance, ERK1/2, and AKT phosphorylation

EGFR overexpression and downstream hyperactivity of ERK1/2 and AKT are associated with worse prognosis in GBM[39,40]. We assessed the abundance of these markers and HDAC6 in GBM by immunohistochemistry, and showed an increase in EGFR, dually phosphorylated (active) ERK1/2, phosphorylated (active) AKT, and HDAC6 compared to control brains (Fig. 6a). To test whether sahaquine impinges on EGFR and the activation of downstream kinases, we measured EGFR abundance, dual ERK1/2 phosphorylation (Thr202/Tyr204), and AKT phosphorylation (Ser473) by Western blotting (Fig. 6b). Sahaquine reduced EGFR concentrations in GBM. Interestingly, combining sahaquine and TMZ abrogated this inhibitory effect. Sahaquine also reduced levels of phosphorylated ERK1/2 and phosphorylated AKT, alone and in combination with quercetin or TMZ. Total ERK1/2 and AKT protein levels remained unchanged (Supplementary Fig. S8).

Discussion

Results from this study show that sahaquine is more effective than TMZ in killing glioblastoma and BTSCs, as well as inhibiting glioblastoma invasiveness. The mode of action of sahaquine implicates in part excessive α-tubulin acetylation due to the selective inhibition of HDAC6, resulting in cytoskeletal reorganization (Supplementary Fig. S9) and reduced invasiveness. Additional modes of action involve decreased EGFR abundance and downstream activity of AKT and ERK1/2. These results are particularly striking in combination with TMZ or quercetin.

TMZ is one of few clinically approved drugs for the treatment of GBM, but a substantial portion of newly diagnosed tumors and recurrent tumors are resistant to this drug[3,41]. HDAC inhibitors are of particular interest for GBM treatment, as their effectiveness is unaltered by mechanisms of resistance upregulated in GBM, such as mismatch-repair, O^6-methylguanine methyltransferase and base-excision repair[3,4,42]. The pan-HDAC inhibitor SAHA is currently in clinical trials for GBM, but results so far showed marginal improvement in overall survival (5.7 months compared to

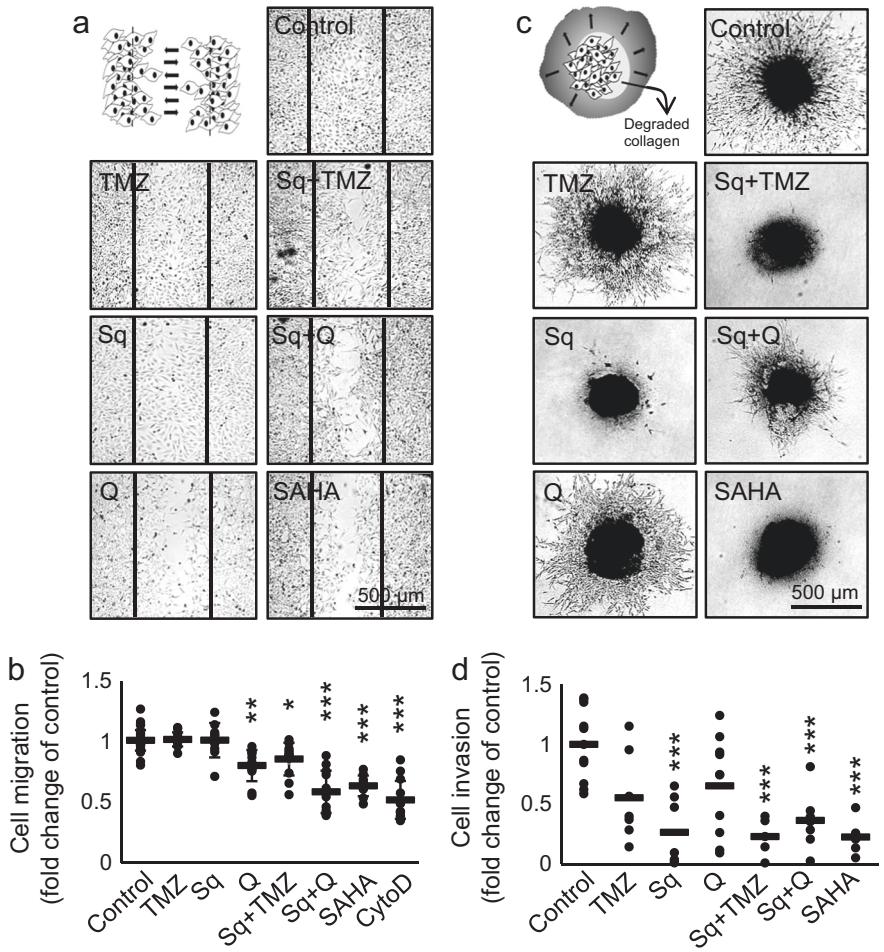

Figure 4 Sahaquine inhibits human glioblastoma cell migration and invasion. Cell migration was measured using the scratch assay, as schematically represented in **a**. Representative micrographs show migration of cells into the scratch (delineated by vertical black bars) after treatment with temozolomide (100 µM, $n = 12$), sahaquine (Sq, 10 µM, $n = 10$), quercetin (Q, 100 µM, $n = 12$) or SAHA (10 µM, $n = 10$), alone or in combination (Sq + TMZ, $n = 12$; Sq + Q, n = 12) for 24 h. Cytochalasin D (40 nM, $n = 13$) served as a positive control. **b** Cell migration was quantified as the area covered by migrating cells. Each point represents a value normalized to the untreated control (set to 1, $n = 35$). Horizontal bars represent the mean (SD) from at least three independent experiments (*$p < 0.05$, **$p < 0.01$, ***$p < 0.001$, Welch's ANOVA with Games–Howell post hoc test). **c** Cell invasion was measured from the radial movement of cells from 3D tumoroids embedded in a collagen matrix, as schematically represented in the first panel. Representative micrographs show cell movement from 3D tumoroids treated with temozolomide (100 µM, $n = 7$), sahaquine (Sq, 10 µM, $n = 7$), quercetin (Q, 100 µM, $n = 10$), or SAHA (10 µM, $n = 5$), alone or in combination (Sq + TMZ, $n = 5$; Sq + Q, $n = 8$) after 4 days. **d** Cell invasion was quantified from the area covered by invading cells. Each point represents a value normalized to the untreated control (set to 1, $n = 11$). Horizontal bars represent the mean from at least three independent experiments (***$p < 0.001$, two-tailed one-way ANOVA with Tukey–Kramer's post hoc test)

4.4 months) and several serious side effects[6–9,43,44]. This and other current therapeutic interventions for GBM are ineffective[28,29,31].

Thus, our goal was to test a new hybrid compound. The development of hybrid molecules is one of the most active areas in therapeutics. Hybrid compounds can have multiple targets, reducing the risk of resistance, lowering effective doses, and decreasing side effects[45,46]. Sahaquine is a hybrid molecule consisting of hydroxamic acid and primaquine linked by a dicarboxylic acid. Primaquine is a strong base (pI = 13.7), but addition of the hydroxamic acid group lowers its pI to 6.48, making sahaquine a weak acid. Weak acids are more advantageous than weak bases as anticancer therapeutics, because they will not be protonated in the acidic tumor environment or trigger lysosomal exocytosis[16–18]. Similarly to primaquine, sahaquine can also inhibit P-glycoprotein activity (Supplementary Fig. S6), thereby preventing multidrug resistance.

One of the great challenges in GBM treatment is heterogeneity, both within and between tumors[47–50]. Interpatient heterogeneity has been shown through genomic and transcriptomic analyses by the Cancer Genome Atlas research network[51,52]. Intratumoral heterogeneity can be attributed to the different cellular lineages and subtypes

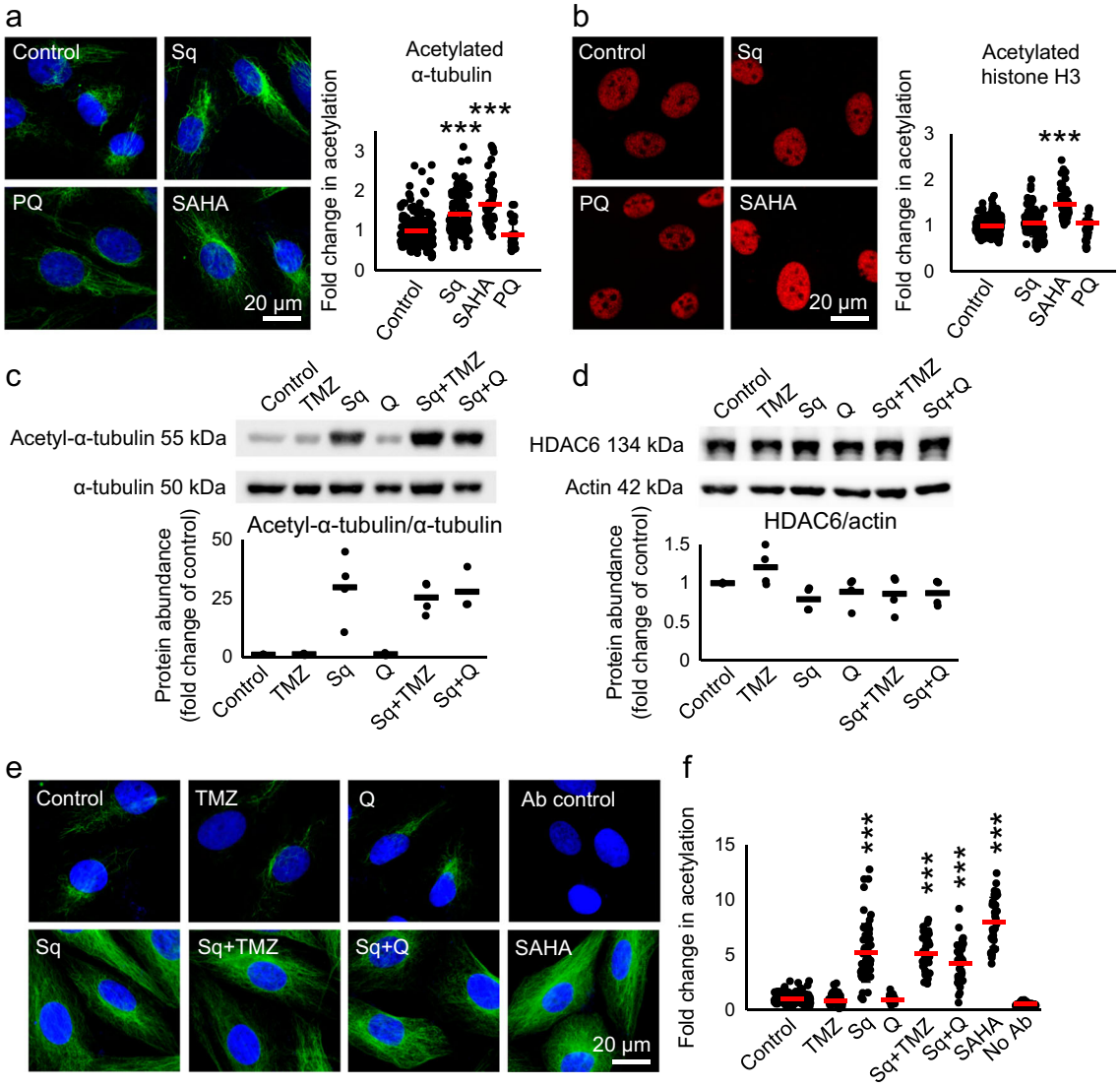

Figure 5 Sahaquine-mediated HDAC6 inhibition results in selective α-tubulin hyperacetylation at nanomolar concentrations. a Representative fluorescence micrographs of GBM α-tubulin acetylation (green) at lysine 40 in response to sahaquine (Sq, 100 nM, $n = 121$ cells), SAHA (100 nM, $n = 54$ cells) or primaquine (PQ, 10 μM, $n = 30$ cells) treatment for 24 h. **b** Representative fluorescence micrographs of GBM histone H3 acetylation (red) at lysine 9/lysine 14 in response to sahaquine (Sq, 100 nM, $n = 120$ cells), SAHA (100 nM, $n = 90$ cells) or primaquine (PQ, 10 μM, $n = 83$ cells) for 24 h. Nuclei (blue) were labeled with Hoechst 33342. Cells were imaged using a fluorescence microscope and fluorescence was analyzed in ImageJ. Shown are averages of fluorescence per cell (SD) normalized to the untreated controls (set to 1) from at least three independent experiments (***$p < 0.001$, Welch's ANOVA with Games–Howell post hoc test). **c** Acetylated α-tubulin ($n = 3$) and **d** HDAC6 protein abundance ($n = 4$) in GBM cells treated with temozolomide (TMZ, 100 μM), sahaquine (Sq, 10 μM) or quercetin (Q, 100 μM) alone or in combination for 24 h, measured by Western blotting. Acetylated α-tubulin and HDAC6 were normalized to total α-tubulin and actin, respectively. Each point represents a value normalized to the untreated control (set to 1). Horizontal bars represent the mean from at least three independent experiments. **e** Representative fluorescence micrographs of GBM α-tubulin acetylation (green) at lysine 40 in response to temozolomide (TMZ, 100 μM, $n = 76$ cells), sahaquine (Sq, 10 μM, $n = 56$ cells), quercetin (Q, 100 μM, $n = 32$ cells) or SAHA (10 μM, $n = 36$ cells) alone or in combination for 24 h. Nuclei (blue) were labeled with Hoechst 33342. **f** Shown are averages (SD) of fluorescence per cell normalized to the untreated control (set to 1, $n = 197$ cells) from at least three independent experiments (***$p < 0.001$, Welch's ANOVA with Games–Howell post hoc test)

present in different parts of the same tumor[53,54], or even in individual cells within a tumor[52,55]. Another cause of GBM heterogeneity is the presence of BTSCs, a subset of glioma cells with the abilities of self-renewal, differentiation, and recapitulation of the original tumor upon xenotransplantation[56–58]. They are resistant to radiation[28] and chemotherapy[59–61], and are thought to promote tumor recurrence[30,31]. Therefore, effective GBM treatment demands a better understanding of tumor origin and heterogeneity to identify new therapeutic targets[3,62].

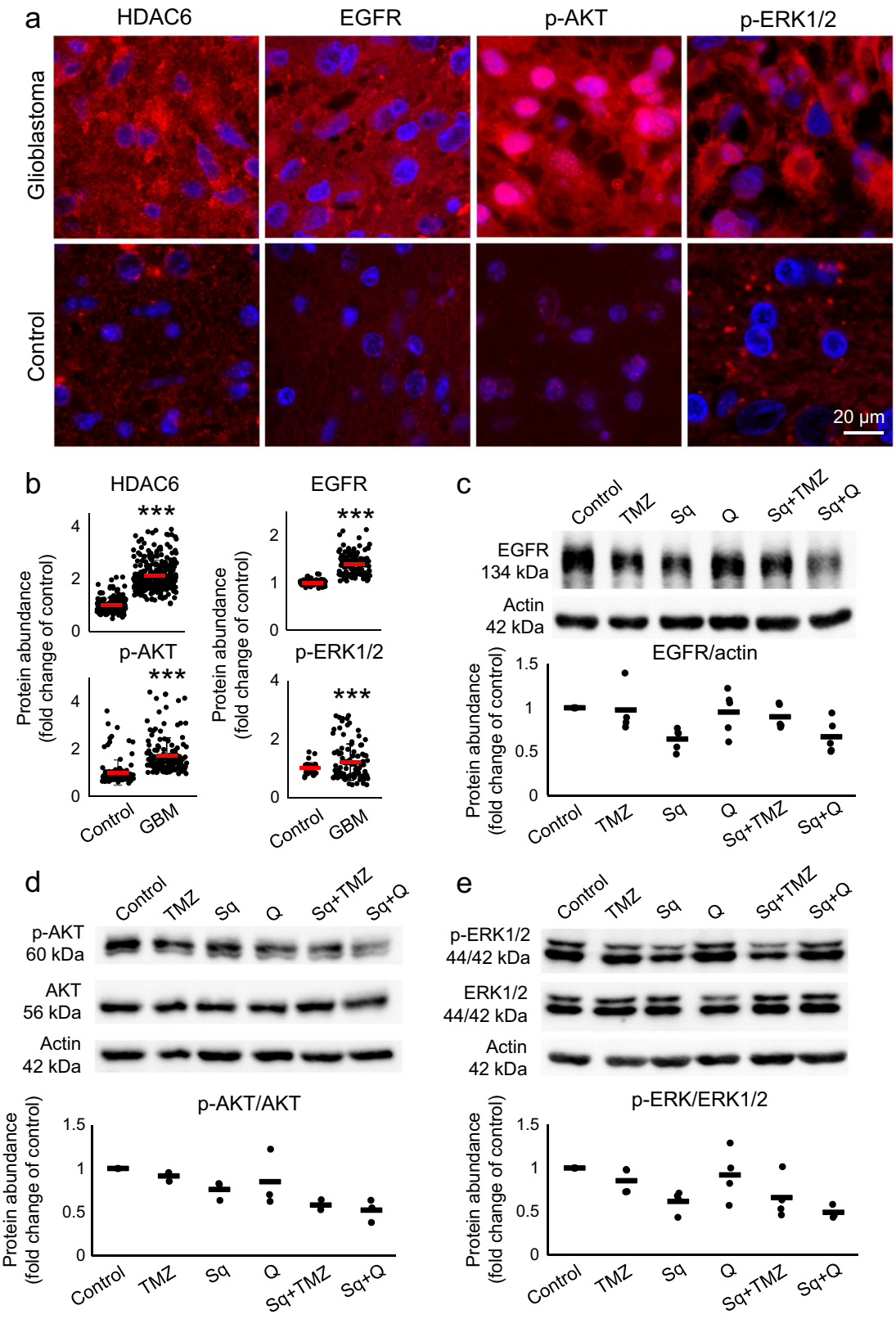

Figure 6 (See legend on next page.)

(see figure on previous page)
Figure 6 Sahaquine reduces EGFR abundance and AKT/ERK1/2 phosphorylation in human glioblastoma. a Representative fluorescence micrographs of human brain sections (GBM or healthy control) labeled for HDAC6, EGFR, phosphorylated AKT (p-AKT), or dually phosphorylated ERK1/2 (p-ERK1/2). Nuclei (blue) were labeled with Hoechst 33342. Cells were imaged using a fluorescence microscope and fluorescence was analyzed in ImageJ. **b** Horizontal bars represent averages of fluorescence per cell (SD) for HDAC6 (control, $n = 181$ cells, GBM, $n = 272$ cells), EGFR (control, $n = 94$ cells, GBM, $n = 116$ cells), p-AKT (control, $n = 115$ cells, GBM, $n = 147$ cells) and p-ERK1/2 (control, $n = 35$ cells, GBM, $n = 104$ cells). Each point represents a value normalized to the healthy control (set to 1) (***$p < 0.001$, Welch's ANOVA with Games–Howell post hoc test). **c** EGFR (TMZ, $n = 4$, Sq, $n = 5$, Q, $n = 5$, Sq + TMZ, $n = 5$, Sq + Q, $n = 5$), **d** phosphorylated AKT ($n = 3$), and **e** phosphorylated ERK1/2 (TMZ, $n = 4$, Sq, $n = 4$, Q, $n = 4$, Sq + TMZ, $n = 4$, Sq + Q, $n = 3$) protein abundances were measured in GBM cells treated with temozolomide (TMZ, 100 μM), sahaquine (Sq, 10 μM), or quercetin (Q, 100 μM) alone or in combination for 24 h, by Western blotting. EGFR protein abundance was normalized to the actin loading control. Phosphorylated AKT and ERK1/2 were normalized to total AKT and total ERK1/2, respectively. Each point represents a value normalized to the untreated control (set to 1). Horizontal bars represent means from at least three independent experiments

Sahaquine (10 μM) abolished the formation of BTSC neurospheres and significantly reduced the size of BTSC aggregates. TMZ was less effective, even at a tenfold higher concentration (100 μM). Quercetin was as effective as sahaquine in killing BTSCs, but showed limited cytotoxicity toward differentiated GBM cells. Sahaquine eliminated both BTSCs and differentiated cancer cells.

Another factor contributing considerably to GBM recurrence is tumor invasiveness. While sahaquine abolished invasiveness and contributed to the loss of tumoroid viability, it did not markedly affect the abundance of secreted MMPs. In contrast, quercetin had limited effects on tumoroid viability, but decreased GBM invasion by inhibiting MMP secretion. Quercetin inhibits nuclear factor-κB (NF-κB) nuclear translocation, which could alter MMP expression[63,64] and enhance cell death through NF-κB-dependent regulation of apoptosis.

In an effort to reduce undesirable side effects in normal cells, selective HDAC inhibitors have been developed[65,66]. Ricolinostat (ACY-1215) is a selective HDAC6 inhibitor currently in clinical trials (phase I and II) in combination with pomalidomide for multiple myeloma[67]. Ricolinostat inhibits heat shock protein 90 deacetylation, resulting in an accumulation of unfolded proteins, disruption of protein homeostasis and cell death[68]. We show that sahaquine selectively inhibits HDAC6 at nanomolar concentrations, which distinguishes it from SAHA, which is non-selective at equimolar concentrations. Interestingly, sahaquine significantly reduced the abundance of heat shock protein 70 in GBM (Supplementary Fig. S10) and altered α-tubulin organization. We have previously shown that celastrol disrupts protein homeostasis[69] and the organization of the F-actin cytoskeleton in GBM[70]. Future studies will have to evaluate how sahaquine affects proteostasis in relation to cytoskeletal dynamics.

Many drugs currently in clinical trials aim at inhibiting proteins and proliferation pathways deregulated in GBM, notably HDAC6, EGFR, AKT, and ERK1/2[71–74]. Our in vitro studies showing enhanced ERK1/2 and AKT phosphorylation are corroborated by immunohistochemical data in tumor sections from GBM patients (Fig. 6a), also showing markedly stronger signals for HDAC6, EGFR, phosphorylated ERK1/2, and phosphorylated AKT compared to normal brain tissue (Fig. 6a). Sahaquine can decrease the abundance of EGFR, phosphorylated AKT, and phosphorylated ERK1/2 in GBM (Fig. 6b), thereby suggesting that similar hybrid molecules are viable candidates for GBM combination therapy. Interestingly, AKT deacetylation by HDAC6 promotes cancer growth and proliferation[75], indicating that sahaquine could reduce AKT activation through HDAC6 inhibition.

Drug resistance is a major problem in glioblastoma therapy[3,41]. A recent study of HDAC inhibitors in drug-resistant melanoma implicated increased levels of reactive oxygen species[76]. Combination of sahaquine with buthionine sulfoximine, which depletes endogenous glutathione levels[77], sensitized GBM cells to reactive oxygen species and enhanced cell death (Supplementary Fig. S11), although buthionine sulfoximine alone in the tested concentration had no effect on GBM viability. Further analysis of the effect of sahaquine on reactive oxygen species production in GBM is warranted.

Taken together, our study reveals sahaquine as a therapeutic agent affecting multiple cellular factors and processes that are critical for GBM treatment (Fig. 7). Sahaquine is superior to the clinical standard TMZ in reducing GBM and BTSC viability, invasiveness, and markers of key survival pathways. These effects are even more profound when sahaquine is combined with TMZ, buthionine sulfoximine, or quercetin. In conclusion, sahaquine is an effective cell death inducer which eliminates not only GBM cells but also BTSCs, thus suggesting that evaluation of sahaquine in combination with other drugs merit further investigations in patient-derived organoids, and eventually in humans.

Materials and methods

Synthesis of sahaquine

Sahaquine **5** was synthesized in four reaction steps (Fig. 1) adapted from the synthetic approach of Zhang et al[45]. Details of these steps are provided in the Supplementary Information. The first step included amide bond

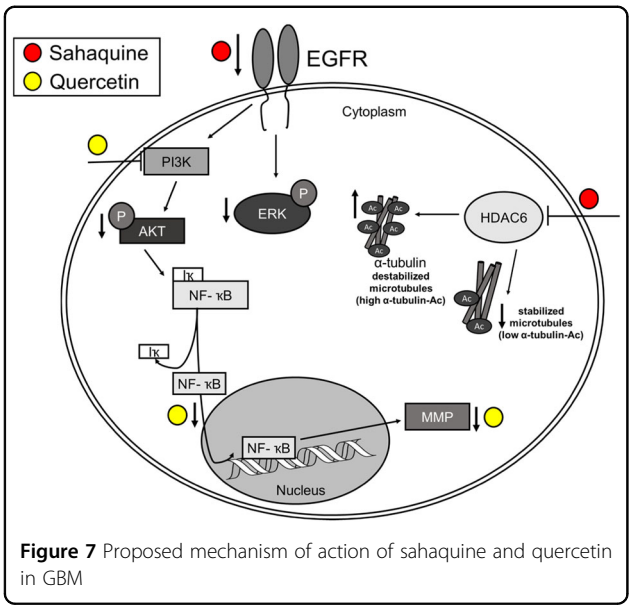

Figure 7 Proposed mechanism of action of sahaquine and quercetin in GBM

formation between mono-methyl glutarate (**1**, Sigma-Aldrich, St. Louis, MO, USA) and primaquine (Sigma-Aldrich, St. Louis, MO, USA), with 1-[*bis*(dimethylamino) methylene]-1*H*-1,2,3-triazolo[4,5-*b*]pyridinium 3-oxid hexafluorophosphate (HATU, Alfa Aesar, Thermo Fisher, Kandel, Germany) as a coupling agent and *N,N*-diisopropylethylamine (DIEA, Alfa Aesar, Thermo Fisher, Kandel, Germany) as a base. The prepared product **2** was further hydrolyzed with lithium hydroxide (Sigma-Aldrich, St. Louis, MO, USA) and gave carboxylic acid **3**. In the next step, **3** was coupled with *O*-benzylhydroxylamine (Sigma-Aldrich, St. Louis, MO, USA) in the presence of HATU/DIEA and yielded *O*-benzylhydroxamic acid **4**, which was deprotected by catalytic hydrogenation and gave the target compound **5** (sahaquine). All reactions proceeded at room temperature.

Cell culture and tissue samples

U251N human glioblastoma cells were originally obtained from the American Type Culture Collection. Cells were cultured in Dulbecco's modified Eagle's media (DMEM, Gibco, Thermo Fischer Scientific, Grand Island, NY, USA) supplemented with 5% (v/v) fetal bovine serum (Wisent, St. Bruno, Canada) and 1% (v/v) penicillin–streptomycin (Thermo Fisher Scientific, Eugene, OR, USA) at 37 °C with 5% CO_2 and 95% relative humidity, unless otherwise indicated. Glioblastoma samples were harvested under a protocol approved by the Montreal Neurological Hospital's research ethics board (NEU-10-066). Consent was given by all patients. At least 116 brain sections from GBM patients aged 55–76 and controls were used. Tissues were from the frontal, temporal, or parietal lobes of the cerebral cortex. Human BTSCs were expanded as neurospheres in complete NeuroCult^{TM} proliferation media (Stemcell Technologies, Vancouver, BC, Canada). NeuroCult^{TM} basal medium contained: NeuroCult^{TM} NS-A proliferation supplement (1/10), recombinant human epidermal growth factor EGF (20 ng/ml), recombinant human basic fibroblast growth factor (20 ng/ml), and heparin (2 μg/ml).

Cell counting assay

U251N cells were seeded in 96-well black plates (Costar, Corning, NY, USA) at 5,000 cells per well in 0.1 ml media and cultured for 24 h. Cells were treated with sahaquine (0.001, 1, 5, 10, 20, 25, 30, 40, and 50 μM), TMZ (0.001, 1, 10, 50, 100, 200, 300, 400, and 500 μM, Sigma-Aldrich, St. Louis, MO, USA), quercetin (0.001, 1, 10, 25, 50, 75, 100, 200, and 300 μM, Sigma-Aldrich, St. Louis, MO, USA), or SAHA (0.001, 0.1, 1, 2, 5, 8, 10, 25, and 50 μM, Cayman Chemical, Ann Arbor, MI, USA) for 24 or 72 h. Combination treatments included increasing concentrations of sahaquine (0.001, 1, 3, 5, 7, 10, 20, and 50 μM) with quercetin (100 μM), increasing concentrations of quercetin (0.001, 1, 10, 25, 50, 100, and 200 μM) with sahaquine (10 μM), TMZ (30 μM) with sahaquine (10 μM), quercetin (140 μM) or SAHA (1 μM), and buthionine sulfoximine (100 μM, Sigma-Aldrich, St. Louis, MO, USA) with sahaquine (10 μM) for 24 h or 72 h. Following treatment, cells were fixed with 4% paraformaldehyde (w/v, 10 min, BDH, Toronto, ON, Canada). Nuclei were labeled with Hoechst 33342 (10 μM, 10 min, Thermo Fisher Scientific, Eugene, OR, USA). Cells were washed with phosphate-buffered saline and imaged using a fluorescence microscope (Leica DMI4000B, Toronto, ON, Canada).

BTSC viability

48EF human brain tumor cells were seeded at 5,000 cells per well in 96-well plates (Sarstedt, Nümbrecht, Germany) and treated for 7 days. Cells were then imaged using light microscopy (Leica DMI4000B) and the surface areas of the neurospheres were measured in ImageJ (version 1.51s).

Scratch assay

U251N cells were seeded in 6-well plates (Sarstedt, Nümbrecht, Germany) at 1,500,000 cells per well in 1 ml media and cultured for 24 h. The scratch was performed by gently dragging a 200 μl pipette tip across the cell monolayer, after which cells were washed with phosphate-buffered saline and incubated in DMEM with or without treatment. Cytochalasin D (40 nM, Sigma-Aldrich, St. Louis, MO, USA) served as positive control. Predetermined areas of the wells were imaged using light microscopy immediately after the scratch (time = 0 h) and after 24 h. The cell-free area of the scratch was measured in ImageJ.

Cell invasion assay

U251N tumoroids were prepared using the hanging drop method[78]. Drops of 30,000 cells in 20 µl medium were pipetted onto the inner side of a 10 cm Petri dish (Thermo Fisher Scientific, Eugene, OR, USA) lid. The lid was quickly flipped to cover the Petri dish filled with 20 ml phosphate-buffered saline. Hanging drops were cultured at 37 °C for 48 h to allow tumoroids to form. Tumoroids were then gently scooped into a medium-filled Petri dish coated with 2% agarose and cultured for 48 h. Tumoroids were implanted in collagen gel (Advanced BioMatrix, San Diego, CA, USA) mixed with DMEM (1×) and sodium hydroxide (10 mM, Sigma-Aldrich, St. Louis, MO, USA). Gels were covered with 500 µl DMEM with or without treatment. Tumoroids were imaged using light microscopy immediately after implantation (time = 0 day) and after 4 days. The area of cell invasion was measured in ImageJ.

Immunocytochemistry

Following treatment, U251N human glioblastoma cells were fixed with 4% paraformaldehyde (10 min), and then permeabilized using 0.1% Triton X-100 (v/v, 10 min, Sigma-Aldrich, St. Louis, MO, USA). Blocking was performed with 10% goat serum (v/v, 1 h, Thermo Fisher Scientific, Eugene, OR, USA) in phosphate-buffered saline, and then samples were incubated with primary antibodies (acetyl-histone H3 K9/K14, 1/500, Cell Signalling, #9677; acetyl-α-tubulin K40, 1/500, Santa Cruz, sc-23950; α-tubulin, 1/1000, Abcam, ab7291) overnight at 4 °C in a humidified chamber. Samples were washed three times with phosphate-buffered saline with 5 min incubation between washes. Secondary antibodies (anti-rabbit Alexa Fluor 488, 1/500, Thermo Fisher Scientific, A11008; anti-mouse Alexa Fluor 647, 1/500, Thermo Fisher Scientific, A28181) were incubated with samples for 1 h in the dark, and then washed off three times with phosphate-buffered saline with 5 min incubation in between washes. Nuclei were labeled with Hoechst 33342 (10 µM, 10 min). Samples were mounted on microscope slides using Aqua-Poly/Mount (Polysciences, Warrington, PA, USA) and dried overnight before imaging with a fluorescence microscope (Leica DMI4000B).

Immunohistochemistry

Human brain sections were dewaxed in xylene, and then rehydrated in ethanol. Antigen retrieval was performed in citrate buffer using a decloaking chamber for 3 h. Samples were washed twice with double-distilled water, three times with phosphate-buffered saline, and then blocked with Protein Block (10 min, Spring Biosciences, Pleasanton, CA, USA). Samples were incubated with primary antibodies (HDAC6, 1/100, Santa Cruz, sc-11420; EGFR, 1/100, Oncogene Science Ab-1; phospho-AKT Ser473, Cell Signalling, #9271; phospho-p44/42 Erk1/2 Thr202/Tyr204, 1/100, Cell Signalling, #9101) overnight at 4 °C in a humidified chamber. Samples were washed twice with IF buffer (0.05% (v/v) Tween 20, 0.2% (v/v) Triton X-100 in phosphate-buffered saline). Secondary antibodies (anti-rabbit Alexa Fluor 647, 1/500, Thermo Fisher Scientific, A21245; anti-rabbit Alexa Fluor 488, 1/1000, Thermo Fisher Scientific, A27034; anti-mouse Alexa Fluor 647, 1/1000, Thermo Fisher Scientific, A-21235) diluted in 2% (w/v) bovine serum albumin (Sigma-Aldrich, St. Louis, MO, USA) in phosphate-buffered saline were incubated with samples for 1 h in the dark at room temperature. Samples were washed three times with IF buffer, and then nuclei were labeled with DAPI (4′,6-diamidino-2-phenylindole; 1 µg/ml, 5 min, Molecular Probes, Eugene, OR, USA). Samples were washed three times with phosphate-buffered saline, then mounted on microscope slides using mounting media (Dako, Mississauga, ON, Canada), and air-dried for at least 30 min. Samples were imaged using a fluorescence microscope (Leica DMI4000B).

Western blotting

Western blot analysis followed published procedures[70]. In brief, crude extracts were separated by sodium dodecyl sulfate–polyacrylamide gel electrophoresis (SDS-PAGE) and blotted onto nitrocellulose membranes. Blocked filters were probed with antibodies against acetyl-α-tubulin K40 (1/10,000, Sigma-Aldrich, St. Louis, MO, USA, #T7451), α-tubulin (1/1000, Santa Cruz, sc-5286), phospho-AKT Ser473 (1/2000, Santa Cruz, sc-7985), pan-AKT (1/1500, Cell Signaling, #9272), HDAC6 (1/1000, Santa Cruz, sc-11420), EGFR (1/1000, Santa Cruz, sc-03), phospho-ERK1/2 Thr202/Tyr204 (1/2000, Cell Signaling, #9106), pan-ERK1/2 (1/2000, Cell Signaling, #4695), and actin (1/100,000, Chemicon, MAB1501). Signals for enhanced chemiluminescence were acquired with a Bio-Rad ChemiDoc™ MP imaging system and quantified.

MTT assay

U251N cells were seeded in 24-well plates (Sarstedt, Nümbrecht, Germany) at 50,000 cells per well in 300 µl media and cultured for 24 h. Cells were treated with sahaquine (0.001, 1, 5, 10, 25, and 50 µM), TMZ (50, 100, 200, 300, 400, and 500 µM), quercetin (10, 50, 100, and 200 µM), or SAHA (0.1, 1, 2, 5, 8, 10, and 50 µM) for 72 h. Combination treatments included increasing concentrations of sahaquine (1, 10, and 50 µM) with a fixed concentration of quercetin (100 µM), or increasing concentrations of quercetin (10, 100, and 200 µM) with a fixed concentration of sahaquine (10 µM) for 72 h. Following treatment, MTT (Sigma-Aldrich, St. Louis, MO, USA) dissolved in phosphate-buffered saline was added to cells (0.5 mg/ml) for 1 h at 37 °C. After MTT-containing media were removed, dimethyl sulfoxide (0.5 ml) was added to each well to lyse cells and dissolve formazan.

Wells were sampled in triplicate and the optical density was measured at 595 nm using a microplate reader (Asys UVM 340, Biochrom, Holliston, MA, USA).

Gelatin zymography

U251N cells were seeded in 60-mm tissue culture dishes (Thermo Fisher Scientific, Rochester, NY, USA) at 1,500,000 cells per dish in 3 ml media and cultured for 24 h. Cells were treated in serum-deprived DMEM for 24 h. Following treatment, culture media were collected and concentrated 15-fold using 30 kDa centrifugal filters (Millipore, Cork, Ireland) following the manufacturer's recommendations. Concentrated media were separated by SDS-PAGE using gelatin (0.1%, w/v) and acrylamide (7.5%, w/v) gels under non-reducing conditions. Gels were washed for 30 min in renaturing solution (2.5% (v/v) Triton X-100 in double-distilled water) and 30 min in developing buffer (50 mM Tris, pH 7.8; 1% (v/v) Triton X-100; 1 µM $ZnCl_2$, 5 mM $CaCl_2$, adjusted to pH 7.45). Gels were then incubated in fresh developing buffer at 37 °C overnight. Gels were stained with 0.5% (w/v) Coomassie Blue G250 (Bio-Rad, Richmond, CA, USA) dissolved in 40% (v/v) ethanol and 10% (v/v) acetic acid for 1 h, and then destained in 40% ethanol and 10% acetic acid diluted in double-distilled water, until clear bands appeared. Quantification of MMP-9 and MMP-2 abundance (as band area) was done in ImageJ.

Tumoroid viability

U251N tumoroids were prepared using the liquid overlay system[79]. The 96-well cell culture plates were coated with 75 µl of 2% (w/v) agarose (Life Technologies, Gaithersburg, MD, USA) dissolved in serum-deprived DMEM. The agarose was cooled for 30 min, then cells were seeded at 5,000 cells per well in 200 µl media, and cultured for 4 days before treatment. Cells were treated for 7 days, and then imaged using a microscope (Leica DMI4000B). The surface area of tumoroids was analyzed in ImageJ.

Calcein-AM uptake

U251N cells were seeded in 96-well black plates at 5,000 cells per well in 0.1 ml media and cultured for 24 h before treatment. Cyclosporine A (Calbiochem, Toronto, Canada) served as a positive control for the inhibition of P-glycoprotein. Following treatment, cells were incubated in phenol-free Hanks' balanced Salt solution containing calcein-AM (0.5 µM, Thermo Fisher Scientific, Eugene, OR, USA) and propidium iodide (3 µM, Sigma-Aldrich, St. Louis, MO, USA) for 30 min at 37 °C. The media were replaced with fresh Hanks' balanced salt solution and cells were imaged using a fluorescence microscope (Leica DMI4000B). Cells positively labeled with propidium iodide were excluded from the analysis.

Statistics

Experiments were performed independently at least three times. Unless otherwise indicated, data are shown as mean (SD). Normality of data distribution was assessed by the Shapiro–Wilk test. For sample sizes larger than 30, the Central Limit Theorem allows the assumption of normal distribution. Equality of variances was assessed by Levene's test. If the assumptions of normality and homogeneity of variance were met, two-tailed one-way analysis of variance (ANOVA) with Tukey–Kramer's post hoc test were performed. If homogeneity of variance was not observed, Welch's ANOVA with the Games–Howell post hoc test were used. A p value smaller than 0.05 was considered statistically significant: $^{*}p < 0.05$, $^{**}p < 0.01$, and $^{***}p < 0.001$.

Acknowledgements

We wish to thank J. Choi and E. Gran for their contribution to initial experiments related to this study. D.M. thanks the Canadian Institute for Health Research (MOP-119425) and the Natural Sciences and Engineering Council of Canada (RGPIN 04994-15). K.P. is grateful to the Brilliant Night Foundation, and B.Z. thanks the Croatian Science Foundation (IP-2014-09-1501) for financial support.

Authors' contributions

D.M. designed and coordinated the project. M.B., I.Z., and U.S. performed the experiments. M.B., I.Z., D.M., and U.S. analyzed and discussed the data. D.M., U. S., P.U.L., K.P., B.Z., and Z.R. contributed with reagents or clinical samples and discussion. M.B., I.Z., and D.M. wrote the manuscript with the help from the rest of the authors.

Author details

[1]Department of Pharmacology and Therapeutics, McGill University, Montreal, QC, Canada. [2]Faculty of Pharmacy and Biochemistry, University of Zagreb, Zagreb, Croatia. [3]Department of Physiology, McGill University, Montreal, QC, Canada. [4]Brain Tumour Research Centre, Montreal Neurological Institute and Hospital, Department of Neurology and Neurosurgery, McGill University, Montreal, QC, Canada

Conflict of interest

The authors declare that they have no conflict of interest.

The online version of this article (https://doi.org/10.1038/s41420-018-0103-0) contains supplementary material, which is available to authorized users.

Received: 16 July 2018 Revised: 10 August 2018 Accepted: 21 August 2018
Published online: 26 September 2018

References

1. Weller, M. et al. European Association for Neuro-Oncology (EANO) guideline on the diagnosis and treatment of adult astrocytic and oligodendroglial gliomas. *Lancet Oncol.* **18**, e315–e329 (2017).
2. Weller, M. et al. MGMT promoter methylation in malignant gliomas: ready for personalized medicine? *Nat. Rev. Neurol.* **6**, 39–51 (2010).
3. Hegi, M. E. et al. MGMT gene silencing and benefit from temozolomide in glioblastoma. *N. Engl. J. Med.* **352**, 997–1003 (2005).

4. Erasimus, H., Gobin, M., Niclou, S. & Van Dyck, E. DNA repair mechanisms and their clinical impact in glioblastoma. *Mutat. Res. Rev. Mutat. Res* **769**, 19–35 (2016).
5. Johnstone, R. W. Histone-deacetylase inhibitors: novel drugs for the treatment of cancer. *Nat. Rev. Drug Discov.* **1**, 287–299 (2002).
6. Galanis, E. et al. Phase II trial of vorinostat in recurrent glioblastoma multiforme: a north central cancer treatment group study. *J. Clin. Oncol.* **27**, 2052–2058 (2009).
7. Hummel, T. R. et al. A pediatric phase 1 trial of vorinostat and temozolomide in relapsed or refractory primary brain or spinal cord tumors: a Children's Oncology Group Phase 1 Consortium Study. *Pediatr. Blood Cancer* **60**, 1452–1457 (2013).
8. Lee, E. Q. et al. Phase I study of vorinostat in combination with temozolomide in patients with high-grade gliomas: North American Brain Tumor Consortium Study 04-03. *Clin. Cancer Res.* **18**, 6032–6039 (2012).
9. Vorinostat and Radiation Therapy Followed by Maintenance Therapy With Vorinostat in Treating Younger Patients With Newly Diagnosed Diffuse Intrinsic Pontine Glioma—Full Text View—ClinicalTrials.gov. https://clinicaltrials.gov/ct2/show/NCT01189266 (accessed 31 May 2018).
10. Weathers, S.-P. & Gilbert, M. R. Advances in treating glioblastoma. *F1000Prime Rep.* **6**, 46 (2014).
11. Glozak, M. A. & Seto, E. Histone deacetylases and cancer. *Oncogene* **26**, 5420–5432 (2007).
12. Lee, D. H., Ryu, H.-W., Won, H.-R. & Kwon, S. H. Advances in epigenetic glioblastoma therapy. *Oncotarget* **8**, 18577–18589 (2017).
13. Grant, S., Easley, C. & Kirkpatrick, P. Vorinostat. *Nat. Rev. Drug Discov.* **6**, 21–22 (2007).
14. Bertrand, S., Hélesbeux, J.-J., Larcher, G. & Duval, O. Hydroxamate, a key pharmacophore exhibiting a wide range of biological activities. *Mini Rev. Med. Chem.* **13**, 1311–1326 (2013).
15. Gialeli, C., Theocharis, A. D. & Karamanos, N. K. Roles of matrix metalloproteinases in cancer progression and their pharmacological targeting. *FEBS J.* **278**, 16–27 (2011).
16. Corbet, C. & Feron, O. Tumour acidosis: from the passenger to the driver's seat. *Nat. Rev. Cancer* **17**, 577–593 (2017).
17. Mahoney, B. P., Raghunand, N., Baggett, B. & Gillies, R. J. Tumor acidity, ion trapping and chemotherapeutics. I. Acid pH affects the distribution of chemotherapeutic agents in vitro. *Biochem. Pharmacol.* **66**, 1207–1218 (2003).
18. Zhitomirsky, B. & Assaraf, Y. G. Lysosomal accumulation of anticancer drugs triggers lysosomal exocytosis. *Oncotarget* **8**, 45117–45132 (2017).
19. van Weert, A. W., Geuze, H. J., Groothuis, B. & Stoorvogel, W. Primaquine interferes with membrane recycling from endosomes to the plasma membrane through a direct interaction with endosomes which does not involve neutralisation of endosomal pH nor osmotic swelling of endosomes. *Eur. J. Cell Biol.* **79**, 394–399 (2000).
20. Kim, J.-H., Choi, A.-R., Kim, Y. K. & Yoon, S. Co-treatment with the anti-malarial drugs mefloquine and primaquine highly sensitizes drug-resistant cancer cells by increasing P-gp inhibition. *Biochem. Biophys. Res. Commun.* **441**, 655–660 (2013).
21. Yang, Z. J., Chee, C. E., Huang, S. & Sinicrope, F. A. The role of autophagy in cancer: therapeutic implications. *Mol. Cancer Ther.* **10**, 1533–1541 (2011).
22. Andres S. et al. Safety aspects of the use of quercetin as a dietary supplement. *Mol. Nutr. Food Res.* **62,** https://doi.org/10.1002/mnfr.201700447 (2018).
23. Srivastava, S. et al. Quercetin, a natural flavonoid interacts with DNA, arrests cell cycle and causes tumor regression by activating mitochondrial pathway of apoptosis. *Sci. Rep.* **6**, 24049 (2016).
24. Calgarotto, A. K. et al. Antitumor activities of Quercetin and Green Tea in xenografts of human leukemia HL60 cells. *Sci. Rep.* **8**, 3459 (2018).
25. Sun, S., Gong, F., Liu, P. & Miao, Q. Metformin combined with quercetin synergistically repressed prostate cancer cells via inhibition of VEGF/PI3K/Akt signaling pathway. *Gene* **664**, 50–57 (2018).
26. Zhang, X., Guo, Q., Chen, J. & Chen, Z. Quercetin enhances cisplatin sensitivity of human osteosarcoma cells by modulating microRNA-217-KRAS axis. *Mol. Cells* **38**, 638–642 (2015).
27. Zanini, C. et al. Inhibition of heat shock proteins (HSP) expression by quercetin and differential doxorubicin sensitization in neuroblastoma and Ewing's sarcoma cell lines. *J. Neurochem.* **103**, 1344–1354 (2007).
28. Bao, S. et al. Stem cell-like glioma cells promote tumor angiogenesis through vascular endothelial growth factor. *Cancer Res.* **66**, 7843–7848 (2006).
29. Chen, J., McKay, R. M. & Parada, L. F. Malignant glioma: lessons from genomics, mouse models, and stem cells. *Cell* **149**, 36–47 (2012).
30. Dagogo-Jack, I. & Shaw, A. T. Tumour heterogeneity and resistance to cancer therapies. *Nat. Rev. Clin. Oncol.* **15**, 81–94 (2018).
31. Johnson, B. E. et al. Mutational analysis reveals the origin and therapy-driven evolution of recurrent glioma. *Science* **343**, 189–193 (2014).
32. Chemicalize—Instant Cheminformatics Solutions. https://chemicalize.com/ (accessed 31 May 2018).
33. Holland, E. C. Glioblastoma multiforme: the terminator. *Proc. Natl. Acad. Sci. USA* **97**, 6242–6244 (2000).
34. Nakada, M., Okada, Y. & Yamashita, J. The role of matrix metalloproteinases in glioma invasion. *Front Biosci.* **8**, e261–e269 (2003).
35. Alaseem A. et al. Matrix metalloproteinases: a challenging paradigm of cancer management. *Semin. Cancer Biol.* https://doi.org/10.1016/j.semcancer.2017.11.008 (2017).
36. Jacobsen, J. A., Major Jourden, J. L., Miller, M. T. & Cohen, S. M. To bind zinc or not to bind zinc: an examination of innovative approaches to improved metalloproteinase inhibition. *Biochim. Biophys. Acta* **1803**, 72–94 (2010).
37. Bieliauskas, A. V. & Pflum, M. K. H. Isoform-selective histone deacetylase inhibitors. *Chem. Soc. Rev.* **37**, 1402–1413 (2008).
38. Schäfer, S. et al. Phenylalanine-containing hydroxamic acids as selective inhibitors of class IIb histone deacetylases (HDACs). *Bioorg. Med. Chem.* **16**, 2011–2033 (2008).
39. Sanchez-Vega, F. et al. Oncogenic signaling pathways in the Cancer Genome Atlas. *Cell* **173**, 321–337.e10 (2018).
40. Shinojima, N. et al. Prognostic value of epidermal growth factor receptor in patients with glioblastoma multiforme. *Cancer Res.* **63**, 6962–6970 (2003).
41. Lee, S. Y. Temozolomide resistance in glioblastoma multiforme. *Genes Dis.* **3**, 198–210 (2016).
42. Caporali, S. et al. DNA damage induced by temozolomide signals to both ATM and ATR: role of the mismatch repair system. *Mol. Pharmacol.* **66**, 478–491 (2004).
43. Yin, D. et al. Suberoylanilide hydroxamic acid, a histone deacetylase inhibitor: effects on gene expression and growth of glioma cells in vitro and in vivo. *Clin. Cancer Res.* **13**, 1045–1052 (2007).
44. Peters, K. B. et al. Phase I/II trial of vorinostat, bevacizumab, and daily temozolomide for recurrent malignant gliomas. *J. Neurooncol.* **137**, 349–356 (2018).
45. Zhang, X. et al. The discovery of colchicine-SAHA hybrids as a new class of antitumor agents. *Bioorg. Med. Chem.* **21**, 3240–3244 (2013).
46. Meunier, B. Hybrid molecules with a dual mode of action: dream or reality? *Acc. Chem. Res.* **41**, 69–77 (2008).
47. Cavalli, F. M. G. et al. Intertumoral heterogeneity within medulloblastoma subgroups. *Cancer Cell.* **31**, 737–754.e6 (2017).
48. Hunter, K. W., Amin, R., Deasy, S., Ha, N.-H. & Wakefield, L. Genetic insights into the morass of metastatic heterogeneity. *Nat. Rev. Cancer* **18**, 211–223 (2018).
49. Meacham, C. E. & Morrison, S. J. Tumour heterogeneity and cancer cell plasticity. *Nature* **501**, 328–337 (2013).
50. Lin, C.-C. J. et al. Identification of diverse astrocyte populations and their malignant analogs. *Nat. Neurosci.* **20**, 396–405 (2017).
51. Cancer Genome Atlas Research Network. Comprehensive genomic characterization defines human glioblastoma genes and core pathways. *Nature* **455**, 1061–1068 (2008).
52. Verhaak, R. G. W. et al. An integrated genomic analysis identifies clinically relevant subtypes of glioblastoma characterized by abnormalities in PDGFRA, IDH1, EGFR and NF1. *Cancer Cell* **17**, 98 (2010).
53. Sottoriva, A. et al. Intratumor heterogeneity in human glioblastoma reflects cancer evolutionary dynamics. *Proc. Natl. Acad. Sci. USA* **110**, 4009–4014 (2013).
54. Morrissy, A. S. et al. Spatial heterogeneity in medulloblastoma. *Nat. Genet.* **49**, 780–788 (2017).
55. Patel, A. P. et al. Single-cell RNA-seq highlights intratumoral heterogeneity in primary glioblastoma. *Science* **344**, 1396–1401 (2014).
56. Galli, R. et al. Isolation and characterization of tumorigenic, stem-like neural precursors from human glioblastoma. *Cancer Res.* **64**, 7011–7021 (2004).
57. Lee, J. et al. Tumor stem cells derived from glioblastomas cultured in bFGF and EGF more closely mirror the phenotype and genotype of primary tumors than do serum-cultured cell lines. *Cancer Cell* **9**, 391–403 (2006).
58. Singh, S. K. et al. Identification of human brain tumour initiating cells. *Nature* **432**, 396–401 (2004).
59. Liu, G. et al. Analysis of gene expression and chemoresistance of CD133+ cancer stem cells in glioblastoma. *Mol. Cancer* **5**, 67 (2006).
60. Bleau, A.-M. et al. PTEN/PI3K/Akt pathway regulates the side population phenotype and ABCG2 activity in glioma tumor stem-like cells. *Cell Stem Cell* **4**, 226–235 (2009).

61. Chen S.-F. et al. Nonadhesive culture system as a model of rapid sphere formation with cancer stem cell properties. *PLoS ONE* **7**, https://doi.org/10.1371/journal.pone.0031864 (2012).
62. Fouse, S. D., Nakamura, J. L., James, C. D., Chang, S. & Costello, J. F. Response of primary glioblastoma cells to therapy is patient specific and independent of cancer stem cell phenotype. *Neuro-Oncology* **16**, 361–371 (2014).
63. Bond, M., Chase, A. J., Baker, A. H. & Newby, A. C. Inhibition of transcription factor NF-kappaB reduces matrix metalloproteinase-1, -3 and -9 production by vascular smooth muscle cells. *Cardiovasc. Res.* **50**, 556–565 (2001).
64. Soubannier, V. & Stifani, S. NF-κB signalling in glioblastoma. *Biomedicines* **5**, https://doi.org/10.3390/biomedicines5020029 (2017).
65. Lee, J.-H. et al. Development of a histone deacetylase 6 inhibitor and its biological effects. *Proc. Natl. Acad. Sci. USA* **110**, 15704–15709 (2013).
66. Santo, L. et al. Preclinical activity, pharmacodynamic, and pharmacokinetic properties of a selective HDAC6 inhibitor, ACY-1215, in combination with bortezomib in multiple myeloma. *Blood* **119**, 2579–2589 (2012).
67. ACY-1215 (Ricolinostat) in Combination With Pomalidomide and Low-dose Dex in Relapsed-and-Refractory Multiple Myeloma—Full Text View—ClinicalTrials.gov. https://clinicaltrials.gov/ct2/show/NCT01997840 (accessed 31 May 2018).
68. Kekatpure, V. D., Dannenberg, A. J. & Subbaramaiah, K. HDAC6 modulates Hsp90 chaperone activity and regulates activation of aryl hydrocarbon receptor signaling. *J. Biol. Chem.* **284**, 7436–7445 (2009).
69. Boridy, S., Le, P. U., Petrecca, K. & Maysinger, D. Celastrol targets proteostasis and acts synergistically with a heat-shock protein 90 inhibitor to kill human glioblastoma cells. *Cell Death Dis.* **5**, e1216 (2014).
70. Maysinger, D., Moquin, A., Choi, J., Kodiha, M. & Stochaj, U. Gold nanourchins and celastrol reorganize the nucleo- and cytoskeleton of glioblastoma cells. *Nanoscale* **10**, 1716–1726 (2018).
71. Combs, S. E. et al. Treatment of primary glioblastoma multiforme with cetuximab, radiotherapy and temozolomide (GERT)—phase I/II trial: study protocol. *BMC Cancer* **6**, 133 (2006).
72. Emrich, J. G. et al. Radioiodinated (I-125) monoclonal antibody 425 in the treatment of high grade glioma patients: ten-year synopsis of a novel treatment. *Am. J. Clin. Oncol.* **25**, 541–546 (2002).
73. Quang, T. S. & Brady, L. W. Radioimmunotherapy as a novel treatment regimen: ^{125}I-labeled monoclonal antibody 425 in the treatment of high-grade brain gliomas. *Int. J. Radiat. Oncol. Biol. Phys.* **58**, 972–975 (2004).
74. ONC201 in Adults With Recurrent H3 K27M-mutant Glioma—Full Text View—ClinicalTrials.gov. https://clinicaltrials.gov/ct2/show/NCT03295396 (accessed 31 May 2018).
75. Iaconelli, J. et al. Lysine deacetylation by HDAC6 regulates the kinase activity of AKT in human neural progenitor cells. *ACS Chem. Biol.* **12**, 2139–2148 (2017).
76. Wang, L. et al. An acquired vulnerability of drug-resistant melanoma with therapeutic potential. *Cell* **173**, 1413–1425.e14 (2018).
77. Du, M., Zhang, L., Scorsone, K. A., Woodfield, S. E. & Zage, P. E. Nifurtimox is effective against neural tumor cells and is synergistic with buthionine sulfoximine. *Sci. Rep.* **6**, https://doi.org/10.1038/srep27458 (2016).
78. Werbowetski-Ogilvie, T. et al. Inhibition of medulloblastoma cell invasion by Slit. *Oncogene* **25**, 5103–5112 (2006).
79. Dhanikula, R. S., Argaw, A., Bouchard, J.-F. & Hildgen, P. Methotrexate loaded polyether–copolyester dendrimers for the treatment of gliomas: enhanced efficacy and intratumoral transport capability. *Mol. Pharm.* **5**, 105–116 (2008).

Supplementary Information

Chemistry

Melting points were measured on a Stuart Melting Point (SMP3) apparatus (Barloworld Scientific, UK) in open capillaries and are uncorrected. IR spectra were recorded on FTIR Perkin Elmer Paragon 500 and UV-Vis spectra on Lambda 20 double beam spectrophotometer (Perkin-Elmer, Waltham, MA, USA). All NMR (^{1}H and ^{13}C) spectra were recorded at 25°C on NMR Avance 600 (Bruker, Rheinstetten, Germany) and Varian Inova 400 spectrometers (Varian, Palo-Alto, CA, USA). Chemical shifts (δ) are reported in parts per million (ppm) using tetramethylsilane as reference in the ^{1}H and the DMSO residual peak as reference in the ^{13}C spectra (39.51 ppm). Coupling constants (J) are reported in Hertz (Hz). Mass spectra were recorded on HPLC-MS/MS (HPLC, Agilent Technologies 1200 Series; MS, Agilent Technologies 6410 Triple Quad, Santa Clara, CA, USA). Mass determination was realized using electron spray ionization (ESI) in positive mode. Elemental analyses were performed on a CHNS LECO analyzer (LECO Corporation, St. Joseph, MI, USA). Primaquine was prepared from primaquine diphosphate (Sigma Aldrich, St. Louis, MO, USA) prior the use. All reactions with primaquine were run light protected.

Synthesis of sahaquine

Compound 2

Mono-methyl glutarate **1** (0.206 g,0.0014 mol, Sigma-Aldrich, St. Louis, MO, USA), HATU (0.532 g, 0.0014 mol, Alfa Aesar, ThermoFisher, Kandel, Germany) and DIEA (0.362 g, 0.0028 mol, Alfa Aesar, ThermoFisher, Kandel, Germany) were dissolved and stirred in dichloromethane at room temperature. After 10 min, a solution of primaquine (0.401 g, 0.0015 mol, Sigma-Aldrich) in dichloromethane was added. After 1h at room temperature, reaction mixture was evaporated under reduced pressure, dissolved in ethyl acetate and washed three times with brine. The organic layer was dried over sodium sulfate, filtered and evaporated under reduced pressure. The crude product was purified by column chromatography (dichloromethane/methanol 95:5) and crystallized from ether to give pure **2**, yellow oil (0.439 g, 81%); IR: ν_{max} 3376, 3246, 3086, 2993, 2961, 2927, 1736, 1632, 1612, 1574, 1520, 1458, 1423, 1386, 1219, 1203, 1172, 1161, 1052, 992, 817, 788, 751, 720, 676 cm^{-1}; ^{1}H NMR (300 MHz, DMSO) δ 8.53(d, J = 2.6, 1H), 8.07 (d, J = 8.2, 1H), 7.78 (t, J = 3, 1H), 7.43-7.41 (m, 1H), 6.47 (d, J = 2.2, 1H), 6.26 (d, J = 2.2, 1H), 6.11 (d, J = 8.8, 1H), 3.82 (s, 3H), 3.64-3.60 (m, 1H), 3.57 (s, 3H), 3.05 (t, J = 6.0, 2H), 2.27 (t, J = 3.0, 2H), 2.07 (t, J = 7.3, 2H), 1.74-1.69 (m, 2H), 1.67-1.62, 1.54-1.44 (2m, 4H), 1.21(d, J = 6.2, 3H; ^{13}C NMR (75 MHz, DMSO) δ 173.00, 171.18, 158.98, 144.60, 144.20, 134.76, 134.50, 129.55, 122.05, 96.08, 91.59, 54.95, 51.14, 46.97, 38.36, 34.28, 33.40, 32.64, 25.93, 20.62, 20.17; MS/MS (*m/z*): $[M]^{+}$ calcd. for $C_{21}H_{29}N_3O_4$, 388.22; found, 388.3; analysis (calcd., found for $C_{21}H_{29}N_3O_4$): C (65.09, 65.35), H (7.54, (7.33), N (10.84, 10.99).

Compound 3

Lithium hydroxide monohydrate (0.126 g, 0.003 mol, Sigma-Aldrich, St. Louis, MO, USA) and ester **2** (0.323 g, 0.0006 mol) were stirred in a mixture of water and methanol for 1 h at room temperature. Methanol was evaporated under reduced pressure and the aqueous residue was neutralized with 10%-HCl and extracted three times with dichloromethane. The organic layer was dried over sodium sulfate, filtered and evaporated under reduced pressure. The crude product was crystallized from ether to give crude product **3** (0.186 g, 88%); pale yellow solid; mp 95–96 °C; IR: ν_{max} 3453, 3324, 2933, 1720, 1643, 1613, 1580, 1524, 1386, 1227, 1204, 1161, 1139, 1058, 822, 786, 675 cm^{-1}; ^{1}H NMR (300 MHz, DMSO) δ 12.00 (s, 1H), 8.55-8.53 (dd, J = 4.2, 1.6, 1H), 8.10-8.07 (dd, J = 8.3, 1.5, 1H), 7.80(t, J = 5.4, 1H), 7.45-7.41 (m, 1H), 6.48 (d, J = 2.4, 1H), 6.27 (d, J = 2.4, 1H), 6.13 (d, J = 8.7, 1H), 3.83 (s, 3H), 3.69-3.55 (m, 1H), 3.09-3.05 (m, 2H), 2.20 (t, J = 7.4, 2H), 2.08 (t, J = 7.4, 2H), 1.75-1.43 (m, 6H), 1.21 (d, J = 6.3, 3H); ^{13}C NMR (75 MHz, DMSO) δ 147.15, 171.36, 159.00, 144.63, 144.23, 134.79, 134.53, 129.57, 122.09, 96.11, 91.60, 54.97, 46.98, 38.38, 34.46, 33.41, 33.04, 25.97, 20.71, 20.19; MS/MS (*m/z*): $[M]^+$ calcd. for $C_{20}H_{27}N_3O_4$, 374.2; found, 374.2; analysis (calcd., found for $C_{20}H_{27}N_3O_4$): C (64.32, 64.21), H (7.29, 7.15), N (11.25, 11.48).

Compound 4

Solution of carboxylic acid **3** (0.224 g, 0.0006 mol), HATU (0.228 g, 0.0006 mol) and DIEA (0.155 g, 0.0012 mol) was stirred in dichloromethane at room temperature. After 10 min, *O*-benzylhydroxylamine hydrochloride (0.112 g, 0.0007 mol, Sigma-Aldrich, St. Louis, MO, USA) and triethylamine (0.071 g, 0.0007 mol, Sigma-Aldrich, St. Louis, MO, USA) were added. The reaction mixture was stirred for 2 h at room temperature, evaporated under reduced pressure, dissolved in ethyl acetate and washed three times with brine. The organic layer was dried over sodium sulfate, filtered and evaporated under reduced pressure. The crude product was purified by column chromatography (dichloromethane/methanol 95:5) and crystallized from ether/petroleum ether to give pure **4** (0.144 g, 50%); pale yellow solid; mp 84–85 °C; IR: ν_{max} 3367, 3325, 3187, 2960, 2931, 2857, 1738, 1677, 1634, 1614, 1518, 1455, 1387, 1219, 1203, 1170, 1157, 1052, 1033, 821, 790, 740, 696, 676 cm^{-1}; ^{1}H NMR (300 MHz, DMSO) δ 10.95 (s, 1H), 8.54-8.53 (dd, J = 4.1, 1.5, 1H), 8.09-8.06 (dd, J = 8.3, 1.4, 1H), 7.78 (t, J = 5.4, 1H), 7.44-7.33 (m, 6H), 6.47 (d, J = 2.4, 1H), 6.26 (d, J = 2.3, 1H), 6.13 (d, J = 8.8, 1H), 4.77 (s, 2H), 3.82 (s, 3H), 3.62-3.56 (m, 1H), 3.08-3.04 (m, 2H), 2.04 (t, J = 7.4, 2H), 1.95 (t, J = 7.3, 2H), 1.74-1.43 (m, 6H), 1.20 (d, J = 6.2, 3H); ^{13}C NMR (75 MHz, DMSO) δ 171.32, 169.03, 159.00, 144.62, 144.23, 136.09, 134.79, 134.52, 129.57, 128.72, 128.26, 128.16, 122.09, 96.10, 91.59, 76.77, 54.97, 46.98, 38.41, 34.57, 33.43, 31.70, 25.99, 21.21, 20.19; MS/MS (*m/z*): $[M]^+$ calcd. for $C_{27}H_{34}N_4O$, 479.26; found 479.3; analysis (calcd., found for $C_{27}H_{34}N_4O$): C (67.76, 67.59), H (7.16, 6.98), N (11.71, 12.04).

Compound 5 (sahaquine)

Suspension of *O*-benzylhydroxamic acid **4** (0,129 g, 0.00027 mol) and 20 mg 10% Pd/C (Sigma-Aldrich, St. Louis, MO, USA) in methanol was stirred for 2 h at room temperature under hydrogen atmosphere. The catalyst was filtered off and methanol was evaporated under reduced pressure. The crude product was crystallized from ether to give pure **5** (0.077g, 73%); pale yellow solid; mp 99–102 °C; IR: ν_{max} 3468, 3375, 3283, 3210, 3008, 2963, 2933, 1744, 1645, 1613, 1520, 1455, 1386, 1204, 1171, 1158, 1056, 821, 789, 677 cm^{-1}; ^{1}H NMR (300 MHz, DMSO) δ 10.32 (s, 1H), 8.63 (s, 1H), 8.55-8.52 (dd, *J* = 4.2, 1.6, 1H), 8.09-8.05 (dd, *J* = 8.3, 1.6, 1H), 7.76 (t, *J* = 5.3, 1H), 7.45-7.39 (m, 1H), 6.47 (d, *J* = 2.4, 1H), 6.26 (d, *J* = 2.4, 1H), 6.11 (d, *J* = 8.7, 1H), 3.82 (s, 3H), 3.68-3.56 (m, 1H), 3.05 (d, *J* = 5.6, 2H), 2.04 (t, *J* = 7.4, 2H), 1.94 (t, *J* = 7.4, 2H), 1.76-1.57, 1.57-1.40 (2m, 6H), 1.21 (d, *J* = 6.3, 3H); ^{13}C NMR (75 MHz, DMSO) δ 171.37, 168.74, 158.98, 144.60, 144.20, 134.75, 134.50, 129.54, 122.05, 96.08, 91.61, 54.95, 46.98, 38.39, 34.73, 33.43, 31.75, 25.95, 21.42, 20.17; MS/MS (*m/z*): $[M]^+$ calcd. for $C_{20}H_{28}N_4O_4$, 389.21; found 389.2; analysis (calcd., found for $C_{20}H_{28}N_4O_4$): C (61.84, 61.69), H (7.27, 7.03), N (14.42, 14.77).

Supplementary Table S1

Structure	IUPAC name	Molecular mass	log*P*	pI
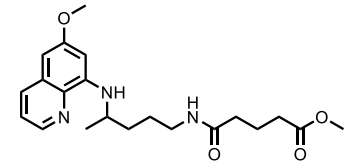	methyl 5-((4-((6-methoxyquinolin-8-yl)amino)pentyl)amino)-5-oxopentanoate	387.48	1.88	9.80
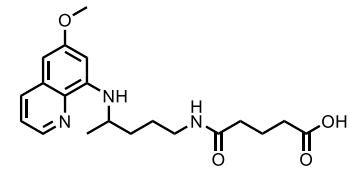	5-((4-((6-methoxyquinolin-8-yl)amino)pentyl)amino)-5-oxopentanoic acid	373.45	1.29	4.19
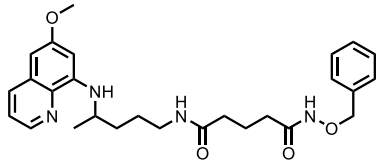	N^1-(benzyloxy)-N^5-(4-((6-methoxyquinolin-8-yl)amino)pentyl)glutaramide	478.58	3.02	6.18

Supplementary Table S1. Structures of sahaquine precursors with basic physicochemical properties, calculated with the Chemicalize.org program (Instant Cheminformatics Solutions. Available online: http://www.chemicalize.org/ (accessed on October 10th, 2017)).

Supplementary Figure S1

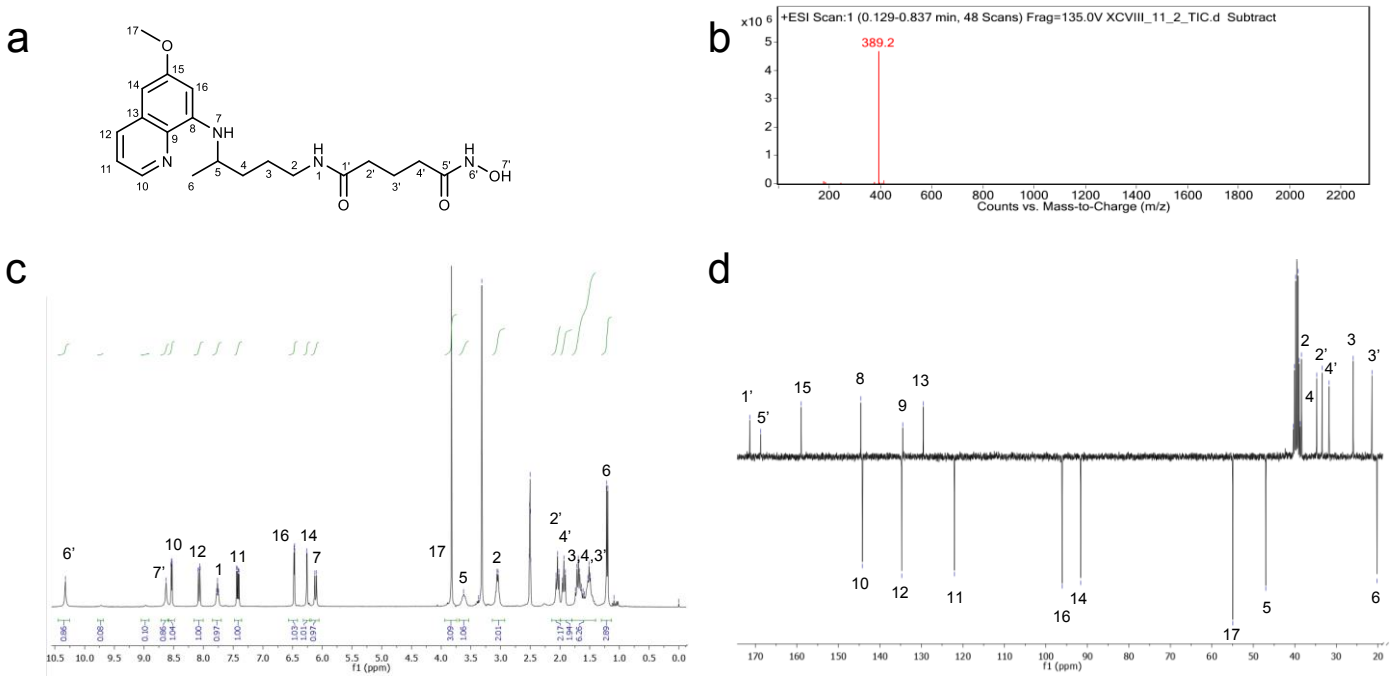

Supplementary Figure S1. Spectra confirming the structure of sahaquine. a) Annotated structure of sahaquine. b) Mass spectra (MS) showing only one peak corresponding to [M+1]. MS was recorded on HPLC-MS/MS. Mass determination was performed using electron spray ionization (ESI) in positive mode. c) 1H and d) 13C NMR spectra with marked peaks. All NMR (1H and 13C) spectra were recorded at 25°C at 300, 400 and 600 MHz for 1H and 75, 100 and 150 MHz for 13C nuclei, respectively. Chemical shifts (δ) are reported in parts per million (ppm) using tetramethylsilane as reference in the 1H and the DMSO residual peak as reference in the 13C spectra (39.51 ppm).

Supplementary Figure S2

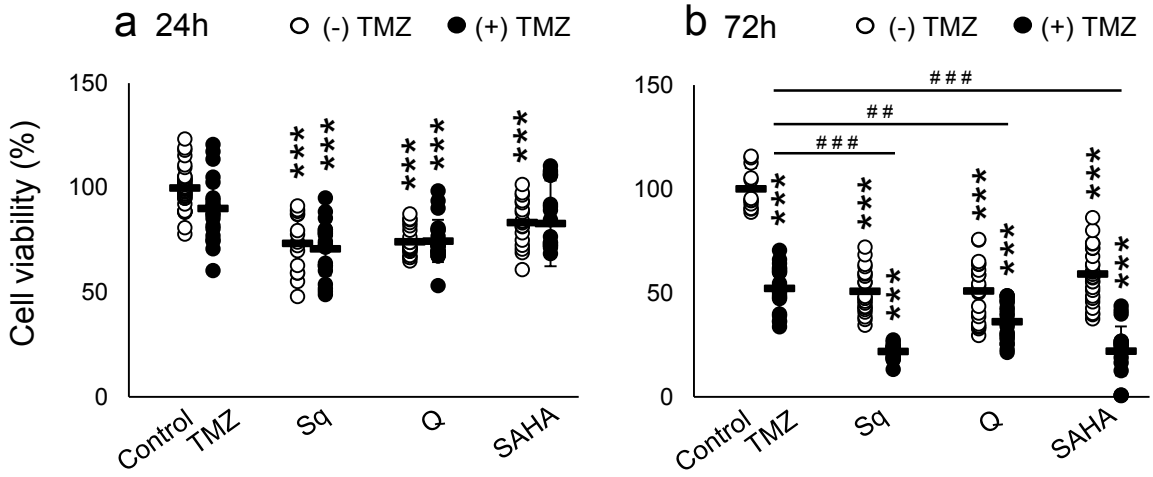

Supplementary Figure S2. Time-dependent decrease in cell viability with temozolomide combination treatments. GBM cells were treated for 24 h or 72 h with the combination of temozolomide (TMZ, 30 μM, 24 h n=21, 72 h n=22) and sahaquine (Sq, 10 μM, 24 h n=15, 72 h n=21; Sq+TMZ, 24 h n=21, 72 h n=21), quercetin (Q, 140 μM, 24 h n=21, 72 h n=22; Q+TMZ, 24 h n=21, 72 h n=21) or SAHA (1 μM, 24 h n=21, 72 h n=26; SAHA+TMZ, 24 h n=21, 72 h n=21) at IC_{50} concentrations. Cell viability was measured by counting Hoechst 33342-labeled nuclei imaged using a fluorescence microscope. Each point represents a percentage value normalized to the untreated control (24 h n=39, 72 h n=12). Horizontal bars represent the mean (SD) from at least three independent experiments (***p<0.001 compared to the untreated control; ##p<0.01, ###p<0.001 compared to TMZ; Welch's ANOVA with Games-Howell post hoc test).

Supplementary Figure S3

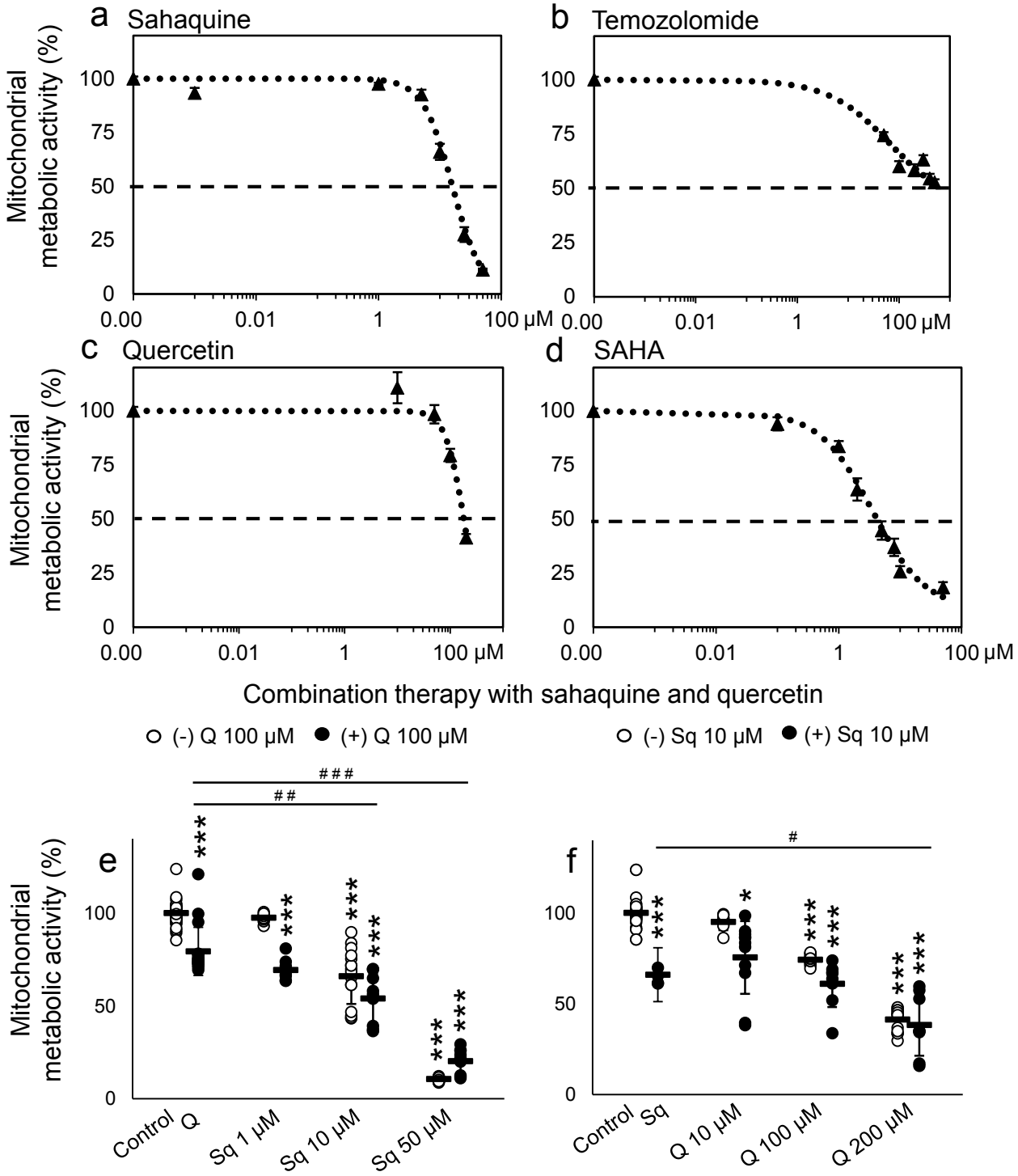

Supplementary Figure S3. Sahaquine diminishes mitochondrial metabolic activity in human glioblastoma cells in a dose- and time-dependent manner. GBM mitochondrial metabolic activity (n=9) following treatment with a) sahaquine (Sq, 0.001-50 µM), b) temozolomide (TMZ, 50-500 µM), c) quercetin (Q, 10-200 µM), and SAHA (0.1-50 µM) for 72 h. Shown are average percentage mitochondrial metabolic activity compared to untreated controls (SEM) from three independent experiments. e-f) Dose-dependent decrease in mitochondrial metabolic activity (72 h) with the combination of either a fixed concentration of quercetin (100 µM, n=18) and increasing concentrations of sahaquine (Sq 1 µM n=12, Sq 10 µM n=16, Sq 20 µM n=20, Sq 1 µM+Q n=9, Sq 10 µM+Q n=9, Sq 20 µM+Q n=9), or a fixed concentration of sahaquine (10 µM, n=16) and increasing concentrations of quercetin (Q 10 µM n=7, Q 100 µM n=15, Q 200 µM n=14, Q 10 µM+Sq n=11, Q 100 µM+Sq n=8, Q 200 µM+Sq n=8). Each point represents a percentage value normalized to the untreated control (e) n=41, f) n=43). Horizontal bars represent the mean (SD) from at least three independent experiments (*p<0.05, ***p<0.001 compared to the untreated control; #p<0.05, ###p<0.001 compared to e) Q 100 µM alone or f) Sq 10 µM alone; Welch's ANOVA with Games-Howell post hoc test). Mitochondrial metabolic activity was measured by the MTT assay.

Supplementary Figure S4

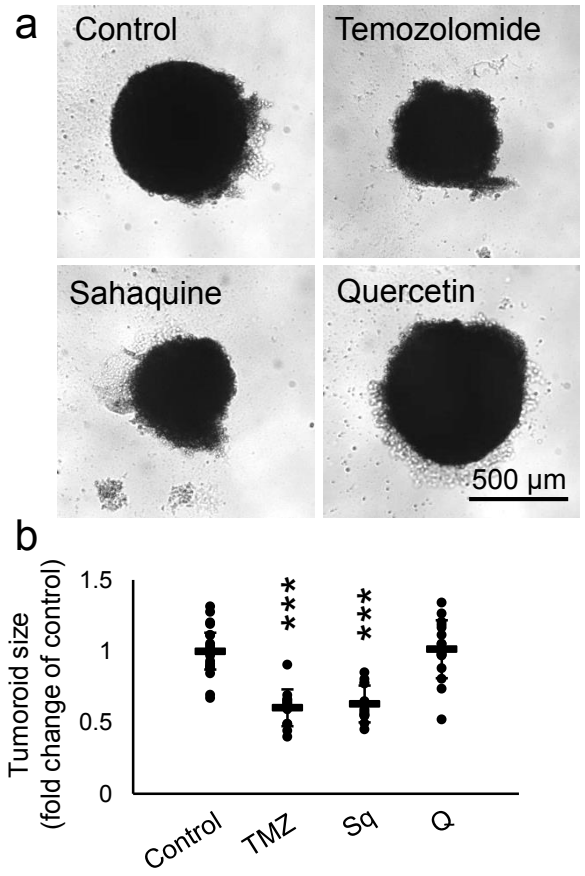

Supplementary Figure S4. Cytotoxic effects of selected drugs on human glioblastoma tumoroids. a) Representative micrographs of GBM tumoroids exposed to temozolomide (TMZ, 100 µM, n=13), sahaquine (Sq, 10 µM, n=13) or quercetin (Q, 100 µM, n=17) for 7 days. b) The size of the tumoroids was measured based on 2D micrographs. Each point represents a value normalized to the untreated control (set to 1, n=19). Horizontal bars represent the mean (SD) from at least three independent experiments (***p<0.001, one-way ANOVA with Tukey-Kramer's post hoc test).

Supplementary Figure S5

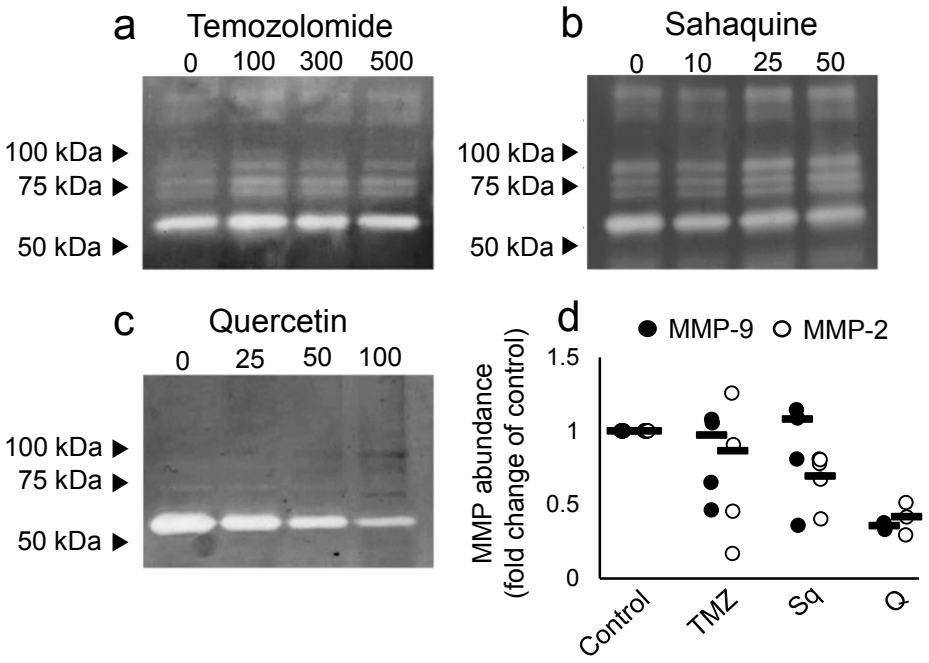

Supplementary Figure S5. The effect of select chemotherapeutic agents on the abundance of secreted MMP-2 and MMP-9 from human glioblastoma. Gelatin zymography of culture media from GBM cells treated with a) temozolomide (TMZ, 100, 300, 500 μM), b) sahaquine (Sq, 1, 10, 25 μM) or c) quercetin (Q, 25, 50, 100 μM) for 24 h. d) Quantification of MMP-9 and MMP-2 from gelatin zymographs (TMZ, 100 μM, n=5; Sq, 10 μM, n=5; Q, 100 μM, n=3). Each point represents a value normalized to the untreated control (set to 1, n=7). Horizontal bars represent the mean from at least three independent experiments.

Supplementary Figure S6

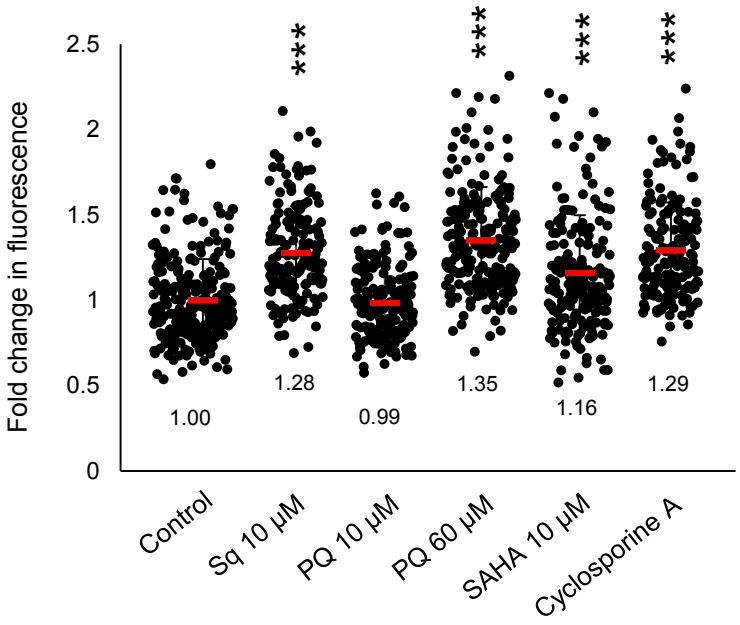

Supplementary Figure S6. Sahaquine inhibits P-glycoprotein activity. The intracellular accumulation of the P-glycoprotein substrate calcein-AM was measured in GBM cells treated with sahaquine (Sq, 10 µM, n=176 cells), primaquine (PQ, 10 µM n=182 cells, 60 µM n=218 cells) and SAHA (10 µM, n=192 cells) for 24 h. Cyclosporine A (10 µM, 30 min, n=172 cells) was included as a positive control for the inhibition of P-glycoprotein. Cells were imaged using a fluorescence microscope and fluorescence was analyzed in ImageJ. Each point represents a value normalized to the untreated control (set to 1, n=310 cells). Horizontal bars represent the mean (SD) for control (1.00±0.24), Sq (1.28±0.27), PQ 10 µM (0.99±0.22), PQ 60 µM (1.35±0.29), SAHA (1.16±0.33) and cyclosporine A (1.29±0.28), from three independent experiments (***$p<0.001$, Welch's ANOVA with Games-Howell post hoc test).

Supplementary Figure S7

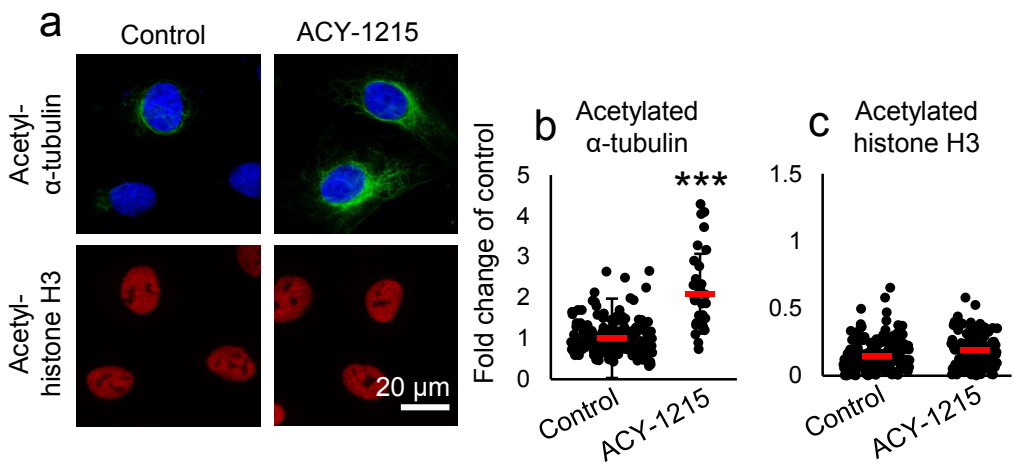

Supplementary Figure S7. Selective HDAC6 inhibition with ACY-1215 and sahaquine-induced α-tubulin reorganization. Representative fluorescence micrographs of GBM a) α-tubulin acetylation (green) at lysine 40 and histone H3 acetylation (red) at lysine 9/lysine 14 in response to HDAC6-selective inhibitor ACY-1215 (100 nM) for 24 h. b-c) Shown are means (SD) of fluorescence per cell for acetylated α-tubulin (n=32 cells) and acetylated histone H3 (n=110 cells) after treatment with ACY-1215 (100 nM) for 24 h. Each point represents a value normalized to the untreated control (set to 1; acetylated α-tubulin n=197 cells; acetylated histone H3 n=158 cells) from at least three independent experiments (*p<0.05, ***p<0.001, Welch's ANOVA with Games-Howell post hoc test). Nuclei (blue) were labeled with Hoechst 33342. Cells were imaged using a fluorescence microscope and fluorescence was analyzed in ImageJ.

Supplementary Figure S8

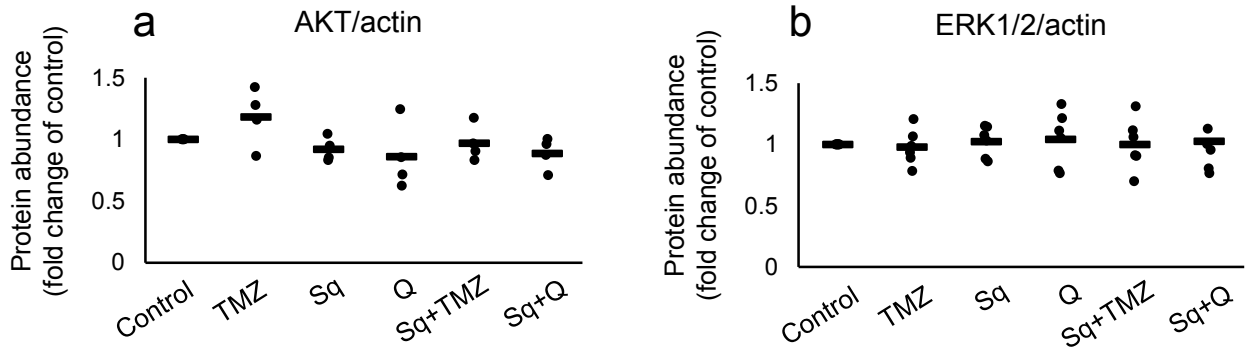

Supplementary Figure S8. Sahaquine does not affect total AKT and ERK1/2 levels in human glioblastoma. a) AKT (n=3) and b) ERK1/2 (TMZ n=4, Sq n=4, Q n=4, Sq+TMZ n=4, Sq+Q n=3) protein abundances were measured in GBM cells treated with temozolomide (TMZ, 100 μM), sahaquine (Sq, 10 μM) or quercetin (Q, 100 μM) alone or in combination for 24 h, by Western blotting. AKT and ERK1/2 protein abundance was normalized to the actin loading control. Each point represents a value normalized to the untreated control (set to 1). Horizontal bars represent means from at least three independent experiments.

Supplementary Figure S9

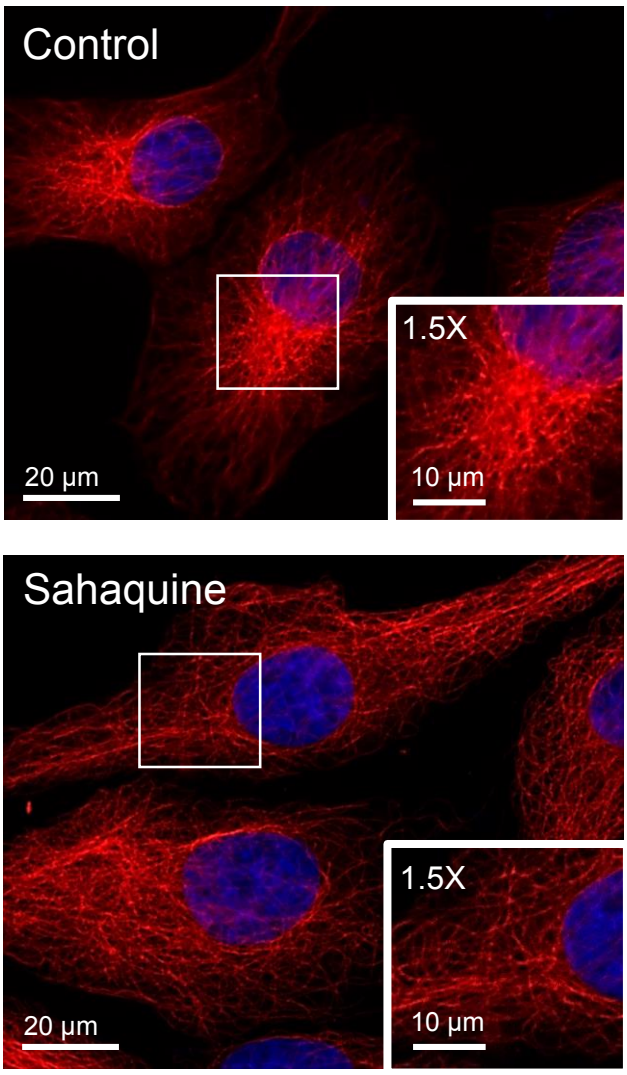

Supplementary Figure S9. Sahaquine-induced α-tubulin reorganization. Representative fluorescence micrographs of GBM α-tubulin (red) reorganization in response to Sq (10 µM) after 24 h treatment. Nuclei (blue) were labeled with Hoechst 33342. Cells were imaged using a fluorescence microscope. Inserts show the microtubule organizing center, where α-tubulin reorganization is observed.

Supplementary Figure S10

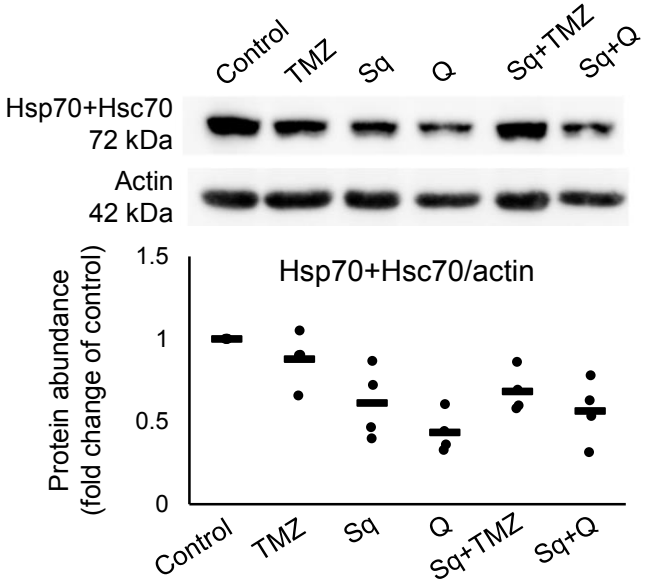

Supplementary Figure S10. Sahaquine and quercetin decrease the abundance of Hsp70/Hsc70 in human glioblastoma. The abundance of heat shock proteins Hsp70 and Hsc70 was measured in GBM cells treated with temozolomide (TMZ, 100 μM), sahaquine (Sq, 10 μM) or quercetin (Q, 100 μM) alone or in combination for 24 h, by Western blotting (n=4). Hsp70/Hsc70 protein abundance was normalized to the actin loading control. Each point represents a value normalized to the untreated control (set to 1). Horizontal bars represent means from four independent experiments.

Supplementary Figure S11

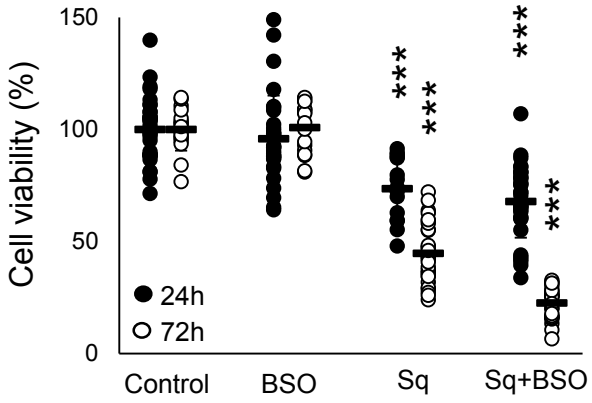

Supplementary Figure S11. Buthionine sulfoximine enhances the cell killing effect of sahaquine in GBM. GBM cell viability following treatment with sahaquine (Sq, 10 μM, 24 h n=15, 72 h n=30), buthionine sulfoximine (BSO, 100 μM, 24 h n=32, 72 h n=18) or combintation of sahaquine and buthionine sulfoximine (Sq + BSO, 24 h n=35, 72 h n=27) for 24 h or 72 h. Cell viability was measured by counting Hoechst 33342-labeled nuclei imaged using a fluorescence microscope. Shown are the average percentage cell viability (SD). Each point represents a value normalized to the untreated control (24 h n=33, 72 h n=18) from three independent experiments (***p<0.001, Welch's ANOVA with Games-Howell post hoc test).

European Journal of Pharmaceutics and Biopharmaceutics 100 (2016) 66–76

Contents lists available at ScienceDirect

European Journal of Pharmaceutics and Biopharmaceutics

journal homepage: www.elsevier.com/locate/ejpb

Research Paper

Pharmacological inhibition of lipid droplet formation enhances the effectiveness of curcumin in glioblastoma

Issan Zhang [a,1], Yiming Cui [a,1], Abdolali Amiri [a], Yidan Ding [b], Robert E. Campbell [b], Dusica Maysinger [a,*]

[a] Department of Pharmacology and Therapeutics, McGill University, Montreal, Canada
[b] Department of Chemistry, University of Alberta, Edmonton, Canada

ARTICLE INFO

Article history:
Received 16 September 2015
Revised 14 December 2015
Accepted in revised form 18 December 2015
Available online 4 January 2016

Keywords:
Glioblastoma
Lipid droplets
Curcumin
Pyrrolidine-2
Caspase-3 sensor
Cell death
Sensitization
Temozolomide
Spheroids
Chemotherapy

ABSTRACT

Increased lipid droplet number and fatty acid synthesis allow glioblastoma multiforme, the most common and aggressive type of brain cancer, to withstand accelerated metabolic rates and resist therapeutic treatments. Lipid droplets are postulated to sequester hydrophobic therapeutic agents, thereby reducing drug effectiveness. We hypothesized that the inhibition of lipid droplet accumulation in glioblastoma cells using pyrrolidine-2, a cytoplasmic phospholipase A2 alpha inhibitor, can sensitize cancer cells to the killing effect of curcumin, a promising anticancer agent isolated from the turmeric spice. We observed that curcumin localized in the lipid droplets of human U251N glioblastoma cells. Reduction of lipid droplet number using pyrrolidine-2 drastically enhanced the therapeutic effect of curcumin in both 2D and 3D glioblastoma cell models. The mode of cell death involved was found to be mediated by caspase-3. Comparatively, the current clinical chemotherapeutic standard, temozolomide, was significantly less effective in inducing glioblastoma cell death. Together, our results suggest that the inhibition of lipid droplet accumulation is an effective way to enhance the chemotherapeutic effect of curcumin against glioblastoma multiforme.

1. Introduction

In cancers such as glioblastoma multiforme, enhanced fatty acid storage and synthesis provide the necessary resources for survival and rapid proliferation [1]. Although otherwise highly heterogeneous, most cancer types present a lipogenic phenotype characterized by the upregulation of key enzymes and transcriptional factors controlling lipid metabolism (e.g. Akt, fatty acid synthase, hypoxia-inducible factor 1-alpha, sterol regulatory element binding proteins, acetyl-CoA carboxylase alpha), and a boost in *de novo* lipogenesis [2–5]. In solid malignancies, the hypoxic conditions found at the core of the tumors induce adaptive pathways aimed at maintaining lipid synthesis, homeostatic pH and cell survival [6]. The resulting metabolic changes correlate with poor prognosis, poor treatment response and recurrence in diseases such as breast, liver and brain cancer [7–10]. Emerging therapeutic approaches have thus targeted lipid synthesis to counter the effects of metabolic reprogramming in cancer cells [11,12].

Aside from their increased *de novo* fatty acid synthesis, cancer cells are also characterized by their increased number of lipid droplets compared to normal tissues [13,14]. Lipid droplets are dynamic organelles that support cells with metabolic fuel, membrane biosynthesis, inflammatory intermediates and signaling mediators [15–17] . Although they can be found in almost all cell types, their increased biogenesis in neoplastic and inflammatory conditions defines them as targets for therapeutic intervention [18]. Aside from fueling the accelerated metabolism of cancer cells, lipid droplets also harbor numerous proteins and transcription factors critical to lipid metabolism and related pathways [19]. The hydrophobic core found in lipid droplets provides a favorable compartment to attract and sequester lipophilic proteins and compounds, fat-soluble vitamins, and even environmental pollutants [20]. As such, lipid droplets can sequester lipophilic drugs and prevent them from reaching their targets, thus decreasing drug effectiveness [21,22]. Therefore, it seems that inhibition by pharmacological or genetic means of enzymes necessary for lipid droplet formation could provide a way to reduce drug sequestration and improve drug effects. We tested this concept in glioblastoma cells treated with curcumin in combination with pyrrolidine-2, and inhibitor of cytosolic phospholipase A2 alpha (cPLA2α). Curcumin, a plant-derived polyphenol isolated from

* Corresponding author.
E-mail address: dusica.maysinger@mcgill.ca (D. Maysinger).
[1] These authors contributed equally to this work.

http://dx.doi.org/10.1016/j.ejpb.2015.12.008
0939-6411/

the turmeric spice, has been shown to be a safe, potent and effective anticancer agent both *in vitro* and *in vivo* [23]. It was found to affect multiple targets, leading to the inhibition of inflammation and cell proliferation [24]. Curcumin has a broad range of effects that are advantageous against multifactorial diseases such as cancer, and clinical trials have suggested biological activity in patients with colorectal and pancreatic cancer [25,26]. Despite being well-tolerated in humans, its poor bioavailability has limited prospects of broader clinical applications [26,27]. Given its lipophilic properties, curcumin has been found to localize in lipid membranes and lipid droplets, thereby decreasing its availability at drug targets. Pyrrolidine-2, also known as pyrrophenone, is a potent and reversible inhibitor of cPLA2α, a key enzyme in the processes of arachidonic acid release, eicosanoid synthesis and lipid droplet formation [28,29]. We hypothesize that pre-treatment of cancer cells with pyrrolidine-2 will enhance the cell killing effect of curcumin by reducing its sequestration in lipid droplets.

Glioblastoma multiforme is a highly aggressive and drug-resistant type of brain cancer which currently lacks effective treatments [30,31]. Temozolomide, a DNA methylating agent, is the first-line drug used in concomitant and adjuvant radiochemotherapy against glioblastoma [32–34]. However, a large subset of patients is resistant to temozolomide due to the expression of the O^6-methylguanine-DNA methyltransferase gene (*MGMT*), a DNA repair protein, and there is an urgent need for alternative mono- and combination therapies [35]. We have investigated the susceptibility of human glioblastoma monolayer (2D) and spheroid (3D) cultures to curcumin and temozolomide used either individually or in combination with pyrrolidine-2. We also compared the effect of pyrrolidine-2 to that of buthionine sulfoximine (BSO), an irreversible inhibitor of gamma-glutamylcysteine synthetase, the rate-limiting enzyme in glutathione synthesis, found to be effective as a sensitizing agent in patient-derived neuroblastoma cell lines [36,37].

We further monitored the mode of cell death induced by these treatments using a newly developed, dimerization-based biosensor which provides a highly sensitive method to visualize and quantify caspase-dependent apoptotic activity in living cells [38]. The cysteine protease caspase-3 is a main executioner caspase in the process of caspase-dependent apoptosis [39,40]. It was shown to be strongly activated in response to curcumin treatment in different cell lines [41–43]. By investigating the activity of caspase-3 in cancer cells in response to chemotherapeutics and sensitizers, we can reveal drug efficacy and underlying mechanisms of cell death.

The objective of these studies was to investigate the sensitization of human glioblastoma cells in 2D and 3D cultures to caspase-3-mediated cell death induced by curcumin. We used the pharmacological agent pyrrolidine-2 to manipulate lipid droplet number in glioblastoma cells and assessed caspase-3 activity in living cells using a recently developed biosensor. The results indicate a significant increase in caspase-3-mediated cell death induced by curcumin when lipid droplet formation is reduced.

2. Materials and methods

2.1. Materials

Curcumin (Sigma–Aldrich, Canada), pyrrolidine-2 (Calbiochem, United States), temozolomide (Sigma–Aldrich, Canada), buthionine sulfoximine (Sigma–Aldrich, Canada), staurosporine (Sigma–Aldrich, Canada), dimethyl sulfoxide (Sigma–Aldrich, Canada), Nile Red (Sigma–Aldrich, Canada), paraformaldehyde (Sigma–Aldrich, Canada), BODIPY 493/503 (Invitrogen, Canada), Hoechst 33342 (Sigma–Aldrich, Canada) and propidium iodide (Sigma–Aldrich, Canada) were used as received.

Table 1
Construct of Plasmid 1 and Plasmid 2, which form the caspase-3 biosensor.

Name	Gene	GenBank accession numbers	Addgene plasmid ID
GA^{NES}-DEVD-B^{NLS}	XhoI-GA-NES-KpnI-DEVD-B-NLS-HindIII	KF976777	50842
RA^{NLS}	XhoI- RA-NLS-HindIII	KF976778	50843

2.2. Cell culture

The U251N human glioblastoma cell line was originally obtained from the American Type Culture Collection. Unless otherwise specified, U251N cells were cultured in Dulbecco's Modified Eagle's Medium (DMEM; Invitrogen, Canada) containing 10% (v/v) fetal bovine serum (Invitrogen, Canada), 2 mM L-glutamine, 100 IU/mL penicillin, 100 μg/mL streptomycin (Invitrogen, Canada), and 1% non-essential amino acids. Cells were incubated at 37 °C with 5% CO_2.

2.3. Spheroid preparation

Spheroid cultures were prepared using a protocol adapted from the previously established liquid overlay system: confluent U251N monolayer cell cultures were detached using 0.05% trypsin–EDTA (Invitrogen, Canada), and seeded at 5,000 cells per well in 96-well plates pre-coated with 2% agarose (Invitrogen, Canada) in serum-deprived DMEM [44]. Spheroids were seeded and maintained in complete DMEM medium for four days before drug treatments. Spheroids expressing the caspase-3 biosensor were prepared following the same method, using transfected cells.

2.4. Cell treatment

Confluent monolayer cell cultures were detached using 0.05% trypsin–EDTA, seeded in 24-well or 96-well cell culture plates (Sarstedt, Canada) at 50,000 or 10,000 cells per well, respectively, and treated after 24 h. For 24 h dose–response experiments, drugs were administered in the following concentrations: curcumin (Cur; 5–100 μM); pyrrolidine-2 (Pyr-2; 1–5 μM). For 72 h dose–response experiments, curcumin was added at concentrations 5–30 μM. For pyrrolidine-2 (3 μM) and buthionine sulfoximine (BSO; 5 mM) pre-treatments, cells were treated for 24 h, after which the medium was refreshed. To establish the time course of drug effects in spheroid cultures, treatments were maintained for 24 h or 72 h. BSO stocks (200 mM) were prepared fresh in purified water. Stock solutions of temozolomide, curcumin, staurosporine and pyrrolidine-2 were prepared in dimethyl sulfoxide (DMSO), and added to cells for a final DMSO concentration <0.5%. Vehicle controls were included in each experiment.

2.5. Lipid droplet labeling, imaging and quantification

After treatment with curcumin (10–30 μM) for 24 h, the media were refreshed, and cells were incubated with Nile Red (2 μM; 10 min). Nile red is a commonly used fluorescent label for lipid droplets [45,46], but it can also bind to hydrophobic protein domains and be employed to probe hydrophobic pockets in purified native proteins [47]. Labeled cells were washed with phosphate buffered saline (PBS), and imaged using a fluorescence microscope (Leica, Canada). To quantify the number of lipid droplets per cell, U251N cells were fixed with paraformaldehyde (4%; 15 min) following treatment, labeled with BODIPY 493/503 (2 μM; 10 min), and then imaged using a fluorescence microscope.

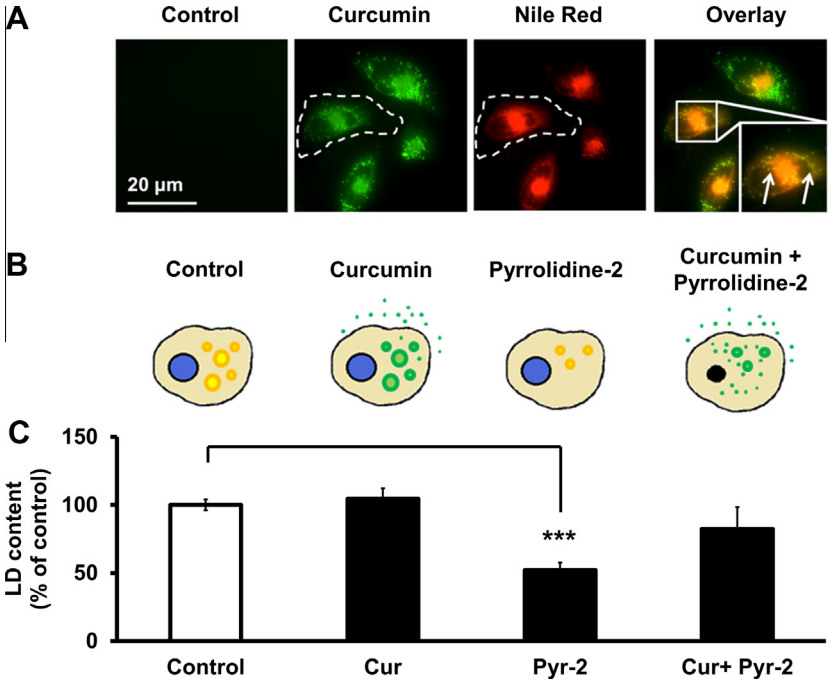

Fig. 1. Curcumin co-localizes with lipid droplets and pyrrolidine-2 reduces lipid droplet content in glioblastoma cells. (A) U251N glioblastoma cells treated with curcumin (10 μM; 4 h) show green fluorescence in the cytoplasm. Co-labeling with Nile Red (2 μM; 10 min) indicated that curcumin localizes in lipid droplets. Fluorescence micrograph overlays were prepared in ImageJ. Insets show details of curcumin co-localized with Nile Red-labeled lipid droplets. (B) Schematic representation of the status of lipid droplets (yellow), and curcumin localization (green) in U251N glioblastoma cells with or without pyrrolidine-2 treatment. Curcumin is sequestered in lipid droplets, and pyrrolidine-2 pre-treatment increases the availability of curcumin at its targets. (C) U251N glioblastoma cells treated with pyrrolidine-2 (3 μM; 24 h) show a significant reduction in lipid droplet content. Cells were labeled with Bodipy 493/503 (2 μM; 10 min) and imaged using a fluorescence microscope. The number of lipid droplets per cell was counted manually (250 cells were analyzed per treatment group). (*** $p < 0.001$). (For interpretation of the references to color in this figure legend, the reader is referred to the web version of this article.)

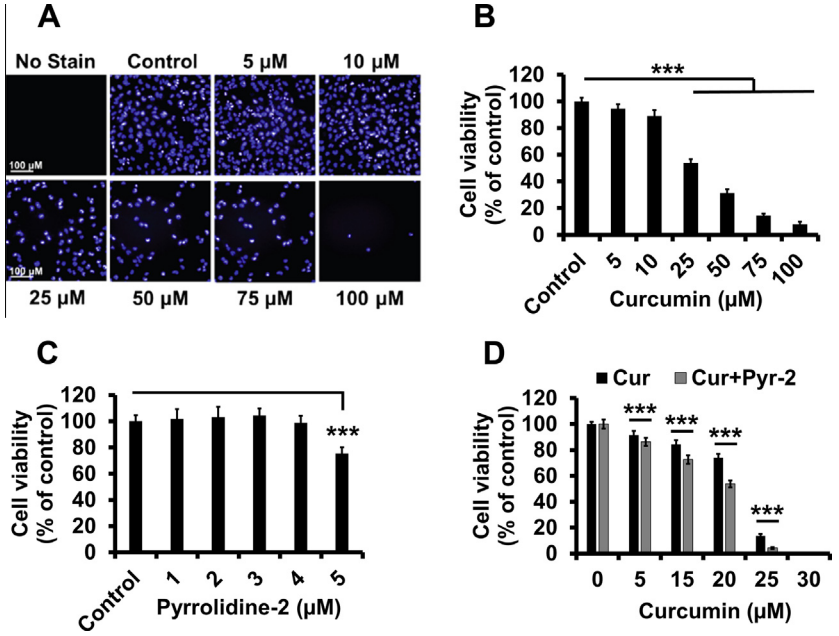

Fig. 2. Sensitization with pyrrolidine-2 increased the cell killing effect of curcumin in U251N glioblastoma cells. (A) U251N glioblastoma cells treated with curcumin (5–100 μM) for 24 h were labeled with Hoechst 33342 and imaged using a high-throughput fluorescence microscope. Fluorescence micrographs show representative fields. (B) The cell viability of U251N glioblastoma cells treated with curcumin (5–100 μM) for 24 h was measured by counting the number of cell nuclei labeled with Hoechst 33342. Cells were imaged using a high-throughput microscope. Cell viability was significantly decreased at curcumin treatments above 25 μM. Shown are average percentage values ± SEM compared to untreated controls from three independent experiments. (*** $p < 0.001$). (C) The cell viability of U251N glioblastoma cells treated with pyrrolidine-2 (1–5 μM) for 24 h was measured by counting the number of cell nuclei labeled with Hoechst 33342. Cells were imaged using a high-throughput microscope. Cell viability was significantly decreased at pyrrolidine-2 treatments above 4 μM. Shown are average percentage values ± SEM compared to untreated controls from three independent experiments. (*** $p < 0.001$). (D) The cell viability of U251N glioblastoma cells treated with curcumin (5–30 μM; 72 h), with or without pyrrolidine-2 sensitization (3 μM; 24 h), was measured by counting the number of cell nuclei labeled with Hoechst 33342. Cells were imaged using a high-throughput microscope. Pyrrolidine-2 sensitization significantly increased cell death compared to treatment with curcumin alone. Shown are average percentage values ± SEM compared to untreated controls from three independent experiments. (*** $p < 0.001$).

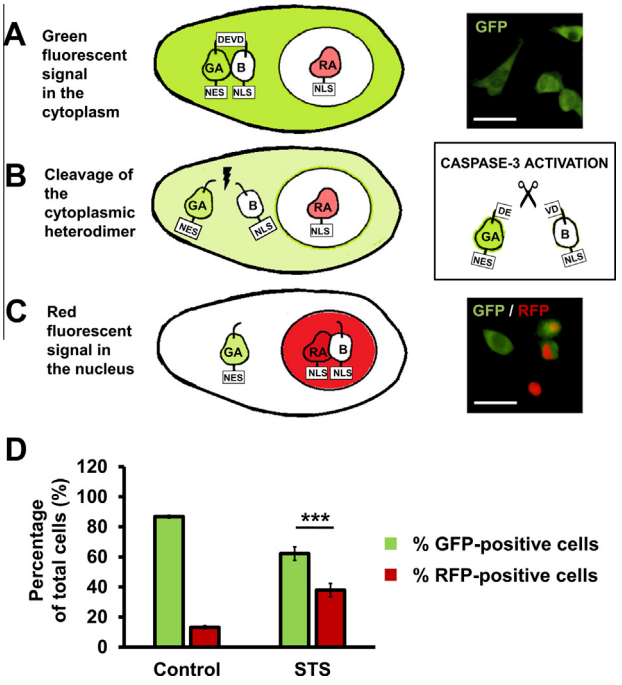

Fig. 3. Principle of caspase-3 detection using the dimerization-based biosensor and measurement of caspase-3 activity. (A) The caspase-3 biosensor is composed of two dimerization-dependent fluorescent proteins: (1) a red fluorescent protein (RA) with a nuclear localization signal (NLS), and (2) a green fluorescent protein (GA) with a nuclear exclusion signal (NES), heterodimerized with a non-fluorescent partner protein (B) through the caspase-3 substrate peptide (DEVD). Fluorescence micrographs show U251N cells with green cytoplasms when GA is heterodimerized with B (scale bar = 50 μm). (B) Upon caspase-3 activation, the caspase-3 substrate DEVD is cleaved, and green fluorescence signal from GA diminishes. (C) The partner protein B translocates into the nucleus by a NLS and heterodimerizes with RA, increasing red fluorescence in the nucleus manyfold. Fluorescence micrographs show U251N cells with red nuclei when RA is heterodimerized (scale bar = 50 μm). (D) Measurement of caspase-3 activity in U251N glioblastoma cells. Cells transfected with the biosensor were imaged using a fluorescence microscope following treatment with staurosporine (STS; 0.5 μM) for 24 h. Cells with active caspase-3 show an increase in red fluorescence (RFP) in the nucleus and a decrease in green fluorescence (GFP) in the cytoplasm. Mean percentage of total transfected cells expressing GFP or RFP ± SEM is shown for three independent experiments (*** $p < 0.001$). (For interpretation of the references to color in this figure legend, the reader is referred to the web version of this article.)

2.6. Hoechst 33342 and propidium iodide labeling

In monolayer cultures, the culture medium was removed following treatment, and cells were fixed with paraformaldehyde (4%; 15 min). Cells were stained with Hoechst 33342 (10 μM; 10 min), and then washed and kept in PBS. Cell imaging was conducted using an automated microscopy platform (Operetta High Content Imaging System; Perkin Elmer, United States). Image analysis and cell counting were performed using the Columbus Image Data Storage and Analysis platform (Perkin Elmer, United States). In spheroid cultures, propidium iodide and Hoechst 33342 fluorescent dyes were added 3 h prior to measurements. At the end of treatment, individual spheroids were carefully transferred onto a microscope slide using a pipette, and flattened under a glass coverslip to facilitate imaging. Imaging was conducted using a fluorescence microscope, and fluorescence intensity was quantified using ImageJ.

2.7. Biosensor construction

The caspase-3 biosensor consists of two parts (Fig. 3). Plasmid 1 encodes the green dimerization-dependent fluorescent protein (GA) linked with a nuclear exclusion signal sequence (NES; LALKLAGLDIGS) [48,49], the caspase-3 substrate sequence (DEVD) [50], and a partner protein (B) linked to a nuclear localization signal (NLS; DPKKKRKVDPKKKRKVDPKKKRKV) [51]. Plasmid 2 encodes the dimerization-dependent red fluorescent protein (RA) linked with a NLS. Expression and purification of constructs 1 and 2 were performed according to procedures previously described in detail [38]. Details of the plasmid constructs are found in Table 1.

2.8. Plasmid preparation and transfection

Stocks of the caspase-3 biosensor plasmids (kindly provided by Dr. Robert E. Campbell, University of Alberta, Canada) were prepared in α-Select *Escherichia coli* (Bioline, United States) using a Miniprep Kit (Qiagen, Canada). DNA concentration was adjusted to 1 μg/μl in purified water, and plasmids were stored at -20 °C. For transfection, U251N cells were seeded in black 96-well plates (Corning, United States) at a density of 10,000 cells per well, and cultured for 24 h. Transfection was conducted in the absence of antibiotics, using Lipofectamine 2000 (Invitrogen, Canada), following the procedure recommended by the manufacturer. The transfection complexes were kept for 24 h, after which the medium was replaced by complete medium, and cells were treated.

2.9. Live cell imaging of the caspase-3 biosensor

Monolayer cells seeded in black 96-well cell culture plates were transfected with the biosensor, and treated for 24 h. Following treatment, cells were imaged using the Operetta High Content Imaging System to analyze green (eGFP) and red (Alexa 594) signals. Caspase-3 activity was quantified as the number of cells with red nuclei, and expressed as a percentage of total transfected cells (expressing green or red fluorescence). The absence of caspase-3 activity was quantified from the number of cells with green cytoplasm, and expressed in the same manner. Eleven fields were analyzed per well, with six wells per treatment group. Negative controls were non-transfected cells in the presence or absence of drugs. Following treatment, transfected spheroids were transferred onto microscope slides, flattened under glass coverslips, and imaged using a fluorescence microscope. Full spheroids were imaged and the number of cells with green fluorescence in the cytoplasm or red fluorescence in the nucleus was counted.

2.10. Statistical analysis

Each experiment was independently performed at least two or three times. Each treatment was performed in three samples (24-well plates) or six samples (96-well plates). All data are expressed as mean ± SEM values. Statistical significance was calculated using one-way ANOVA, followed by the Student's t-test. For multiple comparisons, Bonferroni corrections were applied.

3. Results

3.1. Curcumin is sequestered in lipid droplets

Due to its fluorescent properties, curcumin's intracellular localization can be visualized using a fluorescence microscope (488/509 nm). After treating U251N glioblastoma cells with curcumin (10 μm) for 4 h, green fluorescence was found diffused throughout the cells, located at cell membranes, and concentrated in numerous punctate in the cytoplasm (Fig. 1A). Staining of curcumin-treated cells with Nile Red, a lipophilic stain for intracellular lipids, showed that curcumin co-localized with membrane

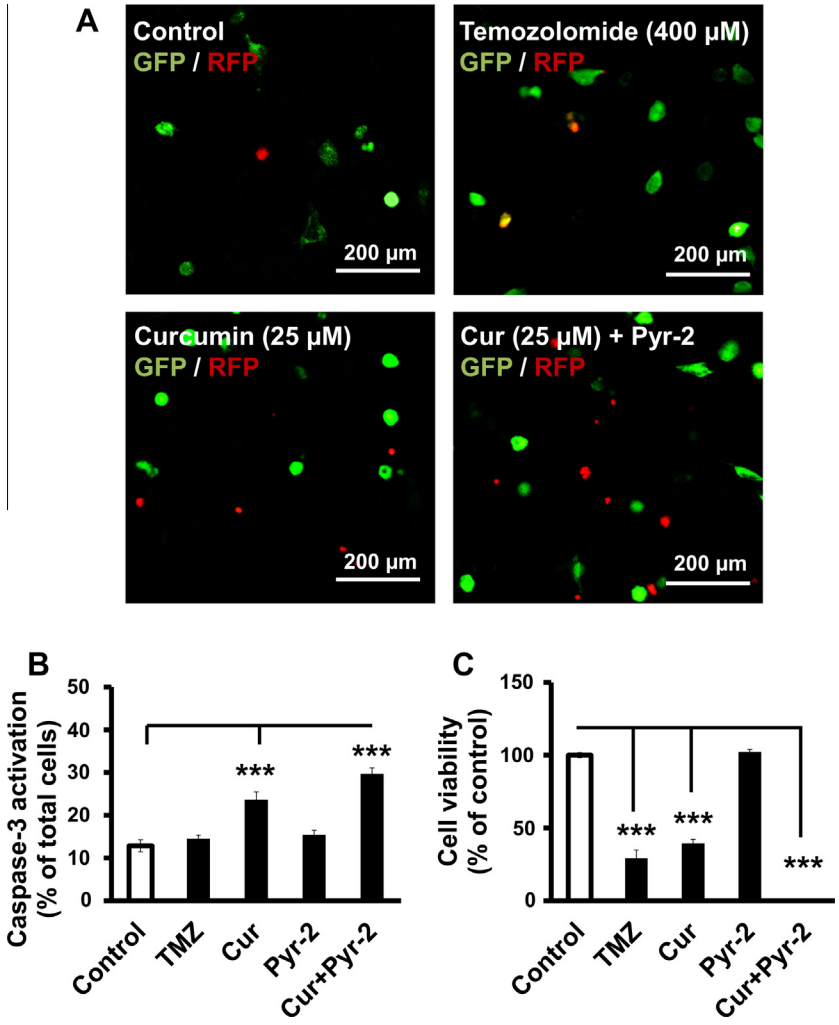

Fig. 4. Curcumin-mediated and pyrrolidine-2-sensitized cell deaths are mediated through caspase-3 activation. (A) Fluorescence micrographs of U251N cells transfected with the caspase-3 biosensor and treated with curcumin (25 µM; 24 h), with or without pyrrolidine-2 (Pyr-2; 3 µM; 24 h) pre-treatment. Temozolomide (TMZ; 400 µM; 24 h) was included as a clinically-relevant drug. Cells with green fluorescence in the cytoplasm express the caspase-3 biosensor, while those with a red nucleus present caspase-3 activity. (B) U251N cells transfected with the caspase-3 biosensor were treated with curcumin (Cur; 25 µM; 24 h), with or without pyrrolidine-2 (Pyr-2; 3 µM; 24 h) pre-treatment. Temozolomide (TMZ; 400 µM; 24 h) was included as a clinically-relevant drug. Caspase-3 activity was assessed using a fluorescence microscope. Mean percentage of total transfected cells expressing caspase-3 activity ± SEM is shown for three independent experiments. (*** $p < 0.001$). (C) Cell viability of U251N cells treated with curcumin (Cur; 25 µM; 24 h), with or without pyrrolidine-2 (Pyr-2; 3 µM; 24 h) pre-treatment. Temozolomide (TMZ; 400 µM; 24 h) was included as a clinically-relevant drug. Cell viability was measured by counting the number of cell nuclei labeled with Hoechst 33342. Cells were imaged using a high-throughput microscope. Shown are average percentage values ± SEM compared to untreated controls from three independent experiments. (*** $p < 0.001$).

lipids and lipid droplets. Given the importance of lipid droplets for cancer cells, we then employed pyrrolidine-2, an inhibitor of cPLA2α, to reduce lipid droplet number in glioblastoma cells. U251N cells normally contain lipid droplets and their number can be reduced using inhibitors of lipid droplet formation, or increased using fatty acids such as oleic acid (Fig. S1). Pyrrolidine-2 treatment (3 µM; 24 h) reduced lipid droplet number to 52 ± 5.7% of untreated control levels (Fig. 1C). Lipid droplet number in cells treated with both curcumin and pyrrolidine-2 was higher (82.3 ± 16.0%) than that of cells treated with pyrrolidine-2 alone.

3.2. Pyrrolidine-2 potentiates the cell killing effect of curcumin

We postulated that U251N glioblastoma cells would be more susceptible to the therapeutic effects of curcumin following the reduction of lipid droplet number by pyrrolidine-2. Cell viability measured by counting cell nuclei labeled with Hoechst 33342 showed that 25 µM of curcumin decreased cell number to 53.8 ± 2.8% after 24 h of treatment (Fig. 2A and B). In turn, pyrrolidine-2 alone did not induce any significant decrease in cell viability up to 4 µM (Fig. 2C). Pre-treatment of U251N cells with pyrrolidine-2 potentiated the cell killing effect of curcumin. Notably, pre-treatment with pyrrolidine-2 (24 h) virtually abolished glioblastoma viability when followed by curcumin treatment (72 h) at concentrations above 20 µM (Fig. 2B). In comparison, pyrrolidine-2 modestly increased the effectiveness of temozolomide, which was included as a clinically relevant comparator (Fig. S2). The effect of pyrrolidine-2 as a sensitizer was compared to that of BSO. Although pre-treatment with BSO increased cell death at lower concentrations of curcumin, it did not substantially increase cell death at higher concentrations (Fig. S3).

3.3. Cell death induced by curcumin and pyrrolidine-2 is mediated by caspase-3

To investigate the mode of cell death induced by curcumin and pyrrolidine-2, we employed a newly developed biosensor for caspase-3 activation. This construct offers a highly sensitive method to detect caspase-3-mediated apoptosis in live cells. In

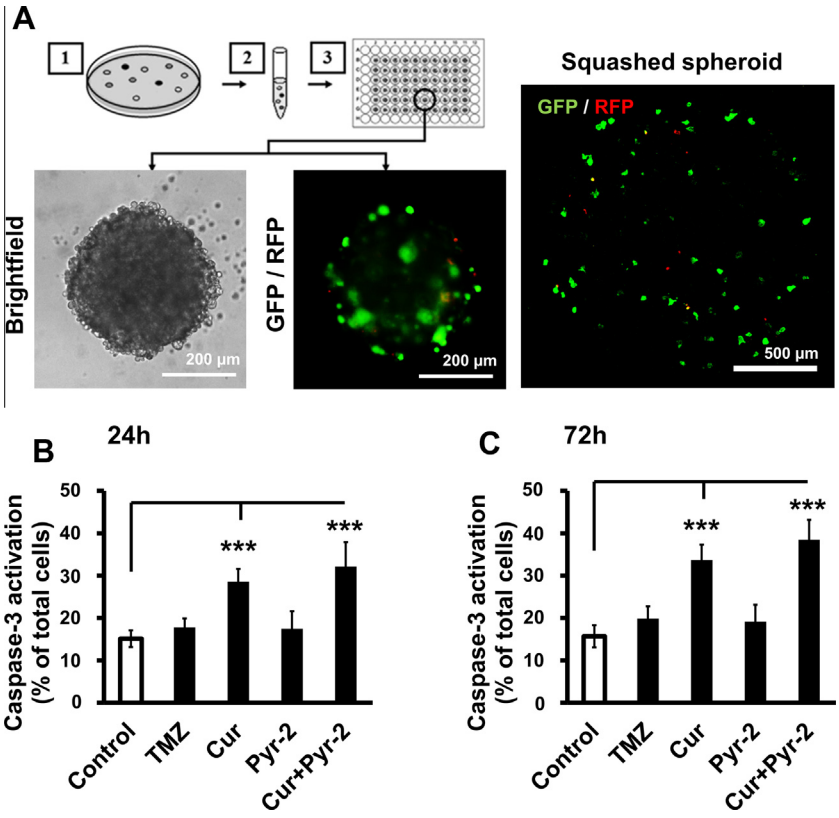

Fig. 5. Curcumin and pyrrolidine-2-sensitization induce caspase-3-mediated cell death in glioblastoma spheroids. (A) U251N spheroids expressing the caspase-3 biosensor were prepared from U251N monolayer cells transfected with the caspase-3 biosensor. Transfected cells were collected and seeded in agarose-coated wells. The fluorescence micrograph shows cells expressing green and red fluorescence within the spheroid. U251N spheroids expressing the caspase-3 biosensor were squashed between a glass coverslip and a microscope slide to facilitate the quantification of cells expressing either green or red fluorescence. (B) U251N spheroids expressing the caspase-3 biosensor were treated with temozolomide (TMZ; 400 µM; 24 h) and curcumin (Cur; 25 µM; 24 h), with or without pre-treatment with pyrrolidine-2 (Pyr-2; 3 µM; 24 h). Following treatment, spheroids were squashed and imaged using a fluorescence microscope. The number of cells expressing either green or red fluorescence was counted. Caspase-3 activity was quantified as the number of cells expressing red fluorescence (the presence of caspase-3 activity) over the total number of transfected cells (cells with either green or red fluorescence). Mean percentage values ± SEM are shown from three independent experiments ran in triplicate. ***($p < 0.001$). (C) U251N spheroids expressing the caspase-3 biosensor were treated with temozolomide (TMZ; 400 µM; 72 h) and curcumin (Cur, 25 µM; 72 h), with or without pre-treatment with pyrrolidine-2 (Pyr-2; 3 µM; 24 h). Following treatment, spheroids were imaged and caspase-3 activity was quantified as in (B). Mean percentage values ± SEM are shown from three independent experiments ran in triplicate. ***($p < 0.001$). (For interpretation of the references to color in this figure legend, the reader is referred to the web version of this article.)

the absence of caspase-3 activity, cells expressing the biosensor display green fluorescence in the cytoplasm. Following the activation of caspase-3, green fluorescence fades and red fluorescence increases in the cell nucleus. Thus, caspase-3 activity can be quantified by counting the number of cells with red fluorescence as a proportion of total transfected cells expressing either green or red fluorescence. Experiments showed that even under control conditions, a small proportion of cells (13.2 ± 1.4%) display caspase-3 activity. In turn, the positive control staurosporine, a potent activator of caspase-3, significantly increased the proportion of cells with a red nucleus (Fig. 3D).

To compare the mode of cell death induced by curcumin and pyrrolidine-2-sensitized curcumin treatments, U251N cells transfected with the caspase-3 biosensor were treated with mono- and combination therapies for 24 h. The results showed that although temozolomide, curcumin and pyrrolidine-2-sensitized treatments all significantly reduced cell viability in U251N cells, only curcumin (alone or in combination) significantly induced caspase-3-mediated cell death (Fig. 4B and C).

3.4. Curcumin and pyrrolidine-2 are effective in glioblastoma spheroids

To further investigate the effectiveness of curcumin and pyrrolidine-2, we used glioblastoma spheroids cultures, which more closely represent brain tumors found *in vivo*. Following the preparation of U251N spheroids using cells transfected with the caspase-3 biosensor, spheroids were treated at drug concentrations found to be effective in monolayer experiments. Due to their 3D structure, spheroids were "squashed" between two glass surfaces in order to disperse the cells and facilitate their imaging (Fig. 5A). Both curcumin and curcumin combined with pyrrolidine-2 induced a time-dependent increase in caspase-3 activity. In contrast, cytotoxic concentrations of temozolomide did not induce caspase-3 activity, even after 72 h (Fig. 5B and C).

To relate caspase-3 activity to overall cell viability, we used Hoechst 33342 and propidium iodide labeling to examine the importance of necrotic cell death (Fig. 6). The results showed that a time-dependent increase in necrotic cell death was seen in response to temozolomide, curcumin and curcumin combined with pyrrolodine-2. Yet, the most dramatic increase was seen with the combination treatment, where the rate of necrotic cell death almost doubled from 24 h to 72 h of treatment (Fig. 6B and C).

4. Discussion

In the nervous system, the presence of lipid droplets in neurons is minimal, and is most noticeable in glia cells under physiological conditions. In many models of neurodegeneration, the excessive accumulation of lipid droplets in glial cells is a hallmark of disease and is linked to mitochondrial dysfunction [19]. In glioblastoma multiforme, the accumulation of lipid droplets serves to fuel tumor

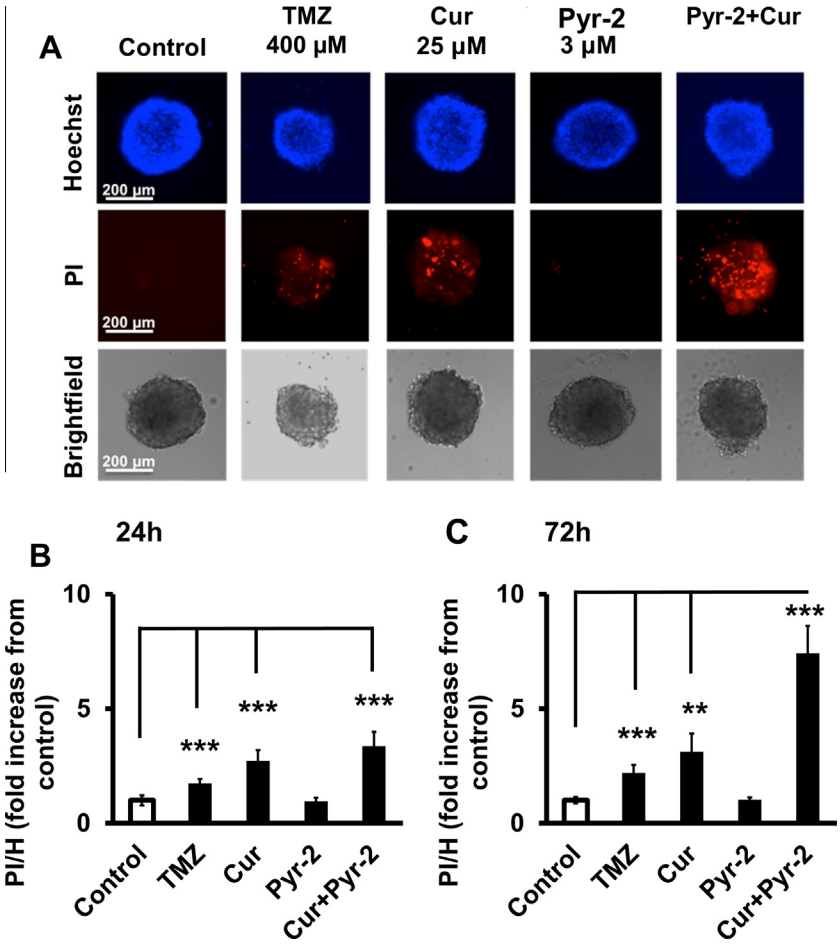

Fig. 6. Pyrrolidine-2-sensitization increases the killing effect of curcumin in glioblastoma spheroids. (A) Fluorescence micrographs of U251N spheroids treated with temozolomide (TMZ; 400 μM; 72 h) and curcumin (Cur; 25 μM; 72 h), with or without pre-treatment with pyrrolidine-2 (Pyr-2; 3 μM; 24 h). Cells were labeled with Hoechst 33342 and propidium iodide (PI) to quantify necrotic cell death. (B) U251N spheroids were treated with temozolomide (TMZ; 400 μM; 24 h) and curcumin (Cur; 25 μM; 24 h), with or without pre-treatment with pyrrolidine-2 (Pyr-2; 3 μM; 24 h). Following treatment, spheroids were imaged using a fluorescence microscope and cell death was quantified by calculating the ratio of propidium iodide to Hoechst 33342 fluorescence. Image analysis was carried out in ImageJ. Shown are mean fold increase values compared to the untreated control (set to 1), from three independent experiments. ***($p < 0.001$). (C) U251N spheroids were treated with temozolomide (TMZ; 400 μM; 72 h) and curcumin (Cur; 25 μM; 72 h), with or without pre-treatment with pyrrolidine-2 (Pyr-2; 3 μM; 24 h). Following treatment, spheroids were imaged using a fluorescence microscope and cell death was quantified by calculating the ratio of propidium iodide to Hoechst 33342 fluorescence. Image analysis was carried out in ImageJ. Shown are mean fold increase values compared to the untreated control (set to 1), from three independent experiments. **($p < 0.01$), ***($p < 0.001$).

growth and resist therapeutic treatments. Aside from providing energy to resist stress induced by chemotherapeutic drugs, it appears that lipid droplets can also directly decrease the amount of drugs available at targets by sequestering them inside the core of the lipid droplets. We hypothesized that the pharmacological inhibition of lipid droplet formation and the reduction of lipid droplet number in glioblastoma cells are viable strategies to increase the effectiveness of lipophilic chemotherapeutic drugs such as curcumin. The mechanisms involved are summarized in Fig. 7. Curcumin is a hydrophobic compound owing to its aromatic phenolic groups and methylene bridge [52,53]. The high lipophilicity of curcumin is indicated by its octanol–water partition coefficient of $2.5 \times 10^4\ M^{-1}$ [54,55]. Curcumin's partition coefficient for 1,2-dioleoyl-*sn*-glycero-3-phosphocholine (DOPC) lipid bilayers and HEPES buffer was $2.4 \times 10^4\ M^{-1}$ [56]. This high partition coefficient clearly indicates curcumin's preference for lipophilic cellular compartments. As such, it can rapidly cross cell membranes and localize in lipid droplets (Fig. 1A). In contrast, analysis using Time-of-Flight Secondary Ion Mass Spectrometry (TOF-SIMS) showed that temozolomide did not localize in lipid droplets (data not shown). The inhibition of lipid droplet formation can thus serve two purposes: (1) to lower the capacity of glioblastoma cells to withstand curcumin-induced stress by reducing their energy stores, and (2) to reduce the amount of compartments where curcumin can be sequestered, thereby increasing drug availability at targets. Different kinds of delivery systems have been used to deliver curcumin to the brain and to glioblastoma *in vivo* [57–59]. Polymeric carriers have the potential to improve the stability and solubility of curcumin [60–62]. Our research group has previously reported the incorporation of curcumin into A2B star polymer micelles and effectiveness of this preparation in glioblastoma [63,64]. A retention of curcumin's biological activity in nanocarriers, an enhanced permeability and retention (EPR) effect and diffusion of curcumin into the neighboring glioblastoma cells could provide an improved therapeutic intervention *in vivo* [65]

Pyrrolidine-2 is an inhibitor of cPLA2α, a key rate limiting enzyme in the synthesis of eicosanoids and a necessary player in the formation of lipid droplets [66,67]. In normal brain tissues, particularly in astrocytes and microglia, excessive PLA2 activation in response to stressors (e.g. glutamate excitotoxicity) can exacerbate inflammatory processes and oxidative stress. In turn, these can promote neurological disorders such as Alzheimer's disease, Parkinson's disease, and traumatic brain injuries [68]. In glioblastoma cells, cPLA2α activity is likely to be upregulated in response

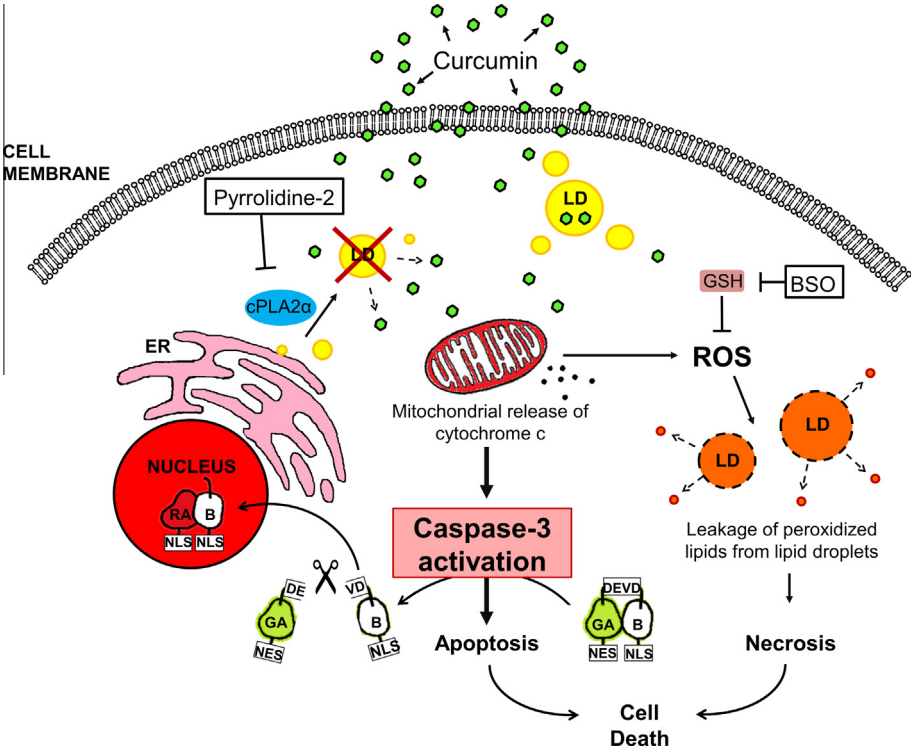

Fig. 7. Proposed mechanisms of drug action for curcumin and pyrrolidine-2-sensitization. Curcumin is a pluripotent agent. It induces apoptosis mainly through the activation of caspase-3-mediated apoptosis. Lipid droplets (LD) can sequester curcumin, reducing the availability and effectiveness of the drug. Sensitization of glioblastoma cells with pyrrolidine-2, an inhibitor of cPLA2α and of lipid droplet formation, can increase curcumin's availability at targets and cell death. In combination with BSO, curcumin also induces necrosis by reducing the levels of the scavenger glutathione (GSH), thereby increasing reactive oxygen species (ROS), leakage of peroxidized lipids from lipid droplets, and cell death.

to chemotherapeutic intervention, allowing cancer cells to stock up in energy and adapt their metabolic pathways. Although pyrrolidine-2 treatment alone does not induce significant loss in cell viability in U251N glioblastoma cells up to 4 μM, its effect becomes apparent when followed by curcumin treatments. Our results show that pyrrolidine-2 pre-treatment dramatically increased the effectiveness of curcumin in U251N cells after 72 h, virtually abolishing cell viability at curcumin concentrations above 20 μM. Interestingly, the lipid droplet number of cells treated with curcumin following pyrrolidine-2 sensitization was higher than that of cells treated with curcumin alone – likely due to the drug-induced cellular stress, previously reported to induce lipid droplet formation [19,69,70]. Sensitization using BSO was comparatively less effective, likely due to the diversity of antioxidants and enzymes that can reduce ROS levels. Nevertheless, the depletion of glutathione by BSO increased curcumin-mediated cell death, possibly through the increased peroxidation of lipid droplets, and necrosis (Fig. 7)[71].

To investigate the mode of cell death induced by curcumin and pyrrolidine-2, we employed a highly sensitive biosensor to detect and measure caspase-3 activity in live cells [38]. The mechanism of the biosensor relies on a bi-modular design, in which two fluorescent proteins with dimerization-dependent brightness are activated in a mutually-exclusive manner. When challenged with pro-apoptotic stimuli, cells transfected with the biosensor manifest a change in fluorescence color, from green to red, and in signal localization, from the cytosol to the nucleus. In the absence of caspase-3 activity, the green cytoplasmic protein is linked with a non-fluorescent partner protein which increases green fluorescence manyfolds. Following the activation of caspase-3 during apoptosis, the caspase-3 substrate (DEVD) contained in the linker region is cleaved, and green fluorescence is dramatically decreased. The partner protein then translocates into the nucleus and associates with high affinity to the red fluorescent protein, enhancing red fluorescence manyfold. Thus, the specificity of detection is based on (1) the caspase-3 substrate, (2) the change in the color of the signal, and (3) the change in the subcellular localization of the signal. It is to note that a small proportion of cells display caspase-3 activity under control conditions. Our results support previous findings stating that curcumin is a strong inducer of caspase-3-mediated apoptosis in cancer cells [41,42]. In contrast, temozolomide-induced cell death did not implicate caspase-3 activation, suggesting the involvement of other modes of cell death, such as autophagy [72]. Autophagy is usually reduced in cells with a large number of lipid droplets, which could partly explain the limited effectiveness of temozolomide against glioblastoma tumors [73,74].

In normal brain tissues, it appears that cPLA2α and lipid droplets play protective roles, notably helping glia cells to support neurons and resist stressors. For example, cPLA2α (+/+) mice were found to be more resistant to hypoxic conditions resulting from brain ischemia than their null counterparts [75]. Excessive cPLA2α activity has also been involved in apoptosis, as it was found to drive arachidonic acid-mediated cytotoxicity and subsequent caspase-3 activation [76]. On the other hand, the protective role of lipid droplets in glioblastoma cells is highly detrimental to cancer patients. The inhibition of cPLA2α is one of several approaches recently investigated to hinder lipid metabolism in cancer cells. Small molecules and gene silencing (e.g. acetyl-CoA carboxylase alpha) were shown to be effective in inhibiting cancer cell proliferation and viability *in vitro* [77–79]. However, most experiments performed in monolayer cancer cell cultures do not accurately reflect the conditions found in *in vivo*, where the intercellular contact, tumor dynamics and overall heterogeneous microenvironment

found in tumors often heighten resistance to radiotherapy and chemotherapy [80–82]. Glioblastoma spheroids harbor hypoxic cores where metabolic pathways, including those involving lipids, are changed [4,83–85]. *De novo* lipogenesis, for instance, was shown to be bypassed in cancer cells in hypoxic conditions. Instead, cancer cells relied on extracellular lipid scavenging to supply for their needs [6]. Thus, we conducted experiments in 3D spheroid, and confirmed that pyrrolidine-2 pre-treatment enhanced the cell killing effect of curcumin in a time- and caspase-3-dependent manner. In contrast, temozolomide alone was significantly less effective at inducing caspase-3 activation and glioblastoma cell death.

Because of the importance of cPLA2α in lipid metabolism and the production of pro-inflammatory mediators, its inhibition has also been studied in the context of inflammatory conditions such as arthritis [86,87]. The microenvironment of glioblastoma tumors is characterized by the infiltration of hyperactivated immune cells, which aggravate disease progression. Thus, it can be hypothesized that inhibition of lipid metabolism can also reduce inflammation at tumor sites [88–90]. However, the potential side effects of pyrrolidine-2 deter its use *in vivo*. One of the best tolerated statins is simvastatin [91]. Statins were tested in some CNS diseases and were suggested as supplemental anticancer agents [92,93]. Thus, the administration of simvastatin in combination with curcumin might be a suitable therapeutic strategy for certain groups of glioblastoma patients.

Taken together, our results indicate that lipid droplets in glioblastoma cells play a protective role by sequestering drugs and promoting cell survival. Decreased lipid droplet formation using pyrrolidine-2 as a sensitizing agent significantly increases the cell killing effect of chemotherapeutic agents such as curcumin.

Acknowledgments

The present study was supported by CIHR (MOP-119425) and NSERC (RGPIN-2015-04994) grants. The authors have no conflicts of interest to declare.

Appendix A. Supplementary material

Supplementary data associated with this article can be found, in the online version, at http://dx.doi.org/10.1016/j.ejpb.2015.12.008.

References

[1] K. Gupta, I. Kalra, P. Salunke, R.K. Vasishta, Lipidized glioblastoma: a rare differentiation pattern, Neuropathology 31 (2011) 93–97.
[2] L.K. Boroughs, R.J. DeBerardinis, Metabolic pathways promoting cancer cell survival and growth, Nat. Cell Biol. 17 (2015) 351–359.
[3] J.A. Menendez, R. Lupu, Fatty acid synthase and the lipogenic phenotype in cancer pathogenesis, Nat. Rev. Cancer 7 (2007) 763–777.
[4] F. Baenke, B. Peck, H. Miess, A. Schulze, Hooked on fat: the role of lipid synthesis in cancer metabolism and tumour development, Dis. Models Mech. 6 (2013) 1353–1363.
[5] F.P. Kuhajda, Fatty acid synthase and cancer: new application of an old pathway, Cancer Res. 66 (2006) 5977–5980.
[6] J.J. Kamphorst, J.R. Cross, J. Fan, E. de Stanchina, R. Mathew, E.P. White, C.B. Thompson, J.D. Rabinowitz, Hypoxic and Ras-transformed cells support growth by scavenging unsaturated fatty acids from lysophospholipids, Proc. Natl. Acad. Sci. USA 110 (2013) 8882–8887.
[7] F.P. Kuhajda, K. Jenner, F.D. Wood, R.A. Hennigar, L.B. Jacobs, J.D. Dick, G.R. Pasternack, Fatty acid synthesis: a potential selective target for antineoplastic therapy, Proc. Natl. Acad. Sci. USA 91 (1994) 6379–6383.
[8] A.D. Patterson, O. Maurhofer, D. Beyoglu, C. Lanz, K.W. Krausz, T. Pabst, F.J. Gonzalez, J.F. Dufour, J.R. Idle, Aberrant lipid metabolism in hepatocellular carcinoma revealed by plasma metabolomics and lipid profiling, Cancer Res. 71 (2011) 6590–6600.
[9] P. Prasanna, A. Thibault, L. Liu, D. Samid, Lipid metabolism as a target for brain cancer therapy: synergistic activity of lovastatin and sodium phenylacetate against human glioma cells, J. Neurochem. 66 (1996) 710–716.
[10] A.G. Renehan, M. Zwahlen, M. Egger, Adiposity and cancer risk: new mechanistic insights from epidemiology, Nat. Rev. Cancer 15 (2015) 484–498.
[11] Nor E. Sounni, J. Cimino, S. Blacher, I. Primac, A. Truong, G. Mazzucchelli, A. Paye, D. Calligaris, D. Debois, P. De Tullio, B. Mari, E. De Pauw, A. Noel, Blocking lipid synthesis overcomes tumor regrowth and metastasis after antiangiogenic therapy withdrawal, Cell Metab. 20 (2014) 280–294.
[12] A. Umemura, Eek J. Park, K. Taniguchi, Jun H. Lee, S. Shalapour, Mark A. Valasek, M. Aghajan, H. Nakagawa, E. Seki, Michael N. Hall, M. Karin, Liver damage, inflammation, and enhanced tumorigenesis after persistent mTORC1 inhibition, Cell Metab. 20 (2014) 133–144.
[13] C.R. Santos, A. Schulze, Lipid metabolism in cancer, FEBS J. 279 (2012) 2610–2623.
[14] J.V. Swinnen, K. Brusselmans, G. Verhoeven, Increased lipogenesis in cancer cells: new players, novel targets, Curr. Opin. Clin. Nutr. Metab. Care 9 (2006) 358–365.
[15] A.D. Barbosa, D.B. Savage, S. Siniossoglou, Lipid droplet-organelle interactions: emerging roles in lipid metabolism, Curr. Opin. Cell Biol. 35 (2015) 91–97.
[16] H.F. Hashemi, J.M. Goodman, The life cycle of lipid droplets, Curr. Opin. Cell Biol. 33 (2015) 119–124.
[17] D.A. Gross, D.L. Silver, Cytosolic lipid droplets: from mechanisms of fat storage to disease, Crit. Rev. Biochem. Mol. Biol. 49 (2014) 304–326.
[18] M.T. Accioly, P. Pacheco, C.M. Maya-Monteiro, N. Carrossini, B.K. Robbs, S.S. Oliveira, C. Kaufmann, J.A. Morgado-Diaz, P.T. Bozza, J.P. Viola, Lipid bodies are reservoirs of cyclooxygenase-2 and sites of prostaglandin-E2 synthesis in colon cancer cells, Cancer Res. 68 (2008) 1732–1740.
[19] M.A. Welte, Expanding roles for lipid droplets, Curr. Biol. 25 (2015) R470–R481.
[20] A.R. Thiam, R.V. Farese Jr., T.C. Walther, The biophysics and cell biology of lipid droplets, Nat. Rev. Mol. Cell Biol. 14 (2013) 775–786.
[21] S. Rak, T. De Zan, J. Stefulj, M. Kosovic, O. Gamulin, M. Osmak, FTIR spectroscopy reveals lipid droplets in drug resistant laryngeal carcinoma cells through detection of increased ester vibrational bands intensity, Analyst 139 (2014) 3407–3415.
[22] D. Lagoutte, V. Nicolas, E. Poupon, A. Fournet, R. Hocquemiller, D. Libong, P. Chaminade, P.M. Loiseau, Antifungal canthin-6-one series accumulate in lipid droplets and affect fatty acid metabolism in Saccharomyces cerevisiae, Biomed. Pharmacother. 62 (2008) 99–103.
[23] S.C. Gupta, S. Patchva, B.B. Aggarwal, Therapeutic roles of curcumin: lessons learned from clinical trials, AAPS J. 15 (2013) 195–218.
[24] J.K. Lin, Molecular targets of curcumin, Adv. Exp. Med. Biol. 595 (2007) 227–243.
[25] A.L. Cheng, C.H. Hsu, J.K. Lin, M.M. Hsu, Y.F. Ho, T.S. Shen, J.Y. Ko, J.T. Lin, B.R. Lin, W. Ming-Shiang, H.S. Yu, S.H. Jee, G.S. Chen, T.M. Chen, C.A. Chen, M.K. Lai, Y.S. Pu, M.H. Pan, Y.J. Wang, C.C. Tsai, C.Y. Hsieh, Phase I clinical trial of curcumin, a chemopreventive agent, in patients with high-risk or pre-malignant lesions, Anticancer Res. 21 (2001) 2895–2900.
[26] N. Dhillon, B.B. Aggarwal, R.A. Newman, R.A. Wolff, A.B. Kunnumakkara, J.L. Abbruzzese, C.S. Ng, V. Badmaev, R. Kurzrock, Phase II trial of curcumin in patients with advanced pancreatic cancer, Clin. Cancer Res. 14 (2008) 4491–4499.
[27] P. Anand, A.B. Kunnumakkara, R.A. Newman, B.B. Aggarwal, Bioavailability of curcumin: problems and promises, Mol. Pharm. 4 (2007) 807–818.
[28] T. Ono, K. Yamada, Y. Chikazawa, M. Ueno, S. Nakamoto, T. Okuno, K. Seno, Characterization of a novel inhibitor of cytosolic phospholipase A2alpha, pyrrophenone, Biochem. J. 363 (2002) 727–735.
[29] A. Gubern, J. Casas, M. Barcelo-Torns, D. Barneda, X. de la Rosa, R. Masgrau, F. Picatoste, J. Balsinde, M.A. Balboa, E. Claro, Group IVA phospholipase A2 is necessary for the biogenesis of lipid droplets, J. Biol. Chem. 283 (2008) 27369–27382.
[30] A.L. Cohen, H. Colman, Glioma biology and molecular markers, Cancer Treat. Res. 163 (2015) 15–30.
[31] V.A. Cuddapah, S. Robel, S. Watkins, H. Sontheimer, A neurocentric perspective on glioma invasion, Nat. Rev. Neurosci. 15 (2014) 455–465.
[32] R. Stupp, W.P. Mason, M.J. van den Bent, M. Weller, B. Fisher, M.J. Taphoorn, K. Belanger, A.A. Brandes, C. Marosi, U. Bogdahn, J. Curschmann, R.C. Janzer, S.K. Ludwin, T. Gorlia, A. Allgeier, D. Lacombe, J.G. Cairncross, E. Eisenhauer, R.O. Mirimanoff, Radiotherapy plus concomitant and adjuvant temozolomide for glioblastoma, N. Engl. J. Med. 352 (2005) 987–996.
[33] K. Petrecca, M.C. Guiot, V. Panet-Raymond, L. Souhami, Failure pattern following complete resection plus radiotherapy and temozolomide is at the resection margin in patients with glioblastoma, J. Neurooncol. 111 (2013) 19–23.
[34] M. Weller, T. Cloughesy, J.R. Perry, W. Wick, Standards of care for treatment of recurrent glioblastoma—are we there yet?, Neuro-Oncology 15 (2013) 4–27
[35] M.E. Hegi, A.C. Diserens, T. Gorlia, M.F. Hamou, N. de Tribolet, M. Weller, J.M. Kros, J.A. Hainfellner, W. Mason, L. Mariani, J.E. Bromberg, P. Hau, R.O. Mirimanoff, J.G. Cairncross, R.C. Janzer, R. Stupp, MGMT gene silencing and benefit from temozolomide in glioblastoma, The New England journal of medicine 352 (2005) 997–1003.
[36] O.W. Griffith, Mechanism of action, metabolism, and toxicity of buthionine sulfoximine and its higher homologs, potent inhibitors of glutathione synthesis, J. Biol. Chem. 257 (1982) 13704–13712.
[37] C.P. Anderson, C.P. Reynolds, Synergistic cytotoxicity of buthionine sulfoximine (BSO) and intensive melphalan (L-PAM) for neuroblastoma cell lines established at relapse after myeloablative therapy, Bone Marrow Transplant. 30 (2002) 135–140.
[38] Y. Ding, J. Li, J.R. Enterina, Y. Shen, I. Zhang, P.H. Tewson, G.C. Mo, J. Zhang, A.M. Quinn, T.E. Hughes, D. Maysinger, S.C. Alford, Y. Zhang, R.E. Campbell,

Ratiometric biosensors based on dimerization-dependent fluorescent protein exchange, Nat. Methods 12 (2015) 195–198.
[39] G. Kroemer, L. Galluzzi, P. Vandenabeele, J. Abrams, E.S. Alnemri, E.H. Baehrecke, M.V. Blagosklonny, W.S. El-Deiry, P. Golstein, D.R. Green, M. Hengartner, R.A. Knight, S. Kumar, S.A. Lipton, W. Malorni, G. Nuñez, M.E. Peter, J. Tschopp, J. Yuan, M. Piacentini, B. Zhivotovsky, G. Melino, Classification of cell death: recommendations of the Nomenclature Committee on Cell Death 2009, Cell Death Differ. 16 (2009) 3–11.
[40] J.M. Brown, L.D. Attardi, The role of apoptosis in cancer development and treatment response, Nat. Rev. Cancer 5 (2005) 231–237.
[41] R.J. Anto, A. Mukhopadhyay, K. Denning, B.B. Aggarwal, Curcumin (diferuloylmethane) induces apoptosis through activation of caspase-8, BID cleavage and cytochrome c release: its suppression by ectopic expression of Bcl-2 and Bcl-xl, Carcinogenesis 23 (2002) 143–150.
[42] E. Sikora, A. Bielak-Zmijewska, A. Magalska, K. Piwocka, G. Mosieniak, M. Kalinowska, P. Widlak, I.A. Cymerman, J.M. Bujnicki, Curcumin induces caspase-3-dependent apoptotic pathway but inhibits DNA fragmentation factor 40/caspase-activated DNase endonuclease in human Jurkat cells, Mol. Cancer Ther. 5 (2006) 927–934.
[43] R. Gogada, M. Amadori, H. Zhang, A. Jones, A. Verone, J. Pitarresi, S. Jandhyam, V. Prabhu, J.D. Black, D. Chandra, Curcumin induces Apaf-1-dependent, p21-mediated caspase activation and apoptosis, Cell Cycle (Georgetown, Tex.) 10 (2011) 4128–4137.
[44] R.S. Dhanikula, A. Argaw, J.F. Bouchard, P. Hildgen, Methotrexate loaded polyether-copolyester dendrimers for the treatment of gliomas: enhanced efficacy and intratumoral transport capability, Mol. Pharm. 5 (2008) 105–116.
[45] R.C. Melo, H. D'Avila, P.T. Bozza, P.F. Weller, Imaging lipid bodies within leukocytes with different light microscopy techniques, Methods Mol. Biol. (Clifton, N.J.) 689 (2011) 149–161.
[46] P. Greenspan, E.P. Mayer, S.D. Fowler, Nile red: a selective fluorescent stain for intracellular lipid droplets, J. Cell Biol. 100 (1985) 965–973.
[47] D.L. Sackett, J. Wolff, Nile red as a polarity-sensitive fluorescent probe of hydrophobic protein surfaces, Anal. Biochem. 167 (1987) 228–234.
[48] W. Wen, J.L. Meinkoth, R.Y. Tsien, S.S. Taylor, Identification of a signal for rapid export of proteins from the nucleus, Cell 82 (1995) 463–473.
[49] S.C. Alford, A.S. Abdelfattah, Y. Ding, R.E. Campbell, A fluorogenic red fluorescent protein heterodimer, Chem. Biol. 19 (2012) 353–360.
[50] X. Xu, A.L. Gerard, B.C. Huang, D.C. Anderson, D.G. Payan, Y. Luo, Detection of programmed cell death using fluorescence energy transfer, Nucleic Acids Res. 26 (1998) 2034–2035.
[51] R.B. Moreland, H.G. Nam, L.M. Hereford, H.M. Fried, Identification of a nuclear localization signal of a yeast ribosomal protein, Proc. Natl. Acad. Sci. USA 82 (1985) 6561–6565.
[52] K.I. Priyadarsini, Chemical and structural features influencing the biological activity of curcumin, Curr. Pharm. Des. 19 (2013) 2093–2100.
[53] B.B. Aggarwal, B. Sung, Pharmacological basis for the role of curcumin in chronic diseases: an age-old spice with modern targets, Trends Pharmacol. Sci. 30 (2009) 85–94.
[54] M. Heger, R.F. van Golen, M. Broekgaarden, M.C. Michel, The molecular basis for the pharmacokinetics and pharmacodynamics of curcumin and its metabolites in relation to cancer, Pharmacol. Rev. 66 (2014) 222–307.
[55] A. Kunwar, A. Barik, R. Pandey, K.I. Priyadarsini, Transport of liposomal and albumin loaded curcumin to living cells: an absorption and fluorescence spectroscopic study, Biochim. Biophys. Acta 1760 (2006) 1513–1520.
[56] W.C. Hung, F.Y. Chen, C.C. Lee, Y. Sun, M.T. Lee, H.W. Huang, Membrane-thinning effect of curcumin, Biophys. J . 94 (2008) 4331–4338.
[57] R.L. Shinde, G.P. Bharkad, P.V. Devarajan, Intranasal microemulsion for targeted nose to brain delivery in neurocysticercosis: role of docosahexaenoic acid, Eur. J. Pharm. Biopharm. Off. J. Arbeitsgemeinschaft fur Pharmazeutische Verfahrenstechnik e.V 96 (2015) 363–379.
[58] S. Wang, P. Chen, L. Zhang, C. Yang, G. Zhai, Formulation and evaluation of microemulsion-based in situ ion-sensitive gelling systems for intranasal administration of curcumin, J. Drug Target. 20 (2012) 831–840.
[59] X. Chen, F. Zhi, X. Jia, X. Zhang, R. Ambardekar, Z. Meng, A.R. Paradkar, Y. Hu, Y. Yang, Enhanced brain targeting of curcumin by intranasal administration of a thermosensitive poloxamer hydrogel, J. Pharm. Pharmacol. 65 (2013) 807–816.
[60] O. Naksuriya, Y. Shi, C.F. van Nostrum, S. Anuchapreeda, W.E. Hennink, S. Okonogi, HPMA-based polymeric micelles for curcumin solubilization and inhibition of cancer cell growth, Eur. J. Pharm. Biopharm. Off. J. Arbeitsgemeinschaft fur Pharmazeutische Verfahrenstechnik e.V 94 (2015) 501–512.
[61] J.M. Rabanel, J. Faivre, G.D. Paka, C. Ramassamy, P. Hildgen, X. Banquy, Effect of polymer architecture on curcumin encapsulation and release from PEGylated polymer nanoparticles: toward a drug delivery nano-platform to the CNS, Eur. J. Pharm. Biopharm. Off. J. Arbeitsgemeinschaft fur Pharmazeutische Verfahrenstechnik e.V 96 (2015) 409–420.
[62] X. Yang, Z. Li, N. Wang, L. Li, L. Song, T. He, L. Sun, Z. Wang, Q. Wu, N. Luo, C. Yi, C. Gong, Curcumin-encapsulated polymeric micelles suppress the development of colon cancer in vitro and in vivo, Sci. Rep. 5 (2015) 10322.
[63] G.M. Soliman, S. Anjali, C. Yiming, S. Rishi, K. Ashok, M. Dusica, Miktoarm star micelles containing curcumin reduce cell viability of sensitized glioblastoma, J. Nanomedine Biotherapeutic Discov. 4 (2014) e1000124.
[64] A. Moquin, A. Sharma, Y. Cui, A. Lau, D. Maysinger, A. Kakkar, Asymmetric AB miktoarm star polymers: synthesis, self-assembly, and study of micelle stability using AF for efficient drug delivery, Macromol. Biosci. (2015).
[65] F. Schütze, F. Röhrig, S. Vorlová, S. Gätzner, A. Kuhn, S. Ergün, E. Henke, Inhibition of lysyl oxidases improves drug diffusion and increases efficacy of cytotoxic treatment in 3D tumor models, Sci. Rep. 5 (2015) 17576.
[66] D.T. Stephenson, J.V. Manetta, D.L. White, X.G. Chiou, L. Cox, B. Gitter, P.C. May, J.D. Sharp, R.M. Kramer, J.A. Clemens, Calcium-sensitive cytosolic phospholipase A2 (cPLA2) is expressed in human brain astrocytes, Brain Res. 637 (1994) 97–105.
[67] K. Seno, T. Okuno, K. Nishi, Y. Murakami, F. Watanabe, T. Matsuura, M. Wada, Y. Fujii, M. Yamada, T. Ogawa, T. Okada, H. Hashizume, M. Kii, S. Hara, S. Hagishita, S. Nakamoto, K. Yamada, Y. Chikazawa, M. Ueno, I. Teshirogi, T. Ono, M. Ohtani, Pyrrolidine inhibitors of human cytosolic phospholipase A(2), J. Med. Chem. 43 (2000) 1041–1044.
[68] G.Y. Sun, P.B. Shelat, M.B. Jensen, Y. He, A.Y. Sun, A. Simonyi, Phospholipases A2 and inflammatory responses in the central nervous system, NeuroMol. Med. 12 (2010) 133–148.
[69] A.G. Cabodevilla, L. Sánchez-Caballero, E. Nintou, V.G. Boiadjieva, F. Picatoste, A. Gubern, E. Claro, Cell survival during complete nutrient deprivation depends on lipid droplet-fueled β-oxidation of fatty acids, J. Biol. Chem. 288 (2013) 27777–27788.
[70] A. Khatchadourian, S.D. Bourque, V.R. Richard, V.I. Titorenko, D. Maysinger, Dynamics and regulation of lipid droplet formation in lipopolysaccharide (LPS)-stimulated microglia, Biochim. Biophys. Acta 2012 (1821) 607–617.
[71] L. Liu, K. Zhang, H. Sandoval, S. Yamamoto, M. Jaiswal, E. Sanz, Z. Li, J. Hui, B.H. Graham, A. Quintana, H.J. Bellen, Glial lipid droplets and ROS induced by mitochondrial defects promote neurodegeneration, Cell 160 (2015) 177–190.
[72] T. Kanzawa, I.M. Germano, T. Komata, H. Ito, Y. Kondo, S. Kondo, Role of autophagy in temozolomide-induced cytotoxicity for malignant glioma cells, Cell Death Differ. 11 (2004) 448–457.
[73] J. Sesen, P. Dahan, S.J. Scotland, E. Saland, V.T. Dang, A. Lemarie, B.M. Tyler, H. Brem, C. Toulas, E. Cohen-Jonathan Moyal, J.E. Sarry, N. Skuli, Metformin inhibits growth of human glioblastoma cells and enhances therapeutic response, PLoS One 10 (2015) e0123721.
[74] Z. Zhang, J. Wang, Y. Shen, C. Guo, K. Sai, F. Chen, X. Mei, F. Han, Z. Chen, Dihydroartemisinin increases temozolomide efficacy in glioma cells by inducing autophagy, Oncol. Lett. 10 (2015) 379–383.
[75] S. Tabuchi, N. Uozumi, S. Ishii, Y. Shimizu, T. Watanabe, T. Shimizu, Mice deficient in cytosolic phospholipase A2 are less susceptible to cerebral ischemia/reperfusion injury, Acta Neurochir. Suppl. 86 (2003) 169–172.
[76] M. Nakanishi, D.W. Rosenberg, Roles of cPLA(2)α and arachidonic acid in cancer, Biochim. Biophys. Acta 1761 (2006) 1335–1343.
[77] M. Hilvo, C. Denkert, L. Lehtinen, B. Muller, S. Brockmoller, T. Seppanen-Laakso, J. Budczies, E. Bucher, L. Yetukuri, S. Castillo, E. Berg, H. Nygren, M. Sysi-Aho, J. L. Griffin, O. Fiehn, S. Loibl, C. Richter-Ehrenstein, C. Radke, T. Hyotylainen, O. Kallioniemi, K. Iljin, M. Oresic, Novel theranostic opportunities offered by characterization of altered membrane lipid metabolism in breast cancer progression, Cancer Res. 71 (2011) 3236–3245.
[78] X. Cai, X. Hu, X. Tan, W. Cheng, Q. Wang, X. Chen, Y. Guan, C. Chen, X. Jing, Metformin induced AMPK activation, G0/G1 phase cell cycle arrest and the inhibition of growth of esophageal squamous cell carcinomas in vitro and in vivo, PLoS One 10 (2015) e0133349.
[79] F.P. Kuhajda, E.S. Pizer, J.N. Li, N.S. Mani, G.L. Frehywot, C.A. Townsend, Synthesis and antitumor activity of an inhibitor of fatty acid synthase, Proc. Natl. Acad. Sci. USA 97 (2000) 3450–3454.
[80] W. He, Y. Kuang, X. Xing, R.J. Simpson, H. Huang, T. Yang, J. Chen, L. Yang, E. Liu, W. He, J. Gu, Proteomic comparison of 3D and 2D glioma models reveals increased HLA-E expression in 3D models is associated with resistance to NK cell-mediated cytotoxicity, J. Proteome Res. 13 (2014) 2272–2281.
[81] D. Zips, H.D. Thames, M. Baumann, New anticancer agents: in vitro and in vivo evaluation, Vivo 19 (2005) 1–7.
[82] M. Hakanson, M. Textor, M. Charnley, Engineered 3D environments to elucidate the effect of environmental parameters on drug response in cancer, Integr. Biol. (Camb.) 3 (2011) 31–38.
[83] P. Kucharzewska, H.C. Christianson, M. Belting, Global profiling of metabolic adaptation to hypoxic stress in human glioblastoma cells, PLoS One 10 (2015) e0116740.
[84] P. Chinnaiyan, E. Kensicki, G. Bloom, A. Prabhu, B. Sarcar, S. Kahali, S. Eschrich, X. Qu, P. Forsyth, R. Gillies, The metabolomic signature of malignant glioma reflects accelerated anabolic metabolism, Cancer Res. 72 (2012) 5878–5888.
[85] D. Ackerman, M.C. Simon, Hypoxia, lipids, and cancer: surviving the harsh tumor microenvironment, Trends Cell Biol. 24 (2014) 472–478.
[86] M.A. Balboa, R. Perez, J. Balsinde, Amplification mechanisms of inflammation: paracrine stimulation of arachidonic acid mobilization by secreted phospholipase A2 is regulated by cytosolic phospholipase A2-derived hydroperoxyeicosatetraenoic acid, J. Immunol. (Baltimore, Md.: 1950) 171 (2003) (1950) 989–994.
[87] N. Tai, K. Kuwabara, M. Kobayashi, K. Yamada, T. Ono, K. Seno, Y. Gahara, J. Ishizaki, Y. Hori, Cytosolic phospholipase A2 alpha inhibitor, pyrroxyphene, displays anti-arthritic and anti-bone destructive action in a murine arthritis model, Inflammat. Res. Off. J. Euro. Histamine Res. Soc. . . . [et al.] 59 (2010) 53–62.
[88] G. Desmarais, G. Charest, D. Fortin, R. Bujold, D. Mathieu, B. Paquette, Cyclooxygenase-2 inhibitor prevents radiation-enhanced infiltration of F98 glioma cells in brain of Fischer rat, Int. J. Radiat. Biol. (2015) 1–10.
[89] J.L. Sowers, K.M. Johnson, C. Conrad, J.T. Patterson, L.C. Sowers, The role of inflammation in brain cancer, Adv. Exp. Med. Biol. 816 (2014) 75–105.

[90] M. Tafani, M. Di Vito, A. Frati, L. Pellegrini, E. De Santis, G. Sette, A. Eramo, P. Sale, E. Mari, A. Santoro, A. Raco, M. Salvati, R. De Maria, M.A. Russo, Pro-inflammatory gene expression in solid glioblastoma microenvironment and in hypoxic stem cells from human glioblastoma, J. Neuroinflammation 8 (2011) 32.
[91] H. Naci, J. Brugts, T. Ades, Comparative tolerability and harms of individual statins: a study-level network meta-analysis of 246 955 participants from 135 randomized, controlled trials, Circ. Cardiovasc. Qual. Outcomes 6 (2013) 390–399.
[92] D. Gaist, J. Hallas, S. Friis, S. Hansen, H.T. Sorensen, Statin use and survival following glioblastoma multiforme, Cancer Epidemiol. 38 (2014) 722–727.
[93] T. Menge, H.P. Hartung, O. Stuve, Statins – a cure-all for the brain?, Nat Rev. Neurosci. 6 (2005) 325–331.

Pharmacological inhibition of lipid droplet formation enhances the effectiveness of curcumin in glioblastoma

Issan Zhang and Yiming Cui, Abdolali Amiri, Yidan Ding, Robert E. Campbell, and Dusica Maysinger

Supplementary Figures

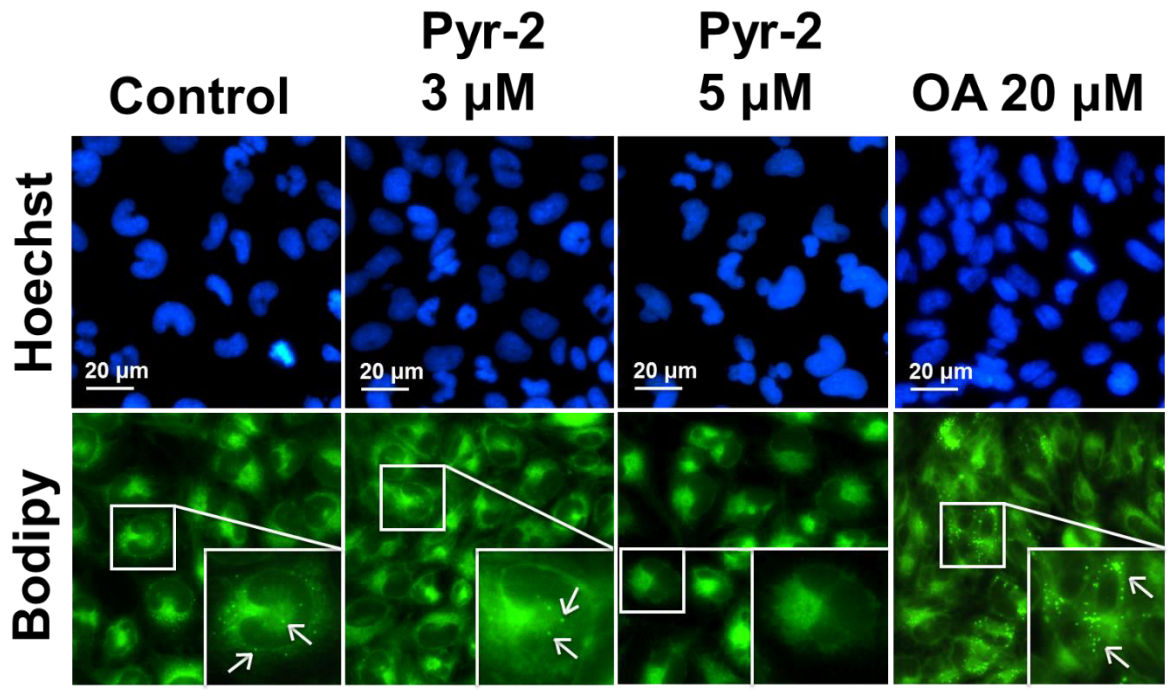

Figure S1. Pyrrolidine-2 decreases lipid droplet accumulation in U251N glioblastoma cells.

Fluorescence micrographs of U251N cells labelled for nuclei (Hoechst 33342) and lipid droplets (Bodipy 493/503). Cells treated with pyrrolidine-2 (Pyr-2) for 24h show a dose-dependent decrease in lipid droplets numbers compared to untreated cells. Cells treated with oleic acid (OA) show increased lipid droplets numbers.

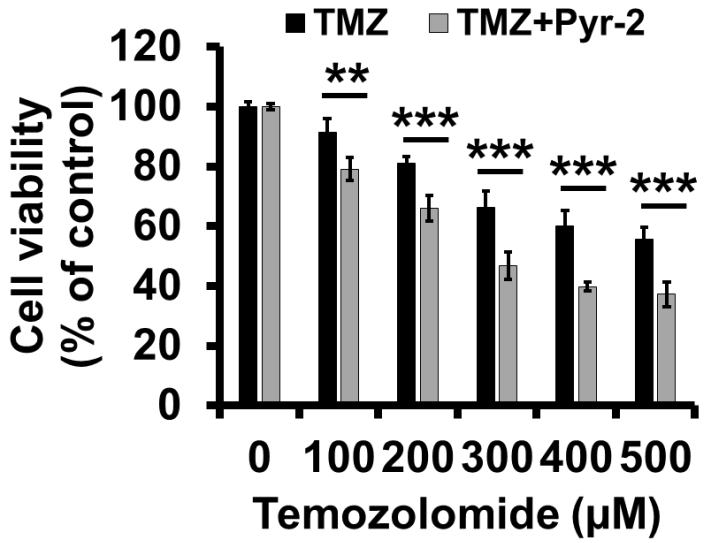

Figure S2. Effect of pyrrolidine-2 on the cell killing effect of temozolomide in U251N glioblastoma cells.

(D) The cell viability of U251N glioblastoma cells treated with temozolomide (100-500 μM; 72h), with and without pyrrolidine-2 sensitization (3 μM; 24h), was measured by counting the number of cell nuclei labelled with Hoechst 33342. Cells were imaged using a high-throughput microscope. Shown are average percentage values ± SEM compared to untreated controls from two independent experiments. (**$p<0.01$; ***$p<0.001$)

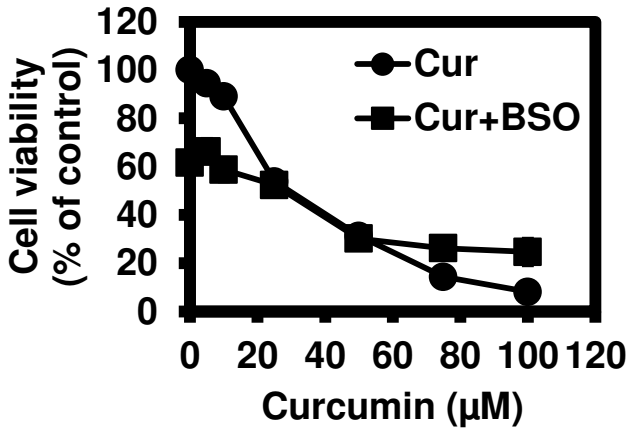

Figure S3. BSO modulates the cell killing effect of curcumin in U251N glioblastoma cells.

Cell viability of U251N cells in response to curcumin (5-100 µM; 24h), in the presence or absence of buthionine sulfoximine (BSO; 5 mM; 24h) pre-treatment, was measured by counting the number of cell nuclei labelled with Hoechst 33342. Cells were imaged using a high-throughput microscope. Shown are mean percentage values ± SEM compared to untreated controls, from three independent experiments.

cells

MDPI

Article

Nanotherapeutic Modulation of Human Neural Cells and Glioblastoma in Organoids and Monocultures

Issan Zhang [1], Paula Lépine [2], Chanshuai Han [2], María Lacalle-Aurioles [2], Carol X.-Q. Chen [2], Rainer Haag [3], Thomas M. Durcan [2] and Dusica Maysinger [1,*]

1 Department of Pharmacology and Therapeutics, McGill University, 3655 Promenade Sir-William-Osler, Montreal, QC H3G 1Y6, Canada; issan.zhang@mail.mcgill.ca

2 The Neuro's Early Drug Discovery Unit (EDDU), McGill University, 3801 University Street, Montreal, QC H3A 2B4, Canada; paula.lepine@mcgill.ca (P.L.); chanshuai.han2@mcgill.ca (C.H.); maria.lacalleaurioles@mcgill.ca (M.L.-A.); xiuqing.chen@mcgill.ca (C.X.-Q.C.); thomas.durcan@mcgill.ca (T.M.D.)

3 Institute of Chemistry and Biochemistry, Freie Universität Berlin, Takustraße 3, 14195 Berlin, Germany; haag@chemie.fu-berlin.de

* Correspondence: dusica.maysinger@mcgill.ca; Tel.: +1-514-398-1264

Received: 23 August 2020; Accepted: 5 November 2020; Published: 7 November 2020

Abstract: Inflammatory processes in the brain are orchestrated by microglia and astrocytes in response to activators such as pathogen-associated molecular patterns, danger-associated molecular patterns and some nanostructures. Microglia are the primary immune responders in the brain and initiate responses amplified by astrocytes through intercellular signaling. Intercellular communication between neural cells can be studied in cerebral organoids, co-cultures or in vivo. We used human cerebral organoids and glioblastoma co-cultures to study glia modulation by dendritic polyglycerol sulfate (dPGS). dPGS is an extensively studied nanostructure with inherent anti-inflammatory properties. Under inflammatory conditions, lipocalin-2 levels in astrocytes are markedly increased and indirectly enhanced by soluble factors released from hyperactive microglia. dPGS is an effective anti-inflammatory modulator of these markers. Our results show that dPGS can enter neural cells in cerebral organoids and glial cells in monocultures in a time-dependent manner. dPGS markedly reduces lipocalin-2 abundance in the neural cells. Glioblastoma tumoroids of astrocytic origin respond to activated microglia with enhanced invasiveness, whereas conditioned media from dPGS-treated microglia reduce tumoroid invasiveness. Considering that many nanostructures have only been tested in cancer cells and rodent models, experiments in human 3D cerebral organoids and co-cultures are complementary in vitro models to evaluate nanotherapeutics in the pre-clinical setting. Thoroughly characterized organoids and standardized procedures for their preparation are prerequisites to gain information of translational value in nanomedicine. This study provides data for a well-characterized dendrimer (dPGS) that modulates the activation state of human microglia implicated in brain tumor invasiveness.

Keywords: cerebral organoids; nanomedicines; astrocytes; microglia; glioblastoma; lipocalin-2; inflammation

1. Introduction

The brain is particularly challenging to model because of its complex structure and functions. Neural cells constantly interact with each other through signaling molecules as well as cell–cell contacts [1–3]. Monocultures are useful to answer cell type-specific questions, but processes involving multiple cell types benefit from the use of co-cultures and organoid models [4–6].

Although primary dissociated and organotypic slice cultures are attractive models to investigate molecular mechanisms and functions, particularly for genetic knock-ins and knock-outs, key differences between human and mouse brains can impact the translational potential of experimental results [7,8]. Primary human neural cells are valuable resources, but their use is often restrained by access or methodological limitations. Advances in stem cell research have led to the development of organoids as in vitro models resembling human tissues in structure and complexity [4–6]. Cerebral organoids differentiated from induced pluripotent stem cells (iPSCs) show organized neurons and astrocytes in three-dimensions (3D) [9,10].

Nanostructures have been extensively studied in different cell lines and rodents [11], but a limited amount of data are available in human primary cells and organoids. Rodent models were valuable for the assessment of absorption, distribution, elimination and metabolism of nanomedicines. They clearly showed problems related to the entry of some nanostructures into the cerebral parenchyma due to the blood–brain barrier [12,13]. Studies in rodents also provided information on how nanostructures can be tuned in terms of size, shape and surface properties to facilitate brain entry. Similar studies are clearly not possible in humans and are rare in non-human primate models (e.g., Onpattro, Abraxane, BIND-014) [14–16]. Organoids therefore offer a valuable platform for the testing of organic and metallic nanostructures.

Among the nanostructures that have been studied in rodents, which showed pronounced intrinsic anti-inflammatory properties, is dendritic polyglycerol sulfate (dPGS) [17–21]. Their structures with terminal sulfate groups resemble that of heparan sulfate, which exerts anti-coagulant effects [17,22–24]. In contrast to heparan sulfate, dPGS shows primarily anti-inflammatory activity with relatively weak anti-coagulant effects that are size- and charge-dependent. Earlier studies indicated that dPGS can effectively reduce hyperactivity of microglia stimulated by danger-associated molecular patterns and lipopolysaccharide (LPS) in mice [18,19,25]. Microglia are the resident immune cells of the central nervous system and constantly survey their surroundings under physiological conditions [26–28]. Their morphology is altered and their phagocytic functions are elevated under many pathological conditions, making them attractive targets for nanotherapeutic interventions. Our previous studies showed that dPGS can modulate microglial activation in response to pathogen-associated molecular patterns and misfolded proteins (e.g., amyloid beta), thereby reducing losses in dendritic spine density of excitatory hippocampal neurons in mouse organotypic slice cultures [18,19,25]. These studies also showed that hyperactive microglia generate reactive astrocytes through the release of acute-phase cytokines such as interleukin-6, tumor necrosis factor alpha and lipocalin-2 (LCN2). However, the abundance and release of LCN2 in human neural cells has not yet been reported. We tested if dPGS can modulate LCN2 in a human cerebral organoid model.

Aside from establishing human cerebral organoids, we also used glioblastoma tumoroids to investigate the effectiveness of nanotherapeutics in the brain tumor microenvironment. Glioblastomas are mainly astrocytomas characterized by their infiltrative nature [29]. Microglia and normal astrocytes in the glioblastoma environment promote disease progression by secreting soluble factors (e.g., cytokines and growth factors) [30–32]. By combining reconstituted 3D models of glioblastoma (tumoroids) with organoids and modulating the activity of microglia with dPGS, we demonstrate that dPGS could be a powerful therapeutic agent that can reduce inflammatory markers and glioblastoma invasiveness.

2. Materials and Methods

2.1. Generation of Cerebral Organoids from Human iPSC

Procedures for culturing human iPSCs, embedding organoids in optimal cutting temperature (OCT) blocks, cryosectioning and immunostaining were all described previously [10]. The cell-line used was the NCRM1 iPSC line obtained from the National Institutes of Health. The method used to generate the 3D cerebral organoids was adapted from the protocol published by Lancaster and Knoblich [9]. Compositions of the different media are the same and reagents used are similar,

except for: DMEM-F12 (Gibco, Ottawa, ON, Canada), human embryonic stem cell (hESC) quality fetal bovine serum (FBS) (Wisent, St-Bruno, QC, Canada), MEM Non-Essential Amino Acids Solution (MEM-NEAA) (Multicell, Montreal, QC, Canada), 2-mercaptoethanol (Millipore Sigma, Oakville, ON, Canada), Y27632 Rho-associated protein kinase (ROCK) inhibitor (Selleckchem, Burlington, ON, Canada), N2 supplement (Gibco) and Penicillin-Streptomycin (Multicell).

For the generation and maintenance of embryoid bodies (EBs, days 0–11), we started from a 100 mm dish with iPSCs at 70% confluence with high quality (less than 10% differentiated cells). Cells were washed with DMEM-F12 and dissociated with Accutase to generate a suspension of single cells. Cells were gently resuspended in hESC media containing ROCK inhibitor [9], basic fibroblast growth factor (FGF-b) and plated at a density of 10,000 cells/well in a 96-well ultra-low attachment U-bottomed plate (Corning, Burlington, ON, Canada). Plates were centrifuged at 1200 rpm for 10 min and incubated at 37 °C, 5% CO_2 for 48 h. During day 2, a half media change was made, followed by a media change every other day up to day 11. Images of EBs were recorded with Evos XL Core Microscope (Thermo Fisher Scientific, Ottawa, ON, Canada) every 2 days during media changes to measure their diameter using the Image J software (U. S. National Institutes of Health, Bethesda, Maryland, USA). Once EBs had reached ≥ 350 µm in diameter, hESC media was switched to be without ROCK inhibitor and FGF-b [9]. When EBs were about 500–600 µm in diameter with smooth and bright edges, the media was switched to neuronal induction media (NIM). EBs were maintained in NIM for 4–5 days until the outer surface was optically translucent and ready to be embedded in Matrigel® (Corning) containing reduced growth factor droplets.

Matrigel® was thawed on ice. After media removal from each well containing the EBs, 30 µL of Matrigel® was added per well and incubated for 30 min at 37 °C. Next, 200 µL of final differentiation media without vitamin A [9] was added per well. Using a 1000 µL cut tip, the Matrigel®-embedded organoids were transferred into an uncoated 6-well ultra-low attachment plate (Corning) with 4 mL of final differentiation media without vitamin A per well. A maximum of five organoids were added and maintained per well to avoid fusion. Following transfer, plates were left for 48 h in stationary culture. After 48 h, media was changed to fresh final differentiation media without vitamin A, followed by a second 48 h incubation. Following the second media change, plates were transferred onto an orbital shaker set at 70 rpm (Scientific Industries Inc., Bohemia, NY, USA) housed in a 37 °C incubator. Media was changed every 3 days with fresh final differentiation media with vitamin A until the organoids were ready for analysis.

2.2. Immunofluorescence (IF) Staining in Organoids

Cerebral organoids were fixed with 4% paraformaldehyde (overnight at 4 °C), washed in phosphate-buffered saline (PBS, Multicell), dehydrated in 20% sucrose (1–3 days) and embedded in OCT Compound (Thermo Fisher Scientific). Blocks were kept at −80 °C until needed. For IF, samples were sectioned (20 µm) in a cryostat (Cryostar NX70, Thermo Fisher Scientific), air dried at room temperature (RT) and kept at −20 °C before IF staining. Cryosections were rehydrated in PBS (15 min) and permeabilized/blocked in blocking solution (1 h at room temperature, RT) containing: 0.2% Triton X-100 (Millipore Sigma), 0.05% bovine serum albumin and 5% normal donkey serum in PBS, before incubation (overnight at 4 °C) with primary antibodies. Antibodies used were as follows: mouse anti-Nestin (1:250, Developmental Studies Hybridoma Bank, Iowa City, IA, USA, rat-401), rabbit anti-SOX2 (1:500, Millipore, Oakville, ON, Canada, AB5603), chicken anti-MAP2 (1:1000, EnCor Biotechnology, Gainesville, FL, USA, CPCA-MAP2), rat anti-CTIP2 (1:500, Abcam, Toronto, ON, Canada, ab18465), rabbit anti-GFAP (1:250 Millipore, MAB144P), chicken anti-Beta III Tubulin (1:400, Millipore, AB9354), rabbit anti-Nestin (1:200, Abcam, ab92391) and rat anti-lipocalin-2 (1:500, R&D Systems, Toronto, ON, Canada, MAB1757). Sections were then washed in PBS (45 min) and incubated (1 h at RT) with secondary antibodies in blocking solution: goat anti-rat Dylight 488 (1:300, Abcam, ab96887), donkey anti-rabbit Dylight 594 (1:400, Abcam, ab96877), donkey anti-chicken Alexa 647 (1:500, Invitrogen, Ottawa, ON, Canada, A21447), donkey anti-mouse Dylight 550 (1:200, Abcam,

ab96876), goat anti-chicken Dylight 650 (1:200, Abcam, ab96950), donkey anti-rabbit Dylight 550 (1:200, Abcam, ab96892) and goat anti-rat Alexa Fluor 647 (1:500, Thermo Fisher Scientific, A21247). Sections were washed (45 min) with PBS and incubated (10 min at RT) with Hoechst 33342 (1:5000, Thermo Fischer Scientific) in PBS, washed in PBS (10 min) and mounted using Aqua-Poly/Mount (Polysciences Inc., Warrington, PA, USA). Samples were imaged on a Leica TCS SP8 confocal microscope (Leica, Richmond Hill, ON, Canada) at a 20× magnification.

2.3. Cell Culture

U251N human glioblastoma cells and HMC3 human microglia were originally obtained from the American Type Culture Collection. Unless otherwise indicated, cells were maintained in Dulbecco's Modified Eagle Medium (DMEM, Thermo Fisher Scientific) supplemented with 5% fetal bovine serum (FBS, Wisent) and 1% Penicillin-Streptomycin (Thermo Fisher Scientific). Primary human astrocytes were obtained from Dr. Jack Antel's lab and maintained in DMEM supplemented with 5% FBS and 1% Penicillin-Streptomycin. Primary astrocytes were kept at passages below five. Conditioned media was obtained from cell cultures maintained in the exponential growth phase and used fresh at 50% (*v*/*v*) in fresh media following centrifugation (3,000 rpm, 5 min) to remove cell debris. When used for the treatment of cerebral organoids, conditioned media was prepared using organoid media.

2.4. Time-Dependent dPG/dPGS Internalization in Organoids and Tumoroids

Human cerebral organoids were treated with dPG-Cy5 (1 μM) or dPGS-Cy5 (1 μM) for 1 h, 4 h or 24 h, then used for IF staining or direct imaging. For direct imaging, organoids were fixed in 4% paraformaldehyde overnight and nuclei were labeled with Hoechst 33342 (10 μM, overnight). Organoids were washed in PBS and imaged using a fluorescence microscope. Fluorescence was analyzed in ImageJ. Glioblastoma tumoroids were treated with dPG-Cy5 (1 μM) or dPGS-Cy5 (1 μM) for 24 h, then washed twice with PBS before imaging using a fluorescence microscope.

2.5. Western Blot

Western blot analysis followed published procedures [33]. In brief, organoids were washed twice in cold PBS, then were cut into small pieces using a razor blade and incubated in RIPA lysis buffer for 30 min on ice. Monolayer cells were washed twice with cold PBS, then incubated in RIPA lysis buffer for 30 min on ice. Lysates were vortexed for 10 sec every 10 min and lastly centrifuged for 30 min at 4 °C and 13,000 rpm. Lysates and media samples were separated by SDS-PAGE and blotted onto PVDF membranes (Bio-Rad, Mississauga, ON, Canada). Blocked membranes were probed with primary antibodies: rat anti-lipocalin-2 (1:500, R&D Systems, MAB1757), rabbit anti-NFκB p65 (1:1000, Abcam, ab16502), mouse anti-STAT3 (1:1000, Abcam, ab119352), mouse anti-β-actin (1:5000, Millipore Sigma, A5316) or mouse anti-alpha-tubulin (1:5000, Abcam, ab7291) overnight at 4 °C. Membranes were washed and incubated with secondary antibodies (goat anti-rat HRP, 1:1000, Thermo Fisher Scientific, 31470, goat anti-rabbit HRP, 1:1000, Bio-Rad, 1706515 and horse anti-mouse HRP, 1:5000, Cell Signaling, Burlington, ON, Canada, 7076S) for 1 h at RT. Membranes were washed and incubated with enhanced chemiluminescence substrate (Bio-Rad) for 5 min, signals were acquired with an Amersham 6000 imager (Amersham, Oakville, ON, Canada) or on film, and quantified in ImageJ.

2.6. Collagen Invasion Assay

U251N tumoroids and human astrocyte spheroids were prepared using the hanging drop method [34]. Briefly, drops of 5,000 cells in 30 μL medium were pipetted onto the inner side of a 100 mm Petri dish (Thermo Fisher Scientific) lid. The lid was quickly flipped to cover the Petri dish filled with 20 mL PBS. Hanging drops were cultured at 37 °C for 48 h to allow tumoroids and spheroids to form. Tumoroids and spheroids were then gently scooped into a medium-filled Petri dish coated with 2% agarose (dissolved in PBS) and cultured for 48 h. Tumoroids and spheroids were implanted in collagen gel (Advanced BioMatrix, San Diego, CA, USA), in the presence or absence of primary human

astrocytes (7,000 cells) and human HMC3 microglia (3,000 cells) dispersed in 200 µL gel. Gels were covered with 200 µL DMEM with or without treatment. Tumoroids and spheroids were imaged using light microscopy immediately after implantation (time = 0 day) and after 6 days. The average distance of cell outgrowth into the surrounding collagen was measured in ImageJ. For invasion assays of tumoroids into organoids, fluorescently-labeled tumoroids were prepared using U251N cells incubated with CellTracker Red (Thermo Fisher Scientific) following recommendations from the manufacturer. Tumoroids were placed in culture with organoids and observed to adhere after 24 h. Cultures were imaged using a fluorescence microscope over 6 days.

2.7. Immunocytochemistry

Cells were seeded at 5,000 cells/coverslip on glass coverslips (Merlan Scientific, Mississauga, ON, Canada) coated with poly-D-lysine (Millipore Sigma). Cells were cultured for 24 h (U251N and HMC3) or 48 h (primary human astrocytes) before treatment. Following treatment, cells were fixed in 4% paraformaldehyde (10 min), permeabilized with 0.1% Triton X-100 (10 min), blocked in 10% goat serum in PBS (Gibco) for 1 h and incubated with primary antibodies overnight at 4 °C: rabbit anti-GFAP (1:500, Abcam, ab7260), mouse anti-Lamp1 (1:500, Developmental Studies Hybridoma Bank, H4A3-c), rat anti-lipocalin-2 (1:500, R&D Systems, MAB1757), rabbit anti-NFkB p65 (1:500, Abcam, ab16502) or rabbit anti-phospho-STAT3 Y705 (1:500, Abcam, ab76315). Cells were washed in PBS three times and incubated with secondary antibodies for 1 h at RT: goat anti-rabbit Alexa Fluor 488 (1:1000, Thermo Fisher, Mississauga, ON, Canada, A27034), goat anti-rat Alexa Fluor 647 (1:500, Thermo Fisher, A21247) or goat anti-mouse Alexa Fluor 488 (1:1000, Thermo Fisher, A28175). Cells were washed with PBS and nuclei were labeled with Hoechst 33342 (10 µM, 10 min). After three more washings with PBS, coverslips were mounted on microscope slides (Diamed, Mississauga, ON, Canada) using Aqua-Poly/Mount. Samples were imaged using a fluorescence microscope (Leica DMI4000B, Leica) and intracellular fluorescence was analyzed in ImageJ. The nuclear and/or cytoplasmic fluorescence of NFκB, LCN2 and phosphor-STAT3 for each cell was measured and normalized to the nuclear or cytoplasmic area. The background fluorescence was subtracted.

2.8. Immunohistochemistry

Immunohistochemistry was performed as previously published [33]. In brief, human brain sections were dewaxed in xylene and rehydrated in ethanol. Antigen retrieval was performed in citrate buffer. Following blocking, samples were incubated with primary antibodies: rat anti-lipocalin-2 (1:500, R&D Systems, MAB1757), mouse anti-IBA1 (1:300, Invitrogen, MA5-27726) or rabbit anti-GFAP (1:250 Millipore, MAB144P) overnight at 4 °C. Samples were washed and incubated with secondary antibodies: goat anti-rat Alexa Fluor 647 (1:500, Thermo Fisher Scientific, A21247), goat anti-mouse Alexa Fluor 647 (1:300, Thermo Fisher Scientific, A28181) or goat anti-rabbit Alexa Fluor 488 (1:500, Thermo Fisher, A27034) for 1 h at RT. Nuclei were labeled with DAPI (1 µg/mL, 5 min, Molecular Probes, Ottawa, ON, Canada) and samples were mounted on microscope slides using Dako mounting medium (Dako, Burlington, ON, Canada). Samples were imaged using a fluorescence microscope. The samples were harvested under a protocol approved by the Montreal Neurological Hospital's research ethics board (NEU-10-066). Consent was given by all patients and controls (aged 55–76). Tissues were from the cerebral cortex.

2.9. Lipid Droplet Imaging

Cells seeded on glass coverslips at 5,000 cells/coverslip were cultured for 24 h before treatment. Following treatment, cells were washed twice with PBS and fixed in 4% paraformaldehyde (10 min). Cells were washed with PBS and incubated with BODIPY 493/503 (10 µM, Thermo Fisher) and Hoechst 33342 (10 µM) for 10 min. Cells were washed with PBS four times, then mounted on microscope slides using EverBrite (Biotium, Burlington, ON, Canada). Samples were imaged using a fluorescence microscope.

2.10. MTT Assay

Following treatment, organoids were washed in PBS twice and incubated in fresh media in the presence of 3-(4,5-dimethylthiazol-2-yl)-2,5-diphenyltetrazolium bromide (MTT) (0.5 mg/mL, Millipore Sigma) for 1 h at 37 °C. The media was removed, and cells were lysed in 500 µL dimethyl sulfoxide (Santa Cruz, Dallas, TX, USA). Samples were measured at 595 nm in triplicate using a microplate reader (Spark 10M, Tecan, Männedorf, Switzerland). Measurements were normalized to the organoid weight.

2.11. Statistics

Statistical significance was determined using one-way ANOVA followed by the Student's *t*-test. *p*-values lesser than 0.05 were deemed significant. The Bonferroni correction was applied for multiple comparisons.

3. Results

3.1. dPGS Are Internalized in 3D Cerebral Organoids

Human cerebral organoids were generated from human iPSCs according to an established protocol [9]. A timeline of organoid formation and biomarkers used to delineate dynamic linage progression is illustrated in Figure S1. We used these organoids after a 100-day maturation to test dendritic polyglycerol sulfate (dPGS) as a model nanostructure with anti-inflammatory properties in human neural cells, as well as other types of emerging nanostructures with biomedical applications, such as metallic gold nanoclusters [35–39]. Gold nanoclusters have been shown to affect cellular stress and organellar function thanks to their unique physicochemical properties, but little work has been done in human neural cells. The nanostructures were screened for cytotoxic effects (Figure 1a and Figure S2) and results showed that they can be studied in human neural cells without jeopardizing the viability of the organoid cultures. This provides the basis for further investigations on nanomedical applications in a translationally-relevant model. The first step was to show if dPGS was internalized by neural cells within the organoids themselves. To this end, we treated organoids with fluorescently (Cy5)-labeled dPGS (Figure 1). Time-course experiments showed that dPGS-Cy5 was internalized within 1 h (12.8 ± 2.2 SEM fold increase over baseline fluorescence), then progressively more over 24 h (64.5 ± 11.4 SEM fold increase) (Figure 1b,c). Compared to dPGS, internalization of the non-sulfated dendritic polyglycerol (dPG) was low (8.7 ± 2.1 SEM fold increase after 24 h) (Figure 1b,c), underlining the important role of the terminal sulfate groups for cell internalization. In the current study, we showed that GFAP-labeled astrocytes within the outermost layer (200–300 µm) of the cerebral organoids contain abundant amounts of dPGS (Figure 1d).

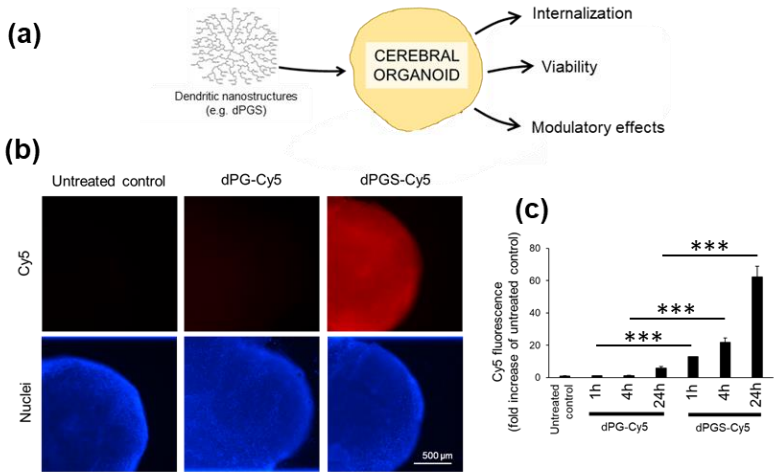

Figure 1. *Cont.*

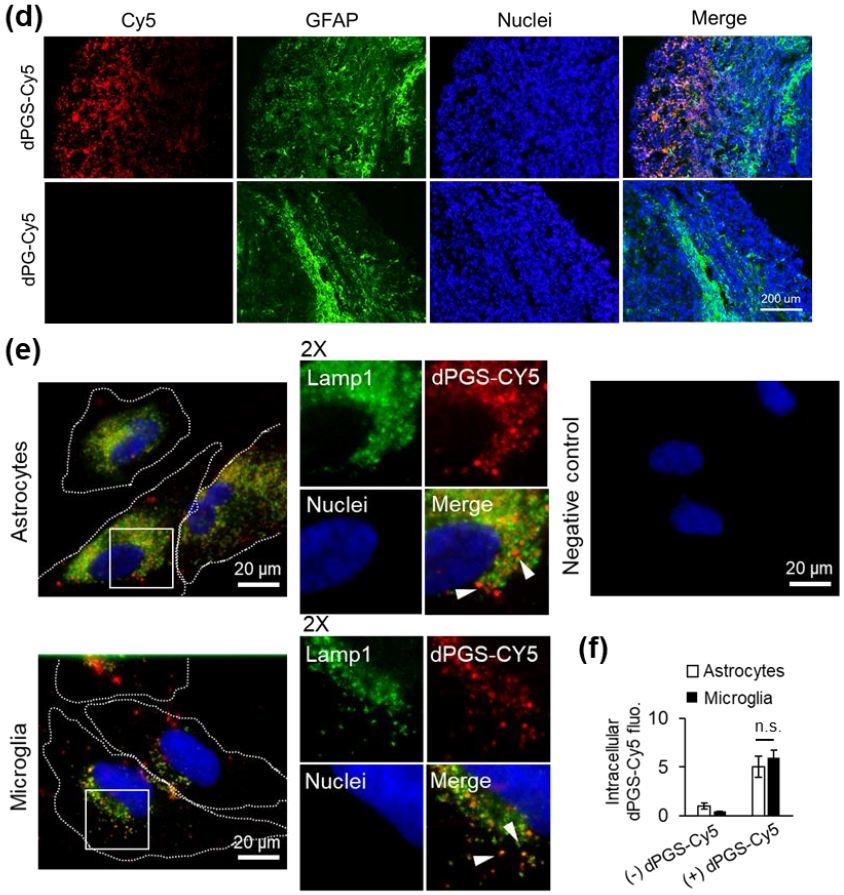

Figure 1. (**a**) Schematic representation of cerebral organoid usage for nanostructure screening. (**b**) Human cerebral organoids were treated with dendritic polyglycerol (dPG)-Cy5 (1 µM) or dendritic polyglycerol sulfate (dPGS)-Cy5 (1 µM) for 1 h, 4 h or 24 h. Nuclei were labeled with Hoechst 33342. Organoids were imaged using a fluorescence microscope. (**c**) Cy5 fluorescence in organoids was analyzed in ImageJ. Shown are the average fluorescence per condition ± SEM. At least 90 organoids were analyzed from three independent experiments. *** $p < 0.001$ (**d**) Fluorescence micrographs of human cerebral organoids treated with dPG-Cy5 (1 µM) or dPGS-Cy5 (1 µM) for 24 h and labeled for glial fibrillary acidic protein (GFAP). Nuclei were labeled with Hoechst 33342. (**e**) Primary human astrocytes and human HMC3 microglia internalization of dPGS-Cy5 (1 µM) after 24 h. dPGS-Cy5 (red) is partially co-localized with Lamp1-labeled lysosomal compartments (green). The negative control was prepared in the absence of dPGS-Cy5 and primary antibody to account for background fluorescence. Nuclei were labeled with Hoechst 33342 (blue). Cells were imaged using a fluorescence microscope. (**f**) Shown are the average intracellular Cy5 fluorescence per cell expressed as fold change from untreated cells ± SD. At least 90 cells were analyzed in two independent experiments. n.s. Non-significant.

3.2. dPGS Internalization in Human Microglia and Normal Astrocytes

Given the importance of glial cells in regulating inflammatory processes in the brain, we further studied the intracellular effects of dPGS in astrocytes and particularly microglia, which are absent from the cerebral organoids. We established in cell monolayer cultures that human microglia and astrocytes internalized comparable amounts of dPGS within 24 h of treatment (Figure 1e,f). Fluorescence imaging at the single cell level showed that dPGS-Cy5 accumulated in the perinuclear area (Figure 1e), and was partially co-localized with lysosomal compartments labeled with Lamp1 [40]. Given that microglia activated by pro-inflammagens (e.g., LPS) are associated with increased sequestration of neutral lipids into lipid droplets (LDs) [41,42] (Figure S3b), we investigated if dPGS could have modulatory effects on lysosomes, which interact with LDs through lipophagy and other processes [43,44]. This was

suggested by changes in lysosomal positioning, with an increase in perinuclear lysosomes (Figure S3a). In turn, treatment with dPGS prevented LPS-induced lipid droplet accumulation (Figure S3b).

3.3. dPGS Reduced Microglia-Stimulated Lipocalin-2 in Cerebral Organoid Models

Considering the importance of microglia-astrocyte crosstalk in rodent [19] and human neural cells [1,3], we measured LCN2 abundance in human neural cells in response to LPS, a prototypical pro-inflammagen whose levels are exacerbated in endotoxemia and sepsis. The presence of microglia is required to stimulate the synthesis of LCN2 in the neural cells, as levels in response to LPS remained comparable to that of the untreated control in the absence of microglia from the organoids (Figure 2a,b and Figure S4). In turn, conditioned media from LPS-stimulated microglia induced a significant increase in intracellular and extracellular LCN2 in the cerebral organoid cultures (Figure 2c–e), confirming that this upregulation is microglia-dependent in human neural cells. Given that astrocytes play a significant role in inflammatory processes in the brain, we investigated if there was increased LCN2 abundance in these cells in response to microglia activation. Similarly to the results from cerebral organoids, direct stimulation of astrocytes with LPS did not have a significant effect (Figure 2f). In contrast, treatment with conditioned media from LPS-activated microglia increased LCN2 abundance, whereas the presence of dPGS returned LCN2 abundance to control levels (Figure 2f). dPGS alone and conditioned media from resting microglia did not have significant effects (Figure 2d–f). Finally, to show that dPGS is not cytotoxic to human neural cells, we measured mitochondrial metabolic activity using the MTT assay. Results from these studies showed that neither dPGS nor dPG affected mitochondrial metabolic activity in 3D organoids for up to 72 h (Figure S2). Our earlier studies indicated that in rodent cells, concentrations of dPGS up to 100 µM did not cause any notable cytotoxicity [18]. These results encouraged us to investigate dPGS as a microglia modulator and indirect suppressor of glioblastoma invasiveness.

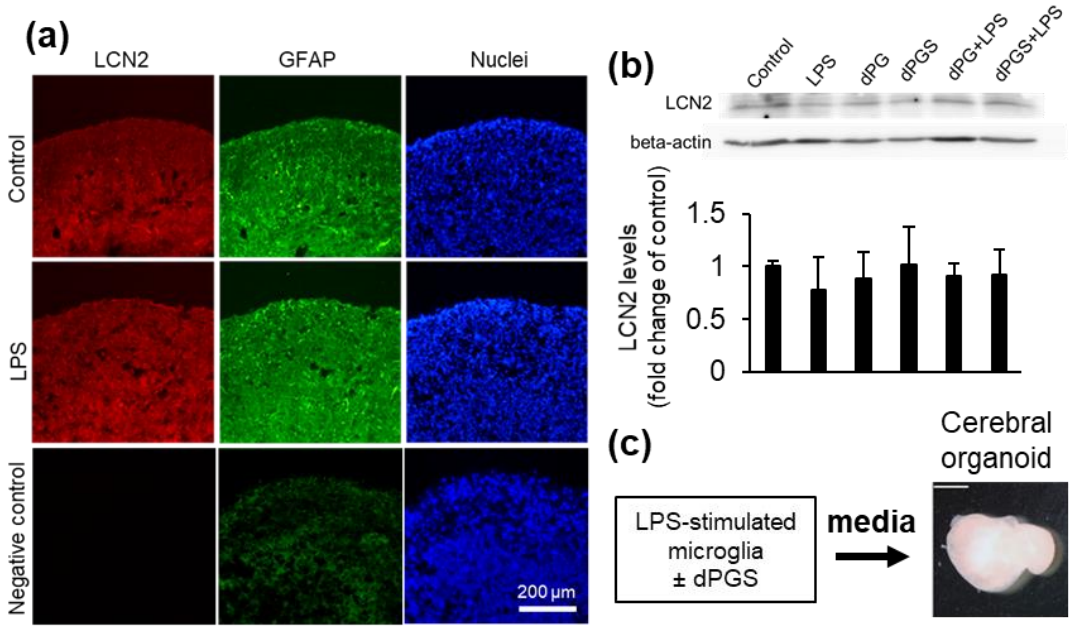

Figure 2. *Cont.*

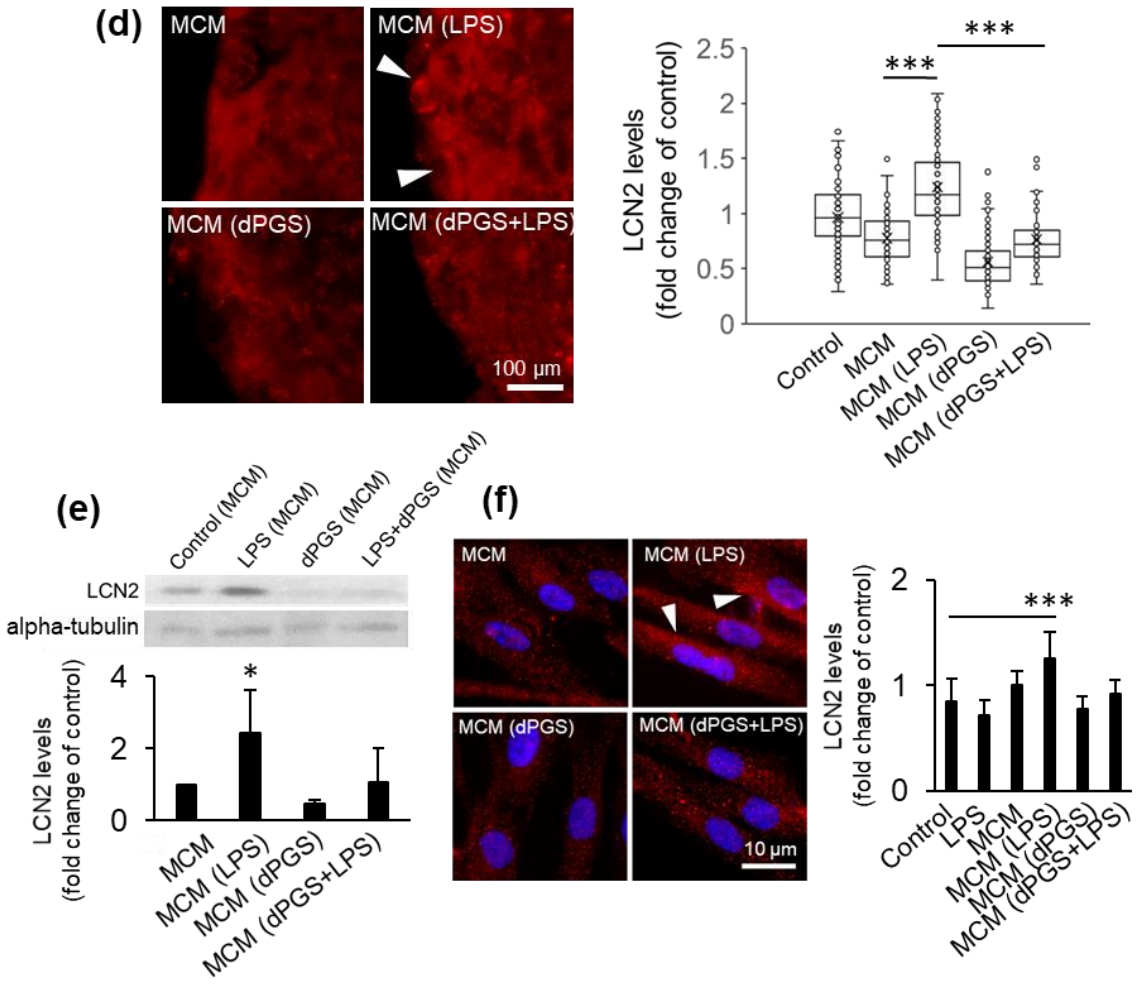

Figure 2. Lipocalin-2 levels in human cerebral organoids. (**a**) Micrographs of lipocalin-2 (LCN2) detected by immunofluorescence in organoid cryosections following treatment with LPS (10 ng/mL) for 24 h. Astrocytes were labeled with GFAP and nuclei with Hoechst 33342. The negative control was prepared in the absence of primary antibodies to account for background fluorescence. Samples were imaged using a fluorescence microscope. (**b**) LCN2 levels in organoids treated with lipopolysaccharide (LPS) (10 ng/mL) with or without dPG (1 µM) and dPGS (1 µM) for 24 h and measured by Western blot, with beta-actin as loading control. Quantification shown are the average intracellular LCN2 levels ±SD in organoids based on immunofluorescence images shown in (**a**). A total of 27 samples were analyzed from three independent experiments. (**c**) Schematic representation of media conditioning from microglia used for cerebral organoid treatment. (**d**) Representative fluorescence micrographs of intracellular LCN2 levels in organoids treated with conditioned media from microglia (MCM) treated with LPS (10 ng/mL), dPGS (1 µM) for 24 h. Quantifications show the average and single-cell levels of LCN2 fluorescence in cryosections. A total of 1017 cells were analyzed from independent experiments. *** $p < 0.001$ (**e**) LCN2 levels from organoids treated as in (**d**) and measured by Western blot, with alpha-tubulin as loading control. Shown are the average LCN2 levels from two independent experiments. * $p < 0.05$ (**f**) Fluorescence micrographs of LCN2 abundance in primary human astrocytes treated as in (**d**) and measured using immunocytochemistry. Shown are the average intracellular LCN2 levels in astrocytes as fold increase of the untreated control. A total of 477 cells from two independent experiments were analyzed. *** $p < 0.001$.

3.4. Microglia and dPGS Modulate Glioblastoma Invasiveness

Glioblastoma multiforme is an aggressive brain tumor of astrocytic origin for which complete resection is often impossible due to its invasive nature [29,45]. To model the impact of microglia and astrocytes on glioblastoma invasiveness, we designed a 3D invasion assay examining the propensity

of the cancer cells to migrate into the surrounding collagen matrix. Human microglia and primary human astrocytes were embedded into the collagen matrix, wherein a tumoroid was then implanted (Figure 3a). Over time, the normal neural cells extend processes while cancer cells migrate radially from the tumoroid. Glioblastoma outgrowth from the tumoroid into the surrounding collagen was facilitated by the presence of microglia and astrocytes (Figure 3a,b), an effect replicated using microglia-conditioned media and inhibited by dPGS (Figure 3c,d). This indicates that neural cells secrete factors (extracellular matrix degradation enzymes, cytokines, growth factors) that can stimulate tumor invasiveness [46–48]. In contrast, tumoroids grown in isolation or within cerebral organoids in the absence of microglia had comparatively less outgrowth over time (Figure 3a,b and Figure S5), and normal human astrocytes migrated in a scattered pattern without radial outgrowth (Figure S6).

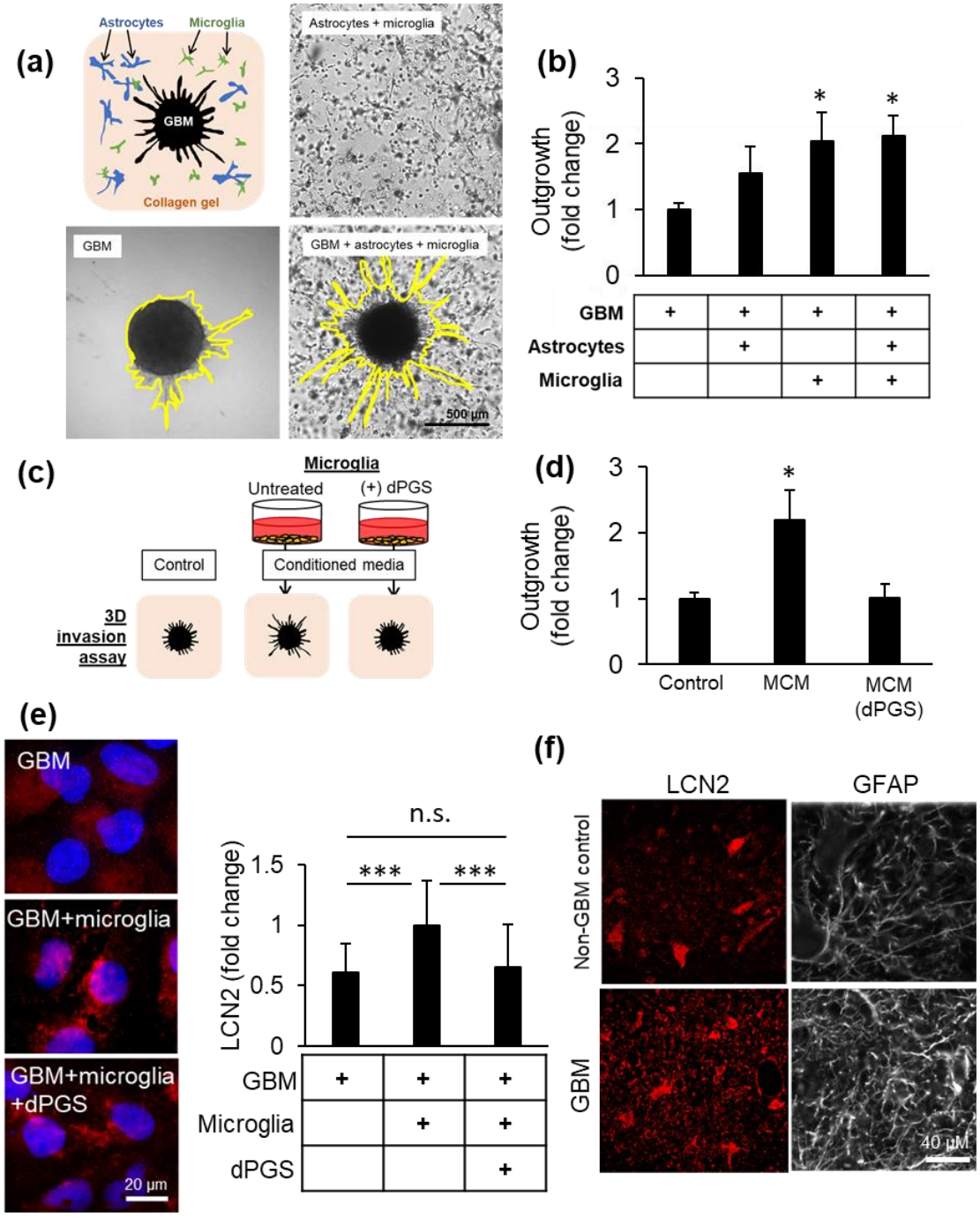

Figure 3. *Cont.*

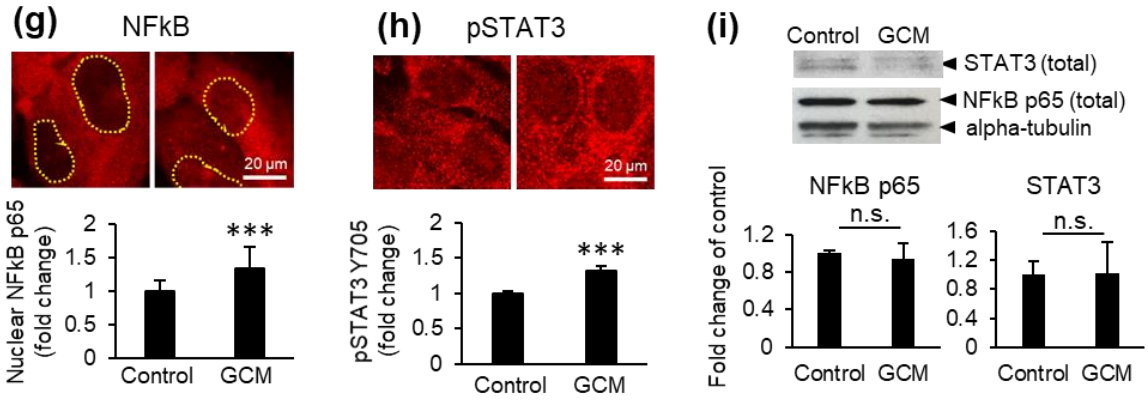

Figure 3. Glioblastoma (GBM) invasiveness in 3D co-cultures. (**a**) Collagen gels were seeded with human primary astrocytes and human HMC3 microglia in the presence or absence of a glioblastoma tumoroid. (**b**) Glioblastoma invasiveness in the presence or absence of microglia and astrocytes in 3D co-cultures after 6 days. Shown are the average distance of outgrowth from the tumoroid as a fold change of the tumoroid monoculture ±SEM. A total of 32 tumoroids were tested from at least three independent experiments. * $p < 0.05$ (**c**) Schematic representation of microglial conditioned media (MCM) used to treat collagen-embedded tumoroids. (**d**) Glioblastoma tumoroid outgrowth in the presence of conditioned media from microglia treated or not with dPGS (1 µM) after 6 days ±SEM. A total of 29 tumoroids were tested from at least four independent experiments. * $p < 0.05$ (**e**) Representative fluorescence micrographs showing intracellular LCN2 (red) in glioblastoma cells in the presence or absence of microglia cells in direct co-culture and dPGS (1 µM) for 24 h. LCN2 was fluorescently immunolabeled and cells were imaged using a fluorescence microscope. Quantifications show the average intracellular LCN2 levels ± SD per cell. At least 500 cells were analyzed from five independent experiments. *** $p < 0.001$; n.s. Non-significant. (**f**) Fluorescence micrographs of LCN2 (red) and GFAP (white) in human brain sections from non-cancerous brain or glioblastoma tumor tissues. LCN2 and GFAP were fluorescently labeled by immunohistochemistry and imaged using a fluorescence microscope. (**g,h**) Activation of transcription factors NFκB and STAT3 in microglia in response to glioblastoma secreted factors. Human HMC3 microglia were treated with glioblastoma conditioned media (GCM) for 24 h, after which NFκB p65 and phosphorylated STAT3 Tyr705 were fluorescently immunolabeled (red) and cells were imaged using a fluorescence microscope. Shown are (g) the average nuclear NFκB p65 level per cell ± SEM (237 cells from three independent experiments) and (h) the average pSTAT3 Y705 level per cell ± SEM (317 cells from three independent experiments) *** $p < 0.001$. (**i**) Total NFκB p65 and STAT3 protein abundance in microglia treated as in (g,h). Protein levels were determined by measurements of immunopositive bands in Western blots. Alpha-tubulin was used as loading control. Shown are the average protein abundance of NFκB p65 and STAT3 from three independent experiments. n.s. Non-significant.

To characterize the effects of glioblastoma on its surrounding immune cells, glioblastoma cells were directly co-cultured with microglia cells and showed significantly higher LCN2 levels compared to glioblastoma cells in monoculture (Figure 3e). High LCN2 and GFAP levels were also observed in tumor tissues from glioblastoma patients as compared to control brain tissues (Figure 3f). To investigate the mechanism behind LCN2 upregulation, microglia were stimulated with glioblastoma-conditioned media. This resulted in increased nuclear NFκB and STAT3 phosphorylation, two key transcription factors for immune activation (Figure 3g,h) that are also hyperactivated in glioblastoma. The protein levels of total NFκB and STAT3 in the cells remained comparable to the control (Figure 3i).

On the other hand, dPGS was internalized into glioblastoma tumoroids (Figure S7) and decreased LCN2 levels in glioblastoma cells in vitro (Figure 3e). This demonstrates proof of concept for using dPGS as a modulator of the tumor microenvironment (Figure 4).

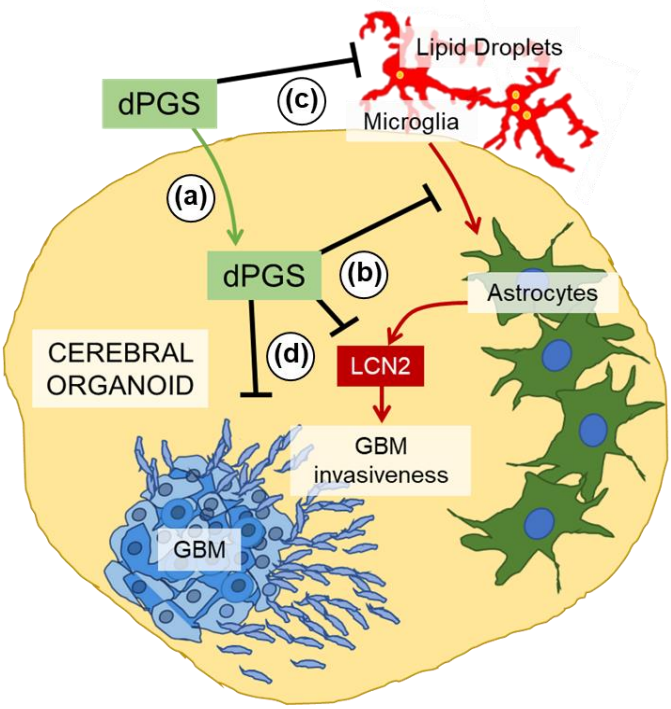

Figure 4. Schematic representation of the proposed modulatory effects of dPGS on microglia, astrocyte and glioblastoma crosstalk. (**a**) dPGS is internalized in cerebral organoids, and (**b**) downregulates LCN2 produced by microglia-induced astrocytes, thereby (**c**) reducing markers of inflammation (e.g., lipid droplets) and (**d**) glioblastoma invasiveness.

4. Discussion

The key question addressed in this study is: can dendritic polyglycerol sulfates with intrinsic anti-inflammatory properties reduce inflammatory markers in cerebral organoids and glioblastoma invasiveness by modulating microglia activity? Mechanistic studies in 3D human neural cultures with new drugs or nanostructures are sparse due to the limited availability of neural tissues. To overcome such a problem, several protocols have been developed for the generation of 3D cerebral organoids and other types of organoids [4,5,7,9]. Human cerebral organoids derived from iPSCs showing properties of different neural cell types are valuable models to study the interactions and effects of nanostructures in 3D. One of the most advanced organoids containing vasculature resembling that of the brain was recently proposed to investigate physiology and pathological changes in neurological disorders [49]. Although our organoids are not as complex as Cakir's, we took advantage of cerebral organoids to reveal how microglia exposed to the pro-inflammagen LPS and the dendritic nanostructure dPGS affect astrocyte reactivity. We show clear anti-inflammatory effects from dPGS and provide the first evidence for this in human brain cells. There are still several limitations to overcome: (1) the integration of resident and peripheral immune cells recruited chemotactically and (2) the contribution of endothelial cells in vasculature as part of the blood–brain barrier.

Our results in organoid cultures showed that the presence of sulfate groups on dPGS was critical for the internalization of nanostructures, as it allowed binding to selectin receptors [17,19,22]. Intracellular changes associated with dPGS included an increase in perinuclear lysosomes, which typically have lower luminal pH and increased degradation activity [44,50], functions often impaired in aging and neurodegenerative diseases. This is interesting given the role of lysosomes in processing LDs, which are upregulated in inflammation and cancer [41,42]. LDs are promiscuous organelles: depending on the cell type, cellular context and their intracellular location, they can play a protective role or become damaging to neural and other cells if peroxidized lipids are released. In aggressive tumors (e.g., glioblastoma and breast), they provide energy for cancer cells to thrive and can sequester lipophilic anticancer

agents, reducing the rate at which they reach their desirable targets [51–53]. Their numbers are highly upregulated in glioblastoma compared to normal astrocytes (Figure S3c,d), and their inhibition was shown to enhance the effectiveness of pharmacological agents [51].

As now shown in human neural cells, LCN2 can be produced by microglia-stimulated astrocytes. Microglia themselves are not significant contributors to LCN2 upregulation due to the LCN2 gene being suppressed by SRSF3 [54]. Instead, they secrete other cytokines (e.g., IL-6, TNFα) and alarmins under pro-inflammatory conditions that can activate astrocytes and other neural cells [54,55]. Several of these were shown to bind heparan sulfate [23,56], suggesting that dPGS prevented microglia-mediated LCN2 production by blocking some soluble factors and preventing downstream signaling (Figure 2d,e). One of the candidate cytokines is interleukin-6 released from microglia, to which dPGS was shown to bind in our earlier studies using surface plasmon resonance [19].

Cytokines and alarmins play key roles in the tumor microenvironment [57–61]. The cancer cells secrete factors that actively recruit microglia and peripheral macrophages to the tumor site. In turn, these immune cells produce cytokine and growth factors that can promote cancer progression [32]. In this context, microglia-astrocyte crosstalk forms a positive feedback loop that maintains an unfavorable tumor microenvironment [30,62]. LCN2 is an acute-phase protein with emerging roles in the brain and in cancer. It was shown to complex with and enhance the activity of metalloproteinase-9, a protease secreted by cancer cells that breaks down the extracellular matrix and promotes invasiveness [63,64]. This is significant given that dPGS can downregulate LCN2 in neural cells and decrease glioblastoma invasiveness. dPGS can bind P-selectin, which is expressed in the tumor endothelium and in glioblastoma cells [65]. As dPGS can also serve as a nanocarrier, it has the potential to deliver anti-cancer agents [65,66]. Nanocarriers such as functionalized dendrimers for siRNA and drug delivery [67–69] merit testing in human organoid models to reveal how combination therapy could affect interplay between cancer cells and the tumor microenvironment. The modulatory effect of dPGS on organelles could impact glioblastoma cells in several ways: (1) the increase in perinuclear lysosomes could decrease lysosomal exocytosis and the release of extracellular matrix-degrading enzymes (e.g., cathepsins) [70,71], (2) a reduction in lipid droplet size and number [72] is an indicator of reduced microglia hyperactivity, thus fewer cytokines and trophic factors contributing to glioblastoma invasiveness and (3) a decrease in lipid droplets prevents the sequestration of lipophilic anti-cancer agents, allowing them to reach their intracellular targets (e.g., curcumin) [51].

5. Conclusions

Our results show that dPGS is an attractive candidate as an anti-inflammatory polyglycerol dendrimer able to modulate human microglia-astrocyte crosstalk. This dendrimer regulated lipocalin 2 abundance in human neural organoids. In the context of inflammation associated with glioblastoma multiforme, dPGS limited glioblastoma invasiveness by modulating microglial activation. Overall, these studies propose the evaluation of well-defined nanostructures in well-characterized human organoids and co-cultures. Cerebral organoids merit further studies as complementary 3D models in nanoscience, but they require rigorous characterization and application of standardized procedures to be widely used [73]. Such three-dimensional systems together with co-cultures and in vivo experiments will provide a valuable evaluation platform for the internalization, cytotoxicity and modulatory effects of nanotherapeutics in human neural cells.

Supplementary Materials: The following are available online at http://www.mdpi.com/2073-4409/9/11/2434/s1, Figure S1: Maturation and characterization of cerebral organoids, Figure S2: Mitochondrial metabolic activity in cerebral organoids following treatment with nanostructures, Figure S3: Changes in lysosomes and lipid droplets in activated microglia, Figure S4: Absence of microglia in the cerebral organoids, Figure S5: Glioblastoma tumoroid invasiveness in cerebral organoids, Figure S6: Movement of normal human astrocytes in 3D culture, Figure S7: Internalization of fluorescent dPGS-Cy5 in glioblastoma tumoroids.

Author Contributions: Conceptualization, D.M. and T.M.D.; investigation, I.Z., P.L., C.H., M.L.-A. and C.X.-Q.C.; writing—original draft preparation, I.Z.; writing—review and editing, I.Z., D.M., T.M.D., R.H., P.L., C.H., M.L.-A. and C.X.-Q.C.; supervision, D.M. and T.M.D.; funding acquisition, D.M. and T.M.D. All authors have read and agreed to the published version of the manuscript.

Funding: This research was funded by Canadian Institutes of Health Research, grant number MOP-119425, and Natural Sciences and Engineering Research Council of Canada, grant number RGPIN 2020-07011.

Acknowledgments: The authors would like to thank Nadine Rades for kindly providing dPG and dPGS nanostructures, Jack Antel for primary human astrocytes, Kevin Petrecca for human brain sections and Rodolphe Antoine for gold nanoclusters. T.M. Durcan and the EDDU acknowledge that funding for the generation of 3D cerebral organoids is through the Sebastian and Ghislaine Van Berkom Foundation, the Alain and Sandra Bouchard Foundation and the McGill Healthy Brains for Healthy Lives.

Conflicts of Interest: The authors declare no conflict of interest. The funders had no role in the design of the study; in the collection, analyses or interpretation of data; in the writing of the manuscript, or in the decision to publish the results.

References

1. Paolicelli, R.C.; Bergamini, G.; Rajendran, L. Cell-to-cell Communication by Extracellular Vesicles: Focus on Microglia. *Neuroscience* **2019**, *405*, 148–157. [CrossRef]
2. Simon, E.; Obst, J.; Gomez-Nicola, D. The Evolving Dialogue of Microglia and Neurons in Alzheimer's Disease: Microglia as Necessary Transducers of Pathology. *Neuroscience* **2019**, *405*, 24–34. [CrossRef]
3. Pósfai, B.; Cserép, C.; Orsolits, B.; Dénes, Á. New Insights into Microglia–Neuron Interactions: A Neuron's Perspective. *Neuroscience* **2019**, *405*, 103–117. [CrossRef]
4. Rossi, G.; Manfrin, A.; Lutolf, M.P. Progress and potential in organoid research. *Nat. Rev. Genet.* **2018**, *19*, 671–687. [CrossRef]
5. Li, M.; Izpisua Belmonte, J.C. Organoids—Preclinical Models of Human Disease. *N. Engl. J. Med.* **2019**, *380*, 569–579. [CrossRef] [PubMed]
6. Takebe, T.; Wells, J.M. Organoids by design. *Science* **2019**, *364*, 956–959. [CrossRef] [PubMed]
7. Marshall, J.J.; Mason, J.O. Mouse vs man: Organoid models of brain development & disease. *Brain Res.* **2019**, *1724*, 146427. [CrossRef] [PubMed]
8. Breschi, A.; Gingeras, T.R.; Guigó, R. Comparative transcriptomics in human and mouse. *Nat. Rev. Genet.* **2017**, *18*, 425–440. [CrossRef]
9. Lancaster, M.A.; Knoblich, J.A. Generation of cerebral organoids from human pluripotent stem cells. *Nat. Protoc.* **2014**, *9*, 2329–2340. [CrossRef] [PubMed]
10. Chen, X.; Rocha, C.; Rao, T.; Durcan, T.M. NeuroEDDU protocols_iPSC culture. *Zenodo* **2019**. [CrossRef]
11. Ioannidis, J.P.A.; Kim, B.Y.S.; Trounson, A. How to design preclinical studies in nanomedicine and cell therapy to maximize the prospects of clinical translation. *Nat. Biomed. Eng.* **2018**, *2*, 797–809. [CrossRef]
12. Aparicio-Blanco, J.; Martín-Sabroso, C.; Torres-Suárez, A.-I. In vitro screening of nanomedicines through the blood brain barrier: A critical review. *Biomaterials* **2016**, *103*, 229–255. [CrossRef]
13. Jackson, S.; Meeks, C.; Vézina, A.; Robey, R.W.; Tanner, K.; Gottesman, M.M. Model systems for studying the blood-brain barrier: Applications and challenges. *Biomaterials* **2019**, *214*, 119217. [CrossRef]
14. Akinc, A.; Maier, M.A.; Manoharan, M.; Fitzgerald, K.; Jayaraman, M.; Barros, S.; Ansell, S.; Du, X.; Hope, M.J.; Madden, T.D.; et al. The Onpattro story and the clinical translation of nanomedicines containing nucleic acid-based drugs. *Nat. Nanotechnol.* **2019**, *14*, 1084–1087. [CrossRef] [PubMed]
15. Havel, H.; Finch, G.; Strode, P.; Wolfgang, M.; Zale, S.; Bobe, I.; Youssoufian, H.; Peterson, M.; Liu, M. Nanomedicines: From Bench to Bedside and Beyond. *AAPS J.* **2016**, *18*, 1373–1378. [CrossRef]
16. Hrkach, J.; Hoff, D.V.; Ali, M.M.; Andrianova, E.; Auer, J.; Campbell, T.; Witt, D.D.; Figa, M.; Figueiredo, M.; Horhota, A.; et al. Preclinical Development and Clinical Translation of a PSMA-Targeted Docetaxel Nanoparticle with a Differentiated Pharmacological Profile. *Sci. Transl. Med.* **2012**, *4*, 128ra39. [CrossRef]
17. Rades, N.; Licha, K.; Haag, R. Dendritic Polyglycerol Sulfate for Therapy and Diagnostics. *Polymers (Basel)* **2018**, *10*, 595. [CrossRef]
18. Maysinger, D.; Groger, D.; Lake, A.; Licha, K.; Weinhart, M.; Chang, P.K.-Y.; Mulvey, R.; Haag, R.; McKinney, R.A. Dendritic Polyglycerol Sulfate Inhibits Microglial Activation and Reduces Hippocampal CA1 Dendritic Spine Morphology Deficits. *Biomacromolecules* **2015**, *16*, 3073–3082. [CrossRef]

19. Maysinger, D.; Lalancette-Hébert, M.; Ji, J.; Jabbour, K.; Dernedde, J.; Silberreis, K.; Haag, R.; Kriz, J. Dendritic polyglycerols are modulators of microglia-astrocyte crosstalk. *Future Neurol.* **2019**, *14*, FNL31. [CrossRef]
20. Budde, H.; Sorns, M.-S.; Welker, P.; Licha, K.; Wolff, H.; Riggert, J.; Wulf, G.; Legler, T.J. Dendritic polyglycerol sulfate attenuates murine graft-versus-host disease. *Ann. Hematol.* **2016**, *95*, 465–472. [CrossRef]
21. Xu, X.; Ballauff, M. Interaction of Lysozyme with a Dendritic Polyelectrolyte: Quantitative Analysis of the Free Energy of Binding and Comparison to Molecular Dynamics Simulations. *J. Phys. Chem. B* **2019**, *123*, 8222–8231. [CrossRef]
22. Dernedde, J.; Rausch, A.; Weinhart, M.; Enders, S.; Tauber, R.; Licha, K.; Schirner, M.; Zügel, U.; von Bonin, A.; Haag, R. Dendritic polyglycerol sulfates as multivalent inhibitors of inflammation. *PNAS* **2010**, *107*, 19679–19684. [CrossRef]
23. Parish, C.R. The role of heparan sulphate in inflammation. *Nat. Rev. Immunol.* **2006**, *6*, 633–643. [CrossRef]
24. Türk, H.; Haag, R.; Alban, S. Dendritic Polyglycerol Sulfates as New Heparin Analogues and Potent Inhibitors of the Complement System. *Bioconjugate Chem.* **2004**, *15*, 162–167. [CrossRef] [PubMed]
25. Maysinger, D.; Ji, J.; Moquin, A.; Hossain, S.; Hancock, M.A.; Zhang, I.; Chang, P.K.Y.; Rigby, M.; Anthonisen, M.; Grutter, P.; et al. Dendritic Polyglycerol Sulfates in the Prevention of Synaptic Loss and Mechanism of Action on Glia. *ACS Chem. Neurosci.* **2018**, *9*, 260–271. [CrossRef]
26. Prinz, M.; Jung, S.; Priller, J. Microglia Biology: One Century of Evolving Concepts. *Cell* **2019**, *179*, 292–311. [CrossRef] [PubMed]
27. Masuda, T.; Sankowski, R.; Staszewski, O.; Prinz, M. Microglia Heterogeneity in the Single-Cell Era. *Cell Rep.* **2020**, *30*, 1271–1281. [CrossRef]
28. Rodríguez-Gómez, J.A.; Kavanagh, E.; Engskog-Vlachos, P.; Engskog, M.K.R.; Herrera, A.J.; Espinosa-Oliva, A.M.; Joseph, B.; Hajji, N.; Venero, J.L.; Burguillos, M.A. Microglia: Agents of the CNS Pro-Inflammatory Response. *Cells* **2020**, *9*, 1717. [CrossRef] [PubMed]
29. Li, C.; Wang, S.; Yan, J.-L.; Piper, R.J.; Liu, H.; Torheim, T.; Kim, H.; Zou, J.; Boonzaier, N.R.; Sinha, R.; et al. Intratumoral Heterogeneity of Glioblastoma Infiltration Revealed by Joint Histogram Analysis of Diffusion Tensor Imaging. *Neurosurgery* **2019**, *85*, 524–534. [CrossRef]
30. Broekman, M.L.; Maas, S.L.N.; Abels, E.R.; Mempel, T.R.; Krichevsky, A.M.; Breakefield, X.O. Multidimensional communication in the microenvirons of glioblastoma. *Nat. Rev. Neurol.* **2018**, *14*, 482–495. [CrossRef]
31. Chen, Z.; Hambardzumyan, D. Immune Microenvironment in Glioblastoma Subtypes. *Front. Immunol.* **2018**, *9*, 1004. [CrossRef]
32. Anfray, C.; Ummarino, A.; Andón, F.T.; Allavena, P. Current Strategies to Target Tumor-Associated-Macrophages to Improve Anti-Tumor Immune Responses. *Cells* **2020**, *9*, 46. [CrossRef]
33. Zhang, I.; Beus, M.; Stochaj, U.; Le, P.U.; Zorc, B.; Rajic, Z.; Petrecca, K.; Maysinger, D. Inhibition of glioblastoma cell proliferation, invasion, and mechanism of action of a novel hydroxamic acid hybrid molecule. *Cell Death Discov.* **2018**, *4*, 41. [CrossRef]
34. Del Duca, D.; Werbowetski, T.; Del Maestro, R.F. Spheroid preparation from hanging drops: Characterization of a model of brain tumor invasion. *J. Neurooncol.* **2004**, *67*, 295–303. [CrossRef]
35. Ji, J.; Moquin, A.; Bertorelle, F.; Ky Chang, P.; Antoine, R.; Luo, J.; McKinney, R.A.; Maysinger, D. Organotypic and primary neural cultures as models to assess effects of different gold nanostructures on glia and neurons. *Nanotoxicology* **2019**, *13*, 285–304. [CrossRef]
36. Bonačić-Koutecký, V.; Antoine, R. Enhanced two-photon absorption of ligated silver and gold nanoclusters: Theoretical and experimental assessments. *Nanoscale* **2019**, *11*, 12436–12448. [CrossRef]
37. Maysinger, D.; Gran, E.R.; Bertorelle, F.; Fakhouri, H.; Antoine, R.; Kaul, E.S.; Samhadaneh, D.A.; Stochaj, U. Gold nanoclusters elicit homeostatic perturbations in glioblastoma cells and adaptive changes of lysosomes. *Theranostics* **2019**. [CrossRef]
38. Hakkinen, H. Atomic and electronic structure of gold clusters: Understanding flakes, cages and superatoms from simple concepts. *Chem. Soc. Rev.* **2008**, *37*, 1847–1859. [CrossRef]
39. Jin, R.; Zeng, C.; Zhou, M.; Chen, Y. Atomically Precise Colloidal Metal Nanoclusters and Nanoparticles: Fundamentals and Opportunities. *Chem. Rev.* **2016**, *116*, 10346–10413. [CrossRef] [PubMed]

40. Macairan, J.-R.; Zhang, I.; Clermont-Paquette, A.; Naccache, R.; Maysinger, D. Optical Sensing: Ratiometric pH Sensing in Living Cells Using Carbon Dots (Part. Part. Syst. Charact. 1/2020). *Part. Part. Syst. Charact.* **2020**, *37*, 2070002. [CrossRef]
41. Olzmann, J.A.; Carvalho, P. Dynamics and functions of lipid droplets. *Nat. Rev. Mol. Cell Biol.* **2019**, *20*, 137–155. [CrossRef]
42. Marschallinger, J.; Iram, T.; Zardeneta, M.; Lee, S.E.; Lehallier, B.; Haney, M.S.; Pluvinage, J.V.; Mathur, V.; Hahn, O.; Morgens, D.W.; et al. Lipid-droplet-accumulating microglia represent a dysfunctional and proinflammatory state in the aging brain. *Nat. Neurosci.* **2020**, *23*, 194–208. [CrossRef]
43. Schulze, R.J.; Sathyanarayan, A.; Mashek, D.G. Breaking fat: The regulation and mechanisms of lipophagy. *Biochim. Biophys Acta* **2017**, *1862*, 1178–1187. [CrossRef] [PubMed]
44. Pu, J.; Guardia, C.M.; Keren-Kaplan, T.; Bonifacino, J.S. Mechanisms and functions of lysosome positioning. *J. Cell Sci.* **2016**, *129*, 4329–4339. [CrossRef]
45. Davis, M.E. Glioblastoma: Overview of Disease and Treatment. *Clin. J. Oncol. Nurs.* **2016**, *20*, S2–S8. [CrossRef]
46. Ramachandran, R.K.; Sørensen, M.D.; Aaberg-Jessen, C.; Hermansen, S.K.; Kristensen, B.W. Expression and prognostic impact of matrix metalloproteinase-2 (MMP-2) in astrocytomas. *PLoS ONE* **2017**, *12*, e0172234. [CrossRef]
47. Vollmann-Zwerenz, A.; Leidgens, V.; Feliciello, G.; Klein, C.A.; Hau, P. Tumor Cell Invasion in Glioblastoma. *Int. J. Mol. Sci.* **2020**, *21*, 1932. [CrossRef]
48. Medema, J.P. Cancer stem cells: The challenges ahead. *Nat. Cell Biol.* **2013**, *15*, 338–344. [CrossRef]
49. Cakir, B.; Xiang, Y.; Tanaka, Y.; Kural, M.H.; Parent, M.; Kang, Y.-J.; Chapeton, K.; Patterson, B.; Yuan, Y.; He, C.-S.; et al. Engineering of human brain organoids with a functional vascular-like system. *Nat. Methods* **2019**, *16*, 1169–1175. [CrossRef] [PubMed]
50. Johnson, D.E.; Ostrowski, P.; Jaumouillé, V.; Grinstein, S. The position of lysosomes within the cell determines their luminal pH. *J. Cell Biol.* **2016**, *212*, 677–692. [CrossRef]
51. Zhang, I.; Cui, Y.; Amiri, A.; Ding, Y.; Campbell, R.E.; Maysinger, D. Pharmacological inhibition of lipid droplet formation enhances the effectiveness of curcumin in glioblastoma. *Eur. J. Pharm. Biopharm.* **2016**, *100*, 66–76. [CrossRef]
52. Dubey, R.; Stivala, C.E.; Nguyen, H.Q.; Goo, Y.-H.; Paul, A.; Carette, J.E.; Trost, B.M.; Rohatgi, R. Lipid droplets can promote drug accumulation and activation. *Nat. Chem. Biol.* **2020**, *16*, 206–213. [CrossRef] [PubMed]
53. Treyer, A.; Mateus, A.; Wiśniewski, J.R.; Boriss, H.; Matsson, P.; Artursson, P. Intracellular Drug Bioavailability: Effect of Neutral Lipids and Phospholipids. *Mol. Pharm.* **2018**, *15*, 2224–2233. [CrossRef]
54. Boutej, H.; Rahimian, R.; Thammisetty, S.S.; Béland, L.-C.; Lalancette-Hébert, M.; Kriz, J. Diverging mRNA and Protein Networks in Activated Microglia Reveal SRSF3 Suppresses Translation of Highly Upregulated Innate Immune Transcripts. *Cell Rep.* **2017**, *21*, 3220–3233. [CrossRef]
55. Liddelow, S.A.; Guttenplan, K.A.; Clarke, L.E.; Bennett, F.C.; Bohlen, C.J.; Schirmer, L.; Bennett, M.L.; Münch, A.E.; Chung, W.-S.; Peterson, T.C.; et al. Neurotoxic reactive astrocytes are induced by activated microglia. *Nature* **2017**, *541*, 481–487. [CrossRef]
56. Mummery, R.S.; Rider, C.C. Characterization of the heparin-binding properties of IL-6. *J. Immunol.* **2000**, *165*, 5671–5679. [CrossRef]
57. Roesch, S.; Rapp, C.; Dettling, S.; Herold-Mende, C. When Immune Cells Turn Bad—Tumor-Associated Microglia/Macrophages in Glioma. *Int. J. Mol. Sci.* **2018**, *19*, 436. [CrossRef] [PubMed]
58. Sims, G.P.; Rowe, D.C.; Rietdijk, S.T.; Herbst, R.; Coyle, A.J. HMGB1 and RAGE in Inflammation and Cancer. *Annu. Rev. Immunol.* **2010**, *28*, 367–388. [CrossRef]
59. Rapoport, B.L.; Steel, H.C.; Theron, A.J.; Heyman, L.; Smit, T.; Ramdas, Y.; Anderson, R. High Mobility Group Box 1 in Human Cancer. *Cells* **2020**, *9*, 1664. [CrossRef]
60. Matarredona, E.R.; Pastor, A.M. Extracellular Vesicle-Mediated Communication between the Glioblastoma and Its Microenvironment. *Cells* **2020**, *9*, 96. [CrossRef]
61. Conti, I.; Varano, G.; Simioni, C.; Laface, I.; Milani, D.; Rimondi, E.; Neri, L.M. miRNAs as Influencers of Cell–Cell Communication in Tumor Microenvironment. *Cells* **2020**, *9*, 220. [CrossRef] [PubMed]
62. Gieryng, A.; Pszczolkowska, D.; Walentynowicz, K.A.; Rajan, W.D.; Kaminska, B. Immune microenvironment of gliomas. *Lab. Invest.* **2017**, *97*, 498–518. [CrossRef]

63. Kobara, H.; Miyamoto, T.; Suzuki, A.; Asaka, R.; Yamada, Y.; Ishikawa, K.; Kikuchi, N.; Ohira, S.; Shiozawa, T. Lipocalin2 enhances the matrix metalloproteinase-9 activity and invasion of extravillous trophoblasts under hypoxia. *Placenta* **2013**, *34*, 1036–1043. [CrossRef]
64. Lin, Y.; Ren, J.; Qu, X. Catalytically active nanomaterials: A promising candidate for artificial enzymes. *Acc. Chem. Res.* **2014**, *47*, 1097–1105. [CrossRef]
65. Ferber, S.; Tiram, G.; Sousa-Herves, A.; Eldar-Boock, A.; Krivitsky, A.; Scomparin, A.; Yeini, E.; Ofek, P.; Ben-Shushan, D.; Vossen, L.I.; et al. Co-targeting the tumor endothelium and P-selectin-expressing glioblastoma cells leads to a remarkable therapeutic outcome. *Elife* **2017**, *6*. [CrossRef]
66. Sousa-Herves, A.; Würfel, P.; Wegner, N.; Khandare, J.; Licha, K.; Haag, R.; Welker, P.; Calderón, M. Dendritic polyglycerol sulfate as a novel platform for paclitaxel delivery: Pitfalls of ester linkage. *Nanoscale* **2015**, *7*, 3923–3932. [CrossRef]
67. Mendes, L.P.; Sarisozen, C.; Luther, E.; Pan, J.; Torchilin, V.P. Surface-engineered polyethyleneimine-modified liposomes as novel carrier of siRNA and chemotherapeutics for combination treatment of drug-resistant cancers. *Drug Deliv.* **2019**, *26*, 443–458. [CrossRef]
68. Subhan, M.A.; Torchilin, V.P. Efficient nanocarriers of siRNA therapeutics for cancer treatment. *Transl Res.* **2019**, *214*, 62–91. [CrossRef]
69. Gerecke, C.; Edlich, A.; Giulbudagian, M.; Schumacher, F.; Zhang, N.; Said, A.; Yealland, G.; Lohan, S.B.; Neumann, F.; Meinke, M.C.; et al. Biocompatibility and characterization of polyglycerol-based thermoresponsive nanogels designed as novel drug-delivery systems and their intracellular localization in keratinocytes. *Nanotoxicology* **2017**, *11*, 267–277. [CrossRef] [PubMed]
70. Machado, E.; White-Gilbertson, S.; van de Vlekkert, D.; Janke, L.; Moshiach, S.; Campos, Y.; Finkelstein, D.; Gomero, E.; Mosca, R.; Qiu, X.; et al. Regulated lysosomal exocytosis mediates cancer progression. *Sci. Adv.* **2015**, *1*, e1500603. [CrossRef]
71. Sundler, R. Lysosomal and cytosolic pH as regulators of exocytosis in mouse macrophages. *Acta Physiol. Scand.* **1997**, *161*, 553–556. [CrossRef]
72. Kepsutlu, B.; Wycisk, V.; Achazi, K.; Kapishnikov, S.; Pérez-Berná, A.J.; Guttmann, P.; Cossmer, A.; Pereiro, E.; Ewers, H.; Ballauff, M.; et al. Cells Undergo Major Changes in the Quantity of Cytoplasmic Organelles after Uptake of Gold Nanoparticles with Biologically Relevant Surface Coatings. *ACS Nano* **2020**, *14*, 2248–2264. [CrossRef]
73. Marx, V. Reality check for organoids in neuroscience. *Nat. Methods* **2020**, *17*, 961–964. [CrossRef]

Supplemental materials

Nanotherapeutic modulation of human neural cells and glioblastoma in organoids and monocultures

Issan Zhang, Paula Lépine, Chanshuai Han, Maria Lacalle-Aurioles, Carol X.-Q. Chen, Rainer Haag, Thomas M. Durcan and Dusica Maysinger

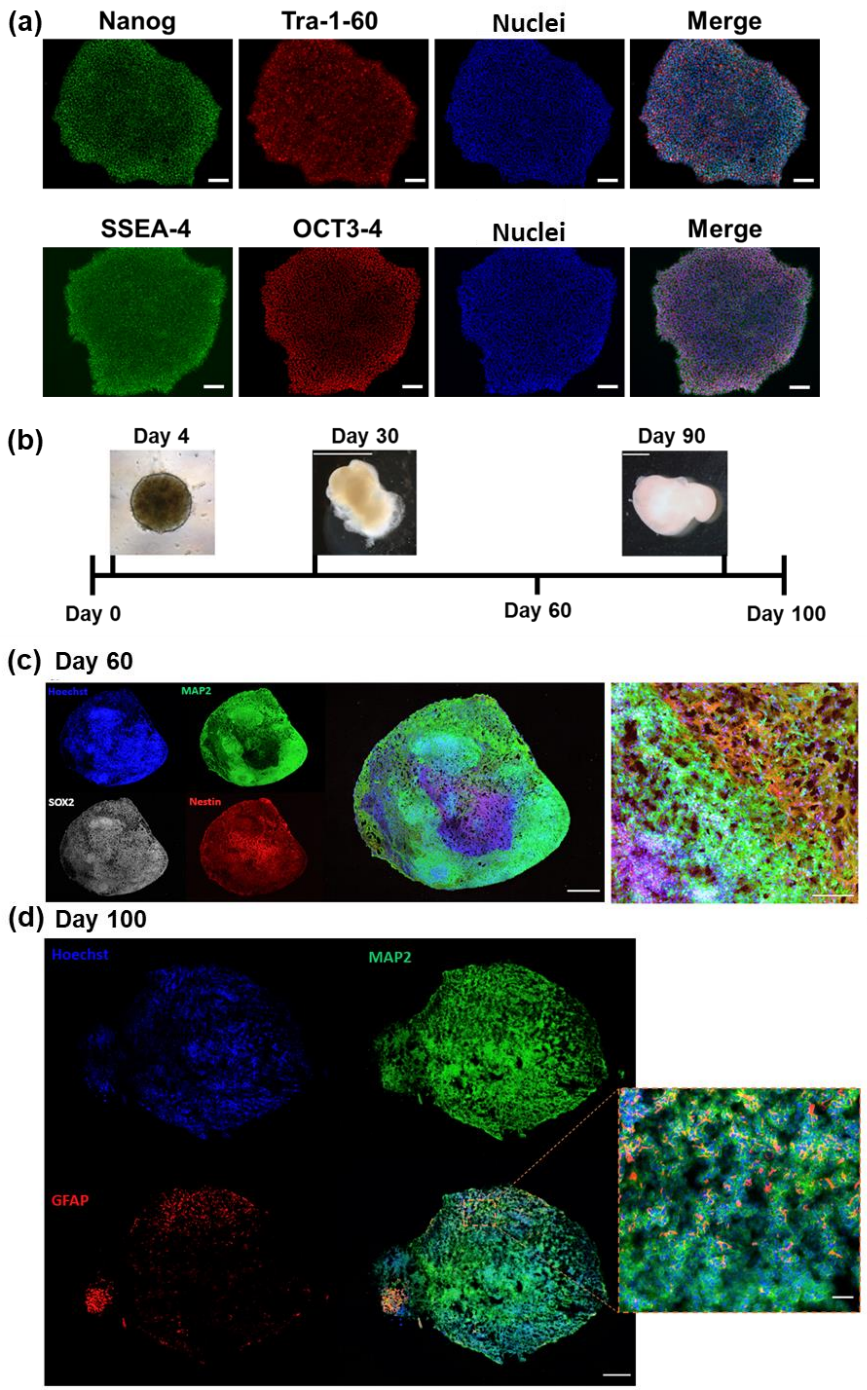

Figure S1. (a) Expression of pluripotency markers in human iPSCs. Immunofluorescence images of NCRM1 cells labelled for the pluripotency markers SSEA-4, Oct3-4, Nanog and Tra-1-60 with nuclear staining (DAPI). Scale bar: 200 μm. **(b)** Timeline of cerebral organoid growth and development from iPSCs, over 100 days. **(c,d)** Stemness (SOX2, Nestin) and neural markers in cerebral organoids at day 60 and 100. Immunofluorescence staining for mature neurons expressing microtubule associated protein 2 (MAP2) and astrocytes expressing glial fibrillary acidic protein (GFAP). Staining of cell nuclei with Hoechst 33342. Scale bar: 200 μm (for higher magnification: scale bar: 25 μm).

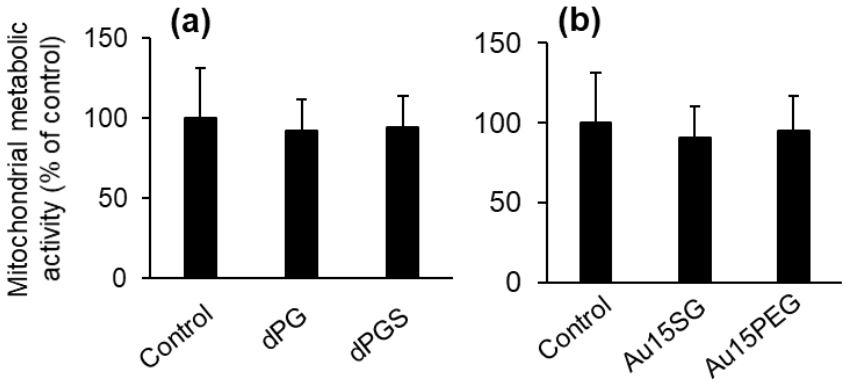

Figure S2. (a) Mitochondrial metabolic activity in cerebral organoids following treatment with dPG and dPGS (1 μM, 72 h), using the MTT assay. Shown are the average percentage mitochondrial metabolic activity ±SD. **(b)** Mitochondrial metabolic activity in cerebral organoids following treatment with gold nanoclusters Au15SG and Au15PEG (1 μM, 72 h), using the MTT assay. Shown are the average percentage mitochondrial metabolic activity ±SD.

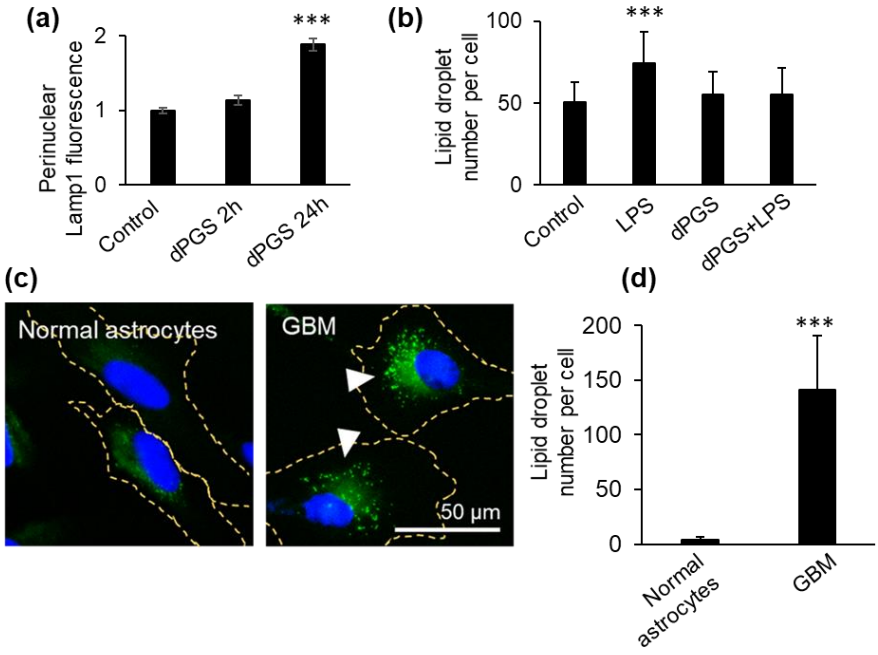

Figure S3. (a) Increase in microglial perinuclear lysosomal marker Lamp1 in response to dPGS treatment. Human HMC3 microglia were treated with dPGS (1 µM) for 2 h or 24 h, then Lamp1 was fluorescently labeled by immunocytochemistry. Cells were imaged using a fluorescent microscope and perinuclear signal (within 5 µm of the nucleus) was measured in ImageJ. Shown are the average perinuclear Lamp1 signal per cell ±SEM. 356 cells were analyzed from two independent experiments. ***p<0.001 **(b)** Increase in microglial lipid droplet numbers in response to LPS and normalization of lipid droplet numbers with dPGS. Human HMC3 microglia were treated with LPS (10 ng/mL) with or without dPGS (1 µM) for 24 h, after which lipid droplets were fluorescently labeled with BODIPY 493/503 and imaged using a fluorescence microscope. The number of lipid droplets per cell was counted manually. Shown are the average number of lipid droplets per cell ±SEM. At least 250 cells from three independent experiments were analyzed. ***p<0.001 **(c)** Fluorescence micrographs of lipid droplets in human primary astrocytes and U251N glioblastoma (astrocytoma) cells. Lipid droplets were labelled as in (b) and imaged using a fluorescence microscope. **(d)** Shown are the average number of lipid droplets in human primary astrocytes and glioblastoma cells ±SD. 51 cells were analyzed from two independent experiments. ***p<0.001

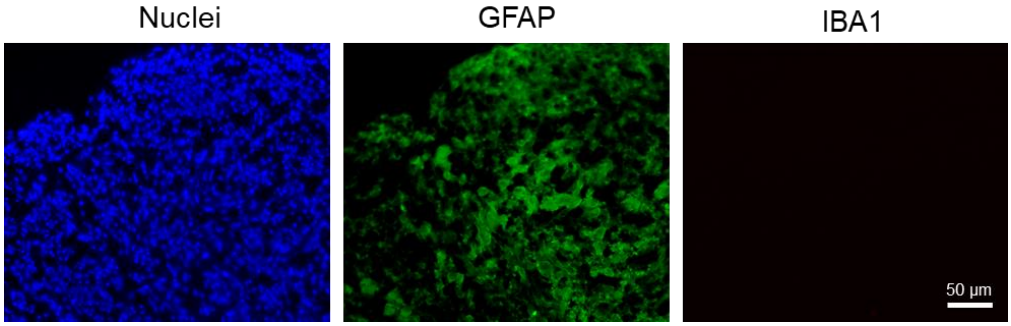

Figure S4. Absence of microglia from the cerebral organoids, as shown by IBA1 labeling. Immunofluorescence staining for astrocytes with GFAP and microglia with IBA1. Staining of cell nuclei with Hoechst 33342.

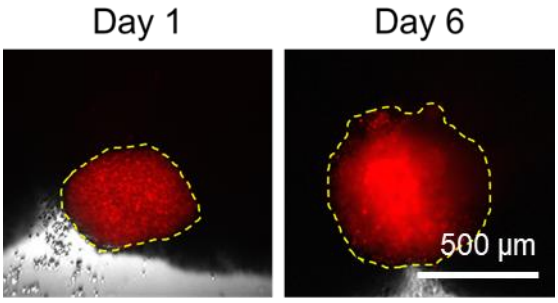

Figure S5. Glioblastoma tumoroid has limited invasiveness in cerebral organoids in the absence of microglia cells. Fluorescently-labeled glioblastoma tumoroids were implanted in cerebral organoids and imaged after 6 days for infiltrative invasiveness using a fluorescence microscope.

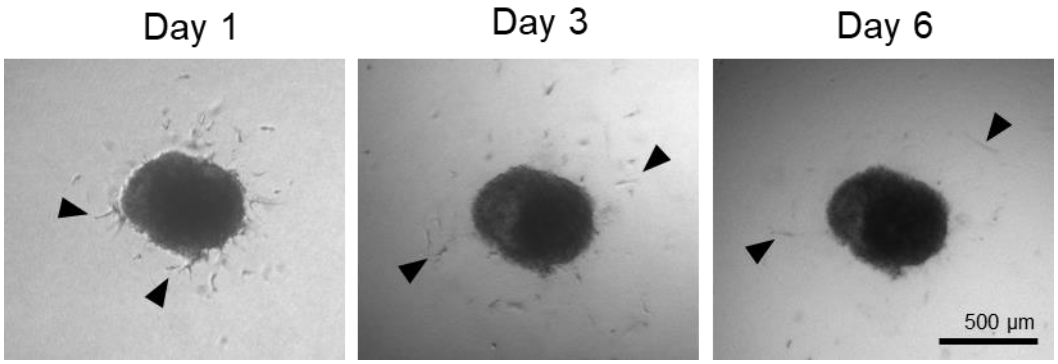

Figure S6. Movement of normal human astrocytes in 3D culture. Human astrocyte spheroids were implanted into collagen gels and cultured for 6 days. Spheroids were imaged using brightfield.

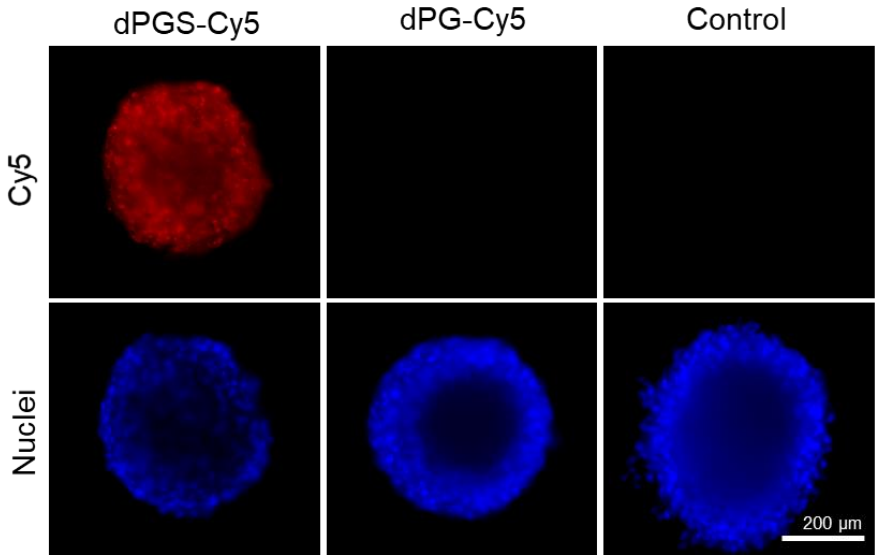

Figure S7. Internalization of fluorescent dPGS-Cy5 in glioblastoma tumoroids. Shown are representative fluorescence micrographs of glioblastoma tumoroids treated with dPGS-CY5 (red) or dPG-Cy5 for 24h at 1 µM. Nuclei were labeled with Hoechst 33342 (blue). Tumoroids were imaged using a fluorescence microscope.